2014

Processing graphene oxide and carbon nanotubes: routes to self- assembly of designed architectures for energy storage applications

Seyed Hamed Aboutalebi
University of Wollongong

UNIVERSITY OF WOLLONGONG

Australian Institute for Innovative Materials (AIIM)

Institute for Superconducting and Electronic Materials (ISEM)

Processing Graphene Oxide and Carbon Nanotubes: Routes to Self-Assembly of Designed Architectures for Energy Storage Applications

Seyed Hamed Aboutalebi

The thesis is submitted in fulfilment of the requirements for the Award of the Degree of

Doctor of Philosophy

University of Wollongong

Feb 2014

Declaration

I, Seyed Hamed Aboutalebi, declare that this thesis, submitted in fulfilment of the requirements for the award of Doctor of Philosophy, at the Australian Institute for Innovative Materials, University of Wollongong, is wholly my own work unless otherwise referenced or acknowledged. The document has not been submitted for qualification at any other academic institution.

Seyed Hamed Aboutalebi

Feb, 2014

This work is dedicated to my parents, Mrs. Fatemeh Mazloum and Mr. Seyed Esfandiyar Aboutalebi for their unconditional love and support through all stages of my life.

Table of Contents

List of Figures

---

sheets are randomly dispersed in the solution. b, c) Upon increasing concentration to 0.25 mg ml^{-1} some nematic ordering starts to appear. At this region, the storage modulus increases and overtakes the loss modulus, while the loss modulus remains almost constant with frequency. This can be attributed to the increase in the volume fraction of colloidal particles imparting elasticity to the system. However, this increase in concentration is very negligible to impart any serious effects on the loss modulus, as the dominating part is still water. d) The dispersion forms a single phase nematic liquid crystal. This phase transformation frees up some additional space in the dispersion resulting in subsequent gain in entropy as well as a drop in elastic modulus. e) Further increase in concentration results in higher packing of nematic phase. An increase in volume fraction of GO sheets results in a frequency dependent plateau-like behaviour which is the direct consequence of sheets being trapped by their neighbours preventing the stress relaxation on the longest time-scale of the measurement. (Jammed systems such as weak polymer gels, entangled polymer networks, concentrated emulsions or biological cells exhibit this generic behaviour).[10, 12, 13] f) In addition to long-range orientation in the nematic phase, some parts in GO exhibit long-range positional order. However, above this critical concentration, as the formation of nematic LC phase is completed, further increase in volume fraction results in the simultaneous increase in both moduli, with the storage modulus increasing much faster than the loss modulus. g and h) smaller monodomains are formed associated to exceptional increase in elastic modulus. 140

Figure 7. 3. (A) Storage and loss moduli of GO suspensions with varying concentration: 13.35 mg ml^{-1}, 4.5 mg ml^{-1}, 2.5 mg ml^{-1}, 0.25 mg ml^{-1} and 0.05 mg ml^{-1}. (B) Storage modulus of GO suspension at 0.01 Hz vs $(\phi - \phi*)$, where ϕ is GO volume fraction. $Go' \sim (\phi - \phi*)\upsilon$: $\phi* \cong 2.3\times10^{-4} \pm 0.7\times10^{-4}$; $\upsilon \cong 2.75 \pm 0.15$. 141

Figure 7. 4. Figure. 2. A correlation between rheological properties and the key prerequisites for various manufacturing techniques enabled us to process and fabricate GO via a wide range

of industrial techniques. a) Ratio of elastic and storage moduli for various GO concentrations measured over a range of testing frequencies. Overlaid are the approximate processing regimes for a number of industrial fabrication techniques. When the viscous modulus (G") dominates, the GO dispersion is suitable for high rate processing methods where the dispersion must spread on contact with the substrate. However, when the elastic modulus (G') is high the rheological properties suit fabrication methods requiring the dispersion to keep its given shape, such as extrusion printing and fibre spinning. b) Photograph of electrospraying of a viscoelastic liquid of GO dispersion at a concentration of 0.05 mg ml^{-1}. c) Photograph of a GO thin film that was spray coated and thermally reduced (overnight at 220 ^{o}C) utilizing a transitional state to viscoelastic liquid GO dispersion of 0.25 mg ml^{-1}. d) Transparency of the spray coated reduced GO thin films as function of coating layers; the numbers show the number of coating layers. e) Ink-jet printed logo using LC GO viscoelastic soft solid at concentration of 0.75 mg ml^{-1}. f) As-prepared wet-spun fibers from LC GO viscoelastic soft solid at concentration of 2.5 mg ml^{-1}. g) Cross section of the wet-spun LC GO fiber, showing that GO sheets are stacked in layers with some degree of folding and are ordered due to the formation of nematic liquid crystals. h) Extrusion printed pattern using LC GO viscoelastic gel of 4.5 mg ml^{-1}. i) Extrusion printed 3D architecture using LC GO viscoelastic gel of 13.3 mg ml^{-1}. j) Dry-spinning of LC GO fibers utilizing LC GO viscoelastic gel of 13.3 mg ml^{-1}. 143

Figure 7. 5. Interpretation of rheological behaviour of LC GO dispersions. a) Yield strain (γ_Y) and yield stress (σ_Y) of various GO suspensions determined at different GO volume fractions. Yield point is considered as where the storage and loss moduli intercept when measured as a function of frequency. b) Storage (elastic) and loss (viscous) moduli of GO suspensions at the frequency of 0.01 Hz at different strains. No strain-stiffening can be observed even at very high concentrations which is consistent with SGM rheology generally exhibiting yielding and

---

Abstract

The development of processing routes, methods and protocols to process graphene oxide and carbon nanotubes for Energy storage applications is presented in this thesis. The main objectives that are addressed in this thesis are: i) developing routes for solvophobic soft self-assembly of ultra-large liquid crystalline (LC) graphene oxide (GO) sheets in a wide range of organic solvents, many of which were not known to afford solvophobic self-assembly prior to this thesis, ii) developing a solid understanding in the required criteria and mechanisms through which the solvophobic self-assembly is enabled and providing new insights contributing to the fundamental understanding of the solvophobic effect and the parameters affecting the self-assembly process, iii) probing and quantifying dynamic rheological behaviour of LC GO dispersions to extend the general understanding of the mechanics involved in order to deliberately translate these intrinsic properties into the design process and device applications, iv) utilizing the fundamental knowledge gained through these investigations to create a platform to process these materials at industrially highly-scalable levels for energy storage applications. As such, a novel soft self-assembly process is first introduced to synthesize graphene oxide liquid crystals with an ultra large sheet size in a wide–range of solvents based on a solution-phase method involving pre-exfoliation of graphite flakes. Spontaneous formation of lyotropic nematic liquid crystals is identified upon the addition of the ultralarge graphene oxide sheets in these solvents above a critical concentration of about 0.025 wt%. It is the lowest filler content ever reported for the formation of liquid crystals from any colloid, arising mainly from the ultrahigh aspect ratio of the graphene oxide sheets of over 30000. It is then, demonstrated that the scalable liquid crystal route can be employed as a new method to prepare unique 3-D framework of graphene oxide layers with proper interlayer spacing as building blocks for cost-effective high-capacity energy storage media. The intercalation of

MWCNTs as 1D spacers between graphene oxide framework results in a strong synergistic effect between the two materials consequently leading to a robust and superior hybrid material with higher capacitance compared to either graphene oxide or MWCNTs and unrivalled hydrogen storage capacity at ambient temperature. Based on rheological insights, an entirely new, scalable, and commercially viable wet-spinning strategy is demonstrated to fabricate unlimited lengths of highly porous, yet densely packed and mechanically robust and flexible all-around multifunctional graphene yarns from liquid crystals of ultra-large graphene oxide sheets, for the first time. The produced yarns, which are the only practical form of these architectures for real-life device applications, are found to be mechanically robust (Young's modulus in excess of 29 GPa), with high native electrical conductivity (2508 ± 632 S m−1) and exceptionally high specific surface area (2605 m2 g-1 before reduction and 2210 m2 g-1 after reduction) and capacitances as high as 410 F g-1/electrode in a practical two electrode configuration set-up. At the next step, the feasibility of achieving biaxial liquid crystals employing hybrid dispersions of one-dimensional and two-dimensional colloidal dispersions is demonstrated. It is shown that the collective behaviour and coordination of individual components in such biaxial liquid crystals enables stigmergic ordering which is the first report on stigmergic-emergent intelligence in non-biological materials. As an example of many promising applications, it is demonstrated that the inherent electrochemical, electrical properties of the final self-constructed architectures are practical in alternative energy storage and conversion devices. The system is shown to exhibit excellent high-rate capability far exceeding the recent literature capacitance values reported for other comparable architectures including aligned/patterned SWNTs thin films supercapacitors and microdevices even at much lower current densities.

Acknowledgement

It would have not been possible to carry out this research without the unconditional help and support of all kind people around me.

Above all, I would like to thank my parents who provided me with unequivocal Love and support.

I would like to thank my principle supervisor Dr. Konstantin Konstantinov whose enthusiasm through all phases of my research project on both academic and personal level served as a great motivation for me. I also like to thank my co-supervisor A/Prof Andrezj Calka for his support during my PhD life.

I would like to acknowledge the valuable discussions with Prof. Philippe Poulin from CNRS, France, Prof. Dennis Tallman from North Dakota State University, USA, and Dr. Pirooz Marashi from Amirkabir University of Technology, Iran.

I would also acknowledge the generous help and support of my friends Dr. Rouhollah Jalili for graphene oxide fiber synthesis, and characterization and Mrs. Dorna Esrafilzadeh for graphene oxide fiber synthesis. Thanks to Dr. Sima Aminorroaya-Yamini for hydrogen storage measurements. Thanks to Dr. Sina Naficy for the help with rheological measurements. Thanks to Mr. Alfred T. Chidembo for his help and support in electrochemical characterization of my samples.

Technical assistance from people at University of Wollongong, Dr. David Wexler, Mr. Darren Attard, Mr. Tony Romeo, A/Prof. Peter Innis, Dr. Sima Aminorroaya-Yamini, Dr. Ivan Nevirkovets, is also highly appreciated.

I would like to thank Dr. Maryam Salari and Dr. Masih Rezaee for their kindness, friendship, and support from the first day that I came to Australia till the last days. Also Dr. Salari's technical help regarding the electrochemical characterization of my samples is gratefully acknowledged. Additionally, I am also grateful to Mr. Mohsen Moazzami Goudarzi for providing me access to his unpublished results and instrumental help. Amongst my fellow postgraduate students I would also like to thank Mrs. Fagol Hasani Bijarboneh, and Mr. Hamid Reza Teymouri for stimulating discussions.

Thanks to all my friends in ISEM and AIIM, who are still here or have left for new adventures, for their support in both work and personal life.

Financial support from the University of Wollongong and the Australian Research Council (ARC, grant No. DP1093952) is also gratefully acknowledged.

Finally I would like to acknowledge ISEM, University of Wollongong and Australian government for the scholarships, awards and financial support for my PhD including APA (Australian Postgraduate Award), UPA (University Postgraduate Award), International Postgraduate Research Scholarship (IPRS), HDR scholarship and Postgraduate Student Excellence Award.

Chapter 1: Introduction

Global warming, Climate change, Clean new energy sources, Green renewable energy, these are the buzzwords that we are bombarded with in the news, in the past few decades , as a result of higher demand for cost-effective energy. However, an integral element to all these technological challenges to achieve a sustainable economy, is the development of stationary energy storage systems for keeping pace with the increasing demand for energy in different sectors. Advancements in Energy storage systems, if realized, can guarantee reliable, affordable energy which is essential for continued expansion of our economy. Moreover, although, there is a projected increase in renewable energy sources, the limiting factor that poses serious problems regarding their world-wide potential use, is our inability to efficiently store the energy and supply it on demand. This challenge, if solved, can provide wide-spread integration of renewable energy sources into the current energy market. Current Energy storage systems can be categorized into either electro-chemical based energy storage devices (batteries and supercapacitors, hydrogen storage systems) or kinetic energy based systems (compressed-air Energy storage, etc.).

No matter what method we want to employ to store energy, to attain such a goal, game-changing breakthroughs, and not incremental changes, in materials, design of new systems, and architectural design of devices should be made. Advanced materials and devices are therefore required to meet performance targets set by the US department of Energy in light of electric power industry needs. In this regard, research activities are focused on two main categories, namely, strategic material selection, and innovative system design. These two factors equally contribute to potential reduction in cost and performance advantage required to boost the so-called-for technological advances. In the current thesis, however, our focus is on strategic materials selection and architectural engineering of these materials both at nano and

macro-scales for potential development of the next generation of electro-chemical energy storage systems (supercapacitors and hydrogen storage systems). In this regard, inspired by nature, we introduce a novel class of self-assembled materials which is both abundant and cheap and has the immense potential to revolutionize the energy storage field; graphene oxide liquid crystals.

Chapter 2: Literature Review

2.1 Energy Storage

The severe environmental impacts of fossil fuel-driven world energy consumption calls for retrieving energy from alternative renewable energy resources. By the end of 2012, the entire global energy consumption was about 15 terawatts (TW) showing an almost 15% increase in power consumption compared to 2005, [1, 2] the equivalent of more than 100 billion barrels of oil. Unfortunately, over 80% of today's world energy consumption is generating from fossil fuel resources with another 6% energy use driven from nuclear power (see Figure 1).[2] Nuclear power is also not a sustainable form of energy generation, as the world's supply of U235, the only desirable isotope of Uranium, is projected to run out in the next 20 years.[2]

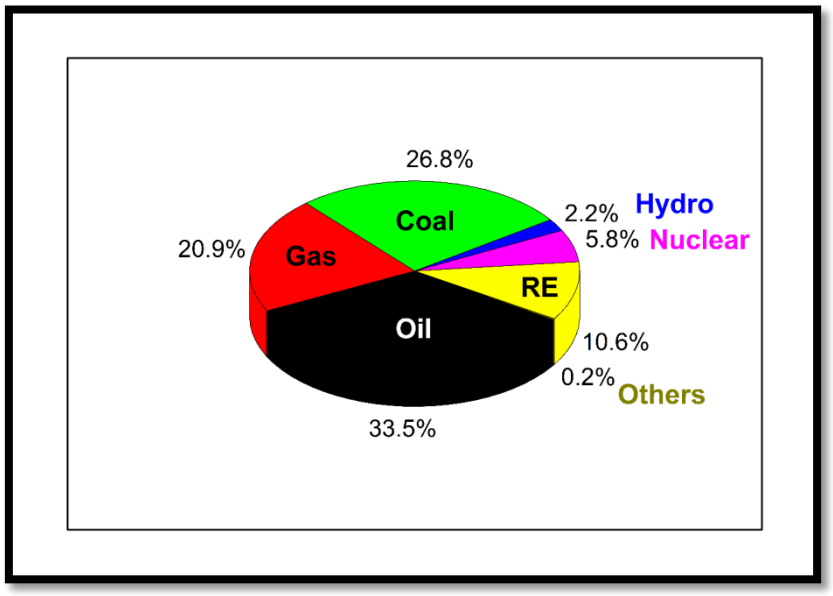

Figure 2. 1. Breakdown of the 2008 world energy consumption, with the total energy consumed being 15 TW and roughly the equivalent of 100 billion barrels of oil. The values are extracted from ref [3].

The dominant form of energy used in the world comes in the form of electric power (electricity makes up to 40% of all energy consumption in the United States by 2002).[4] The projected world-wide electricity demand suggests a 100% increase by the middle of the century.[4] However, more than 68% of world's electricity demand is supplied by fossil fuels which poses two main problems. The first and foremost problem is regarding the greenhouse gas emissions (One-megawatt electricity generated from coal-powered reactor, releases more than 1.17 million kg of CO2 per year) and the resource constraints.[1, 4] These challenges combined with energy security concerns have necessitated the need in an ever-increasing electric energy generation from renewable sources. However, the most abundant forms of renewable sources, wind and solar, are not constant and reliable sources of power, because of their variable nature. To address such intermittency, low cost electrical energy storage systems should be developed to enable smart green grid technologies. Moreover, the substantial increase in the percentage of electricity supply from renewable sources, demands for new strategies and technologies, including energy storage, to balance supply with demand.[1, 2, 4, 5]

Improvements in stationary electrical energy storage systems (SEES), therefore, can impact the reliability and the overall use of the power system. SEES can potentially be employed at large scale to power future smart grid systems by regulating generation, storage and power supply. Such a smart system can also be the answer to localized power quality issues and reactive power support (Figure 2).[4]

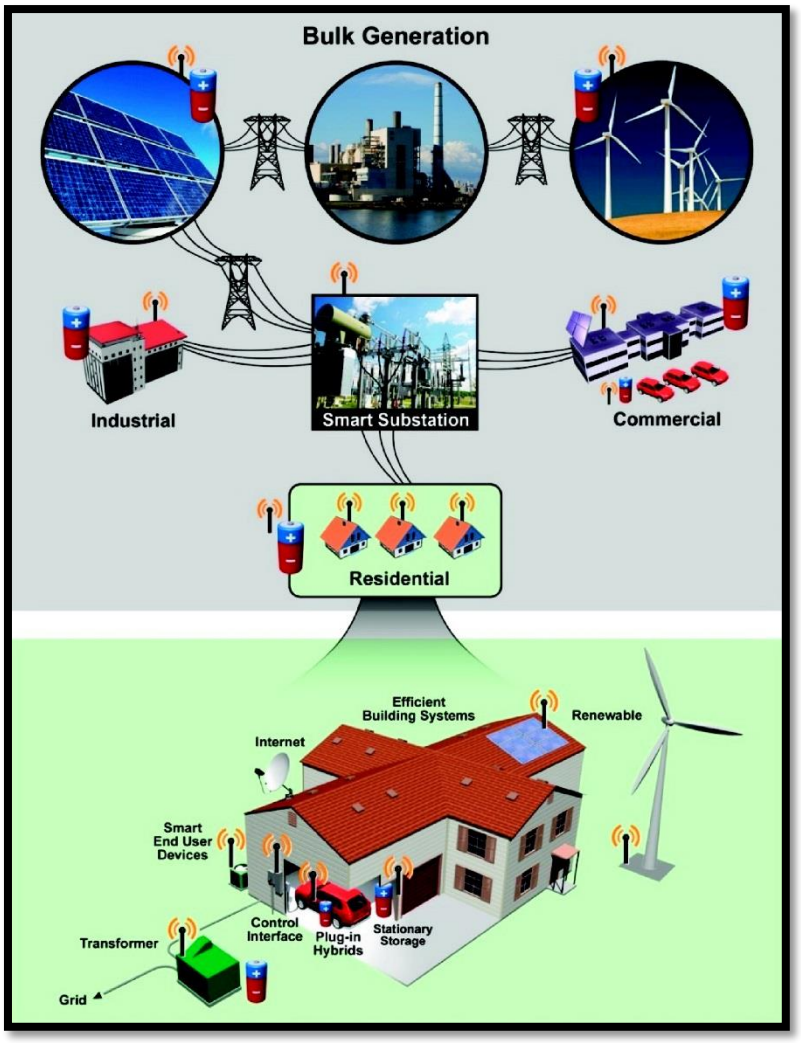

Figure 2. 2. Schematic of applications of electricity storage for generation, transmission, distribution, and end customers and future smart grid that integrates with intermittent renewables and plug-in hybrid vehicles through two-way digital communications between loads and generation or distribution grids.[6]

Smart grid system can, in principle, store electrical energy in its charging cycle while being able to inject electricity into the power grid, while there is no electricity usage, in its discharge cycle. The fast-changing dynamic profile usage of electricity requires SEES units which can quickly respond to such behaviour. Electrochemical SEES units, as a much better suited option, are now replacing conventional slow gas or steam turbine technologies for performing this duty, as they can quickly respond to grid condition. In order to have a reliable grid service, the

system needs to have fast-responding contingency reserves. It should be noted that, the faster a grid contingency reserve responds, the sooner the contingency can be managed and the less capacity is needed by the system. Therefore, fast-responding SEES units are essential assets of a smart grid system which not only can provide reliability service but also can result in higher economic efficiency of the grid. However, SEES units only contribute to only 10% of installed generation capacity in Europe. In comparison, this percentage is much lower in US, the main producer of carbon footprint, largely because of government policies.[4] Given these requirements, the potential technologies that can be used in these systems are limited. These candidates can be categorized into two domains based on how they store energy (Figure 3). The first class consists of capacitors and supercapacitors which can directly store electricity. Alternatively, the second class can store electricity by converting it into another form of energy (either kinetic, potential or chemical energy). Batteries make up for the largest portion of this class of energy storage systems.

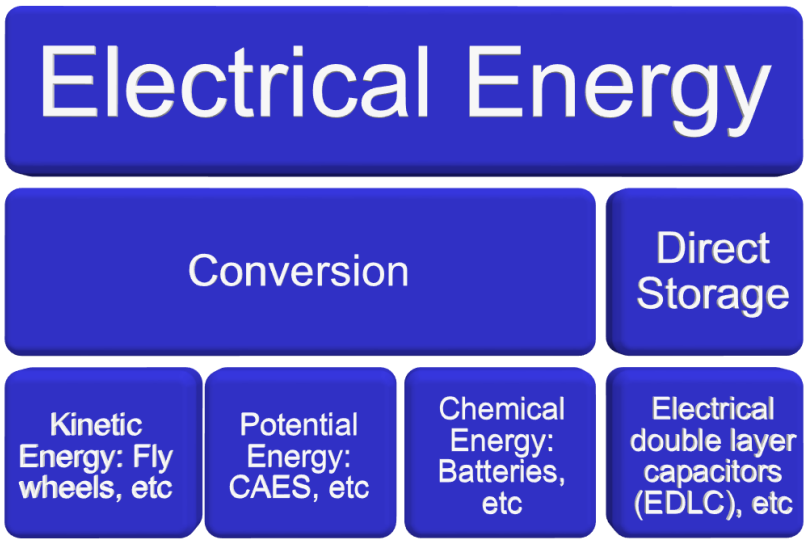

Figure 2. 3. Classification of potential electrical storage options for stationary applications.

With much less of charging time and capability to store more power compared to batteries, a new research interest in supercapacitors has been reinstated in recent years. Moreover, as supercapacitors can typically withstand millions of charge-discharge cycles (i.e. dramatic reduction in associated replacement costs and consequently greener alternative to batteries), they are more appealing to the forefront intermittent nature of renewable energy production. However, in contrast to batteries, supercapacitors suffer from very low energy density which has delayed their potential market penetration. In plain terms, the high power density of supercapacitors compared to batteries means they can enjoy much faster power delivery/uptake consequently leading to much less charging time compared to batteries. Conversely, this comes at the expense of delivering lower energy compared with batteries. Figure 4. illustrates the Ragone plot, power density vs. energy density, for the most common range of batteries and supercapacitors.

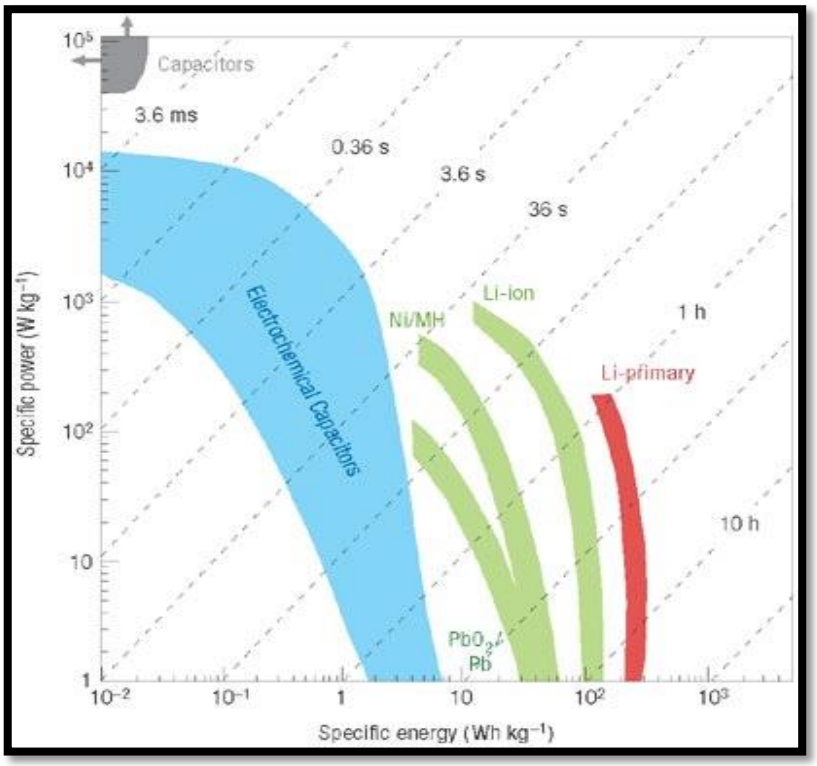

Figure 2. 4. Ragone plot of most common forms of batteries and electrochemical capacitors also known as supercapacitors. [7]

The specific power in the Ragone plot presented in Figure 4 can be interpreted of how fast an electric powered vehicle can go and the specific energy can be used as an indicator that how far such an electric vehicle can go. Clearly for an electric powered system both terms are equally important, as also indicated by a recent report by US department of Energy.[7] As such, supercapacitors are being increasingly used across a wide-range of industries with automotive and aviation industries being at the forefront.

As an example, a new European Union legislation enforces the compliment of all passenger cars with a fleet-average emissions target of 130 g CO_2/km by 2015 and 95 g CO_2/km by 2020. Just the elimination of stop-start idle in cars can reduce up to 15% related CO_2 emissions in urban driving. This necessitates a need for fast-response units which only supercapacitors can deliver.[8]

Airline industry is also responsible for an annual 2-3% of total carbon emissions. As a guideline, an airbus a380-800, with a max landing weight of 391000 kgs, in order to land has to rapidly reduce its speed from 250 to 10 km h^{-1} in less than 30 seconds. The energy waste from such a fast speed reduction is equal to 270 kWh. However, no battery system can harvest this amount of energy in such a short time period. The same scenario also applies while taking off which requires high energy consumption in very short time.

These examples can clearly demonstrate the need for fast changes in developing more efficient and more advanced supercapacitors. However, the question still remains on what materials and what architectures should be used in order to achieve such high standards.

2.2 Structure of Electrochemical supercapacitors (ECs)

In terms of structure, an EC is similar to a battery. As presented in Figure 2.5, an EC consists of two electrodes, which can be either identical or non-identical, a separator, and an electrolyte.

The whole EC system is isolated from the surrounding environment usually in a coin cell setup like batteries or different types of containers. [9] For an EC system to achieve its ultimate performance, all components are of utmost importance.[10] However, the focus of today's research is mostly on the materials used as EC electrodes as they are the most important key factor in determining the final performance of a device.

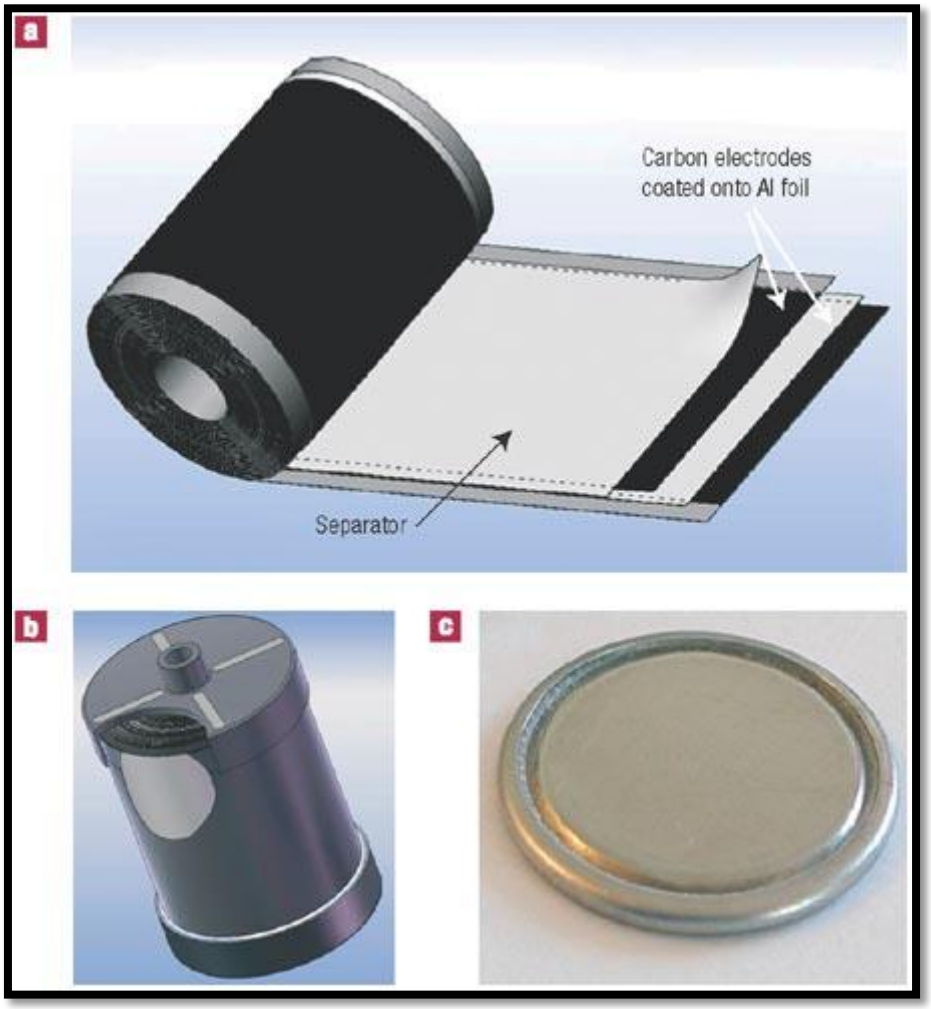

Figure 2. 5. a) Schematic of a commercial spirally wound double layer capacitor. b) Assembled device weighing 500 g and rated for 2600 F. (Photo courtesy of Batscap, Groupe Bolloré, France.) c) A small button cell, which is just 1.6 mm in height and stores 5 F. (Photo courtesy of Y-Carbon, US.) Both devices operate at 2.7 V.[7]

2.3. Supercapacitors: Basics

2.3.1. Capacitance measurements

The most important structural parameter in a supercapacitor which determines the ultimate performance of the device is the intrinsic capacitance of the active material. The capacitance shows the ability of the electro-active material to store charge and can be calculated using following equation (equation 2.1).

$$C = \frac{q}{V} \tag{2.1}$$

In which, C is the specific capacitance, q is the total amount of transferred charge and V is the applied voltage. Specific capacitance can also be reported based on the amount of charge transferred per unit mass (F g^{-1}), surface area (F cm^{-2}) or volume (F cm^{-3}) following equation 2.2.

$$C_s = \frac{I \times \Delta t}{\Delta V \times m/s} \tag{2.2}$$

where, C_s is the specific capacitance (F g^{-1}), I is the charge-discharge current (A), m is the active material mass (g), s is the specific surface area (cm^2), ΔV is the potential window (V), and Δt is the discharge time (s).

2.3.2 Energy density

Energy stored per unit of mass (Wh kg^{-1}) or volume (Wh L^{-1}) is another term which is widely used to assess the performance of a supercapacitor device. Equation 2.3 shows that the energy stored is proportional to voltage squared which is why one of the main focus of research nowadays is to increase the potential window in which the supercapacitor device can operate.

$$E_s = \frac{1}{2} \times C_s \Delta V^2 \tag{2.3}$$

where, E_s is the specific Energy density (Wh kg^{-1}) or (Wh L^{-1}), C_s is the specific capacitance (F g^{-1}) or (F L^{-1}), and ΔV is the potential window.

2.3.3 Power density

The power density of a supercapacitor device shows the capability of the device to transfer the specific energy (Wh kg^{-1}) or (Wh L^{-1}) in a given unit of time (h). Power density is usually reported per unit of mass (W kg^{-1}) or volume (W L^{-1}) following equation 2.4.

$$P_s = \frac{E_s}{\Delta t} \tag{2.4}$$

Where, P_s is the specific Power density (W kg^{-1}) or (W L^{-1}), E_s is the specific energy density (Wh kg^{-1}) or (Wh L^{-1}), and Δt is the discharge time.

2.3.4 Cycle life

Cycle life is another important criteria which differentiates supercapacitors from mediocre batteries. Cycle life shows the number of charge-discharge cycles an EC can be subjected to before it experiences a serious fall-down in measured capacitance.

2.3.5 Measurements for systems based on two-electrode configuration

Calculations for specific capacitance, (Csp), energy density (E) and power density (P) can be obtained following Equations 2.5, 2.6, and 2.7. In which, C_{sp} is the specific capacitance, I_d is the discharge current, ΔT_d is the discharge time, V is the potential difference during discharge excluding the portion of the iR drop, and m is the mass of one electrode.

$$C_{sp(CD)} = \frac{2I_d \Delta T_d}{\Delta V m} \tag{2.5}$$

$$E = \frac{1}{8} CV^2 \tag{2.6}$$

$$P = \frac{E}{\Delta T_d} \tag{2.7}$$

2.4 Classification of Supercapacitors

Supercapacitors can be classified into two main categories based on the mechanism through which they store charge and the type of active material (Figure 5). The most common class of supercapacitors that is widely used at present time in commercial applications implements the use of carbon based active materials, such as carbon active. This class mainly relies on high-surface area active materials and the electric double layer mechanism to trap and store electric charge. Therefore, this class is mostly known as electric double layer capacitors (EDLCs). The second main class consists of transition metal oxides or conducting polymers and relies on redox mechanism. This class is known as pseudo-capacitors or redox capacitors. Combining either of these two mechanisms with a battery can give rise to another class of supercapacitors known as hybrid supercapacitors.

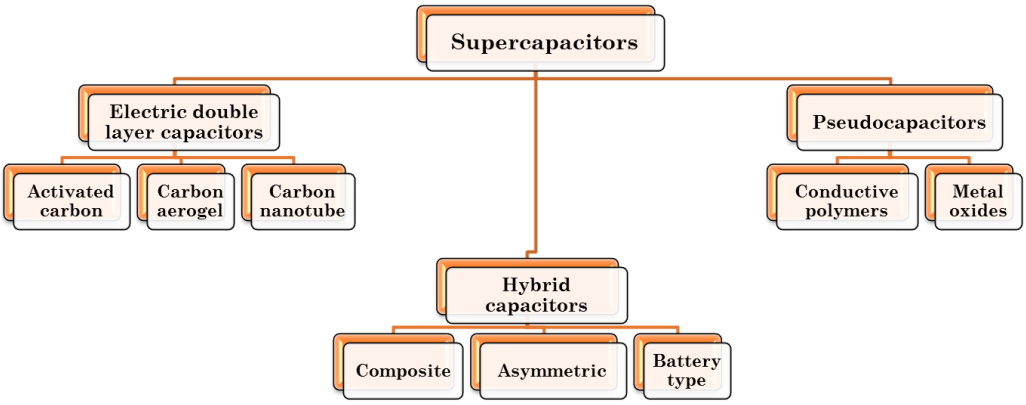

Figure 2. 6. Different categories of supercapacitors

2.4.1 Pseudo-capacitors

Pseudo-capacitors take advantage of fast redox reactions on active materials which are reversible in nature. By relying on redox reactions pseudo-capacitors can exceed specific

capacitance of carbon based electrodes. However, the same as batteries, pseudo-capacitors suffer from the loss of their capacitance as they rely on redox reactions. As such, the overall stability of these systems is not typically suitable for applications where stability and long cycle life are needed. Pseduo-capacitors can be categorized into two main sub-groups of metal oxides with the most famous ones being RuO_2, Co_3O_4, NiO, MnO_2 ,and Mn_3O_4 and conducting polymers including polyaniline, polypyrrole, polythiophene pedot:pss and their derivatives.

RuO_2, because of its three distinct oxidative states which are accessible in a 1.2 potential window, is the most eminent metal oxide used as supercapacitor electrode. In acidic electrolytes, the electron transfer in redox reactions are known to be fast and reversible (see Figure 2.7).

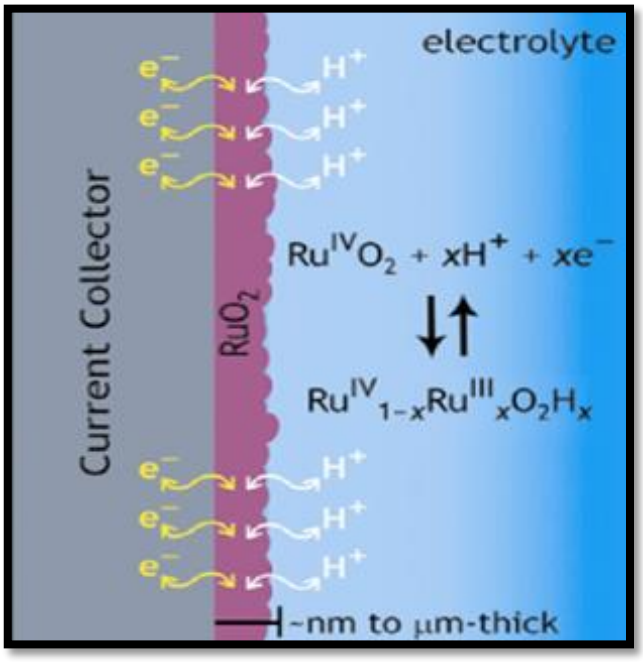

Figure 2. 7. Mechanism of reactions in a pseudo-capacitor of choice: RuO_2

This, combined with an protons electro-adsorption on the surface of RuO_2 results in specific capacitance values over 600 F g^{-1}. However, the most prominent problems which most high–

performance metal oxide pseudo-capacitors encounter are the high toxicity of these materials except for mangenese oxides and the high costs associated with the preparation of these materials stemming from the high cost of the starting material. Moreover, the potential window of these materials is limited to around 1V because of redox reactions limitations. As such, these materials cannot be used for high-energy demand applications.

Nevertheless many research efforts have been focused on increasing the capacitance of pseudo-capacitors. Owing to the fact that the pseudo-capacitance charge-storage mechanism is a surface-related property which occurs in the very first nanometers of the surface, nanostructuring has been applied as the first resort to increase the capacitance of these materials. With the aim of decreasing the size of metal-oxide particles and going into nano-scale dimensions, many research groups have developed different strategies to increase the specific surface area and consequently the ultimate specific capacitance of metal oxides.

Conducting polymer, on the other hand, have been shown to exhibit high specific capacitance over a wide potential window of about 3V. However, conducting polymers suffer from the lack of stability during cycling when used as bulk supercapacitor electrodes.

2.4.2 Electrochemical double layer capacitors (EDLCs)

The concept of EDLCs was first presented in 1957 in a patent by Becker, when he introduced the use of high specific surface area carbon in an aqueous electrolyte (sulphuric acid) for application as an electrochemical capacitor.[11] Almost a decade later, in 1971, NEC announced the first commercial aqueous electrochemical capacitors for use in power-saving units.

The charge-storage mechanism in an EDLC relies on reversible adsorption of ions of the electrolyte onto active materials. As a result, the surface area of the active material and its electrochemical stability both play important roles in the effective capacitance of the material. Helmholtz model simply describes the mechanism according to equation 2.8.

$$\frac{C}{A} = \frac{\varepsilon_r \varepsilon_0}{d} \quad (2.8)$$

Where C is the capacitance, A is the electrode surface area, ε_r is the electrolyte dielectric constant, ε_0 is the dielectric constant of the vacuum and d is the charge-separation distance. However, this model did not adequately consider factors such as diffusion of ions into solution.

Gouy and Chapman later refined the model by introducing a diffuse model for the double layer. They formulated that the accumulation of ions close to the surface is a function of distance from the electro-active material (i.e. metals in their studies). They also established that the electric potential decreases exponentially from the surface.

However, their model fails to explain the behaviour of highly charged double layers. In order to explain such behaviour, Stern came up with the idea of combining both Helmholtz and Gouy-Chapman models. He suggested that some ions can adhere onto the surface of the electro-active material (internal Stern layer) while others form a Gouy-Chapman diffuse layer (schematics of all models are given in Figure 2.8).

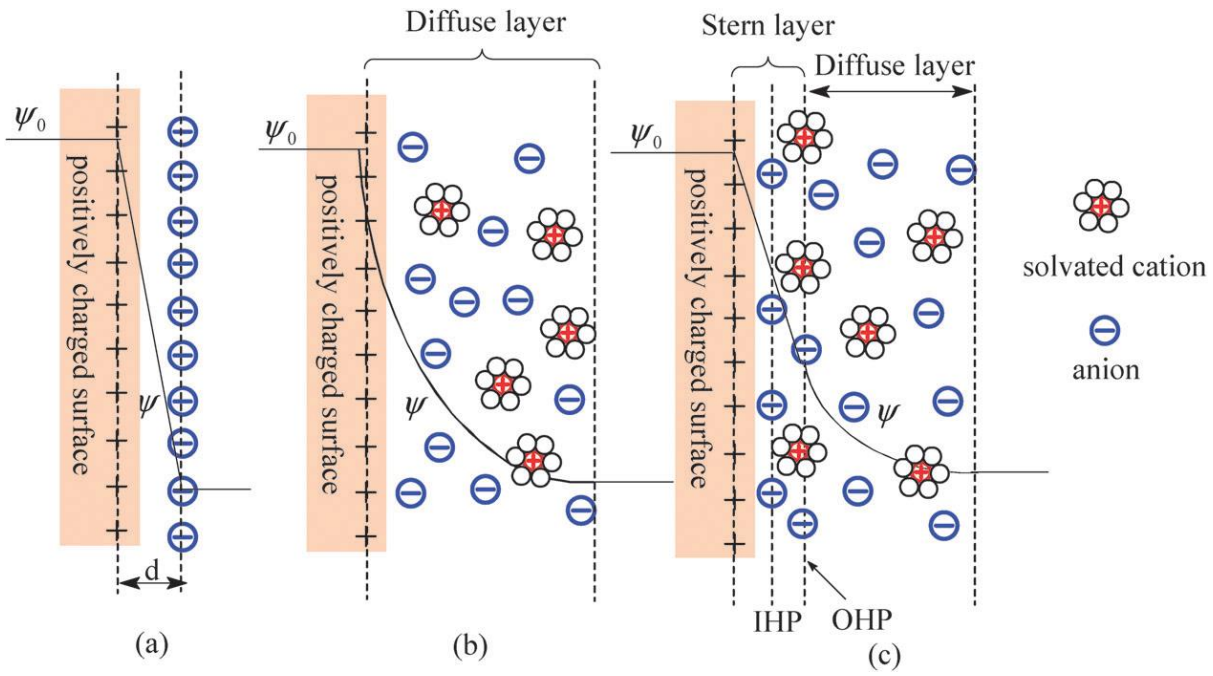

Figure 2. 8. Double-layer models at the positively charged surface: (a) Helmholtz monolayer, (b) Gouy-Chapman diffuse layer, and (c) Stern model, showing the inner Helmholtz plane (IHP) distance of closest approach of specifically adsorbed ions and the outer Helmholtz plane (OHP) where the diffuse layer begins; Ψ_0 and Ψ are the potentials on the electrode surface and the electrode/electrolyte interface, respectively. [12]

However, Stern model treats ions as point charges and simply assume all interactions are Columbic in nature, and the viscosity and dielectric permittivity are constant through the double layer. As the charge-storage mechanism is simply electrostatic, no redox (faradic) reactions take place at the surface of EDLCs. Moreover, it means that electrochemical kinetics through polarization resistance cannot limit the performance of an EDLC leading to very fast charge-discharge process and considerably higher power performance compared to batteries and pseudo-capacitors. As there is no redox reaction involved in the process, an EDLC does not suffer from swelling problems typically associated with batteries and pseudo-capacitors and can sustain its original capacitance over millions of cycles with little or no decay. Another important advantage that EDLCs enjoy in comparison with batteries is that the solvent does

not participate in the charge-storage mechanism meaning no limitation in the choice of solvents. This leads to a much wider temperature window for EDLCs. However, as the charging mechanism is only electrostatic EDLCs suffer from low energy density.

2.5. The choice of Active Materials for EDLCs

As indicated by Helmholtz formulae, the active material should indeed exhibit high surface area. Moreover, the active material should be electrically conducting, too. The most prominent material of choice is, therefore, graphitic carbon which satisfies all requirements for a good EDLC material due to its open porosity, electrochemical stability and high electrical conductivity. [7, 13-15] To increase the performance of graphitic carbon, especial treatments are usually conducted on the material to increase the porosity and consequently the specific capacitance of the material. [16] As such, many types of high surface area carbon materials including activated carbon, [17] carbon nanotubes, [18] carbon aerogels, [19] carbon onions, [20, 21] carbon nanohorns,[22, 23] and graphene [9, 24, 25] have been tested as electro-active materials of choice for supercapacitor applications. As mentioned, many types of carbon materials have been assessed in order to achieve the ultimate performance. The outlook, so far, is not promising in the case of all carbon materials except for graphene based electrodes. Carbon nanotubes and/or carbon fibers are limited to a very medicore performance of 50-80 F g^{-1} with the highest capacitance of 120 F g^{-1} being the best performer in a lithium based electrolyte.[7, 26, 27] However, the higher end of capacitance can be usually achieved by grafting oxygen functional groups (introducing multi-functionalities) to the surface of carbon nanotubes which usually comes at the expense of cycle life which is another important parameter for the assessment of a supercapacitor device.[7, 27] Activated carbon fabrics and activated carbon powders are usually good performers with a capacity of around 100 F g^{-1}, however, their high cost to performance ration has severely hindered their general application.

In order to increase the capacitance, many theoretical works were published showing that pore sizes smaller than 0.5 nm are not accessible to ions in the electrolyte.[28, 29] Those studies suggested a pore size distribution of 2-5 nm in order to maximize the capacitive performance of the material as a result of the presence of the solvated shell ions in the electrolyte which are usually half that pore size.[30-33] However, even fine-tuned mesopore carbon materials also failed to achieve high performance with an average capacitance value of just 100-120 F g^{-1} being the best to date.[7, 33] This, in turn, resulted in a renewed interest in microporous carbon. The new theoretical studies suggest that partial desolvation of ions can occur which can consequently result in an enhancement of capacitance in the system.[34] Furthermore, experimental results in the case of microporous carbon materials showed interesting capacitance values ranging from 80 to 120 F g^{-1} contradicting previous theories regarding solvated ion shell adsorption. [35-39] The experimental results in the case of carbide derived carbons (CDC) also interestingly showed the enhancement of capacitance in pore sizes smaller than solvated shell ions suggesting partial or complete removal of solvated shell during the adsorption process.[40-43] Nevertheless, no reliable relationship between specific surface area and pore size of the material yet exists which makes the process of the synthesis of designed materials for supercapacitor applications extremely difficult if not impossible. [7, 39] Table 1 shows a summary of the properties and characteristics of various carbon and carbon-based materials as supercapacitors electrode materials.

Table 2. 1. Properties and characteristics of various carbon-based materials as supercapacitors

			Aqueous electrolyte		Organic electrolyte	
Materials	**Specific surface area/m^2 g^{-1}**	**Density/g cm^{-3}**	**/F g^{-1}**	**/F cm^{-3}**	**/F g^{-1}**	**/F cm^{-3}**
Carbon materials						
Commercial activated carbons (ACs)	1000–3500	0.4–0.7	< 200	< 80	< 100	< 50
Particulate carbon from SiC/TiC	1000–2000	0.5–0.7	170–220	< 120	100–120	< 70
Functionalized porous carbons	300–2200	0.5–0.9	150–300	< 180	100–150	< 90
Carbon nanotube (CNT)	120–500	0.6	50–100	< 60	< 60	< 30
Templated porous carbons (TC)	500–3000	0.5–1	120–350	< 200	60–140	< 100
Activated carbon fibers (ACF)	1000–3000	0.3–0.8	120–370	< 150	80–200	< 120
Carbon cloth	2500	0.4	100–200	40–80	60–100	24–40
Carbon aerogels	400–1000	0.5–0.7	100–125	< 80	< 80	< 40
Carbon -based composite materials						
TC–RuO_2 composite	600	1	630	630	—	—
CNT–MnO_2 composite	234	1.5	199	300	—	—
AC–polyaniline composite	1000	—	300	—	—	—

As an alternative, graphene–based architectures, including both graphene and graphene oxide, are attractive mainly because of their intrinsic high surface area. Graphene-based materials

have also been shown to exhibit interesting life-cycle stability and high rate capability which differentiate them from activated carbon (AC) based supercapacitors. With capacities in excess of 130 F $g^{-1}$and a theoretical capacity of 550 F g^{-1}, [9, 44] graphene sheets look lucrative for potential EC applications. Nevertheless, the main problems with graphene are the high costs associated with the production of pure graphene sheets and problems in processing which strictly limits the practical application of graphene sheets in device applications. On the other hand, Graphene oxide (GO) has a great deal to offer in this regard as the direct consequence of its low-cost, and scalable production methods. [45] Notwithstanding such great attributes, GO suffers from very low conductivity which renders it useless for EC applications. Such a challenge, therefore calls for new strategies to make new classes of supercapacitors.

2.6. Graphene for EC applications: a brief history

The concept of employing graphene-based architectures for EDLC applications was first introduced by Stoller and co-workers in 2008. [44] To overcome the high electrical resistivity problem they used hydrazine as a chemical reducing agent to remove oxygen multifunctional groups on the surface of graphene oxide and obtain reduced form of graphene oxide which is known as reduced graphene oxide (rGO) or chemically modified graphene. However, the first results were limited to a maximum performance of 130 F g^{-1} which although promising, fell short of AC capacitance values. Since then many research efforts have been dedicated to increase the performance of graphene-based devices. These efforts mainly span around finding the best reduction method to reduce and chemically modify graphene oxide structure, either by employing reducing agents such as urea or directly reducing the structure through thermal methods such as hydrothermal route. [5] Nonetheless, all these methods, basically failed to materialize the promise to make breakthroughs across the EC domain which is ascribed to the detrimental effect of restacking of graphene sheets and consequently reduction of specific

surface area during its processing as a result of the strong sheet-to-sheet van der Waals interactions.[9, 46-49] In order to realize such breakthroughs other strategies were developed to produce high surface area rGO using chemical activation method,[24] and laser reduction of GO.[9] It is suggested that the presence of a continuous 3D carbon network with a wide pore size distribution greatly benefits ion transportation through the system resulting in an overall enhancement in capacitance. However even the best capacitance values reported to date, 265 F g^{-1} in the case of laser reduced GO, although very promising, still falls short of the theoretical capacitance value of 550 F g^{-1}. This suggests there are still key factors affecting the final performance of graphene and graphene oxide based ECs, which should be addressed in order to realize the full potential of these structures.

2.7. Graphene: structure

Graphene is the two dimensional (2D) form of graphite comprising a flat monolayer of carbon atoms which are tightly packed into a honeycomb lattice. Graphene can be considered the basic building block of all graphitic materials allotropes such as 0D fullerenes, 1D CNTs and 3D graphite (see Figure 2.9).[50]

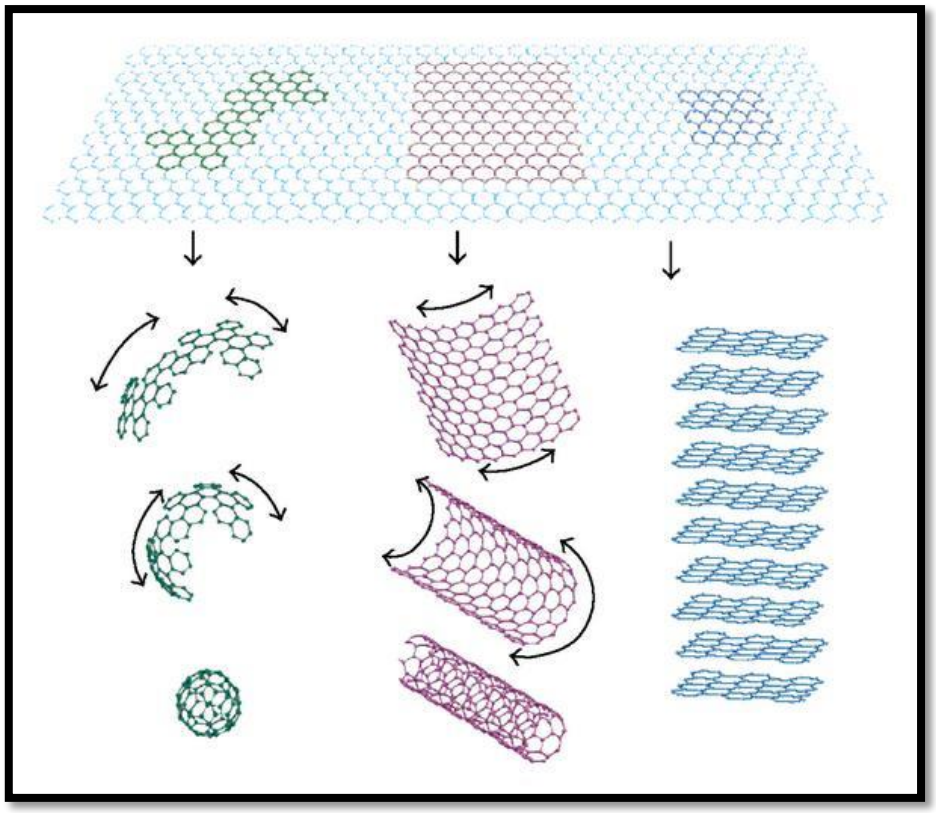

Figure 2. 9. Graphene is a 2D building material for carbon materials of all other dimensionalities. It can be wrapped up into 0D buckyballs, rolled into 1D nanotubes or stacked into 3D graphite.[50]

Theoretically, graphene has been studied for the last sixty years to explain the specific properties of different carbon-based materials.[51-53] However, it was not until 2004, when Geim and Novoselov introduced free-standing graphene for the first time, that graphene attracted a great deal of attention.[54, 55] Before the discovery of free-standing graphene, graphene was mostly treated as an academic material which could not exist in free state.[56] However, recent theories argue that as the obtained 2D crystals are extracted from 3D materials, they are indeed quenched in a metastable state and thermal fluctuations cannot destabilize the system. Another complementary perspective also suggests that graphene sheets can be intrinsically stable as a result of crumpling in the third dimension causing a

substantial increase in elastic energy while simultaneously suppressing thermal vibrations resulting in an overall minimization of the total free energy (see Figure 2.10).

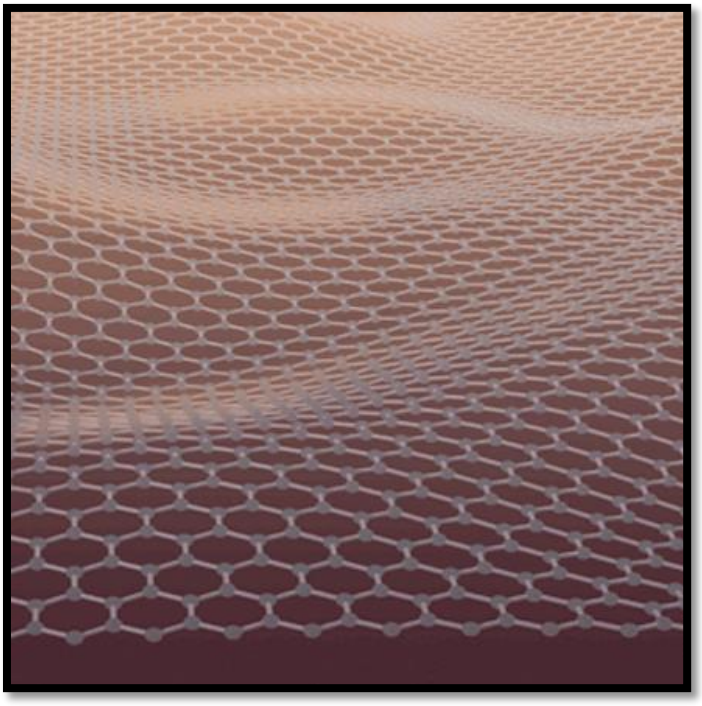

Figure 2. 10. Crumpled graphene sheet

2.8. But what is a 2D crystal?

For the case of graphene sheets, only monolayer carbon and sometimes its bilayer can be defined as 2D crystals, as the electronic structure evolves rapidly beyond bilayer graphene sheets. Any more layer, and the structure should be considered as thin film of graphite. Also the screening length in graphite is around 0.5 nm. Therefore, from the experimental point of view the practical properties of graphene and its thicker counterparts are completely different. This is also another contributing factor to the low performance of devices made of presumably graphene, as many of these perceived structures are usually much thicker and therefore they cannot deliver outstanding electrical, mechanical and electrochemical results. Henceforth, one

should differentiate between these structures and graphene even if they are as thick as just 3 or four layers.[54, 57, 58] Such a control in obtaining high quality monolayer sheets is in fact an extremely difficult, time consuming and costly task. Therefore, many methods are being developed to address such a challenge through the reduction of cheap abundant and easily attainable graphene oxide.

2.9. Graphene oxide: a brief history

The most common approach to the synthesis of exfoliated graphite by chemical methods is the use of one or more concentrated acids in the presence of a strong oxidizing agent to yield graphite oxide. For the first time, Brodie demonstrated the synthesis of graphite oxide in 1859 by adding potash of chlorate (potassium chlorate; $KClO_3$) to a slurry of graphite in fuming nitric acid (HNO_3).[59] Almost 40 years later, this method was further modified Staudenmaier and Hamdi who improved it by adding the chlorate in multiple aliquots over the course of the reaction into a mixture of concentrated sulfuric acid (H_2SO_4) and fuming nitric acid (to increase acidity of the mixture) rather than in a single step as Brodie had done, making the process more practical to be conducted in a single reaction vessel. [60] Hummers later reported an alternative, less hazardous and more efficient method by reacting graphite with a mixture of potassium permanganate ($KMnO_4$) and concentrated sulfuric acid which is basically the foundation of the methods which are commonly used today.[61, 62] This process is accompanied by an increase in the distance among graphene layers from about 0.34 to 0.6-1.2nm -directly related to the degree of oxidation and hydration level- determining the easiness of the intercalation of water molecules in graphene oxide layers resulting in the easy dispersion of GO in water media. [63] A schematic representing the process is shown in Figure 2.11.

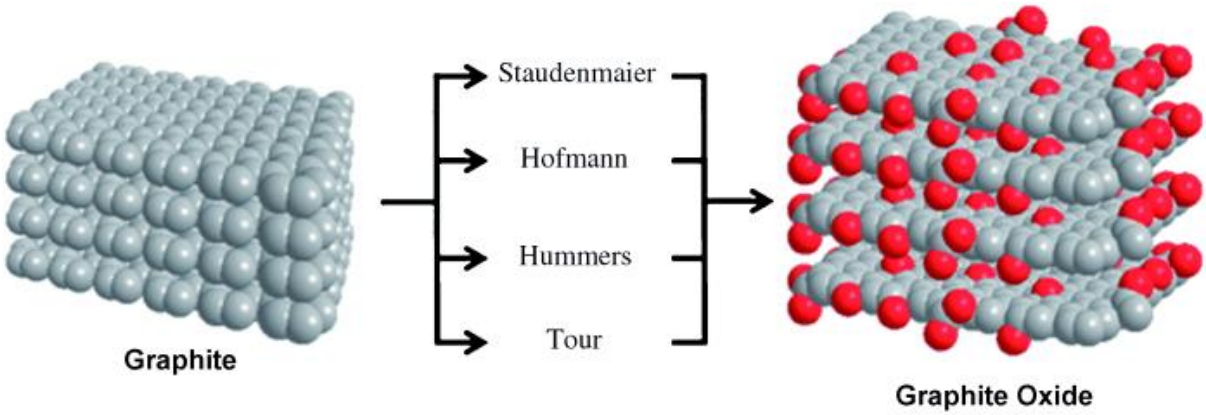

Figure 2. 11. Schematic representing the increase in the inter-layer distance of graphenic platelets in graphite after oxidation into graphite oxide.[64]

2. 10. Graphene oxide: structure

Although graphite oxide has been around for the last 150 years, its precise chemical structure is still under debate. The main reasons contributing to such an ambiguity in the structure are sample-to sample-variation, nonstoichiometric atomic composition and the lack of analytical techniques to precisely characterize this material. [65] The first attempt to characterize the structure of GO was made by Hofmann and Holst which proposed a repeated structure comprising epoxy groups uniformly spread on the basal planes of graphite with a molecular formulae of $C_2O_{0.18}$. [66] Ruess suggested a modified model incorporating hydroxyl groups into the basal planes to account for the presence of hydrogen in GO. He also reformed Hoffman's model by presenting sp^3 hybridized system in contrast to sp^2 hybridized system proposed by Hoffman.[67]

Scholz and Boehm proposed yet another model for the structure of GO by replacing regular quinoidal species in a corrugated backbone instead of epoxide groups. [68] Nakajima and Matsuo also further modified the structure by suggesting a lattice framework akin to

poly(dicarbon monofluoride), $(C_2F)_n$, which forms a stage 2 graphite intercalation compound (GIC). [69, 70] A summary of these models is presented in Figure 2.12.

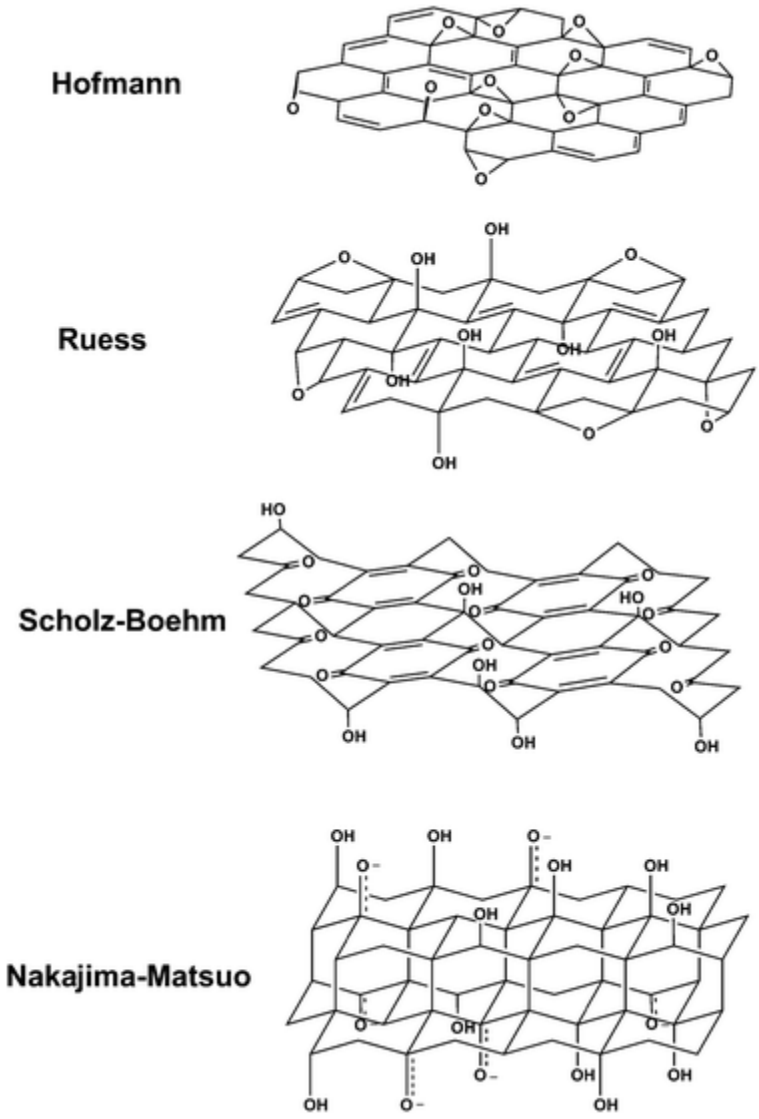

Figure 2. 12. Summary of older models proposed for GO.[71, 72]

However, the latest models proposed by Lerf and Kliowski by solid state nuclear magnetic resonance have rejected the lattice-based model proposals for the structure of GO and alternatively suggested a nonstoichiometric, amorphous structure (Figure 2.13). [73, 74]

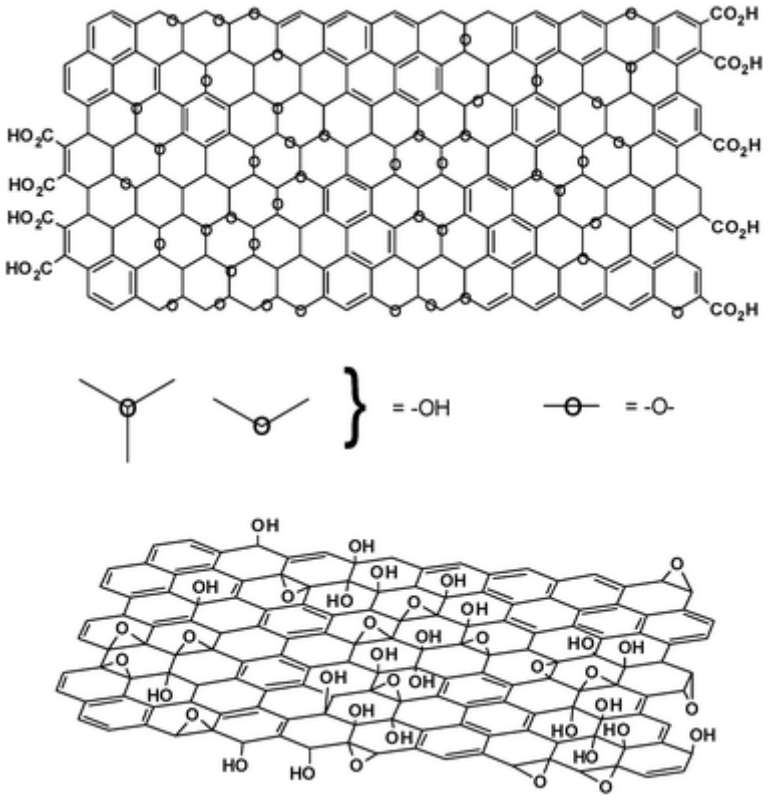

Figure 2. 13. Variations of the Lerf-Klinowski model indicating ambiguity regarding the presence (top, adapted from ref. [75]) or absence (bottom, adapted from ref. [75]) of carboxylic acids on the periphery of the basal plane of the graphitic platelets of GO. [65]

However, Wilson and co-workers later showed that the models for the structure of GO needs a serious revisiting. They demonstrated that GO consists of a stable complex of oxidative debris which is adhered to functionalized graphene-like sheets with sp^2 hybridized system. They also showed that the oxidative debris can be washed –out from graphene-like sheets by using simple base-wash. [76]

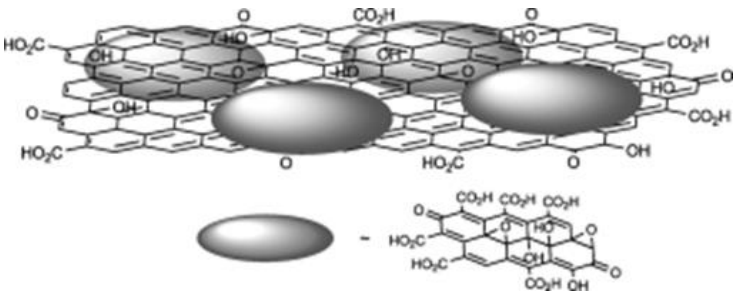

Figure 2. 14. Schematic representation of a GO: large oxidatively functionalized graphene-like sheets with surface-bound debris. Note that the graphene-like sheets extend further than depicted. [76]

Nevertheless the precise structure of GO is still under debate. But in no way it means that this fascinating material cannot be used for different applications.

2.11. But why GO instead of graphene?

The first samples of pristine graphene were deposited by mechanical exfoliation. [54] Since then, many promising applications of graphene have been introduced to put the fascinating properties of graphene into practice, which requires the development of new routes for effective, low cost graphite exfoliation, processing and mass production with high quality.[24, 48, 62, 65, 71, 77-79] Graphite oxide (GO) is an intriguing and interesting new class of carbon-based nano-scale materials with some unusual and fascinating properties that are distinct from those of other graphitic systems.[80] GO has recently emerged as an alternative precursor offering the potential of low cost to fabricate graphene.[62, 65, 77, 81] Among these methods, the chemical reduction of graphite oxide has been successfully used to fabricate covalently functionalized single-layer GO.[82] The presence of these oxygen-containing functional groups provides potential advantages for numerous applications mainly because they can be used to introduce multifunctionalities, which causes the solubility of graphene oxide in water and other solvents. [83] Currently, the solution-phase method shows unrivalled advantages, in

terms of yield and cost, over the other methods such as micromechanical exfoliation,[54] chemical vapour deposition, [84] and epitaxial growth,[85] which exhibit extremely low yield and cannot be used in bulk applications. Hence, the solution phase method has been considered as the most effective way to meet the demands of large-scale applications of graphene. Solution processing can open up a range of potential large-scale applications, from device and sensor fabrication to liquid-phase chemistry. However, the general solution processing route is very limited in offering tools to exercise rational control over the formation and processability, and consequently final properties of graphene oxide dispersions which is needed to realize the development of bottom-up device fabrication processes. In this thesis, we aim to identify the principal conditions through which such levels of control can be exercised to fine-tune dispersion properties for further processing. This challenge, if resolved can serve as a platform to process these materials at industrially highly-scalable levels for a whole range of both novel and existing applications such as coatings, fillers, molecular electronics, wearables, smart garments, RDIF devices, printed electronics, organic field effective transistors and 3D bionic scaffolds. By identifying these elements, we show how we can use these tools to extend our general understanding of the mechanics involved in order to deliberately translate these intrinsic properties into the design process and device applications. We then employ this fundamental understanding to devise graphene oxide based architectures which are suitable for EC applications.

2.12 References

1. Kalyanasundaram, K. and M. Gratzel, *Themed issue: nanomaterials for energy conversion and storage.* Journal of Materials Chemistry, 2012. **22**(46): p. 24190-24194.
2. Dillon, A.C., *Carbon Nanotubes for Photoconversion and Electrical Energy Storage.* Chemical Reviews, 2010. **110**(11): p. 6856-6872.
3. Agency, S.E., *Energiläget i siffror 2010 /Energy in Sweden facts and figures 2010*. 2010, Eskilstuna: Swedish Energy Agency. 46.
4. Yang, Z., et al., *Electrochemical Energy Storage for Green Grid.* Chemical Reviews, 2011. **111**(5): p. 3577-3613.
5. Xu, C., et al., *Graphene-based electrodes for electrochemical energy storage.* Energy & Environmental Science, 2013. **6**(5): p. 1388-1414.
6. Yang, Z., et al., *Enabling renewable energy—and the future grid—with advanced electricity storage.* JOM, 2010. **62**(9): p. 14-23.
7. Simon, P. and Y. Gogotsi, *Materials for electrochemical capacitors.* Nat Mater, 2008. **7**(11): p. 845-854.
8. Gogotsi, Y. and P. Simon, *True Performance Metrics in Electrochemical Energy Storage.* Science, 2011. **334**(6058): p. 917-918.
9. El-Kady, M.F., et al., *Laser Scribing of High-Performance and Flexible Graphene-Based Electrochemical Capacitors.* Science, 2012. **335**(6074): p. 1326-1330.
10. Vivekchand, S., et al., *Graphene-based electrochemical supercapacitors.* Journal of Chemical Sciences, 2008. **120**(1): p. 9-13.
11. Wang, G., L. Zhang, and J. Zhang, *A review of electrode materials for electrochemical supercapacitors.* Chemical Society Reviews, 2012. **41**(2): p. 797-828.
12. Zhang, L.L. and X.S. Zhao, *Carbon-based materials as supercapacitor electrodes.* Chemical Society Reviews, 2009. **38**(9): p. 2520-2531.

13. Futaba, D.N., et al., *Shape-engineerable and highly densely packed single-walled carbon nanotubes and their application as super-capacitor electrodes.* Nat Mater, 2006. **5**(12): p. 987-994.

14. Portet, C., et al., *Electrochemical characterizations of carbon nanomaterials by the cavity microelectrode technique.* Electrochimica Acta, 2008. **53**(26): p. 7675-7680.

15. Yang, C.-M., et al., *Nanowindow-Regulated Specific Capacitance of Supercapacitor Electrodes of Single-Wall Carbon Nanohorns.* Journal of the American Chemical Society, 2006. **129**(1): p. 20-21.

16. Halper, M.S. and J.C. Ellenbogen, *Supercapacitors: A Brief Overview*. 2006, MITRE Nanosystems Group: Virginia. p. 41.

17. Wang, H., et al., *From symmetric AC/AC to asymmetric AC/graphite, a progress in electrochemical capacitors.* Journal of Power Sources, 2007. **169**(2): p. 375-380.

18. Kaempgen, M., et al., *Printable Thin Film Supercapacitors Using Single-Walled Carbon Nanotubes.* Nano Letters, 2009. **9**(5): p. 1872-1876.

19. Fang, B. and L. Binder, *Enhanced surface hydrophobisation for improved performance of carbon aerogel electrochemical capacitor.* Electrochimica Acta, 2007. **52**(24): p. 6916-6921.

20. Pech, D., et al., *Ultrahigh-power micrometre-sized supercapacitors based on onion-like carbon.* Nat Nano, 2010. **5**(9): p. 651-654.

21. Choucair, M. and J.A. Stride, *The gram-scale synthesis of carbon onions.* Carbon, 2012. **50**(3): p. 1109-1115.

22. Izadi-Najafabadi, A., et al., *High-Power Supercapacitor Electrodes from Single-Walled Carbon Nanohorn/Nanotube Composite.* ACS Nano, 2011. **5**(2): p. 811-819.

23. Hiralal, P., et al., *Enhanced supercapacitors from hierarchical carbon nanotube and nanohorn architectures.* Journal of Materials Chemistry, 2011. **21**(44): p. 17810-17815.

24. Zhu, Y., et al., *Carbon-Based Supercapacitors Produced by Activation of Graphene.* Science, 2011. **332**(6037): p. 1537-1541.

25. Yang, X., et al., *Liquid-Mediated Dense Integration of Graphene Materials for Compact Capacitive Energy Storage.* Science, 2013. **341**(6145): p. 534-537.

26. Pandolfo, A.G. and A.F. Hollenkamp, *Carbon properties and their role in supercapacitors.* Journal of Power Sources, 2006. **157**(1): p. 11-27.

27. Park, S.K., Q. Mahmood, and H.S. Park, *Surface functional groups of carbon nanotubes to manipulate capacitive behaviours.* Nanoscale, 2013. **5**(24): p. 12304-12309.

28. Shi, H., *Activated carbons and double layer capacitance.* Electrochimica Acta, 1996. **41**(10): p. 1633-1639.

29. Qu, D. and H. Shi, *Studies of activated carbons used in double-layer capacitors.* Journal of Power Sources, 1998. **74**(1): p. 99-107.

30. Qu, D., *Studies of the activated carbons used in double-layer supercapacitors.* Journal of Power Sources, 2002. **109**(2): p. 403-411.

31. Kim, Y.J., et al., *Correlation between the pore and solvated ion size on capacitance uptake of PVDC-based carbons.* Carbon, 2004. **42**(8–9): p. 1491-1500.

32. Jurewicz, K., et al., *Capacitance properties of ordered porous carbon materials prepared by a templating procedure.* Journal of Physics and Chemistry of Solids, 2004. **65**(2–3): p. 287-293.

33. Fernández, J.A., et al., *Performance of mesoporous carbons derived from poly(vinyl alcohol) in electrochemical capacitors.* Journal of Power Sources, 2008. **175**(1): p. 675-679.

34. Eliad, L., et al., *On the Mechanism of Selective Electroadsorption of Protons in the Pores of Carbon Molecular Sieves.* Langmuir, 2005. **21**(7): p. 3198-3202.

35. Eliad, L., et al., *Assessing optimal pore-to-ion size relations in the design of porous poly(vinylidene chloride) carbons for EDL capacitors.* Applied Physics A, 2006. **82**(4): p. 607-613.

36. Vix-Guterl, C., et al., *Electrochemical energy storage in ordered porous carbon materials.* Carbon, 2005. **43**(6): p. 1293-1302.

37. Arulepp, M., et al., *The advanced carbide-derived carbon based supercapacitor.* Journal of Power Sources, 2006. **162**(2): p. 1460-1466.

38. Arulepp, M., et al., *Influence of the solvent properties on the characteristics of a double layer capacitor.* Journal of Power Sources, 2004. **133**(2): p. 320-328.

39. Raymundo-Piñero, E., et al., *Relationship between the nanoporous texture of activated carbons and their capacitance properties in different electrolytes.* Carbon, 2006. **44**(12): p. 2498-2507.

40. Gogotsi, Y., et al., *Nanoporous carbide-derived carbon with tunable pore size.* Nat Mater, 2003. **2**(9): p. 591-594.

41. Chmiola, J., et al., *Anomalous Increase in Carbon Capacitance at Pore Sizes Less Than 1 Nanometer.* Science, 2006. **313**(5794): p. 1760-1763.

42. Huang, J., B.G. Sumpter, and V. Meunier, *Theoretical Model for Nanoporous Carbon Supercapacitors.* Angewandte Chemie International Edition, 2008. **47**(3): p. 520-524.

43. Huang, J., B.G. Sumpter, and V. Meunier, *A Universal Model for Nanoporous Carbon Supercapacitors Applicable to Diverse Pore Regimes, Carbon Materials, and Electrolytes.* Chemistry – A European Journal, 2008. **14**(22): p. 6614-6626.

44. Stoller, M.D., et al., *Graphene-Based Ultracapacitors.* Nano Letters, 2008. **8**(10): p. 3498-3502.

45. Xu, B., et al., *What is the choice for supercapacitors: graphene or graphene oxide?* Energy & Environmental Science, 2011. **4**(8): p. 2826-2830.

46. Wang, Y., et al., *Supercapacitor Devices Based on Graphene Materials.* The Journal of Physical Chemistry C, 2009. **113**(30): p. 13103-13107.

47. Weng, Z., et al., *Graphene–Cellulose Paper Flexible Supercapacitors.* Advanced Energy Materials, 2011. **1**(5): p. 917-922.

48. Zhu, Y., et al., *Exfoliation of Graphite Oxide in Propylene Carbonate and Thermal Reduction of the Resulting Graphene Oxide Platelets.* ACS Nano, 2010. **4**(2): p. 1227-1233.

49. Gao, W., et al., *Direct laser writing of micro-supercapacitors on hydrated graphite oxide films.* Nat Nano, 2011. **6**(8): p. 496-500.

50. Geim, A.K. and K.S. Novoselov, *The rise of graphene.* Nat Mater, 2007. **6**(3): p. 183-191.

51. Wallace, P.R., *The Band Theory of Graphite.* Physical Review, 1947. **71**(9): p. 622-634.

52. McClure, J.W., *Diamagnetism of Graphite.* Physical Review, 1956. **104**(3): p. 666-671.

53. Slonczewski, J.C. and P.R. Weiss, *Band Structure of Graphite.* Physical Review, 1958. **109**(2): p. 272-279.

54. Novoselov, K.S., et al., *Electric Field Effect in Atomically Thin Carbon Films.* Science, 2004. **306**(5696): p. 666-669.

55. Novoselov, K.S., et al., *Two-dimensional atomic crystals.* Proceedings of the National Academy of Sciences of the United States of America, 2005. **102**(30): p. 10451-10453.

56. Fradkin, E., *Critical behaviour of disordered degenerate semiconductors. II. Spectrum and transport properties in mean-field theory.* Physical Review B, 1986. **33**(5): p. 3263-3268.

57. Zhang, Y., et al., *Electric Field Modulation of Galvanomagnetic Properties of Mesoscopic Graphite.* Physical Review Letters, 2005. **94**(17): p. 176803.

58. Partoens, B. and F.M. Peeters, *From graphene to graphite: Electronic structure around the point.* Physical Review B, 2006. **74**(7): p. 075404.

59. Brodie, B.C., *On the Atomic Weight of Graphite.* Philosophical Transactions of the Royal Society of London, 1859. **149**(ArticleType: research-article / Full publication date: 1859 /): p. 249-259.

60. Staudenmaier, L., *Verfahren zur Darstellung der Graphitsäure.* Berichte der deutschen chemischen Gesellschaft, 1898. **31**(2): p. 1481-1487.

61. Hummers, W.S. and R.E. Offeman, *Preparation of Graphitic Oxide.* Journal of the American Chemical Society, 1958. **80**(6): p. 1339-1339.

62. Medhekar, N.V., et al., *Hydrogen Bond Networks in Graphene Oxide Composite Paper: Structure and Mechanical Properties.* ACS Nano, 2010. **4**(4): p. 2300-2306.

63. Hontoria-Lucas, C., et al., *Study of oxygen-containing groups in a series of graphite oxides: Physical and chemical characterization.* Carbon, 1995. **33**(11): p. 1585-1592.

64. Chua, C.K., Z. Sofer, and M. Pumera, *Graphite Oxides: Effects of Permanganate and Chlorate Oxidants on the Oxygen Composition.* Chemistry – A European Journal, 2012. **18**(42): p. 13453-13459.

65. Dreyer, D.R., et al., *The chemistry of graphene oxide.* Chemical Society Reviews, 2010. **39**(1): p. 228-240.

66. Hofmann, U. and R. Holst, *Über die Säurenatur und die Methylierung von Graphitoxyd.* Berichte der deutschen chemischen Gesellschaft (A and B Series), 1939. **72**(4): p. 754-771.

67. Ruess, G., *Über das Graphitoxyhydroxyd (Graphitoxyd).* Monatshefte für Chemie und verwandte Teile anderer Wissenschaften, 1947. **76**(3-5): p. 381-417.

68. Scholz, W. and H.P. Boehm, *Untersuchungen am Graphitoxid. VI. Betrachtungen zur Struktur des Graphitoxids.* Zeitschrift für anorganische und allgemeine Chemie, 1969. **369**(3-6): p. 327-340.

69. Nakajima, T., A. Mabuchi, and R. Hagiwara, *A new structure model of graphite oxide.* Carbon, 1988. **26**(3): p. 357-361.

70. Nakajima, T. and Y. Matsuo, *Formation process and structure of graphite oxide.* Carbon, 1994. **32**(3): p. 469-475.

71. Zhou, X. and Z. Liu, *A scalable, solution-phase processing route to graphene oxide and graphene ultralarge sheets.* Chemical Communications, 2010. **46**(15): p. 2611-2613.

72. Szabó, T., et al., *Evolution of Surface Functional Groups in a Series of Progressively Oxidized Graphite Oxides.* Chemistry of Materials, 2006. **18**(11): p. 2740-2749.

73. He, H., et al., *Solid-State NMR Studies of the Structure of Graphite Oxide.* The Journal of Physical Chemistry, 1996. **100**(51): p. 19954-19958.

74. Lerf, A., et al., *Structure of Graphite Oxide Revisited.* The Journal of Physical Chemistry B, 1998. **102**(23): p. 4477-4482.

75. He, H., et al., *A new structural model for graphite oxide.* Chemical Physics Letters, 1998. **287**(1–2): p. 53-56.

76. Rourke, J.P., et al., *The Real Graphene Oxide Revealed: Stripping the Oxidative Debris from the Graphene-like Sheets.* Angewandte Chemie International Edition, 2011. **50**(14): p. 3173-3177.

77. Aboutalebi, S.H., et al., *Spontaneous Formation of Liquid Crystals in Ultralarge Graphene Oxide Dispersions.* Advanced Functional Materials, 2011. **21**(15): p. 2978-2988.

78. Hernandez, Y., et al., *High-yield production of graphene by liquid-phase exfoliation of graphite.* Nat Nano, 2008. **3**(9): p. 563-568.

79. Lotya, M., et al., *Liquid Phase Production of Graphene by Exfoliation of Graphite in Surfactant/Water Solutions.* Journal of the American Chemical Society, 2009. **131**(10): p. 3611-3620.

80. Dikin, D.A., et al., *Preparation and characterization of graphene oxide paper.* Nature, 2007. **448**(7152): p. 457-460.

81. Li, D., et al., *Processable aqueous dispersions of graphene nanosheets.* Nat Nano, 2008. **3**(2): p. 101-105.

82. Park, S. and R.S. Ruoff, *Chemical methods for the production of graphenes.* Nat Nano, 2009. **4**(4): p. 217-224.

83. Mkhoyan, K.A., et al., *Atomic and Electronic Structure of Graphene-Oxide.* Nano Letters, 2009. **9**(3): p. 1058-1063.

84. Kim, K.S., et al., *Large-scale pattern growth of graphene films for stretchable transparent electrodes.* Nature, 2009. **457**(7230): p. 706-710.

85. Berger, C., et al., *Electronic Confinement and Coherence in Patterned Epitaxial Graphene.* Science, 2006. **312**(5777): p. 1191-1196.

Chapter 3: Scope of the thesis

3.1 Motivation

Although chemical approaches have been practically used for more than a century to produce graphite oxide, there are some issues which have remained elusive, yet. One of the major issues associated with the conventional chemical approaches is small graphene sheets in terms of lateral size, which is in the range of hundreds of nanometers to a few micrometers at best. The reason behind that lies in the way that these graphene sheets are prepared. In almost all synthesis methods, the ultrasonication step has been employed, typically resulting in severe breakage of graphene sheets.[1, 2] The size is often too small for the fabrication of electronic devices using microelectronic processes.[3] There are numerous advantages which can be realized upon the production of large size graphene oxide sheets in the areas of electronics,[4] molecular sensors,[5] and composite materials.[3, 6] Previously we reported a general route based on modified hummer's method to produce ultra-large graphene oxide sheets. [7, 8] In chapters 5 and 6, we demonstrate that the large sheet size of GO dispersions and their amphiphilicity can be employed as a new method to prepare unique 3-D framework of graphene oxide layers with proper interlayer spacing as building blocks for cost-effective high-capacity supercapacitor electrode and hydrogen storage media. By integrating MWCNTs into these nanostructures, we observed a strong synergistic effect between the two materials consequently leading to a robust and superior hybrid material with higher capacitance compared to either graphene oxide or MWCNTs. The mechanisms involved in the intercalation procedure are fully discussed. And we further propose that the main concept behind intercalating one-dimensional spacers in between giant GO sheets represents a versatile and highly scalable route to fabricate devices with superior performance.

Amongst the many remarkable properties of these graphene oxide (GO) sheets, their ability to form liquid crystals has recently drawn attention. [9-11] The amphiphilicity of GO and the self-assembly properties, [7, 8, 12-14] more pronounced in the case of ultra-large GO sheets, [7, 8, 14] have been utilized to prepare liquid crystalline (LC) dispersions of GO in water. [8-11, 14] The use of LC GO dispersions for fabrication enables the formation of novel self-assembled 3D architectures.[8-11, 14] Moreover, the use of large GO sheets has enabled the use of a wet-spinning route to produce ultra-strong and electrically conducting graphene fibres.[10, 15] However, the ultimate properties of these architectures are critically linked to the initial LC GO dispersion quality and hence necessitate a fundamental understanding in order to facilitate the appropriate processes encountered during fabrication. Therefore, in Chapter 7 we establish principal guidelines that enable rational control over the formation of a lyotropic liquid crystalline state in GO dispersions to reproducibly engineer LC GO for a wide range of industrially processing techniques. We also show that graphene oxide (GO) dispersions exhibit unique viscoelastic properties which constitute them as a new class of soft materials. The fundamental insights accrued here provide the basis for the development of fabrication protocols for these two dimensional soft materials in a diverse array of processing techniques. In chapter 8, based on the fundamental knowledge gained in chapter 7, we demonstrate an entirely new, scalable, and commercially viable wet-spinning strategy to fabricate unlimited lengths of highly porous, yet densely packed and mechanically robust and flexible all-around multifunctional graphene yarns from liquid crystals of ultra-large graphene oxide sheets, for the first time. We propose that these graphene yarns can lead the way to the realization of powerful next-generation multifunctional renewable wearable energy storage systems with their extraordinary electrochemical capacitance values approaching the theoretical capacitance value of graphene.

In chapter 9, we report the discovery of solvophobic soft self-assembly of ultra-large liquid crystalline (LC) graphene oxide (GO) sheets in a wide range of organic solvents, many of which were not known to afford solvophobic self-assembly prior to this report. This discovery could provide practical solutions to the processability of a wide range of materials that require organic solvents because of solubility issues and/or water sensitivity (i.e. metal oxides, polymers and nanomaterials) which is of both technological and fundamental interest for different applications. We develop a solid understanding in the required criteria and mechanisms through which the solvophobic self-assembly is enabled. The new knowledge gained through our findings contributes to the fundamental understanding of the solvophobic effect and the parameters affecting the self-assembly process. Based on the processing knowledge gained in chapter chapters 5-9, in chapter 10, we experimentally demonstrate the long-time predicted but never experimentally realized the formation of biaxial liquid crystals employing the hybrid dispersions of one-dimensional and two-dimensional colloidal dispersions. Such biaxial liquid crystals can, in practice, enable multi-level ordering in contrast to simple nematic LCs resulting in the realization of higher ordered complex 3D architectures. We show that the collective behaviour and coordination of individual components in such biaxial liquid crystals enables stigmergic ordering which is the first report on stigmergic-emergent intelligence in non-biological materials. As an example of many promising applications, we demonstrate that the inherent electrochemical, electrical properties of the final self-constructed architectures are practical in alternative energy storage and conversion devices. The system showed excellent high-rate capability far exceeding the recent literature capacitance values reported for other comparable architectures including aligned/patterned SWNTs thin films supercapacitors and microdevices even at much lower current densities.

In the appendix part, I have put some general questions that referees asked during the review process of publications resulted from this thesis and my responses to them.

3.2 References

1. Geng, Y., S.J. Wang, and J.-K. Kim, *Preparation of graphite nanoplatelets and graphene sheets.* Journal of Colloid and Interface Science, 2009. **336**(2): p. 592-598.
2. Gudarzi, M.M. and F. Sharif, *Characteristics of polymers that stabilize colloids for the production of graphene from graphene oxide.* Journal of Colloid and Interface Science, 2010. **349**(1): p. 63-69.
3. Eda, G. and M. Chhowalla, *Graphene-based Composite Thin Films for Electronics.* Nano Letters, 2009. **9**(2): p. 814-818.
4. Wang, S., et al., *High Mobility, Printable, and Solution-Processed Graphene Electronics.* Nano Letters, 2009. **10**(1): p. 92-98.
5. Robinson, J.T., et al., *Reduced Graphene Oxide Molecular Sensors.* Nano Letters, 2008. **8**(10): p. 3137-3140.
6. Mkhoyan, K.A., et al., *Atomic and Electronic Structure of Graphene-Oxide.* Nano Letters, 2009. **9**(3): p. 1058-1063.
7. Moazzami Gudarzi, M., et al., *Self-aligned Graphene Sheets-Polyurethane Nanocomposites.* MRS Online Proceedings Library, 2011. **1344**: p. null-null.
8. Aboutalebi, S.H., et al., *Spontaneous Formation of Liquid Crystals in Ultralarge Graphene Oxide Dispersions.* Advanced Functional Materials, 2011. **21**(15): p. 2978-2988.
9. Guo, F., et al., *Hydration-Responsive Folding and Unfolding in Graphene Oxide Liquid Crystal Phases.* ACS Nano, 2011. **5**(10): p. 8019-8025.
10. Xu, Z. and C. Gao, *Graphene chiral liquid crystals and macroscopic assembled fibres.* Nat Commun, 2011. **2**: p. 571.
11. Kim, J.E., et al., *Graphene Oxide Liquid Crystals.* Angewandte Chemie International Edition, 2011. **50**(13): p. 3043-3047.

12. Cote, L.J., et al., *Tunable assembly of graphene oxide surfactant sheets: wrinkles, overlaps and impacts on thin film properties.* Soft Matter, 2010. **6**(24): p. 6096-6101.

13. Kim, J., et al., *Graphene Oxide Sheets at Interfaces.* Journal of the American Chemical Society, 2010. **132**(23): p. 8180-8186.

14. Yousefi, N., et al., *Self-alignment and high electrical conductivity of ultralarge graphene oxide-polyurethane nanocomposites.* Journal of Materials Chemistry, 2012. **22**(25): p. 12709-12717.

15. Jalili, R., et al., *Scalable One-Step Wet-Spinning of Graphene Fibers and Yarns from Liquid Crystalline Dispersions of Graphene Oxide: Towards Multifunctional Textiles.* Advanced Functional Materials, 2013. **23**(43): p. 5345-5354.

Chapter 4: Experimental section

4.1 Synthesis of liquid crystalline graphene oxide (LC GO)

The experimental set-up and procedure for the synthesis of graphene oxide (GO) liquid crystals were based on our previously reported synthesis method.[1] Expandable graphite flakes (3772, Asbury Graphite Mills, US) were thermally treated at 1050 °C for 15 sec to produce expanded graphite (EG) and then used as the precursor for graphene oxide (GO) synthesis. In a typical GO synthesis, 1 g of EG and 200 ml of sulphuric acid (H_2SO_4) (95.5–96.5%, General Chemical) were mixed and stirred in a three neck flask for 24 hrs. 5 g of $KMnO_4$ was added to the mixture and stirred at room temperature for 24 hrs. The mixture was then cooled in an ice bath and 200 ml of deionised water and 50 ml of H_2O_2 were poured slowly into the mixture resulting in a colour change to light brown followed by stirring for 30 min. The resulting dispersion was washed and centrifuged three times with a HCl solution (9:1 vol water:HCl). Repeated centrifugation-washing steps with deionised water were carried out until a solution pH $\geq$6 was achieved. Large GO sheets were re-dispersed in deionised water by gentle shaking.

N-N-dimethylformamide (DMF), N-Cyclohexyl-2-pyrrolidone (CHP), tetrahydrofuran (THF), acetone, ethylene glycol, N-methyl pyrrolidone (NMP), dimethyl acetamide (DMAc), methanol, isopropanol and absolute ethanol, all from Sigma, have been chosen for investigation. LC GO dispersions in various organic solvents were prepared by extraction of water from the parent aqueous LC GO dispersion *via* repeated centrifugation-washing steps (6 times of 10 to 30 minutes at 11000 rpm, ProSciTech TG16WS) using the selected solvent. Briefly, 15 ml of the parent aqueous LC GO (2.5 mg ml^{-1}) was poured into a 50 ml centrifuge tube (Nalgene centrifuge tube) to which 20 ml of the selected solvent was added and then mixed

vigorously by vortex shaking. After centrifugation, 30 ml of the supernatant was extracted, replaced with 30 ml of the selected solvent and then mixed vigorously by vortex shaking. This process was repeated 5 times to replace the water with the selected organic solvent.

Synthesis of MWCNT-GO hybrid composites

For the dispersion experiments, carbon nanotubes (CNT, Sigma, multiwalled, diameter between 6-13 nm) powder was added into 25 mL of diluted GO dispersion in water with a mass ratio of 1:3 (CNT/GO). Then the dispersion was sonicated for 30 min using a conventional bath sonicator followed by 30 min sonication in an ultrasonicator (Sonics, VC505, 500 watts, tip diameter 13 mm). A maximum amplitude of 40% was employed for CNT samples, respectively.

4.2 Layer-by-layer self-assembly of the LC GO-SWNT composite

SWNTs dispersion was prepared by adding 15 mg of HiPCO-SWNTs to 15 ml of CHP. This dispersion was subjected to a 3 hr of high-power tip sonication (SONICS Vibra Cell 500 W, 30 % amplitude) followed by a one day low-power bath sonication (Branson B5500R-DTH). The SWNTs/CHP (1 mg ml $^{-1}$) dispersion was then mixed with LC GO in DMF or in CHP (2.5 mg ml^{-1}) at the weight ratio of (10:90) followed by 10 min of vortex mixing. A self-assembled layer-by-layer composite was fabricated by casting 2 ml of the composite formulation into a Teflon mold (2 cm X 2 cm) and then oven dried at 110 ^{o}C for 2 days. The resultant oven-dried GO-SWNT paper was washed several times by DMF, acetone and dried in air to remove the remaining solvent. GO paper, as control, was made using GO in DMF; however, SWNT in CHP was not form free standing paper using simple casting.

4.3 GO-SWNT hybrid synthesis in CHP

SWNTs dispersion was prepared employing pour previously described method [20] by adding 50 mg of Hipco-SWNTs to 50 ml of CHP. This dispersion was subjected to 3h of high-power tip sonication (SONICS Vibra Cell 500 W, 30 % amplitude) followed by one day low-power bath sonication (Branson B5500R-DTH). The dispersion was then centrifuged at 4000 rpm (3000g) for 90 min and the supernatant was carefully decanted. The concentration of the post-centrifuge dispersion was determined from absorbance measurements. Post-centrifuged SWNTs (0.5 mg ml $^{-1}$) and GO (5 mg ml $^{-1}$) dispersions in CHP were then mixed at the mass ratio of (80:20) followed by 10 min vortex mixing.

4.4 Characterization

AFM analysis was carried out by first depositing GO sheets from their dispersions on pre-cleaned and silanized silicon wafer (300 nm SiO_2 layer). Silane solution was prepared by mixing 3-Aminopropyltriethoxysilane (Sigma) with water (1:9 vol) and one drop of hydrochloric acid (Sigma). Pre-cut silicon substrates were silanized by immersing them in aqueous silane solution for 30 min and then washed thoroughly with Millipore water. LC GO in each solvent was first diluted to ~50 µg ml^{-1}, then GO sheets were deposited onto silanized silicon substrates by immersing a silicon substrate into the GO dispersion for 5 seconds, then immersed in the solvent bath (the same solvent used to form the LC GO) for 30 seconds and then dried under nitrogen flow at room temperature. The CHP based sample was then heated up to 70^{o}C to be dried due to its higher boiling point compared to the other solvents. Prior to AFM analysis, GO sheets were observed under an optical microscope to ensure uniform GO sheet deposition was achieved. Atomic force microscopy (MFP-3D AFM *Asylum Research, CA*) was carried out in tapping mode under ambient conditions. X-ray diffraction (XRD)

studies were performed using a powder XRD system (Philips1825) with CuKα radiation (λ=0.154 nm) operating at 40 keV and with a cathode current of 20 mA. Thermal gravimetric analyses (TGA) were carried out in nitrogen atmosphere from room temperature to 250 ^{o}C at a temperature ramp rate of 1 ^{o}C min^{-1}. The birefringence of LC GO dispersions was examined by polarized optical microscopy (POM,Leica CTR 6000) operated in transmission mode by looking at a drop of LC GO on a glass slide. UV/Vis-near-IR spectra were recorded using a Shimadzu UV-3600 spectrometer from 600 nm to 1400nm. The conductivity of LC GO-SWNTs paper was measured using a JANDEL 4-point probe resistivity system (Model RM2) with a linear four-point probe head. The mechanical properties of the composite paper were measured using a Shimadzu tensile tester (EZ-S) at a strain rate of 0.5 % min^{-1} parallel to the GO plain in the paper. Youngs modulus (Y), tensile strength (σ), breaking strain (ε), and breaking energy (toughness) were calculated, and the average reported for 10 samples. The thickness of the composite papers was ~10 µm and the papers are cut in 20 mm by 5 mm. The obtained strips were mounted on aperture cards with commercial superglue and allowed to air dry. Note, only 10 mm of each sample was exposed to the applied strain as 5 mm from each side is used for gluing to the aperture card.

4.5 Wet-spinning of GO and rGO fibers and yarns

Wet-spinning was carried out using a custom-built wet-spinning apparatus using acetone as a coagulation bath. Wet-spinning of GO fibers using $CaCL_2$ and NaOH coagulation bathes were also carried out similar to our previous report. [2] Dried GO fibers were obtained by air-drying under tension at room temperature. Reduction of GO fibers (rGO) was carried out by overnight annealing at 220 °C under vacuum. In addition to single filament fiber-spinning, we were also able to demonstrate multi-filament spinning to directly prepare GO fiber yarns using a multi-orifice spinneret (each orifice diameter is 120 µm).

4.6 Characterization of fibers

SEM analyses were carried out by first depositing GO sheets from their dispersions on pre-cleaned and silanised silicon wafer (300 nm SiO_2 layer). rGO sheets were obtained by annealing graphene oxide sheets deposited on silanised silicon wafer overnight at 220 °C under vacuum. As-deposited rGO sheets were directly examined by scanning electron microscopy (SEM, JEOL JSM-7500FA). X-ray diffraction studies were performed using a powder XRD system (Philips1825) with CuKα radiation (λ=0.154 nm) operating at 40 keV and with a cathode current of 20 mA. X-Ray photoelectron spectroscopy (XPS) was carried out on fibers deposited onto a 1 cm^2 silicon wafer and allowed to dry. The XPS spectra were recorded using Al Kα radiation (1486.6eV). The survey scan was recorded at 0.05 eV s^{-1} at 1eV resolution, and at 0.2 eV s^{-1} at 0.1 eV resolution for the high resolution regions involving the C and O excitations. The birefringence of GO fiber was examined by polarised optical microscopy (Leica DM EP) operated in transmission mode.

4.7 Raman and Rheological characterization

Raman measurements were performed using a high resolution micro-Raman spectrometer (Horiba Jobin Yvon LabRAM HR) with a 632.8 nm He-Ne laser and a 300-line grating to achieve a resolution of ± 1.25 cm^{-1}.

The rheological properties of dispersions were investigated using a rheometer (AR-G2 TA Instruments) with a conical shaped spindle (angle: 2°, diameter: 60 mm). Approximately 2.1 ml of dispersions was loaded into the rheometer with great care taken not to shear or stretch the sample. A solvent trap filled with distilled water was used to prevent GO samples of losing water over the course of long experiments.

Shear stress and viscosity were measured at shear rates between 0.001 to 10 using logarithmic steps (total 200 points) for at least two complete (ascending and descending) cycles. Shear rate was kept constant at each point till the last five readings at each point reported the same value within 5% error (i.e. reaching equilibrium). Considering the size of the particles and the concentrations studied here, it was crucial to apply a conditioning step before each rheological test to ensure the consistency of the results. Briefly, fresh sample was used for every experiment. To eliminate the effect of flow history during the loading, samples were allowed to equilibrate for 1 hr at 25^{o}C, while the rheometer head was locked to avoid any disturbance. The relaxation dynamics of dispersions were studied by measuring the storage modulus and loss modulus of dispersions with various concentration as a function of frequency at a constant strain amplitude of 0.1. This strain amplitude was chosen to prevent samples of going under large deformations.

4.8 Supercapacitor measurements for MWCNT-GO hybrid composites

The working electrode was prepared by coating the active material onto stainless steel sheets (1cm X 1cm) previously polished with sand paper and ultrasonicated in ethanol for an hour. 7 mg of active material (MWCNT-GO, GO, and MWCNT) were mixed with 2 mg of carbon black and 1 mg of PVDF binder (ratio:7:2:1) in an argate motar in NMP (N-methyl pyrrolidinone) solvent and ground using a pestle. The resulting slurry was then spread on to the polished stainless steel surface and allowed to dry in a vacuum oven for 24 hours. The end loading of active material for each electrode was 1mg/cm^2.

Electrochemical experiments were performed on the CHI660C (CH Instruments, Inc) electrochemical workstation using the three electrode system in a beaker type cell at room temperature. An electrolyte solution of 1M H_2SO_4, a silver/silver chloride reference electrode and a platinum foil as a counter electrode were used. Cyclic voltammetry (CV) was performed

over a voltage range of -0.2 to 0.5 V at various scan rates (5 to 100 mVs^{-1}) with specific capacitance being calculated at the lowest scan rate of 5 mVs^{-1}. Another method used to calculate capacitance, chronopotentiometry was performed at varying current densities (0.4 to 8 Ag^{-1}) over a potential window range from -0.1 to 0.5 V. The highest specific capacitance was recorded at 0.4 Ag^{-1} for charge/ discharge (CD). Electrochemical Impedance Spectroscopy (EIS) measurement was carried out between 10 kHz and 0.01 Hz using a 5mV rms sinusoidal modulation at a bias potential of 0.2 V.

4.9 Hydrogen uptake measurements

The hydrogen storage properties of all samples were measured by a volumetric method using Sieverts' apparatus designed by Advanced Materials Corporation, PA, USA at room temperature and 50 atm.

4.10 Supercapacitor measurements

Supercapacitor performance was investigated using cyclic voltammetry (CV) (EDAQ e-corder ADI Instruments) and galvanostatic charge-discharge (CD) (BioLogic Science Instruments VMP3) experiments in a two electrode set-up when rGO fiber yarns deposited on a titanium current collector and separated by a PVDF membrane. All CV and CD data were repeatable and the data reported were all averaged. To calculate the capacitance from CD curves, the same experimental conditions were also applied on plain charge collectors and then the resulting capacitance contribution of the metal plates were subtracted before calculating their gravimetric capacitance for the graphene fibers.

It should be noted that the electrochemical method to characterize the performance of GO, CNTs and GO/CNTs hybrid thin films was designed to evaluate the potential of each of these architectures. As such, three-electrode configuration was used to demonstrate the potential from the fundamental point of view. However, for fiber experiments, two-electrode configuration was used to evaluate the electrochemical performance of the fibers due to the fact that for fibers we had targeted the commercial practical application.

4.11 References

1. Aboutalebi, S.H., et al., *Spontaneous formation of liquid crystals in ultralarge graphene oxide dispersions.* Adv. Funct. Mater., 2011. **21**(15): p. 2978-2988.
2. Jalili, R., et al., *Scalable One-Step Wet-Spinning of Graphene Fibers and Yarns from Liquid Crystalline Dispersions of Graphene Oxide: Towards Multifunctional Textiles.* Advanced Functional Materials, 2013. **23**(43): p. 5345-5354.

Chapter 5: Comparison of GO, GO/MWCNTs composite and MWCNTs as potential electrode materials for supercapacitors

5.1 Supercapacitors

Supercapacitor research has undergone immense growth over the last decade due to the high demand for high performing and long lasting energy devices. Much of the focus has been on increasing the energy density of these devices as they already exhibit high power density as compared to conventional batteries.

Carbonaceous materials such as carbon nanotubes, carbon aerogels, activated carbon and carbon nanofibres are some of the materials of choice used for fabrication of electrode materials. [1-4] These materials give rise to a class of supercapacitors called electrical double layer capacitors (EDLCs). EDLCs operate on a mechanism that involves non-Faradaic reactions taking place on the electrical double layer. High surface area, good conductivity and low cost of these materials have contributed to their attractiveness with carbon nanotubes playing a leading role. [5] Multi-walled carbon nanotubes (MWCNTs) have been reported to exhibit capacitance ranging from 4-135 Fg^{-1}. [6] A major disadvantage for unfunctionalized MWCNTs has been the difficulty to disperse uniformly in any solvent as they tend to agglomerate. To solve this problem, functionalization of carbon nanotubes with nitric acid has been widely reported to boost capacitance while unfunctionalised carbon nanotubes have

been sidelined due to their low capacitance. [6] To further enhance the capacitance, MWCNTs have been mixed with conducting polymers, [2, 7, 8] and metal oxides. [9, 10]

Another class of supercapacitors are the pseudocapacitors which rely on the Faradaic reactions taking place on the electrode surface. Metal oxides, [3, 11] and conducting polymers are typical pseudocapacitive materials that have been vastly reported. [12, 13] To further enhance the capacitance, MWCNTs have been mixed with conducting polymers, [2, 7, 8] and metal oxides. [9, 10]

5.2 GO and hybrid materials of GO-MWCNTs supercapacitors

Graphite oxide (GO), first prepared almost 150 years ago, [14] represents an intriguing and interesting new class of carbon-based nanoscale materials with some unusual and fascinating properties that are distinct from those of other graphitic systems. GO has recently emerged as an alternative precursor offering the potential of a low cost method to fabricate graphene. The first samples of pristine graphene were deposited by mechanical exfoliation. [15] Since then, many promising applications of graphene have been introduced to put the fascinating properties of graphene to practical use, which requires the development of new routes for effective, low cost graphite exfoliation, processing and mass production with high quality. [16] Among these methods, the chemical reduction of graphite oxide - a layered material often simplistically assumed to consist of hydrophilic oxygenated graphene sheets, or graphene oxide sheets, bearing oxygen functional groups in the form of carboxyl, hydroxyl or epoxy groups on their basal planes and edges, [17, 18] has been successfully used to fabricate covalently functionalized single-layer GO. [19] The presence of these oxygen-containing functional groups provides potential advantages for numerous applications, mainly because they can be used to introduce multifunctionalities, [18] which are responsible for the solubility of graphene oxide in water and other solvents. [20] Recently graphene has received great attention as a

possible electrode material for lithium ion batteries, [21, 22] as well as supercapacitors. [23-25] Capacitances as high as 135 Fg^{-1} have been reported by Stoller et al.. [26] Composites of graphene oxide and metal oxides such as ZnO, [27] and MnO_2, [28] have also been reported over the last year with capacitances as high as 197.2 Fg^{-1}. Although some attempts have been made to combine CNTs and GO or reduced GO (rGO), [29-33] the use of functionalized CNTs or complicated procedures employed in these methods quite effectively reduce the practicality and reproducibility in everyday use.

The present chapter addresses the above-mentioned issue by introducing a facile method based on the amphiphilic properties of GO and reports the highest recorded capacitance values reported for GO or hybrid materials of GO-MWCNTs, which are even higher than the values reported for GO-metal oxides composites. These results offer a novel yet simple and effective way of designing advanced materials with extraordinary properties by incorporating two different materials neither one of which alone might be essentially perfect for the required applications. It is suggested that the synergistic effect of the combination of these materials combined with the preferential electro-reduction of GO gives rise to these remarkable values. The hybrid materials were prepared based on the method explained in Chapter 4.

5.3 Structural characterization

5.3.1 XRD

The suspension of GO in water exhibited clear anisotropy in its texture even after gentle shaking, which is typical for graphene sheets with large sizes and high aspect ratios. [16] Inspired by the amphiphilic properties of GO, [32] GO was employed as a molecular dispersing agent to process MWCNTs in water in order to make a hybrid material, GO-MWCNTs. The size dependent amphiphilic properties of GO offer a simple way to engineer the structure and fine tune its amphiphilicity, which therefore makes it an ideal candidate as a water processable

material. The basal plane of GO consists of many π-conjugated aromatic domains which in theory can strongly interact with the surface of CNTs through π–π attractions. [32] There are also some earlier reports on the adsorption of drug or dye molecules through π–π interactions. [34, 35] The dispersion of GO/CNTs remained stable for some days. Although a small portion of the suspended CNTs eventually settled down, a gentle shaking was more than enough to readily redisperse the suspension. Figure 5.1 shows the X-ray diffraction patterns of the samples of both GO and GO mixed with MWCNTs sample.

The x-ray pattern of the as- prepared GO shows a distinct peak at 10.76º corresponding to a layer-to-layer distance (d-spacing) of about 8.22 Å for a typical sample which is due to an approximately one-molecule-thick layer of water trapped and presumably hydrogen-bonded between the graphene oxide sheets. [36] This peak is typical of graphene oxide materials and depends on both the method of preparation and the level of humidity. However the introduction of MWCNTs downshifts the peak to 1.152º which is analogous to a d-spacing of about 70.88 Å demonstrating an increase in the space between the layers. For XRD, the interlayer spacing of the materials is proportional to the degree of oxidation. The XRD pattern further proves the complete oxidation of graphite intercalated compound (GIC) samples. Moreover, the mean crystallite size of GO sheets in the dried suspension that are oriented perpendicularly to the diffracting plane was calculated from the full width at half maximum (FWHM) of the X-ray diffraction peak using the Scherrer's equation, and was found to be 4.05 ± 0.13 nm.

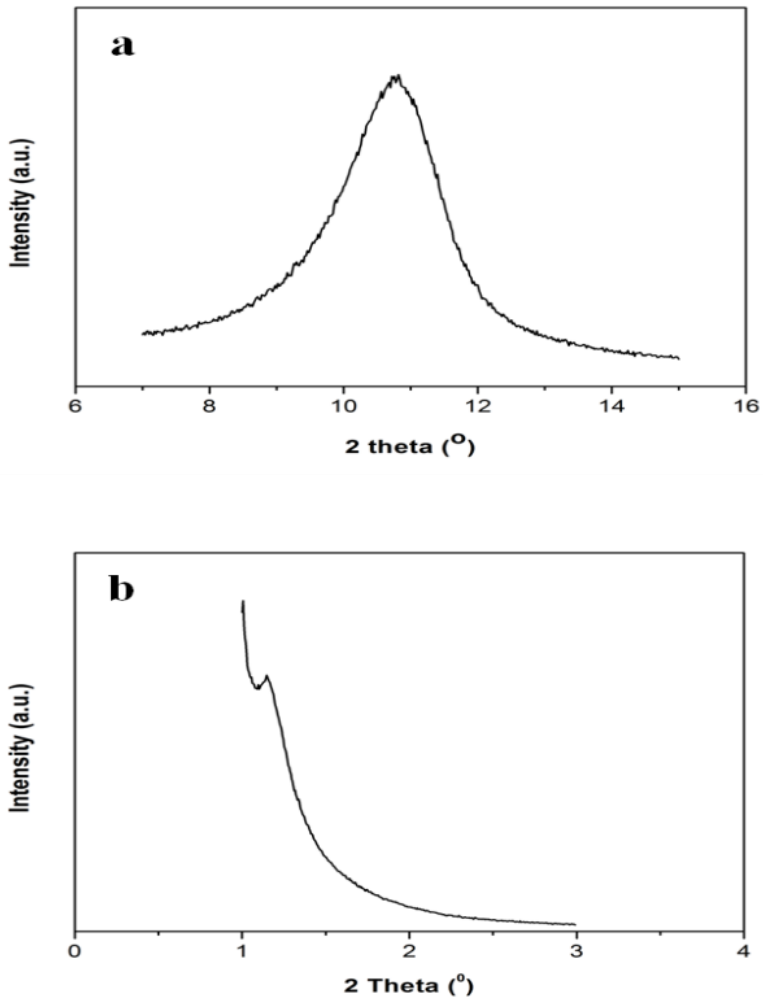

Figure 5. 1. XRD patterns of (a) GO and (b) GO mixed with MWCNTs sample.

5.3.2 XPS

Figure 5.2 shows the X-ray photoelectron spectra of both samples. The spectra for the C region demonstrate the sp^2 hybridized C1s peak attributed to the pristine graphene at 284.7 eV with its well-known asymmetric line shape.

The C1s spectra were compared in both samples by deconvoluting each spectrum into three peaks that correspond to the following functional groups: carbon sp^2 (C=C, 284.8 eV), carbon sp^3 (285.6 eV), epoxy/hydroxyls (C-O, 286.2 eV), and carboxylates (O-C=O, 289.0 eV). Carbon sp^2 and carbon sp^3 peaks are overlaid and indicated as carbon-carbon bonds. Substantial

changes can be observed in the C1s spectra collected after the introduction of MWCNTs, and the C1s spectrum is where the most significant change is observed. The X-ray photoelectron spectroscopy (XPS) analysis (Figure 5.2) demonstrates that the ratio of carbon-carbon bonds to epoxy/hydroxyls and carboxylate groups increases remarkably after the introduction of MWCNTs into the structure, implying an efficient addition of carbon groups during the fabrication process and a simultaneous increase in sp^2 C–C bonds which is an indication of graphitic carbon. [37]

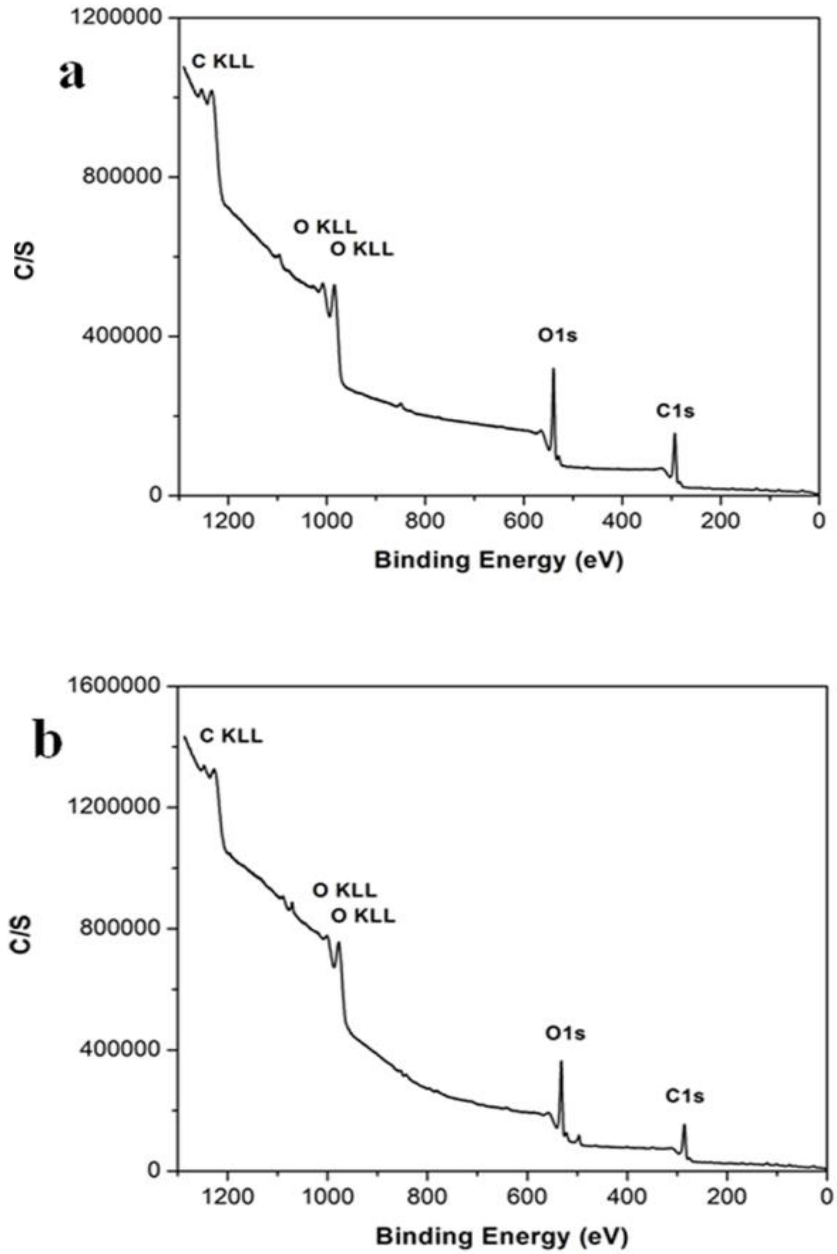

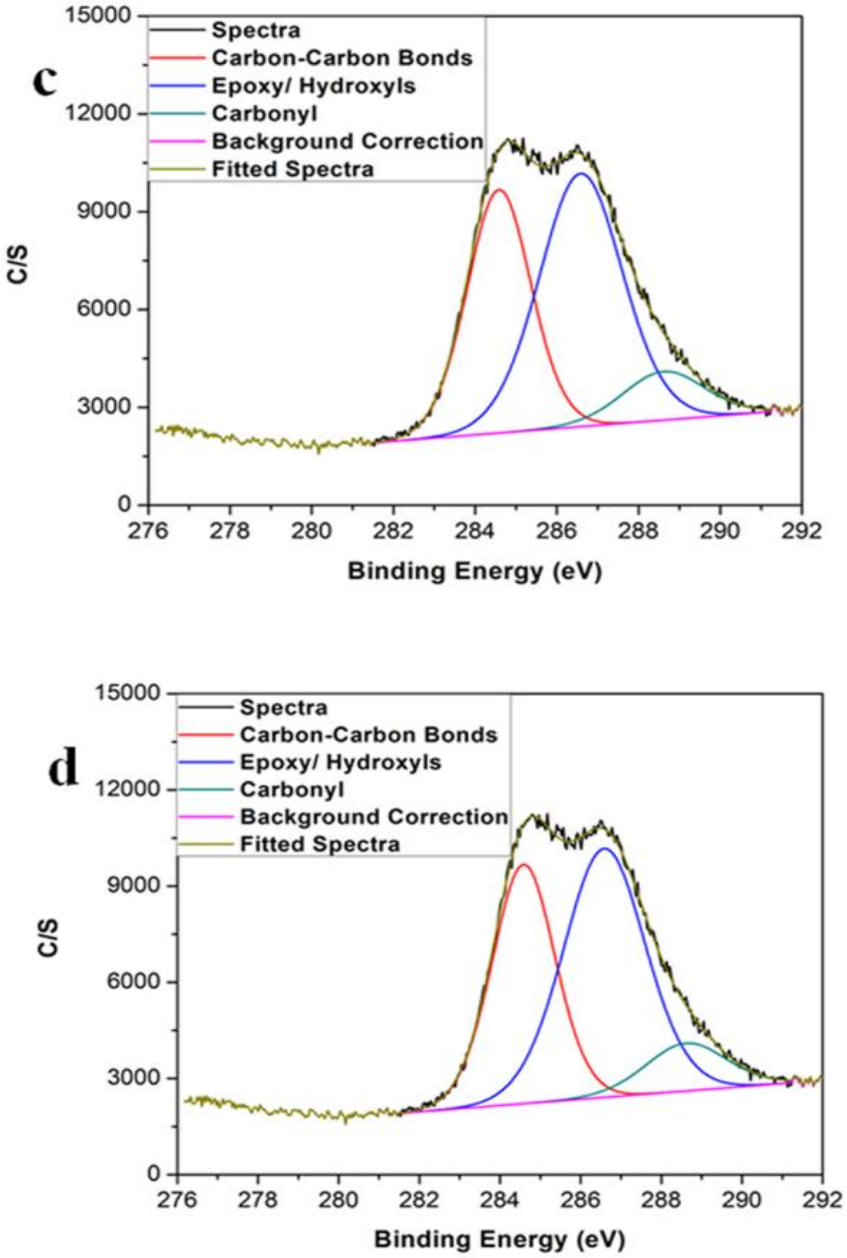

Figure 5. 2. XPS spectra of (a) GO, (b) GO-MWCNTs (c) fitted spectrum of GO in carbon region and d) fitted spectrum of GO-MWCNTs in carbon region.

5.3.3 Raman spectroscopy

A major issue during Raman spectroscopy is the sample damage induced by laser heating because of the fact that GO could undergo local decomposition when irradiated with focused laser spots even at moderate power levels. [38] It is well known that the G band is assigned to the first-order scattering of the E_{2g} mode observed for sp^2 carbon domains and a pronounced D

band is associated with disordered structural defects (e.g., amorphous carbon or edges that can break the symmetry and selection rule). The Raman spectra shown in Figure 5.3 indicate a total decrease of the I(D)/I(G) ratio upon the introduction of MWCNTs as well as a red shift of the peak positions.

Moreover the Raman spectrum of MWCNTs shows a distinct radial breathing mode (RBM) feature at low frequencies and a tangential (G-band) multi-feature at higher frequencies which is typical of both SWCNTs and DWCNTs but also can be observed in case of the present MWCNTs serving as a sign that the innermost diameter is less than 2 nm. Since the low-frequency region is considered a silent region in the case of other carbon materials, the peaks should be attributed to the thin tubes with diameter less than 2 nm which is typical for MWCNTs fabricated employing arc synthesis method. It might also originate from the so-called coupled breathing-like modes (BLMs), rather than individual RBMs. These structural features can also be observed in the case of the hybrid material albeit with a significant change in the position and intensity of the pronounced D peak.

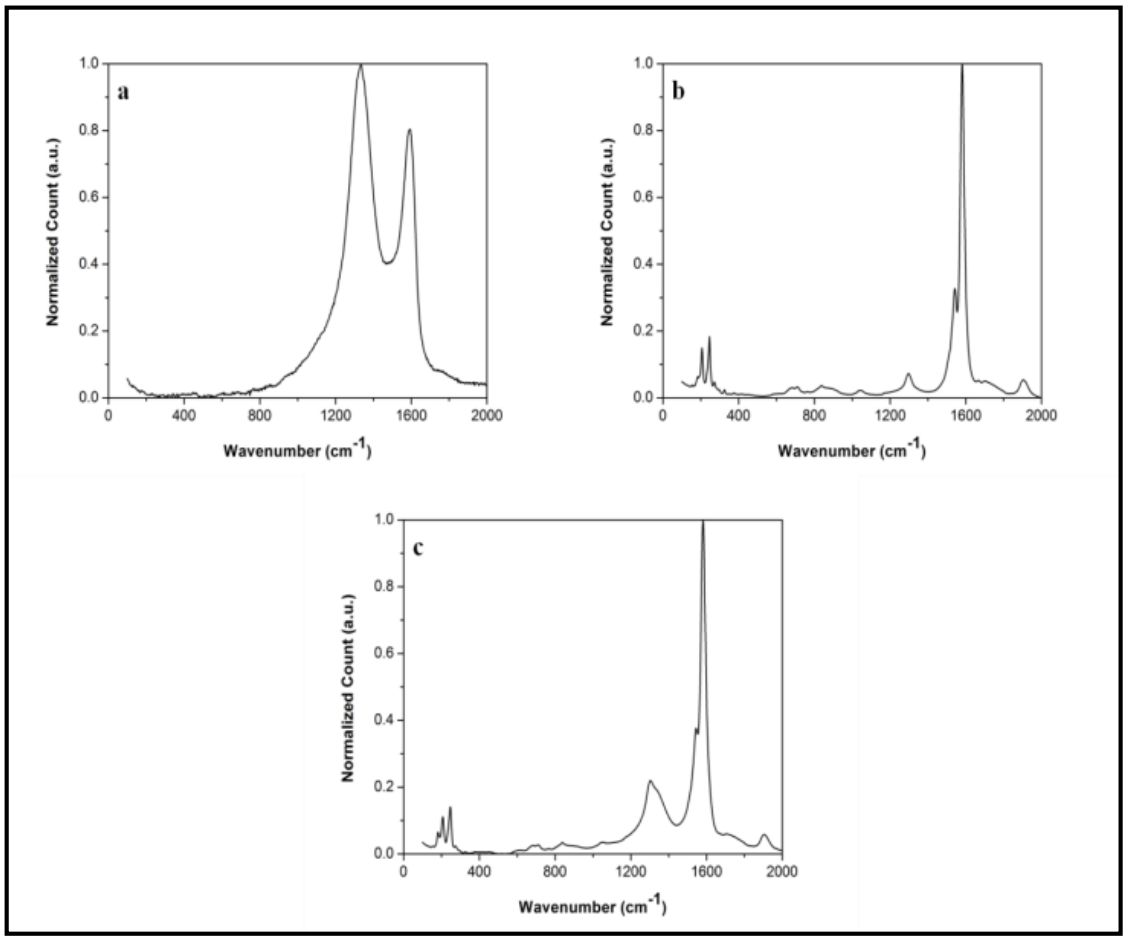

Figure 5. 3. Raman spectra of (a) as-prepared GO, (b) pristine MWCNTs and (c) GO-MWCNTs.

Figure 5.4 presents the UV/Vis spectra of both as-prepared GO suspensions and the GO mixed with MWCNTs. The peak in the UV/Vis spectrum of GO in the region of 227-231nm determines the degree of remaining conjugation (π-π* transition). [39, 40] The shoulder around 300 nm can be ascribed to the n-π* transition of carbonyl groups. [39] While almost no structural peaks can be observed in the case of MWCNTs suspended in sodium dodecyl sulfate (SDS), as shown in Figure 5.4, another absorption peak at 205 nm, beside the pristine GO dispersion peak at 231 nm, can be seen in the mixture indicating π–π attractions between the surface of the CNTs and the basal planes of GO further strengthening the hypothesis that the π-conjugated aromatic domains of the GO have interacted with the surface of the CNTs.

The UV/Vis results demonstrate that the suspension of MWCNTs can be effectively stabilized using GO sheets. The ionization of oxygen groups typically leads to high stability of a GO aqueous dispersion. Considering the case of GO platelets, which are flexible in nature unlike hard disks, the interparticle interaction is completely based on the charge stabilization and double layer extension. [41]

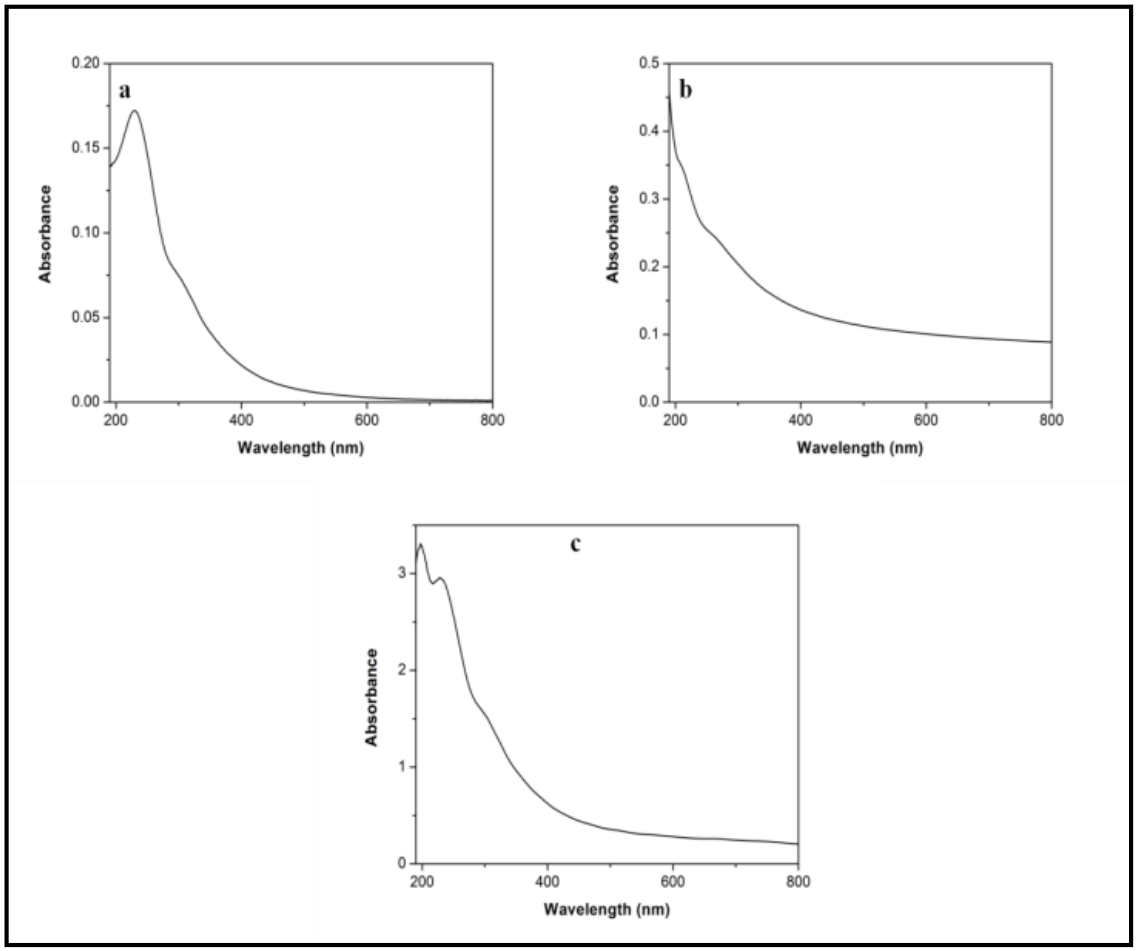

Figure 5. 4. UV/Vis spectra of (a) as-prepared GO dispersion (b) MWCNTs and (c) GO mixture with MWCNTs

5.3.4 Zeta potential

To better illustrate this point, zeta potential study was carried out on GO and the hybrid material. Zeta potential confers the degree of repulsion between charged particles in a dispersion. Therefore, a high zeta potential is an indicator that the dispersion resists aggregation

and consequently remains stable. A Zeta potential study of GO and the hybrid material, reveals that GO sheets are negatively charged which results in high charge density and consequently high hydrophilicity of the GO sheets significantly increasing the colloidal stability.

In contrast, pristine MWCNT dispersions in water are not stable and tend to agglomerate. However, in the case of the hybrid material, the zeta potential becomes significantly more negative significantly (from -39 to -49 mV) suggesting higher stability of the mixed solution. The higher zeta potential implies higher electrostatic repulsion and reduced overlapping areas. This, in turn, supports the view that the hydrophobic domains in the basal plane of GO have strongly interacted with the hydrophobic surface of MWCNTs through π–π attractions. Although both particles are negatively charged, the negative groups are mostly located on the edges of GO leaving behind hydrophobic graphitic islands which can interact with the hydrophobic surface of MWCNTs forming a hybrid structure.

5.3.4 STEM

In order to observe and assess the structural morphology of the hybrid material, scanning transmission electron microscopy (STEM) was employed. Figure 5.5 presents the corresponding SEM, STEM and dark field micrographs of the as-prepared GO-MWCNT sample, which is in good agreement with the results obtained from UV/Vis and zeta potential measurements. The micrographs demonstrate that MWCNTs are adsorbed on the islands on the surface of GO and not on the edges which are typically hydrophilic. Also, the dark field imaging technique proved to be useful to illustrate the faint features of MWCNTs on the surface of GO. The fragmentation and breakage of GO sheets is also observed which is inevitable due to the breakage during the sonication process.

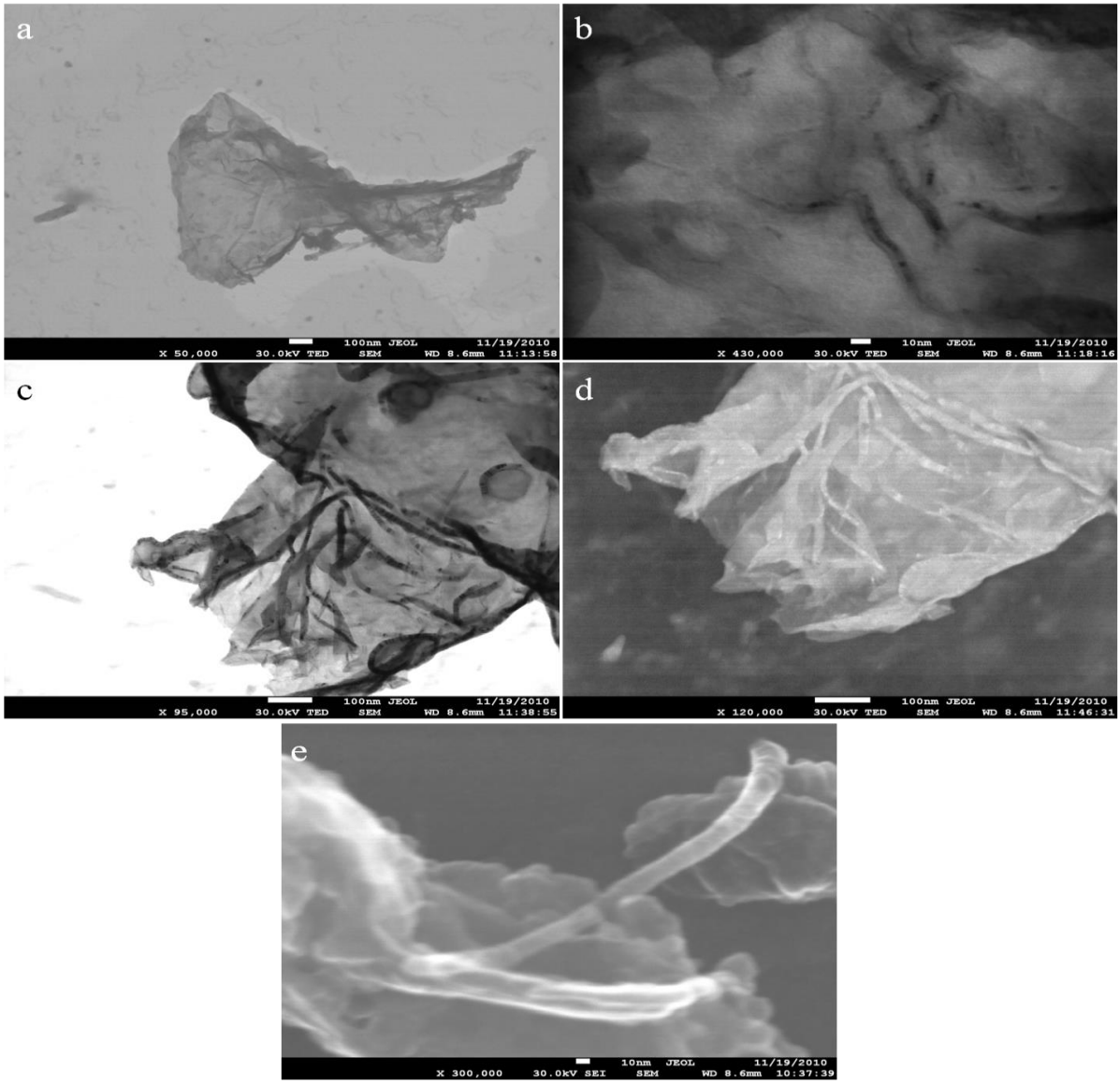

Figure 5. 5. (a) STEM micrograph of an isolated GO-MWCNT, (b) High resolution STEM image showing MWCNTs, (c) STEM micrograph of MWCNTs on the surface of an isolated GO sheet, (d) Dark Field micrograph of the same sheet, better revealing the MWCNTs, (e) SEM micrograph of an isolated MWCNT acting as a bridge between GO sheets.

5.3.4 Raman spectroscopy after electrochemical reduction

The Raman spectra shown in Figure 5.6 indicate an enhancement of the D peak upon the electrochemical reduction of GO as well as a shift of the D peak position. Although a prominent D peak is typically an indication of disorder in the Raman spectrum of carbon materials and

there are some reports on the decrease of I(D)/I(G) ratio. [42] These observations are consistent with previous reports on reduced GO (rGO). The same phenomenon was observed by Ruoff et al., [43] Ajayan and coworkers, [44] etc. [45-48] This strong D peak observed in rGO should be further investigated. However, Ajayan and coworkers had concluded that these defects might be due to the smaller size of the graphene sheets as well as the remaining functionalities. [44] This enhancement of the D peak might also be due to the decrease in the size of the newly formed graphene like sp^2 domains, which are smaller than the domains in the initial sample before electrochemical reduction. [43] Ferrari et al., [49] also proposed that GO is in an amorphous state and that a graphite-like state is only recovered after reduction, implying that the I(D)/I(G) ratio cannot be directly compared between the two states.

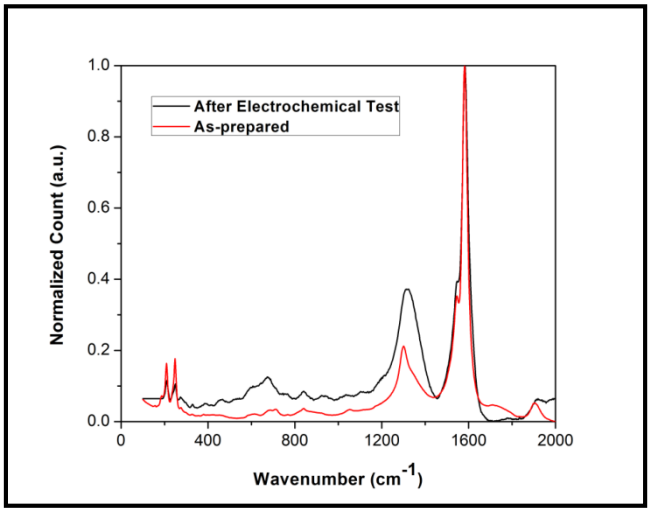

Figure 5. 6. Raman spectra of as-prepared electrode and the same electrode after the electrochemical tests.

5.4 Electrochemical Characterization

5.4.1 CV

Cyclic voltammetry (CV) is usually the first method used for diagnostic testing of supercapacitor performance (Figure 5.7). The specific capacitance of the three electrodes was

therefore calculated using the following formula.

$$C_s = \frac{1}{m\upsilon(V_a - V_c)} \int_{-0.2}^{0.5} I(V)dV \quad (5.1)$$

where *m* is the mass of the active material, *v*, the scan rate, (*Va – Vc*) represents the potential window and the integral area under the cyclic voltammograms.

The calculated specific capacitance for GO-MWCNT, MWCNT and GO were recorded to be 251, 85 and 60 Fg^{-1} respectively. These results are consistent with the range of 15 to 80 Fg^{-1} expected for MWCNTs reported in literature by Frackowiak et al.[50, 51] and much higher than the 10.9 Fg^{-1} for GO, [52] possibly due to a much larger size of the GO sheets employed here (1-2 orders of magnitude).

Figure 5.7(a) shows cyclic voltammograms for the MWCNTs, GO and GO-MWCNTs composite electrodes recorded at $5mVs^{-1}$. MWCNTs typically show an almost rectangular cyclic voltammogram while a distorted rectangular shape is observed for the GO and GO-MWCNT composite due to the pseudocapacitance behaviour originating from oxygen groups on the surface of the GO. No peaks were observed for the MWCNTs electrode as would be expected for carbon material showing classically double layer capacitor behaviour. However, a broad peak characteristic of carbon material with oxygen groups is observed between 0.4 and 0.5 V for the GO-MWCNT electrode (Figure 5.7(a)). The peak can be attributed to the transition between quinone/hydroquinone groups on the carbon material. [53]

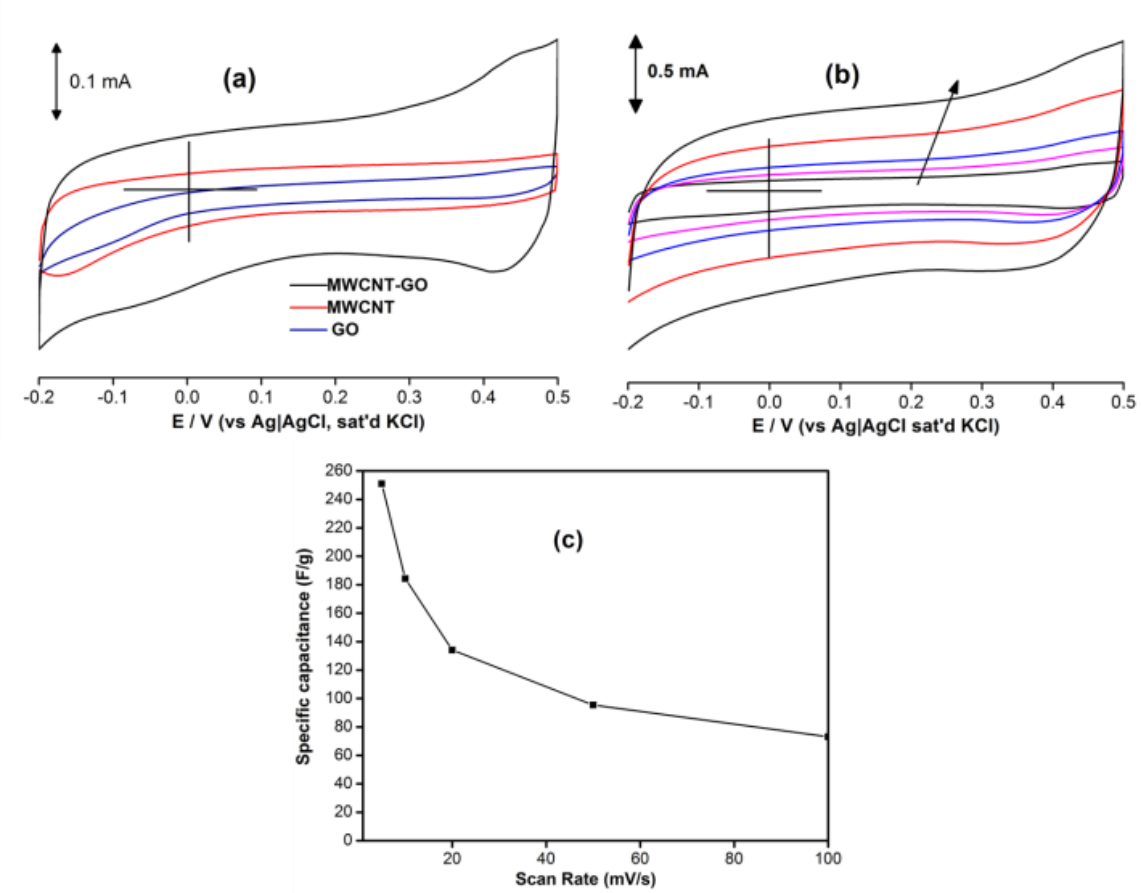

Figure 5. 7. (a) Comparative cyclic voltammograms for GO-MWCNTs, MWCNTs and GO at 5 mVs^{-1}, (b) Scan rate studies for GO-MWCNT in 1M H_2SO_4 at 5, 10, 20, 50 and 100 mVs^{-1}, as indicated by the arrow. (c) Variation of specific capacitance with scan rate for GO-MWCNTs.

The shape of the CV curve for the GO-MWCNTs composite is maintained even at a high scan rate of 100 mVs^{-1} (see Figure 5.7(b)) indicating good capacitive behaviour, rapid diffusion of electrolyte ions from the solution into the pores of the modified electrode and low ESR. [54] The data obtained for Figure 5.7(a) also yielded a linear relationship between the current and the scan rate indicative of a surface-bound redox system. A possible explanation of this phenomenon could be the high conductivity of the two constituent materials coupled with the high porosity of the electrode material which results in a synergistic behaviour of the material and allows penetration by electrolyte ions to the electrode surface as supported by the shape of

the CV curve at high scan rate. MWCNTs can act as conducting wires between the graphene oxide sheets providing a conductive path for movement of electrons. Graphene oxide sheets are well known to agglomerate resulting in a smaller surface area accessible for ion exchange and electrical double layer. A mixture of carbon nanotubes and the graphene sheets results in an increase in the space between the layers as explained earlier by the XRD results. This enhances capacitance by increasing the effective surface area for charge storage and channels for ion exchange. Therefore, CNTs act effectively as a spacer and inhibit the restacking of Graphene oxide sheets and therefore facilitate the diffusion of electrolyte. Furthermore, a recent theoretical study revealed that for cylinders with radius less than 20 nm, increase in double layer capacitance can be observed, providing an enhanced electrochemical driving force for electron transfer and a possible partial cause for altered electrode kinetics at carbon nanotube modified electrodes. [55] Small CNTs are therefore expected to afford higher energetic driving force for electron transfer. This effect can be more pronounced in case of individual and fully separated CNTs entangled between GO sheets. Bundling of CNTs can inhibit the diffuse double layer to extend further into the solution, however, based on the SEM pictures, no bundling of CNTs can be observed in our case which might be partially responsible for the observed enhancement in capacitance. It is proposed that a combination of these factors might be responsible for the observed synergistic effect.

The highest specific capacitance for the composite was recorded at 5 mVs^{-1} and decreased steadily with increasing scan rate as is usually expected due to diffusion limitations in the pores on the electrode surface as shown in Figure 5.7c.

5.4.2 CD

Galvanostatic charge-discharge (CD) was performed on the three electrodes in a potential window from -0.1 to 0.5 V to give a more accurate measurement of the capacitance. Figure 5.8(a) shows the charge-discharge profiles of the MWCNT, GO and GO-MWCNT electrodes

at a current density of 0.4 Ag^{-1}. A common feature of the three electrodes is the linear charging and discharging profiles indicating purely capacitive behaviour. Furthermore, the electrodes showed no observable IR drop. The specific capacitance was calculated using Eq. (5.2):

$$C = \frac{i \times \Delta t}{m \times \Delta E} \tag{5.2}$$

where i is the discharge current, Δt, the discharge time, m, the mass of the active material and ΔE, the potential window.

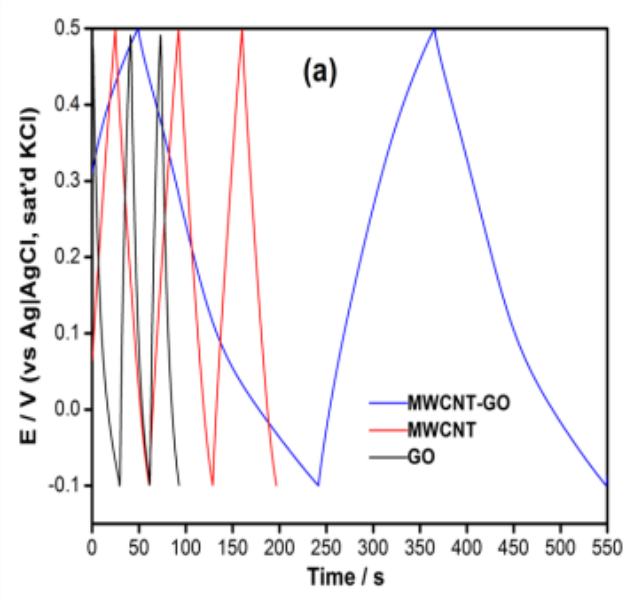

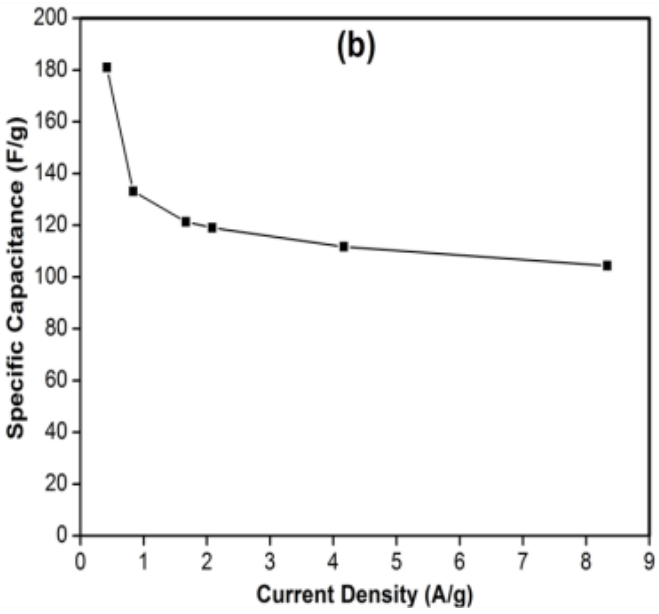

Figure 5. 8. (a) Charge-discharge curves for GO-MWCNTs electrode on stainless steel at 0.4 Ag^{-1}. (b) Specific capacitance as a function of current density in 1 M H_2SO_4.

The specific capacitance calculated from the charge discharge profiles in Figure 5.8(a) was 181, 36 and 20 Fg^{-1} for GO-MWCNT, MWCNT and GO, respectively. The higher capacitance of the composite can be attributed to the improvement in conductivity and good dispersion of the MWCNTs in the presence of GO.

The results are in agreement with those calculated using cyclic voltammetry where a synergistic effect between the GO and MWCNTs is observed. However, the recorded values here are lower than those obtained using cyclic voltammetry. Figure 5.8(b) shows the variation of specific capacitance with current density. A sharp decrease in specific capacitance is observed at low current densities but decreases steadily at higher current densities indicating good power capability of the electrode. The decrease could be attributed to the decreased access to the active surface by ions as current density increases.

5.4.3 EIS

Electrochemical impedance spectroscopy is a powerful technique that gives a wealth of information regarding internal resistance of the electrode material and resistance between the electrode and the electrolyte. Electrochemical impedance measuremetns were therefore performed from 10 kHz to 10 mHz at a potential of 0.2 V *vs.* Ag|AgCl reference electrode (Figure 5.9). Nyquist and Bode plots for the three electrodes were plotted and analysed. To better understand the processes taking place on the electrode surface the interpretation of this data was divided into two regions, the high frequency and the low frequency regions.

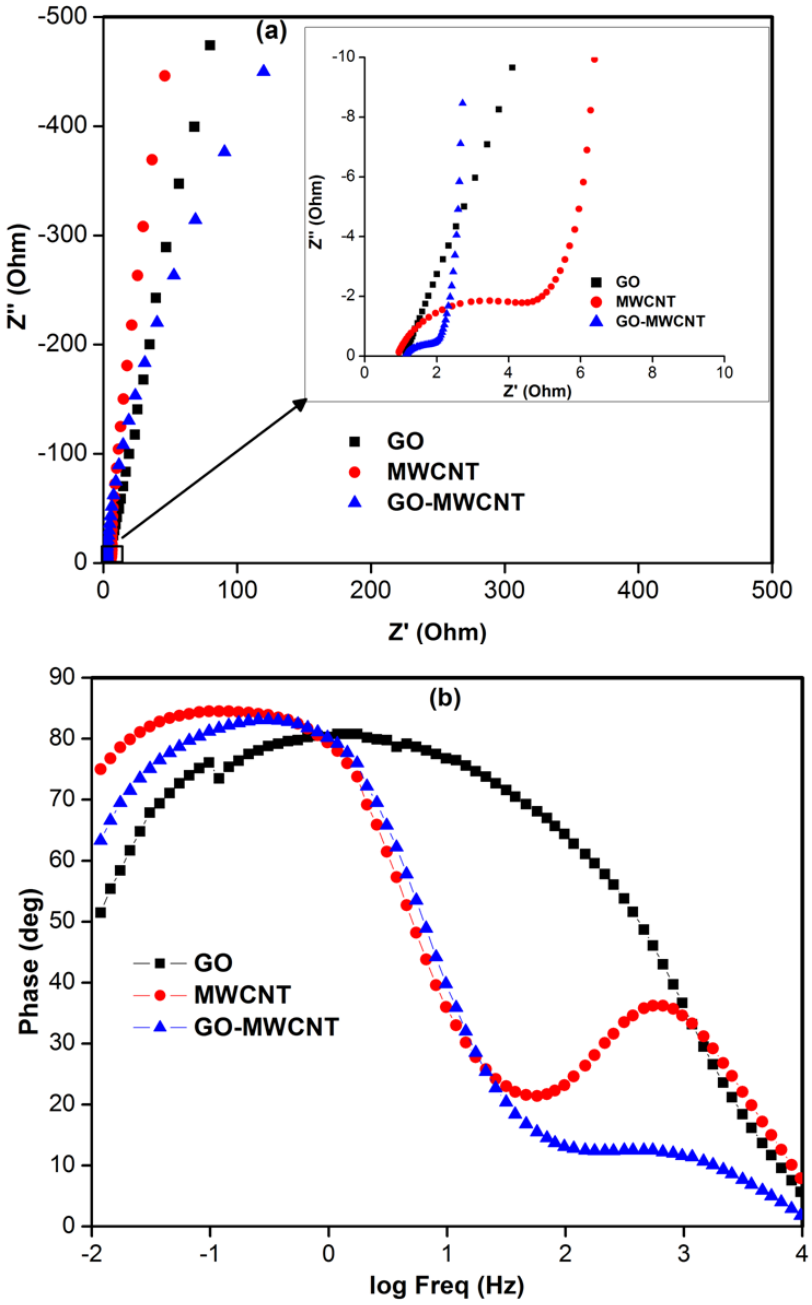

Figure 5. 9. (a): Nyquist plot for GO-MWCNT composite (inset: magnified high frequency region) (b) Bode angle plot for the composite.

At high frequency, the intercept between the impedance plot and the real impedance (Z') axis gives the magnitude of the solution resistance (Rs) of the cell. The solution resistance for the three materials was very low at 0.91, 1.17, and 1.17Ω for the MWCNT, GO and GO-MWCNT. Another interesting feature in the high frequency region is the semicircle observed for the

MWCNT and GO-MWCNTs electrodes. The impedance experiment was performed on all three electrodes after 20 cycles to activate the electrode materials, which explains the presence of the semicircle which was not present at the beginning of the stability tests in Figure 5.9(b). Charge transfer resistance represents the electrode resistance and is closely related to the surface area and conductivity of the electrode. The diameter of the semicircle in the high frequency region gives an indication of the charge transfer resistance (R_{CT}). The MWCNTs electrode recorded an R_{CT} of 5.13Ω and no semicircle was observed for the GO electrode due to the good conductivity of the material. A combination of these two materials resulted in the lowering of the charge transfer resistance in the GO-MWCNT electrode (1.12Ω) implying lower resistance to ion movement from the pores of the composite. The synergistic effect of the MWCNT and GO electrodes is therefore apparent from the Nyquist plot, and from the CV and CD data in Figure 5.7(a), 5.8(a) and 5.9(a).

At low frequencies, supercapacitor electrodes exhibit typical capacitive behaviour, where an almost vertical line is observed on the Nyquist plot and a phase angle close to 90° on the Bode plot (Figure 5.9). MWCNTs and GO are known to exhibit almost ideal capacitance and this is confirmed by the phase angle almost reaching 90°. However, the slope on the Nyquist plot deviates from a perfect vertical line possibly due to pseudocapacitance effects from the oxygen groups on the GO. A purely capacitive element (C_{dl}) was therefore replaced by a constant phase element (CPE) in the electrical equivalent circuit to obtain a good fit with low relative errors.

$$Z_{CPE} = \frac{1}{[Q(j\omega)^n]} \tag{5.3}$$

where *Q* is defined as the frequency independent constant relating to the surface electroactive properties, ω is the radial frequency; the exponent *n* arises from the slope of log *Z vs.* log *f*. The value of *n* varies between -1 and 1. When *n=0*, the CPE represents a pure resistor. At *n=1*, a pure capacitor and an inductor at *n= -1*.At *n= 0.5*, the CPE corresponds to Warburg impedance (Z_W). Two CPE elements were defined to cater for the deviation from ideal capacitor behaviour

[56]. The values of *n* for the two CPEs are both very close to 1 which denotes a pure capacitor, implying highly capacitive behaviour by the electrode. The presence of the CPE also indicates the porous nature of the electrode as explained by Girija et al.[57]. R_1 and R_3 represent the solution resistance and the ionic resistance through the electrode material, respectively, while R_2 is the charge transfer resistance.The values of all the other fitting elements from the modified Randles circuit are shown in Table 5.1, including the error values. Electrical equivalent circuit used in fitting the experimental EIS data obtained from the GO-MWCNT electrode is also given in Figure 5.10.

Table 5. 1. Equivalent circuit parameters for the MWCNT-GO composite electrode

Element	*Value*	*% Error*
R1 (Ω)	1.17	1.14
Q1 (mF)	14.04	21.91
n1	0.85	3.23
R2 (Ω)	1.12	4.21
Q2 (mF)	0.0086	3.7187
n2	0.97	0.75
R3 (Ω)	164.09	5.38

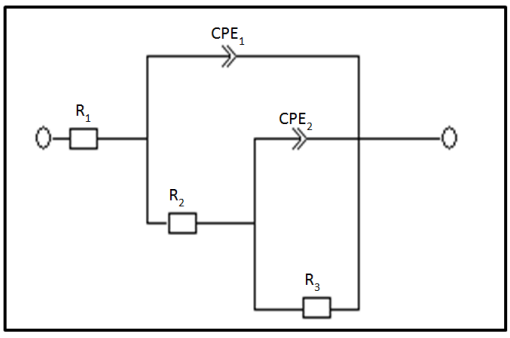

Figure 5. 10. Electrical equivalent circuit used in fitting the experimental EIS data obtained from the GO-MWCNT electrode.

5.5 Stability

Stability studies were performed for the GO-MWCNT using cyclic voltammetry and EIS. An interesting phenomenon was observed where the specific capacitance increased significantly with increasing cycle number as shown in Figure 5.11 (a).

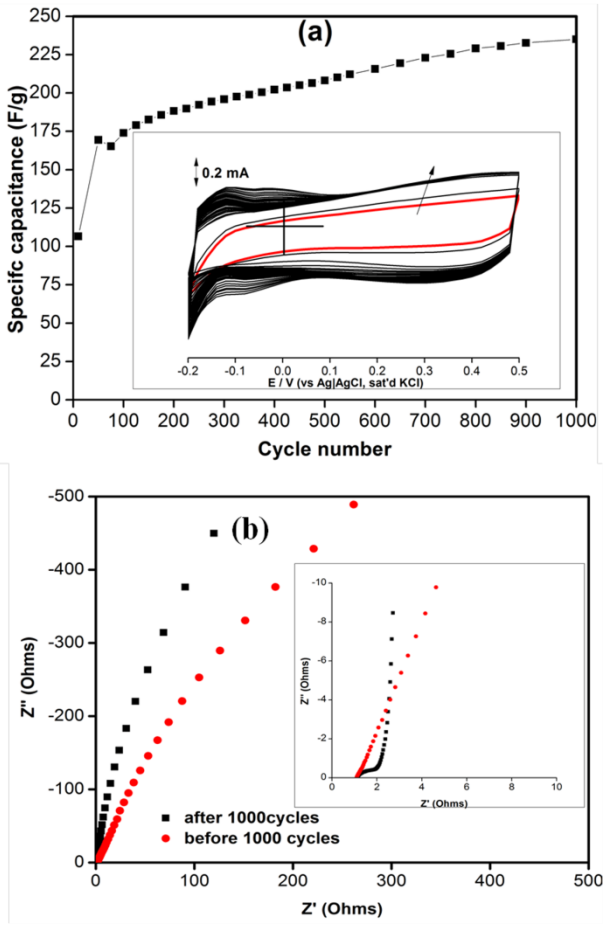

Figure 5. 11. (a) Change in specific capacitance with increase in cycle number, calculated from cyclic voltammetry data at 20 mVs^{-1}. Inset shows the growth of CV's with increase in cycle number. (b) Comparative Nyquist plots before and after 1000 cycles.

The electrode was cycled for 1000 times at a scan rate of 20 mVs^{-1}. In the first 100 cycles, the rapid increase in the capacitance can be attributed to the activation of the electrode material and electrochemical reduction of the GO. In the second segment starting from 100 to 1000 cycles, a steady increase in capacitance is observed possibly due to the depletion of oxygenated

groups on the electrode surface as the reduction of GO progresses. This is supported by the XPS spectra in Figure 5.12. The loss of oxygen functionality is clearly evident in the core C1s spectra (Figure 5.12). However the high energy tail at 289.7 eV suggests that some residual oxygen functionalities (mainly carboxylates) still remain even after the electrochemical reduction of GO.

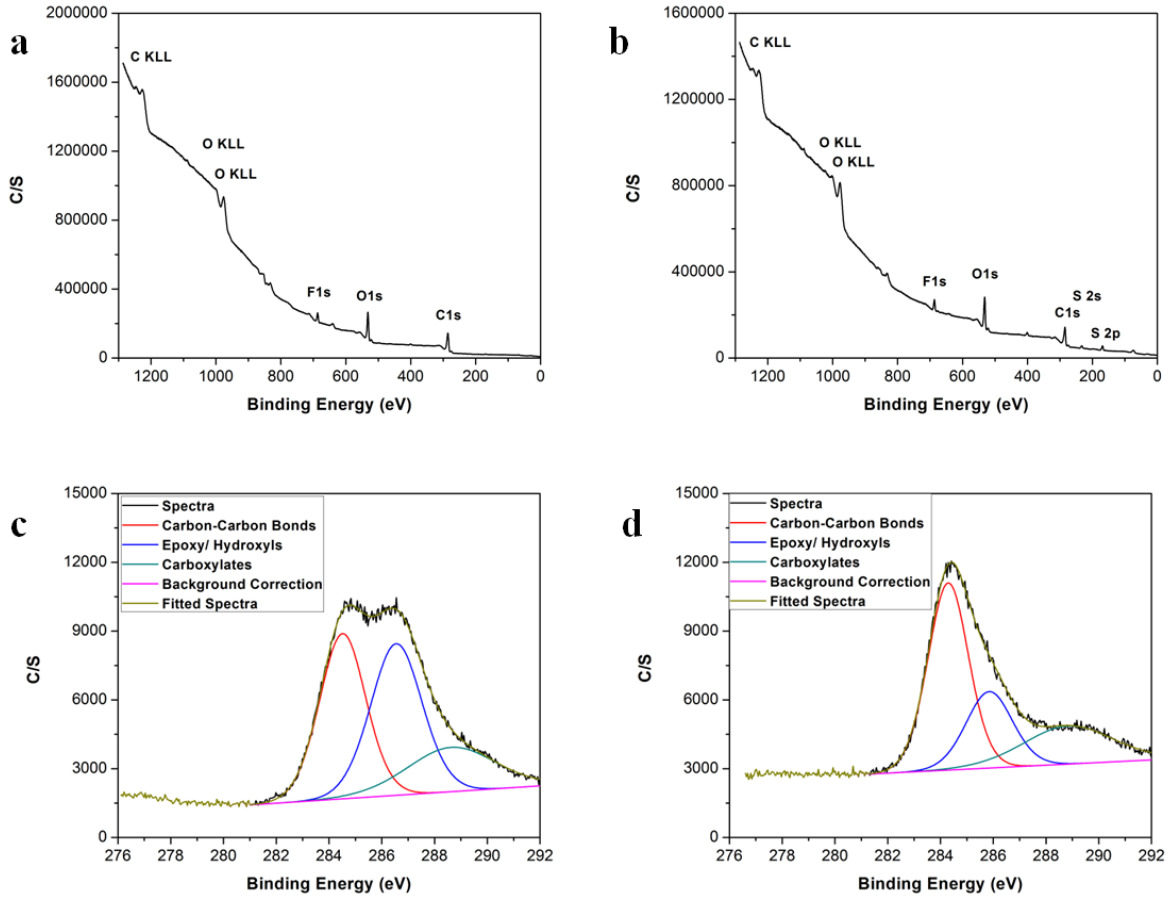

Figure 5. 12. XPS spectra of (a) as-prepared electrode, (b) the same electrode after the electrochemical tests (c) fitted spectra of as-prepared electrode in carbon region and (d) fitted spectra of the same electrode after the electrochemical tests in carbon region.

It is usually assumed that employing MWCNTs in composite or hybrid materials leads to low percolation thresholds, meaning very little material is needed for conduction. Thus, even a small amount of CNTs is capable of delivering higher conductivity through the system. Therefore, MWCNTs can channel electrical current to some preferential sites on the surface of

GO, providing that the electrical current passes through the GO layers, and thus GO is partially reduced to rGO upon deoxygenation of GO. Joule heat generated during the application of current through GO might make it possible to reduce GO to rGO. GO is essentially a water absorbant compound. As a result, hydroxyl groups which are highly reactive can be readily ionized to give out H^+ with the presence of water. Therefore, the existence of this absorbed water favours the reduction of GO. [58, 59] Based on the XPS results, the amount of hydroxyl groups decreases dramatically after the reduction of GO which might be considered as a consequence of the protonation involved in the electro-reduction process, which is known to be facilitated at lower pH values. [59]

$$GO + aH_3O^+ + be^- \longrightarrow rGO + cH_2O \quad (5.4)$$

A total increase in specific capacitance by 120.5 % is recorded in 1000 cycles reaching a maximum of 235 Fg^{-1} at 20 mVs^{-1}. Cycling of the GO-MWCNT composite in H_2SO_4 contributed to the reduction of GO to reduced graphene oxide (rGO) and hence an increase in capacitance. A similar trend has been reported by Shao et al. [60] and Chen et al..[53] It is interesting to note that in the presence of MWCNTs, the peak at ~ -0.1 V continues to grow with increase in the number of cycles. This could possibly have been due to the MWCNT having a catalytic effect on the reduction of GO and intercalation of sulphur in the pores.

Due to this peculiar phenomenon observed with the increase in the CV area for the GO-MWCNT electrode, we performed electrochemical impedance spectroscopy and XPS after cycling. From the XPS (Figure 5.12), a significant increase in the ratio of carbon-carbon bonds to epoxy/hydroxyls and carboxylate groups (from 0.65 to 1.09) after the electrochemical reduction of the electrode was observed. Finally, a peak attributing to Sulphur (S2p) which can be in the form of either HSO_4^{-1} or SO_4^{-2}, corresponding to 6.98 at% sulphur on the surface of the sample, can be observed suggesting the accumulation of sulphur during the electrochemical reduction of the prepared electrode.

In the high frequency region, of the Nyquist plot, a semicircle was observed after 1000 cycles but was not detected before cycling. A plausible explanation could have been an increase in charge transfer resistance with increase in cycle number due to intercalation of ions on the electrode surface between GO layers as shown by the XPS spectra where the amount of sulphur ions intercalated between GO layers increased to 6% as previously discussed. The cyclic voltammograms also change shape with increase in scan number becoming more rectangular (see Figure 5.11(a) inset).

5.6 Conclusions

In conclusion, the feasibility of designing a new generation of hybrid electrochemical supercapacitors for use in advanced energy devices based on the synergistic behaviour of GO-MWCNT electrodes was demonstrated. The dispersant free nature of the combination of these materials offers a great flexibility in the creation of high performance novel GO-MWCNT based nanocomposites with many other nanostructures (possibly metal-oxide or polymer systems). The hybrid nanostructured material demonstrated a strong synergistic effect leading to higher capacitance compared to either graphene oxide or MWCNTs. The mixture of GO-MWCNT showed exceptional stability due to the $\pi-\pi$ interactions between the two carbonaceous materials. A maximum capacitance of 251 Fg^{-1} was observed at 5 mVs^{-1} and a total increase of 120.5 % was recorded in 1000 cycles for the hybrid material at a scan rate of 20 mVs^{-1}. It is assumed that MWCNTs can channel the electrical current to some preferential sites on the surface of GO resulting in a partial recovery of GO to rGO.

5.7 References

1. Chidembo, A.T., et al., *Nickel(ii) tetra-aminophthalocyanine modified MWCNTs as potential nanocomposite materials for the development of supercapacitors.* Energy & Environmental Science, 2010. **3**(2): p. 228-236.
2. Canobre, S.C., et al., *Synthesis and characterization of hybrid composites based on carbon nanotubes.* Electrochimica Acta, 2009. **54**(26): p. 6383-6388.
3. Khomenko, V., E. Raymundo-Piñero, and F. Béguin, *Optimisation of an asymmetric manganese oxide/activated carbon capacitor working at 2 V in aqueous medium.* Journal of Power Sources, 2006. **153**(1): p. 183-190.
4. Wu, M.-S. and K.-H. Lin, *One-step Electrophoretic Deposition of Ni-Decorated Activated-Carbon Film as an Electrode Material for Supercapacitors.* The Journal of Physical Chemistry C, 2010. **114**(13): p. 6190-6196.
5. Schindall, J., *The Charge of the Ultracapacitors.* Spectrum, IEEE, 2007. **44**(11): p. 42-46.
6. Frackowiak, E., et al., *Nanotubular materials for supercapacitors.* Journal of Power Sources, 2001. **97-98**: p. 822-825.
7. Hughes, M., et al., *Electrochemical Capacitance of a Nanoporous Composite of Carbon Nanotubes and Polypyrrole.* Chemistry of Materials, 2002. **14**(4): p. 1610-1613.
8. Khomenko, V., E. Frackowiak, and F. Béguin, *Determination of the specific capacitance of conducting polymer/nanotubes composite electrodes using different cell configurations.* Electrochimica Acta, 2005. **50**(12): p. 2499-2506.

9. Wang, B., et al., *Synthesis of nanosized vanadium pentoxide/carbon composites by spray pyrolysis for electrochemical capacitor application.* Electrochimica Acta, 2009. **54**(5): p. 1420-1425.

10. Reddy, A.L.M. and S. Ramaprabhu, *Nanocrystalline Metal Oxides Dispersed Multiwalled Carbon Nanotubes as Supercapacitor Electrodes.* The Journal of Physical Chemistry C, 2007. **111**(21): p. 7727-7734.

11. Fan, Z., et al., *Preparation and capacitive properties of cobalt-nickel oxides/carbon nanotube composites.* Electrochimica Acta, 2007. **52**(9): p. 2959-2965.

12. Gupta, V. and N. Miura, *High performance electrochemical supercapacitor from electrochemically synthesized nanostructured polyaniline.* Materials Letters, 2006. **60**(12): p. 1466-1469.

13. Sivaraman, P., et al., *All-solid supercapacitor based on polyaniline and sulfonated poly(ether ether ketone).* Journal of Power Sources, 2003. **124**(1): p. 351-354.

14. Dreyer, D.R., et al., *The chemistry of graphene oxide.* Chemical Society Reviews, 2010. **39**(1): p. 228-240.

15. Novoselov, K.S., et al., *Electric Field Effect in Atomically Thin Carbon Films.* Science, 2004. **306**(5696): p. 666-669.

16. Zhou, X. and Z. Liu, *A scalable, solution-phase processing route to graphene oxide and graphene ultralarge sheets.* Chemical Communications, 2010. **46**(15): p. 2611-2613.

17. Dikin, D.A., et al., *Preparation and characterization of graphene oxide paper.* Nature, 2007. **448**(7152): p. 457-460.

18. Petit, C., M. Seredych, and T.J. Bandosz, *Revisiting the chemistry of graphite oxides and its effect on ammonia adsorption.* Journal of Materials Chemistry, 2009. **19**(48): p. 9176-9185.

19. Park, S. and R.S. Ruoff, *Chemical methods for the production of graphenes.* Nat Nano, 2009. **4**(4): p. 217-224.

20. Mkhoyan, K.A., et al., *Atomic and Electronic Structure of Graphene-Oxide.* Nano Letters, 2009. **9**(3): p. 1058-1063.

21. Guo, P., H. Song, and X. Chen, *Electrochemical performance of graphene nanosheets as anode material for lithium-ion batteries.* Electrochemistry Communications, 2009. **11**(6): p. 1320-1324.

22. Ng, S.-H., et al., *Highly Reversible Lithium Storage in Spheroidal Carbon-Coated Silicon Nanocomposites as Anodes for Lithium-Ion Batteries.* Angewandte Chemie International Edition, 2006. **45**(41): p. 6896-6899.

23. Xian Du, P.G., Huaihe Song, Xiaohong Chen, *Graphene nanosheets as electrode material for electric double-layer capacitors.* Electrochimica Acta, 2010. **55**: p. 4812-4819.

24. Vivekchand, S., et al., *Graphene-based electrochemical supercapacitors.* Journal of Chemical Sciences, 2008. **120**(1): p. 9-13.

25. Liu, C., et al., *Graphene-Based Supercapacitor with an Ultrahigh Energy Density.* Nano Letters, 2010. **10**(12): p. 4863-4868.

26. Stoller, M.D., et al., *Graphene-Based Ultracapacitors.* Nano Letters, 2008. **8**(10): p. 3498-3502.

27. Zhang, Y., et al., *Capacitive behaviour of graphene-ZnO composite film for supercapacitors.* Journal of Electroanalytical Chemistry, 2009. **634**(1): p. 68-71.

28. Kim, K.S., et al., *Large-scale pattern growth of graphene films for stretchable transparent electrodes.* Nature, 2009. **457**(7230): p. 706-710.

29. Tung, V.C., et al., *Low-Temperature Solution Processing of Graphene-Carbon Nanotube Hybrid Materials for High-Performance Transparent Conductors.* Nano Letters, 2009. **9**(5): p. 1949-1955.

30. Cai, D., M. Song, and C. Xu, *Highly Conductive Carbon-Nanotube/Graphite-Oxide Hybrid Films.* Advanced Materials, 2008. **20**(9): p. 1706-1709.

31. Yu, A., et al., *Enhanced Thermal Conductivity in a Hybrid Graphite Nanoplatelet – Carbon Nanotube Filler for Epoxy Composites.* Advanced Materials, 2008. **20**(24): p. 4740-4744.

32. Kim, J., et al., *Graphene Oxide Sheets at Interfaces.* Journal of the American Chemical Society, 2010. **132**(23): p. 8180-8186.

33. Yu, D. and L. Dai, *Self-Assembled Graphene/Carbon Nanotube Hybrid Films for Supercapacitors.* The Journal of Physical Chemistry Letters, 2009. **1**(2): p. 467-470.

34. Liu, Z., et al., *PEGylated Nanographene Oxide for Delivery of Water-Insoluble Cancer Drugs.* Journal of the American Chemical Society, 2008. **130**(33): p. 10876-10877.

35. Yang, X., et al., *High-Efficiency Loading and Controlled Release of Doxorubicin Hydrochloride on Graphene Oxide.* The Journal of Physical Chemistry C, 2008. **112**(45): p. 17554-17558.

36. Medhekar, N.V., et al., *Hydrogen Bond Networks in Graphene Oxide Composite Paper: Structure and Mechanical Properties.* ACS Nano, 2010. **4**(4): p. 2300-2306.

37. Gómez-Navarro, C., et al., *Atomic Structure of Reduced Graphene Oxide.* Nano Letters, 2010. **10**(4): p. 1144-1148.

38. Krauss, B., et al., *Laser-induced disassembly of a graphene single crystal into a nanocrystalline network.* Physical Review B, 2009. **79**(16): p. 165428.

39. Marcano, D.C., et al., *Improved Synthesis of Graphene Oxide.* ACS Nano, 2010. **4**(8): p. 4806-4814.

40. Li, D., et al., *Processable aqueous dispersions of graphene nanosheets.* Nat Nano, 2008. **3**(2): p. 101-105.

41. van der Kooij, F.M. and H.N.W. Lekkerkerker, *Formation of Nematic Liquid Crystals in Suspensions of Hard Colloidal Platelets.* The Journal of Physical Chemistry B, 1998. **102**(40): p. 7829-7832.

42. Wang, S.J., et al., *Fabrication of highly conducting and transparent graphene films.* Carbon, 2010. **48**(6): p. 1815-1823.

43. Yang, D., et al., *Chemical analysis of graphene oxide films after heat and chemical treatments by X-ray photoelectron and Micro-Raman spectroscopy.* Carbon, 2009. **47**(1): p. 145-152.

44. Gao, W., et al., *New insights into the structure and reduction of graphite oxide.* Nat Chem, 2009. **1**(5): p. 403-408.

45. Chen, W., L. Yan, and P.R. Bangal, *Preparation of graphene by the rapid and mild thermal reduction of graphene oxide induced by microwaves.* Carbon, 2010. **48**(4): p. 1146-1152.

46. Tung, V.C., et al., *High-throughput solution processing of large-scale graphene.* Nat Nano, 2009. **4**(1): p. 25-29.

47. Wei, Z., et al., *Nanoscale Tunable Reduction of Graphene Oxide for Graphene Electronics.* Science, 2010. **328**(5984): p. 1373-1376.

48. Stankovich, S., et al., *Synthesis of graphene-based nanosheets via chemical reduction of exfoliated graphite oxide.* Carbon, 2007. **45**(7): p. 1558-1565.

49. Ferrari, A.C. and J. Robertson, *Interpretation of Raman spectra of disordered and amorphous carbon.* Physical Review B, 2000. **61**(20): p. 14095.

50. Frackowiak, E., et al., *Nanotubular materials as electrodes for supercapacitors.* Fuel Processing Technology, 2002. **77-78**: p. 213-219.

51. Frackowiak, E., et al., *Enhanced capacitance of carbon nanotubes through chemical activation.* Chemical Physics Letters, 2002. **361**(1-2): p. 35-41.

52. Berger, C., et al., *Electronic Confinement and Coherence in Patterned Epitaxial Graphene.* Science, 2006. **312**(5777): p. 1191-1196.

53. Chen, Y., et al., *High performance supercapacitors based on reduced graphene oxide in aqueous and ionic liquid electrolytes.* Carbon, 2011. **49**(2): p. 573-580.

54. Conway, B.E., *Electrochemical Supercapacitor: Scientific Fundamentals and Technological Application* 1999: New York:Kluwer Academic/Plenum Publisher.

55. Henstridge, M.C., E.J.F. Dickinson, and R.G. Compton, *On the estimation of the diffuse double layer of carbon nanotubes using classical theory: Curvature effects on the Gouy-Chapman limit.* Chemical Physics Letters, 2010. **485**(1-3): p. 167-170.

56. Bonora, P.L., F. Deflorian, and L. Fedrizzi, *Electrochemical impedance spectroscopy as a tool for investigating underpaint corrosion.* Electrochimica Acta. **41**(7-8): p. 1073-1082.

57. Girija, T.C. and M.V. Sangaranarayanan, *Analysis of polyaniline-based nickel electrodes for electrochemical supercapacitors.* Journal of Power Sources, 2006. **156**(2): p. 705-711.

58. Yao, P., et al., *Electric Current Induced Reduction of Graphene Oxide and Its Application as Gap Electrodes in Organic Photoswitching Devices.* Advanced Materials, 2010. **22**(44): p. 5008-5012.

59. Zhou, M., et al., *Controlled Synthesis of Large-Area and Patterned Electrochemically Reduced Graphene Oxide Films.* Chemistry – A European Journal, 2009. **15**(25): p. 6116-6120.

60. Shao, Y., et al., *Facile and controllable electrochemical reduction of graphene oxide and its applications.* Journal of Materials Chemistry, 2010. **20**(4): p. 743-748.

Chapter 6: Comparison of GO, GO/MWCNTs Composite and MWCNTs as Potential Electrode Materials for Hydrogen Storage

6.1 Hydrogen storage and materials for hydrogen storage: current limitations

The world's demand for energy, as well as concerns about climate change and global warming has inspired intensive research to develop new clean energy sources that can replace oil and fossil fuels. Hydrogen is a clean form of energy that has the potential to fuel vehicles. However, efficient hydrogen storage for developing a sustainable hydrogen economy remains a significant challenge. [1]

Hydrogen storage materials can be mainly categorized into two distinct groups, namely chemical storage, where hydrides are stored and physical storage, where hydrogen molecules are stored. A feasible hydrogen storage material is required to absorb/adsorb hydrogen strongly enough to form thermodynamically stable state but weakly enough to release it by a small temperature rise. For on board applications, however, metal hydrides, which can chemically absorb hydrogen, either exhibit very low gravimetric densities such as hydrides of heavy transition metals and rare based elements or thermodynamics of H bonding is either too strong or too weak such as alanyte (A_lH_3). [2] Although complex metal hydrides and chemical hydrides can operate within the temperature-pressure conditions set by United States

Department of Energy (DOE), many of the reactions are exothermic and dehydrogenated products are very stable resulting in an overall energy inefficiency. [2]

6.2 Materials for hydrogen storage

6.2.1 Traditional materials

There have been many attempts to use carbon adsorbents, which give rise to the second class of hydrogen storage materials through physical adsorption of hydrogen molecules, as reversible hydrogen storage materials. However, most of the measurements so far have been conducted at 77K which exhibits limited practicality as the plan devised by DOE, in light of automotive industry plans, clearly states that hydrogen storage materials should be able to absorb/adsorb and release hydrogen at temperature range of 30-50 °C (300-320 K). [2] While there are many reports regarding the hydrogen capacity of pure carbon-based materials and metal-organic frameworks, it is generally agreed and demonstrated that these types of materials merely physisorb a small amount of hydrogen (typically less than 1wt%) at ambient temperature and excessive pressure range (up to 10 MPa). [3-7]

6.2.2 Advanced materials

A number of new compounds are continuously being introduced as hydrogen storage materials [8]. However, no known material exhibits all of the attributes required for a viable storage system. Recently, two dimensional (2-D) carbon materials such as graphene, [4, 9] graphene oxide (GO), [10-12] few-layered graphene sheets, [13] or graphene decorated with metal particles, [14, 15] have attracted attention for hydrogen storage applications. Theoretical calculations have demonstrated that graphene may have great potential for hydrogen storage. However, the layers should be separated without filling the interlayer gaps. [12, 16-18] Therefore, architecturally engineered carbon-based nanostructured materials such as pillared graphene oxide and graphene oxide framework materials which can create unique nano-assemblies have been studied extensively. [9-11, 17, 19, 20] However, in practice, achieving

these types of ordering at small length scales is a strenuous task if not impossible. Nevertheless, most of the work conducted on these materials has been purely theoretical modeling, as these frameworks can only be achieved through the use of highly sophisticated instruments and long processing time such as Langmuir−Blodgett (LB) deposition. [21] In contrast, the use of liquid crystal route, as a promising technique, possesses unrivaled advantages in terms of yield and cost.

In previous chapters, it was demonstrated that the liquid crystallinity of GO can be utilized to fabricate macroscopically ordered layer-by-layer GO frameworks. [22] Compared to other approaches developed to align GO sheets, the novel liquid crystal route is particularly attractive to achieve self-aligned and chemically-tunable assemblies. [22-24] GO undergoes a transition to a liquid crystalline state in aqueous media which in turn facilitates the processing of GO for many emerging applications. Apart from the liquid crystal route, the gain in exclusion volume can play an important role as a driving force to align GO sheets in a specific direction and therefore forces the formation of other constituent parts based on the GO structure.

In the current chapter, the processability of GO dispersions can be further exploited to fabricate self-aligned GO-Multiwalled carbon nanotube (MWCNT) hybrid frameworks with a high degree of orientation. [25] Furthermore, the hydrogen storage properties of both layer-by-layer spatially engineered 3D-GO and GO-MWCNT papers have been studied. The remarkable synergistic properties from combining GO and MWCNTs in a hybrid structure offer a novel yet simple way of designing GO based hybrid frameworks with extraordinary hydrogen storage capacities by incorporating two different materials neither one of which alone might be completely perfect for the required application.

6.3 Microscopic characterization of GO and GO-MWCNT hybrid materials

Large area graphene sheets are highly desirable for forming three-dimensional graphene-based networks and fabricating optoelectronic devices mainly because of the much-lower degree of defects on their basal planes, arising from the lower degree of non-stoichiometric oxygen. In order to assess the sheet size of the as-prepared GO sheets, the as-prepared GO sample was analysed by SEM and AFM (Figure 6.1).

The As-prepared GO dispersions contain giant monolayer GO sheets predominantly in the order of 50 μm. It is widely believed that the electrostatic repulsion of the ionizable edge carboxylic acid groups allows graphite oxide to be fully delaminated and to form stable single layer GO aqueous dispersions. [25, 26] AFM studies and especially scanning electron microscopy well confirm the formation of mostly monolayer GO sheets in our as-prepared GO aqueous dispersions. Figure 6.1a shows an ultra large wrinkled GO sheet. The apparent thickness of the GO sheet is around 0.89 nm which is in complete agreement with inter layer spacing value obtained from XRD results (0.826 nm) (Figure 5.8). From the AFM image (Figure 6.1b) it is also apparent that the thickness of individual wrinkles is mostly in the range of 3 to 10 nm. A recent study has also suggested that the hydrogen bonding between the carboxylic acid edge groups which is more pronounced under acidic conditions might be responsible for the wrinkling behaviour. [27] In essence, this wrinkling behaviour might be of utmost importance, mainly because according to new theoretical insights certain areas on the buckled sheets of graphene can preferentially bind hydrogen. [28]

In the case of the hybrid material, no bundling of MWCNTs can be observed in TEM micrograph (Figure 6.1c), demonstrating that MWCNTs are uniformly dispersed and adsorbed on the islands on the surface of GO.

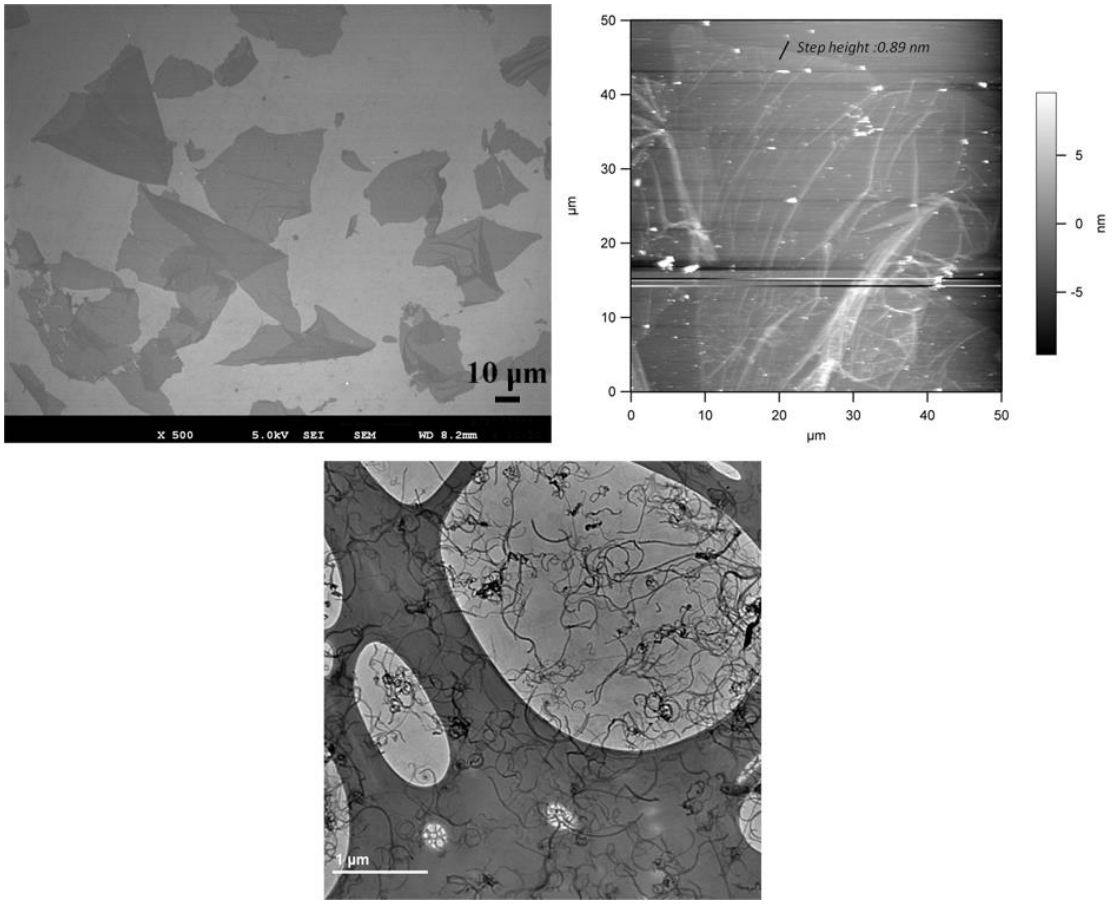

Figure 6. 1. a) SEM, b) AFM micrographs of as-prepared GO sheets and c) TEM micrograph of as-prepared GO-MWCNTs.

Single-layer graphene and graphene oxide are the weakest object so far available with respect to electron scattering. [29, 30] High resolution transmission electron microscopy was performed on samples to detect the number of graphene layers per stack. Figure 6.2 represents the corresponding HR-TEM micrographs of both as-prepared GO and GO-MWCNT samples. HR-TEM micrograph supports the assertion that the hybrid material sheets indeed consist of MWCNTs attached to single layer graphene oxide sheets.

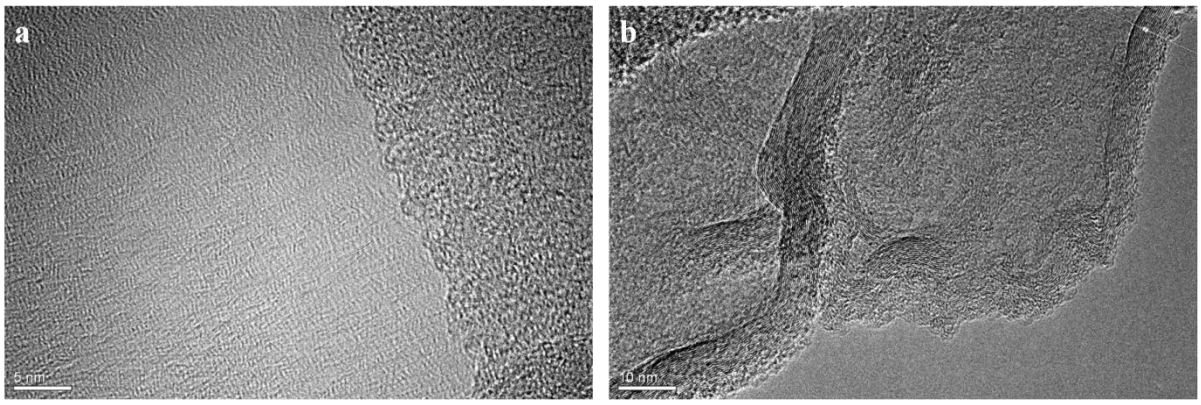

Figure 6. 2. High resolution TEM micrographs of a) GO, and b) GO-MWCNT samples.

In the case of multi-layer GO sheets, the number of edge lines is a sign of the number of layers. However, in the current study as it is illustrated in the micrograph, just one edge line can be observed in both GO and GO-MWCNTs samples indicating that GO sheets are monolayer in nature. It is pertinent to mention that the introduction of MWCNTs to GO clearly does not affect the ordering of GO sheets and MWCNTs act only as spacers between GO layers and also inhibit uncontrolled restacking. This ordering in turn results in a fully intercalated 3D structure (as shown in Figure 6.3d).

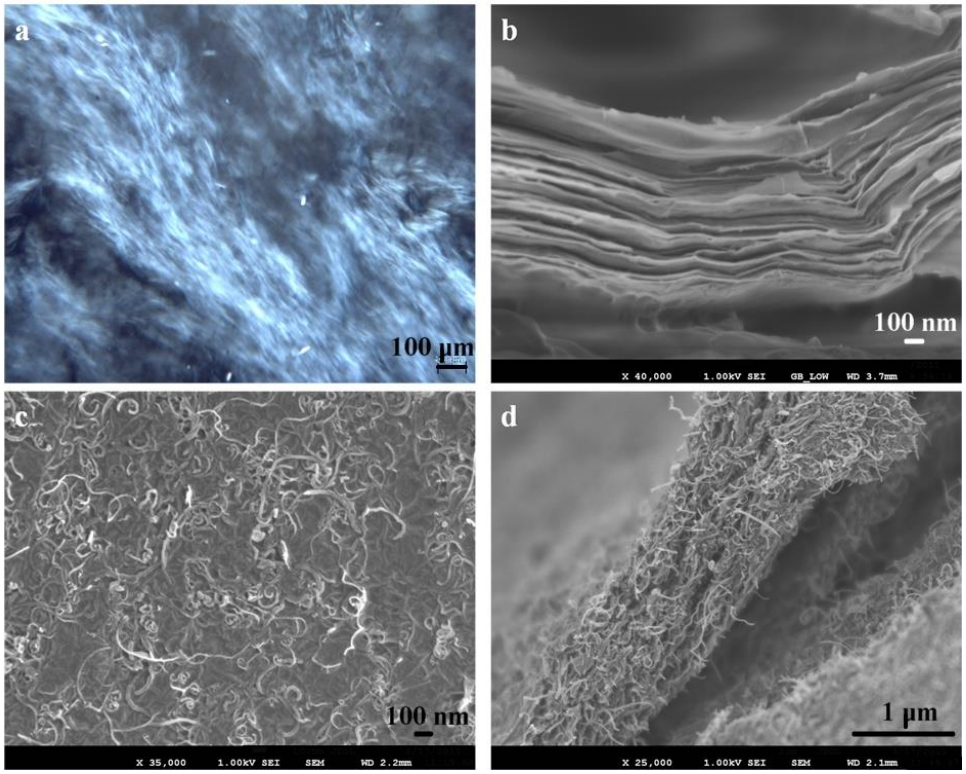

Figure 6. 3**.** a) Polarized optical micrograph of LC graphene oxide dispersion and SEM micrographs of b) GO paper, c) MWCNTs distributed on GO layer and d) layer-by-layer assembled GO platelets decorated by MWCNTs.

In contrast with graphene that only goes through the liquid crystalline (LC) state at high concentration in super acids, [31] GO can form lyotropic nematic liquid crystals at concentrations as low as 1 mg ml^{-1} in aqueous medium [22]. Images between crossed polarisers confirm that the GO dispersions show the typical birefringence behaviour of liquid crystals (Figure 6.3a). The LC properties of GO sheets induce a spontaneous self-assembly into engineered long range ordered layer-by-layer 3D structures upon simple casting and drying as shown in the scanning electron microscope micrograph in Figure 6.3b. The interlayer spacing of this GO paper which is in excess of 0.82 nm provides a platform to accommodate and intercalate hydrogen atoms.

In a colloidal suspension containing GO sheets and other constituents with significantly different sizes, the sheets generate excluded volume for smaller sheets giving rise to entropic

rearrangement of sheets to form long range ordering. Therefore, GO was employed as a dispersing agent to process MWCNTs in water and consequently fabricate highly aligned, and macroscopically periodic self-assembled structures of GO-MWCNTs hybrid material. Strong π–π attractions between the basal planes of GO sheets, which normally consist of π-conjugated aromatic domains, and the surface of the MWCNTs, makes the decoration of the GO platelets with MWCNTs possible (see details in Chapter 5). [26] Moreover, the introduction of one-dimensional spacers, nanotubes, nanowires and nanorods, effectively inhibits the re-stacking of individual two-dimensional GO sheets and further increase the spacing of GO sheets. [25, 32] Furthermore, GO sheets can effectively separate MWCNTs from each other. This separation can consequently result in an increase in effective surface area of MWCNTs. Similar to nematic liquid crystal phases, based on the excluded volume theory, the ends of any individual GO sheets tend to be further apart from each other. This in turn facilitates the easy accommodation and alignment of π–π bonded MWCNTs within the structure. The SEM micrograph of GO-MWCNTs in Figure 6.3c shows the distribution of MWCNTs on graphene layers while Figure 6.3d clearly demonstrates the highly aligned, layered and well-packed structure of GO platelets that are spaced by MWCNTs.

6.4 Hydrogen storage properties of GO and GO-MWCNT hybrid materials

The hydrogen storage capacities of GO, MWCNTs, GO-MWCNTs and reduced GO-MWCNTs were measured at room temperature and 5 MPa hydrogen pressure (Figure 6.4).

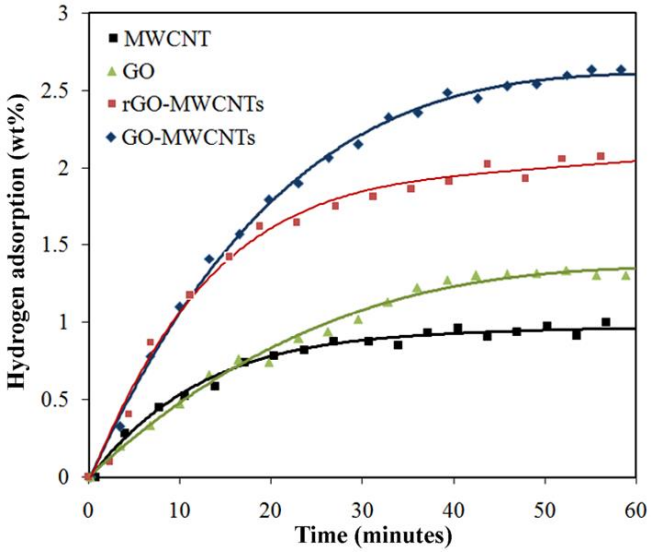

Figure 6. 4. Hydrogen adsorption of GO, MWCNTs, GO-MWCNTs and rGO-MWCNTs as a function of time.

The hydrogen uptake of MWCNTs and GO was around 0.9 wt% and 1.4 wt%, respectively, while the hydrogen capacity of GO-MWCNTs reached 2.6 wt% which is even more than the total capacity of the individual composite constituents, *i.e.* GO and MWCNTs. The adsorption capacity of our samples at moderately high pressure and room temperature surpasses the hydrogen uptake values given for metal–organic frameworks (MOFs) and both chemically activated and high surface area carbon based materials. For clarity, hydrogen uptake of various materials from state-of-the-art metal-organic frameworks to carbon based materials is given in Table 6.1. It should also be noted that the desorption process happened instantaneously as it is expected in the case of carbon materials. Figure 6.5 compares the absolute hydrogen adsorption values of all four materials at two different hydrogen pressures.

Table 6. 1. Hydrogen uptake of various materials

Materials	**H_2 Uptake (wt%)**	**Conditions**	**Ref**

Graphene Oxide-Multiwalled Carbon Nanotube	2.6	298K 50 bar	Current Study
Reduced Graphene Oxide-Multiwalled Carbon Nanotube	2.1	298K 50 bar	Current Study
Graphene Oxide	1.4	298K 50 bar	Current Study
Zn4O(BDC)3, MOF-5 or IRMOF-1	0.4	298K 100 bar	[33]
Pt/AC+MOF-5 mixture	1.6	298K 100 bar	[33]
Mn3[(Mn4Cl)3(BTT)8]2	0.8	298K 50 bar	[34]
Pt/AC+MOF-177 mixture (spillover)	1.5	298K 100 bar	[35]
[Mn(DMF)6]3[(Mn4Cl)3(BTT)8(H2O)12]2 · 42CH3OH	1.5	298K 90 bar	[34]
SNU-5	0.5	298K 100 bar	[36]
MOF-177	0.5	298K 100 bar	[36]
Pt@MOF-177	2.5 @1st cycle and 0.5 2nd cycle	298K 144 bar	[36, 37]
AC1	0.28	298K 50 bar	[3]
AC2	0.45	298K 50 bar	[3]
ACF	0.33	298K 50 bar	[3]
Graphite	0	298K 50 bar	[3]
SWNH	0.15	298K 50 bar	[3]
SWNH-773	0.4	298K 50 bar	[3]
Graphene-like nanosheets	0.72	298K 100 bar	[7]
A-Carbon	0.81	298K 100 bar	[38]

KUA5	0.78	298K 100 bar	[39]
KUA6	0.68	298K 100 bar	[39]
AX21	0.68	298K 100 bar	[39]
ACF-2300	0.5	298K 100 bar	[40]
Thermally modulated multi-layered graphene oxide	0.5	298K 90 bar	[41]
Gr-Pt (Graphene-Platinum)	0.15	303K 57 bar	[42]
Gr-Pd (Graphene-Palladium)	0.156	303K 57 bar	[42]
Graphene	0.9	298K 100 bar	[6]

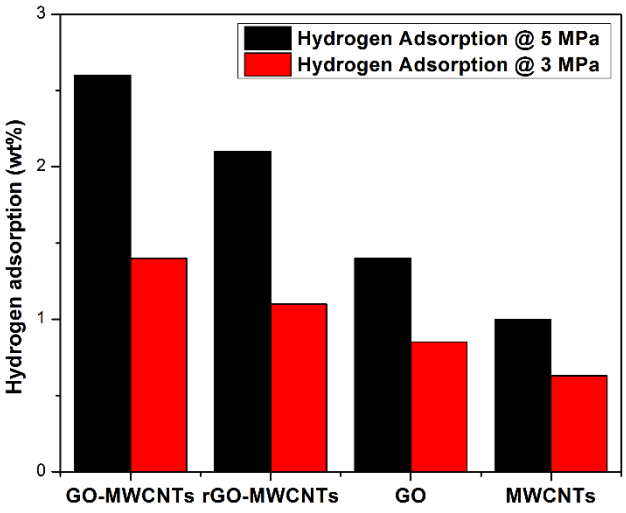

Figure 6. 5. Comparative Hydrogen adsorption of GO, MWCNTs, GO-MWCNTs and rGO-MWCNTs at different Hydrogen Pressures.

In the case of carbon based materials, hydrogen adsorption can occur with a Langmuir isotherm behaviour, which does not lead to obvious plateaus at lower temperature. This effect is more pronounced at room temperature

6.4.1 Hydrogen adsorption isotherm of GO-MWCNTs

The Hydrogen adsorption isotherm of GO-MWCNTs hybrid material is also given in Figure 6.6. In general, sorption in hydride-forming compounds such as metal hydrides can occur at an approximately fixed pressure where the change to the hydride phase takes place [43], however, it should be noted that in the case of carbon based materials, hydrogen adsorption can occur with a Langmuir isotherm behaviour, which does not lead to obvious plateaus at lower temperature [44]. Such adsorption is much smaller at room temperature and often not detectable [43, 44]. Therefore, the pressure plateau affiliated with hydrogen sorption which is expected in the case of metal hydrides cannot be essentially observed in hydrogen adsorption of our materials at room temperature.

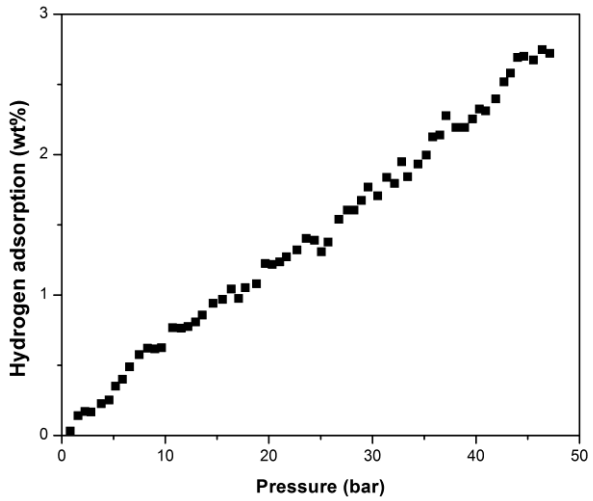

Figure 6. 6. Hydrogen adsorption isotherm of GO-MWCNTs as a function of pressure.

6.4.2 Ideal hydrogen storage behaviour

An ideal hydrogen storage material should be stable to any potential hazards such as impurities present in H_2 gas and to accidental exposure to the atmosphere[45]. However, some of the best known and highest performance MOFs, such as $Zn_4O(BDC)_3$ and $Mn_3[(Mn4Cl)_3(BTT)_8]_2$, are known to decompose in air which should be taken into consideration in the design of a storage system [45]. To overcome this issue, frameworks featuring strong metal-ligand bonds have been proposed which exhibit improved chemical stability [36, 46-48]. However, the H_2 uptake decreases sharply with increasing temperature (typically less than 1 wt% at room temperature), and none of the (MOFs) yet satisfies the proposed DOE target at room temperature [2, 36, 45, 49]. As an example, the room temperature H_2 uptake capacity of one of the best MOFs (SNU-5) is still not so satisfactory, 0.5 wt % at 100 bar. It is also reported that Pt@MOF-177 can possibly adsorb 2.5 wt % of H_2 at room temperature at excessive pressure of 144 bar in the first adsorption cycle. However, in the second cycle, the storage capacity considerably decreased to 0.5 wt %, which was close to the value of pure MOF-177 [36, 37]. Another interesting feature is that increasing the surface area and creating open metal sites cannot guarantee a high H_2 storage capacity at room temperature [36]. The same criteria also apply to carbon based materials. The significance of these results is more pronounced if we take into account that the maximum experimental hydrogen absorption value as yet reported for GO at 77 K has been 0.2 wt% [11], whereas our as-cast LC-GO dispersions show 1.4 wt% hydrogen uptake even at room temperature. This disparity might be due to the highly ordered, 3D structure of GO fabricated by the LC route. As pointed out by Pumera [18], to improve the binding capacity, sandwich like structures should be created to take H_2 in-between the graphene sheets and relying on just increasing the surface of graphene has no meaning. Although there are many reports regarding increasing the surface area in order to increase the hydrogen uptake [3, 7, 50], careful evaluation of the results presented in literature shows no clear correlation between surface area and hydrogen uptake [3, 7]. For instance, the results presented by Srinivas et al. [7], show relatively

high capacity of low surface area samples (less than 750 m^2/g) compared to high surface area carbons. Therefore, it is suggested that the only possible way to increase the hydrogen uptake of carbon materials is through the introduction of the optimum pore size within the structure which is approximately around 0.7nm to 0.8 nm [3, 18]. The well-defined layered GO structure obtained here offers the possibility of accumulating hydrogen in greater quantities. First-principle calculations also suggest that GO is primarily made up of low-energy oxygen-containing structural motifs on the surface of graphene sheets which is highly desirable for hydrogen storage [12]. The LC route gives us the possibility of fabricating 3D ordered open GO structures with an interlayer spacing of around 0.8 nm, which is ideal as a basic platform for hydrogen storage. However, as there are both a number of multifunctionl groups and water molecules present on the surface of the GO, it can be concluded that not all of this interlayer spacing is accessible to hydrogen. Currently, the precise atomic structure of GO is under debate. Under normal conditions, GO usually contains different functional oxide groups as well as available sp^2 carbon [12].

6.5 Insights into hydrogen storage properties of composite materials

It is worth noting that the amount of available sp^2 carbon just accounts for 25% of the as–fabricated GO structure (based on XPS results shown in Figure 6.7), this in fact corresponds well with the theoretical predictions that at a separation of around 8 Å, the hydrogen capacity of bare graphene would be around 5-6.5 wt% [18]. Another interesting feature demonstrated by XPS, is the reduction in the ratio of Epoxy/Hydroxyl groups compared to C=O and carboxylates groups from the initial value of 2.76 to 1.28 in the case of the hybrid material (GO-MWCNT), which might suggest the reduction of graphene oxide upon the addition of MWCNTs. Although the underlying mechanism is still unclear, the observed phenomena might be attributed to the always present oxidation debris on the surface of acid purified carbon nanotubes [51]. The

oxidative debris mainly comprises a mixture of complex aromatic structures containing COH rich functional groups [51, 52]. These functional groups can then serve as reducing agents to reduce graphene oxide similar to previous reports regarding the reduction of graphene oxide under alkaline conditions [53].

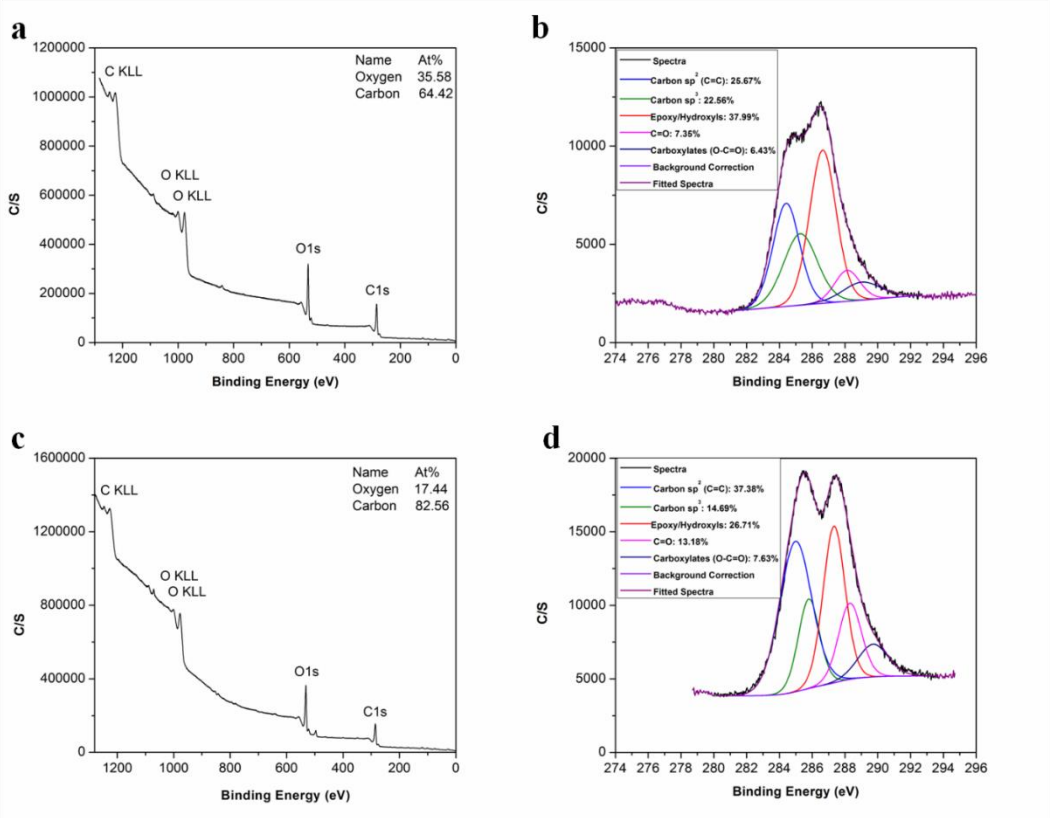

Figure 6. 7. XPS spectra: a) GO, b) fitted spectrum of GO, c) GO-MWCNTs, d) fitted spectrum of GO-MWCNTs in carbon region.

This assertion is further supported by the observed decrease in the zeta potential value of the hybrid material compared to bare graphene oxide from -39 to -49mV (Figure 6.8). Zeta potential is regarded as the manifestation of the electrical properties of interfaces under steady-state isothermal conditions [54]. Zeta potential study revealed that the hydrophobic graphitic islands located on the surface of GO can strongly interact with the hydrophobic surface of MWCNTs consequently resulting in the formation of a stable hybrid structure with significant decrease in the zeta potential (from -39 in GO to -49 mV in GO-MWCNT). However, pristine MWCNT

dispersions in water are unstable and tend to agglomerate. The higher electrostatic repulsion and reduced overlapping areas lead to an electrically stabilized structure.

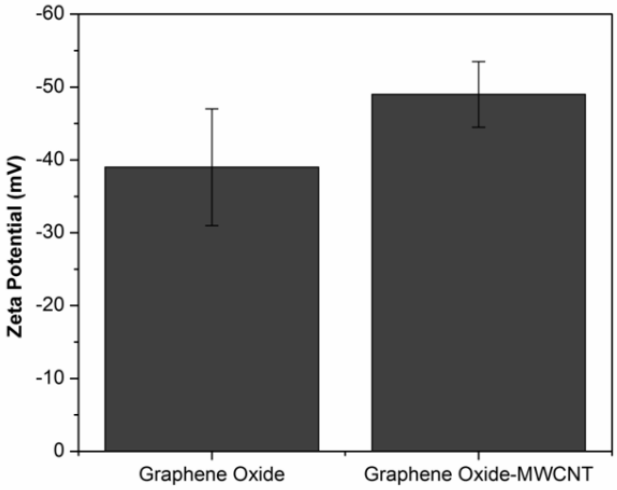

Figure 6. 8. Zeta potential of GO and GO-MWCNTs.

In order to use GO for hydrogen storage, open carbon sites on the surface of GO layers should be accessible when the GO layers are packed together. By keeping several angstroms of space between the graphene oxide sheet layers, the available accessible open carbon sites to store hydrogen is increased substantially leading to superior performance of GO frameworks obtained from the LC route. Furthermore, large GO sheets typically exhibit much lower degree of defects on their basal planes and show higher capacity compared to small GO sheets due to the limited contact points in the final structure. Therefore, employing exceptionally large GO sheets used in this study resulted in the formation of layered sheets with less structural defects which can result in much higher hydrogen adsorption.

In the case of the hybrid material (GO-MWCNTs), the MWCNTs used in this study, as spacers, effectively increase the interlayer spacing to about 7 nm [25]. However, adding CNTs although increases this interlayer spacing does not positively or negatively affect the hydrogen

capacitance. However, it might just facilitate the access to open sp^2 sites. But the degree of this accessibility should be negligible as the required spacing (0.8nm) to accommodate hydrogen in GO architectures is already created. The reason behind the synergistic effect observed here, is therefore because of the effective separation and debundling of MWCNTs using graphene oxide sheets. This separation can consequently result in an increase in effective accessible surface of MWCNTs because of the debundling. Bundling of MWCNTs can inhibit the diffusion of hydrogen in between the MWCNTs and can significantly reduce the accessible open surface. Individual MWCNTs are therefore expected to afford higher hydrogen uptake. Therefore, hydrogen uptake can be more pronounced in the case of individual and fully separated CNTs entangled between separated GO sheets. No bundling of MWCNTs can be observed in our case, as it is shown in TEM and SEM micrographs. This in turn results in much higher hydrogen uptake in the hybrid material (GO-MWCNTs). It is, therefore, proposed that a combination of these factors might be responsible for the high measured hydrogen capacity of the hybrid material. A schematic representing of hydrogen storage on both GO and the hybrid material is shown in Figure 6.9.

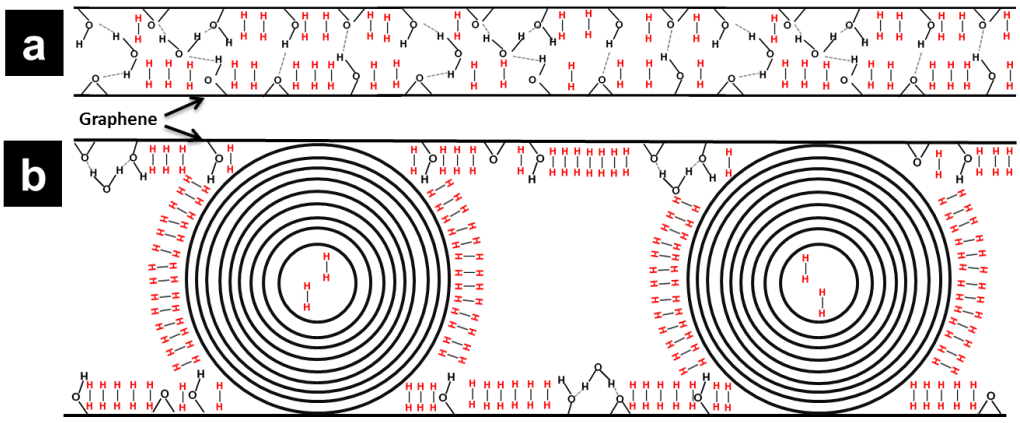

Figure 6. 9. Schematic representing of hydrogen storage on a) GO and b) the hybrid material.

A thermal reduction process was also employed to remove multifunctional groups and open up more carbon sp^2 sites to determine the effect of increasing open sites on hydrogen storage

capacity. In contrast with the as-prepared GO paper, the thermal reduction of graphene oxide resulted in an interlayer d-spacing of around 0.34 nm which is not considered to be suitable for hydrogen adsorption (Figure 6.10).

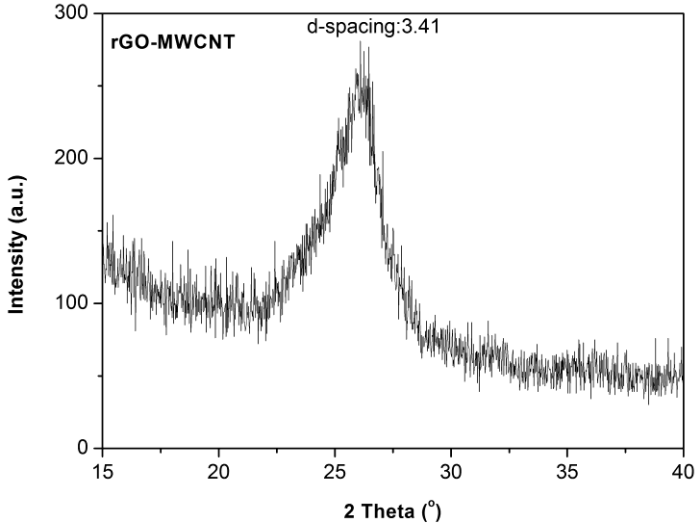

Figure 6. 10. XRD pattern of rGO-MWCNT hybrid material.

In order to determine the degree of reduction, X-ray photoelectron spectroscopy (XPS) was also performed on reduced GO (rGO)-MWCNT samples (Figure 6.11a and 6.11b).

The C1s spectrum of GO-MWCNTs mainly consists of 5 individual peaks namely: carbon sp^2, carbon sp^3, epoxy/hydroxyls, C=O groups and carboxylates. In comparison with the C1s XPS spectrum of as-prepared GO-MWCNT sample, that of partially reduced GO consists of only carbon sp^2, carbon sp^3 C=O groups and carboxylates, which suggests that upon annealing at 350°C, Epoxy/Hydroxyl groups are completely removed from the structure. Furthermore, a substantial decrease in the amount of other functional groups can be observed. Although removing multifunctional groups will result in much higher available carbon sites (around 41%), it decreases the space in-between the layers dramatically. Therefore, annealing the hybrid

material in order to remove multifunctionalities on the surface of GO sheets did not improve the hydrogen uptake.

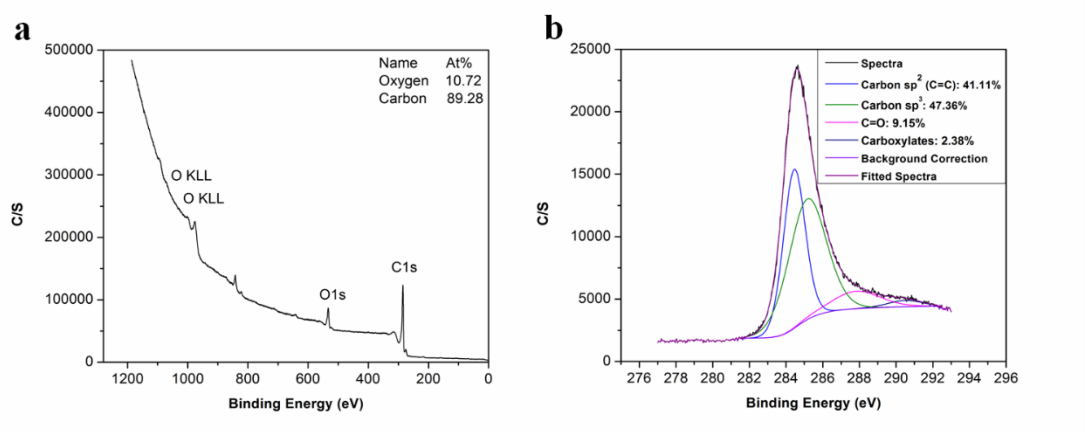

Figure 6. 11. XPS spectra of a) rGO-MWCNTs, and b) fitted spectrum of rGO-MWCNTs in carbon region.

6.6 Conclusion

In summary, it was successfully demonstrated that the LC route can be utilized to prepare unique 3D platforms of graphene oxide layers with proper spacing dimensions as building blocks for cost-effective high-capacity hydrogen storage media. It is also suggested that the addition of MWCNTs within graphene layers can induce the reduction of graphene oxide. Moreover, introducing MWCNTs as 1D spacers resulted in a strong synergistic effect leading to higher hydrogen storage capacity (approximately 2.6 wt%). However, going that extra mile to reduce GO to rGO proved to be ineffective suggesting that the adsorption capacity mainly relies on the spacing in-between the layers. Therefore, it is suggested that the key behind the fabrication of devices with higher hydrogen capacity would be in utilising 1D spacers with high hydrogen capacity to enhance this synergistic effect and not in reducing graphene oxide which results in inadequate interspacing between layers. The main concept of this approach can be a viable alternative route for highly scalable hydrogen storage media. The ease of synthesis and the exceptional hydrogen uptake properties can potentially start a new research direction based

on environmentally friendly GO as a framework for designing of a new generation of hybrid hydrogen energy storage devices in both conventional fields and new emerging areas.

High hydrogen capacity (up to 2.6 wt%) is reported for highly aligned structures of Graphene oxide-Multiwalled carbon nanotubes composite at room temperature. It is demonstrated that the scalable liquid crystal route can be employed as a new method to prepare unique 3-D framework of graphene oxide layers with proper interlayer spacing as building blocks for cost-effective high-capacity hydrogen storage media. The strong synergistic effect of the intercalation of MWCNTs as 1-D spacers within graphene oxide frameworks resulted in unrivalled high hydrogen capacity at ambient temperature. The mechanisms involved in the intercalation procedure are fully discussed. The main concept behind intercalating one-dimensional spacers in between giant GO sheets represents a versatile and highly scalable route to fabricate devices with superior hydrogen uptake.

6.7 References

1. Schlapbach, L. and A. Zuttel, *Hydrogen-storage materials for mobile applications.* Nature, 2001. **414**(6861): p. 353-358.

2. Yang, J., et al., *High capacity hydrogen storage materials: attributes for automotive applications and techniques for materials discovery.* Chemical Society Reviews, 2010. **39**(2): p. 656-675.

3. Xu, W.C., et al., *Investigation of hydrogen storage capacity of various carbon materials.* International Journal of Hydrogen Energy, 2007. **32**(13): p. 2504-2512.

4. Jin, Z., et al., *Nano-Engineered Spacing in Graphene Sheets for Hydrogen Storage.* Chemistry of Materials, 2011. **23**(4): p. 923-925.

5. Bhattacharya, A., et al., *Transition-Metal Decoration Enhanced Room-Temperature Hydrogen Storage in a Defect-Modulated Graphene Sheet.* The Journal of Physical Chemistry C, 2010. **114**(22): p. 10297-10301.

6. Wang, L., N.R. Stuckert, and R.T. Yang, *Unique hydrogen adsorption properties of graphene.* AIChE Journal, 2011. **57**(10): p. 2902-2908.

7. Srinivas, G., et al., *Synthesis of graphene-like nanosheets and their hydrogen adsorption capacity.* Carbon, 2010. **48**(3): p. 630-635.

8. Jeon, K.-J., et al., *Air-stable magnesium nanocomposites provide rapid and high-capacity hydrogen storage without using heavy-metal catalysts.* Nat Mater, 2011. **10**(4): p. 286-290.

9. Paul, R.K., et al., *Synthesis of a Pillared Graphene Nanostructure: A Counterpart of Three-Dimensional Carbon Architectures.* Small, 2010. **6**(20): p. 2309-2313.

10. Tylianakis, E., G.M. Psofogiannakis, and G.E. Froudakis, *Li-Doped Pillared Graphene Oxide: A Graphene-Based Nanostructured Material for Hydrogen Storage.* The Journal of Physical Chemistry Letters, 2010. **1**(16): p. 2459-2464.

11. Burress, J.W., et al., *Graphene Oxide Framework Materials: Theoretical Predictions and Experimental Results.* Angewandte Chemie International Edition, 2010. **49**(47): p. 8902-8904.

12. Wang, L., et al., *Graphene Oxide as an Ideal Substrate for Hydrogen Storage.* ACS Nano, 2009. **3**(10): p. 2995-3000.

13. Subrahmanyam, K.S., et al., *Chemical storage of hydrogen in few-layer graphene.* Proceedings of the National Academy of Sciences, 2011. **108**(7): p. 2674-2677.

14. Wang, Y., et al., *Hydrogen storage in a Ni-B nanoalloy-doped three-dimensional graphene material.* Energy & Environmental Science, 2011. **4**(1): p. 195-200.

15. Lee, H., et al., *Calcium-Decorated Graphene-Based Nanostructures for Hydrogen Storage.* Nano Letters, 2010. **10**(3): p. 793-798.

16. Abergel, D.S.L., et al., *Properties of graphene: a theoretical perspective.* Advances in Physics, 2010. **59**(4): p. 261-482.

17. Dimitrakakis, G.K., E. Tylianakis, and G.E. Froudakis, *Pillared Graphene: A New 3-D Network Nanostructure for Enhanced Hydrogen Storage.* Nano Letters, 2008. **8**(10): p. 3166-3170.

18. Pumera, M., *Graphene-based nanomaterials for energy storage.* Energy & Environmental Science, 2011. **4**(3): p. 668-674.

19. Hammond, P.T., *Form and Function in Multilayer Assembly: New Applications at the Nanoscale.* Advanced Materials, 2004. **16**(15): p. 1271-1293.

20. Hong, J. and S.W. Kang, *Hydrophobic properties of colloidal films coated with multi-wall carbon nanotubes/reduced graphene oxide multilayers.* Colloids and Surfaces A: Physicochemical and Engineering Aspects, 2011. **374**(1–3): p. 54-57.

21. Cote, L.J., F. Kim, and J. Huang, *Langmuir−Blodgett Assembly of Graphite Oxide Single Layers.* Journal of the American Chemical Society, 2008. **131**(3): p. 1043-1049.

22. Aboutalebi, S.H., et al., *Spontaneous Formation of Liquid Crystals in Ultralarge Graphene Oxide Dispersions.* Advanced Functional Materials, 2011. **21**(15): p. 2978-2988.

23. Kim, J.E., et al., *Graphene Oxide Liquid Crystals.* Angewandte Chemie International Edition, 2011. **50**(13): p. 3043-3047.

24. Xu, Z. and C. Gao, *Aqueous Liquid Crystals of Graphene Oxide.* ACS Nano, 2011. **5**(4): p. 2908-2915.

25. Aboutalebi, S.H., et al., *Comparison of GO, GO/MWCNTs composite and MWCNTs as potential electrode materials for supercapacitors.* Energy & Environmental Science, 2011. **4**(5): p. 1855-1865.

26. Kim, J., et al., *Graphene Oxide Sheets at Interfaces.* Journal of the American Chemical Society, 2010. **132**(23): p. 8180-8186.

27. Cote, L.J., et al., *Tunable assembly of graphene oxide surfactant sheets: wrinkles, overlaps and impacts on thin film properties.* Soft Matter, 2010. **6**(24): p. 6096-6101.

28. Tozzini, V. and V. Pellegrini, *Reversible Hydrogen Storage by Controlled Buckling of Graphene Layers.* The Journal of Physical Chemistry C, 2011. **115**(51): p. 25523-25528.

29. Kim, J., F. Kim, and J. Huang, *Seeing graphene-based sheets.* Materials Today, 2010. **13**(3): p. 28-38.

30. Zhu, Y., et al., *Graphene and Graphene Oxide: Synthesis, Properties, and Applications.* Advanced Materials, 2010. **22**(35): p. 3906-3924.

31. Behabtu, N., et al., *Spontaneous high-concentration dispersions and liquid crystals of graphene.* Nat Nano, 2010. **5**(6): p. 406-411.

32. Qiu, L., et al., *Dispersing Carbon Nanotubes with Graphene Oxide in Water and Synergistic Effects between Graphene Derivatives.* Chemistry – A European Journal, 2010. **16**(35): p. 10653-10658.

33. Li, Y. and R.T. Yang, *Hydrogen Storage in Metal−Organic Frameworks by Bridged Hydrogen Spillover.* Journal of the American Chemical Society, 2006. **128**(25): p. 8136-8137.

34. Dincă, M., et al., *Hydrogen Storage in a Microporous Metal−Organic Framework with Exposed Mn2+ Coordination Sites.* Journal of the American Chemical Society, 2006. **128**(51): p. 16876-16883.

35. Li, Y. and R.T. Yang, *Gas Adsorption and Storage in Metal−Organic Framework MOF-177.* Langmuir, 2007. **23**(26): p. 12937-12944.

36. Suh, M.P., et al., *Hydrogen Storage in Metal–Organic Frameworks.* Chemical Reviews, 2011. **112**(2): p. 782-835.

37. Proch, S., et al., *Pt@MOF-177: Synthesis, Room-Temperature Hydrogen Storage and Oxidation Catalysis.* Chemistry – A European Journal, 2008. **14**(27): p. 8204-8212.

38. Thomas, K.M., *Hydrogen adsorption and storage on porous materials.* Catalysis Today, 2007. **120**(3–4): p. 389-398.

39. Jordá-Beneyto, M., et al., *Hydrogen storage on chemically activated carbons and carbon nanomaterials at high pressures.* Carbon, 2007. **45**(2): p. 293-303.

40. Bénard, P. and R. Chahine, *Determination of the Adsorption Isotherms of Hydrogen on Activated Carbons above the Critical Temperature of the Adsorbate over Wide Temperature and Pressure Ranges.* Langmuir, 2001. **17**(6): p. 1950-1955.

41. Kim, B.H., et al., *Thermally modulated multilayered graphene oxide for hydrogen storage.* Physical Chemistry Chemical Physics, 2012. **14**(4): p. 1480-1484.

42. Huang, C.-C., et al., *Hydrogen storage in graphene decorated with Pd and Pt nano-particles using an electroless deposition technique.* Separation and Purification Technology, 2011. **82**(0): p. 210-215.

43. Tibbetts, G.G., G.P. Meisner, and C.H. Olk, *Hydrogen storage capacity of carbon nanotubes, filaments, and vapor-grown fibers.* Carbon, 2001. **39**(15): p. 2291-2301.

44. Ye, Y., et al., *Hydrogen adsorption and cohesive energy of single-walled carbon nanotubes.* Applied Physics Letters, 1999. **74**(16): p. 2307-2309.

45. Murray, L.J., M. Dinca, and J.R. Long, *Hydrogen storage in metal-organic frameworks.* Chemical Society Reviews, 2009. **38**(5): p. 1294-1314.

46. Wu, H., W. Zhou, and T. Yildirim, *Hydrogen Storage in a Prototypical Zeolitic Imidazolate Framework-8.* Journal of the American Chemical Society, 2007. **129**(17): p. 5314-5315.

47. Wang, X.-L., et al., *Metal Nuclearity Modulated Four-, Six-, and Eight-Connected Entangled Frameworks Based on Mono-, Bi-, and Trimetallic Cores as Nodes.* Chemistry – A European Journal, 2006. **12**(10): p. 2680-2691.

48. Choi, H.J., M. Dincă, and J.R. Long, *Broadly Hysteretic H2 Adsorption in the Microporous Metal−Organic Framework Co(1,4-benzenedipyrazolate).* Journal of the American Chemical Society, 2008. **130**(25): p. 7848-7850.

49. Hu, Y.H. and L. Zhang, *Hydrogen Storage in Metal–Organic Frameworks.* Advanced Materials, 2010. **22**(20): p. E117-E130.

50. Texier-Mandoki, N., et al., *Hydrogen storage in activated carbon materials: Role of the nanoporous texture.* Carbon, 2004. **42**(12–13): p. 2744-2747.

51. Verdejo, R., et al., *Removal of oxidation debris from multi-walled carbon nanotubes.* Chemical Communications, 2007(5): p. 513-515.

52. Wang, Z., et al., *The surface acidity of acid oxidised multi-walled carbon nanotubes and the influence of in-situ generated fulvic acids on their stability in aqueous dispersions.* Carbon, 2009. **47**(1): p. 73-79.

53. Fan, X., et al., *Deoxygenation of Exfoliated Graphite Oxide under Alkaline Conditions: A Green Route to Graphene Preparation.* Advanced Materials, 2008. **20**(23): p. 4490-4493.

54. Jeong, Y. and T.C.M. Chung, *Mono-dispersed transition metal nanoparticles on boron-substituted carbon support and applications in hydrogen storage.* Carbon, 2011. **49**(1): p. 140-146.

Chapter 7: Graphene Oxide Dispersions: Tuning Rheology to Enable Fabrication of Advanced 3D Architectures

7.1 The importance of rheological behaviour

The recent discovery of liquid crystalline behaviour in graphene oxide (GO) dispersions in water,[1-5] and various organic solvents,[6, 7] can be implemental in guiding material assembly at atomic level through π–π stacking and hydrogen bonding interactions.[1, 5, 6, 8] Original rheological behaviour is expected, since monolayer GO dispersions constitute a new class of soft material with rich unique properties in between rigid 2D nanoplatelets and 1D polymers.[9] Probing and quantifying this dynamic behaviour will be instrumental in generating novel applications, such as coatings, fillers and molecular electronics by advancing our fundamental knowledge of soft materials.[10] Despite the importance for fundamental, practical, and industrial applications, the rheological behaviour of GO monolayer dispersions and its origin remains an unexplored area. This, in turn, hinders the development of fabrication protocols for two dimensional soft materials, including GO dispersions. Moreover, fabricating practical devices in large-scale with advanced architectural design is still a big challenge, unresolved.

Likewise, formulation of functional composite inks for industrially scalable fabrication methods such as electrospraying, spray coating, and printing techniques, is always hindered by the high concentration of supporting media (such as graphene, GO, LCs and polymers). Therefore, low concentration of the supporting media is desirable to simultaneously permit processing while making the preparation of composite inks with high concentrations of multi-functional materials possible. This challenge, if resolved, can be used to create geometrically

complex multi-functional 3D architectures fabricated for use in areas such as printed electronics, organic field effective transistors and 3D bionic scaffolds.

7.2 An overview of the chapter

Here, with the aim of investigating the rheological behaviour of GO to enable further processing, fabrication and integration of GO into complex architectures, ultra large GO sheets are employed as a model material with high aspect ratio (~ 45000, Figure 7.1) to study the phase transitions from the so-called isotropic phase to liquid crystal (LC) phase and finally to an LC gel phase at higher loadings. We demonstrate that GO dispersions exhibit unique viscoelastic behaviour, wherein the rheological behaviour varies considerably with dispersion concentration. We show that finite yield stress in ultra large GO dispersions occurs at a critical concentration approximately three orders of magnitude lower than the theoretical value for colloidal suspensions ($\phi_{this\ study} \approx 2.2\times10^{-4}$ *vs.* $\phi_c \approx 0.5$) enabling the processing of this 2D material at the lowest concentration ever reported for any dispersions allowing the self-assembly of multi-functional architectures. Our experiments reveal that there are four distinct regions: viscoelastic liquid, a transition state consisting of viscoelastic liquid and viscoelastic soft solid, viscoelastic soft solid (behaving like a solid below yield stress yet flow readily above a yield stress)[11] and viscoelastic gel. Each of these unbinding regions were found amenable to unique processing techniques, some of which never before shown possible in case of GO, warranting the process of this fascinating material based on its inherent complex flow properties.

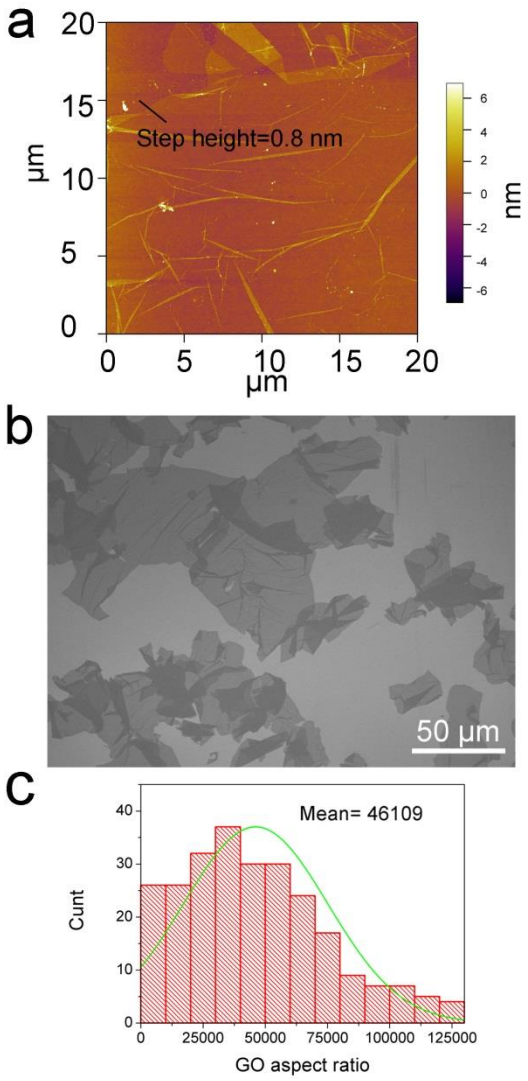

Figure 7. 1. a) Representative AFM image of an ultra large GO sheet. The marked line in the AFM image shows the place which we measured the thickness of the GO sheet confirming the presences of a monolayer of GO with apparent thickness of 0.8 nm. Also, AFM studies show that GO dispersions predominantly contained monolayer of GO sheets. b) SEM image of GO sheets present in as-prepared GO dispersions contain ultra large GO sheets. Both AFM and SEM images present highly wrinkled nature of the GO sheets which confirms flexibility. c) The corresponding distribution of the aspect ratio of GO sheets.

7.3 Rheological investigations and links to processability

Control over the rheological properties can be achieved by adjusting the volume fraction (concentration) of GO particles. To this end, we probed, as plotted in Figure 7.2 and 7.3, the flow behaviour of a series of GO dispersions by the cone-plate method (see experimental section). The elastic G' (storage) and viscous G" (loss) moduli of GO dispersions were determined as a function of frequency at a constant strain amplitude of 0.01.

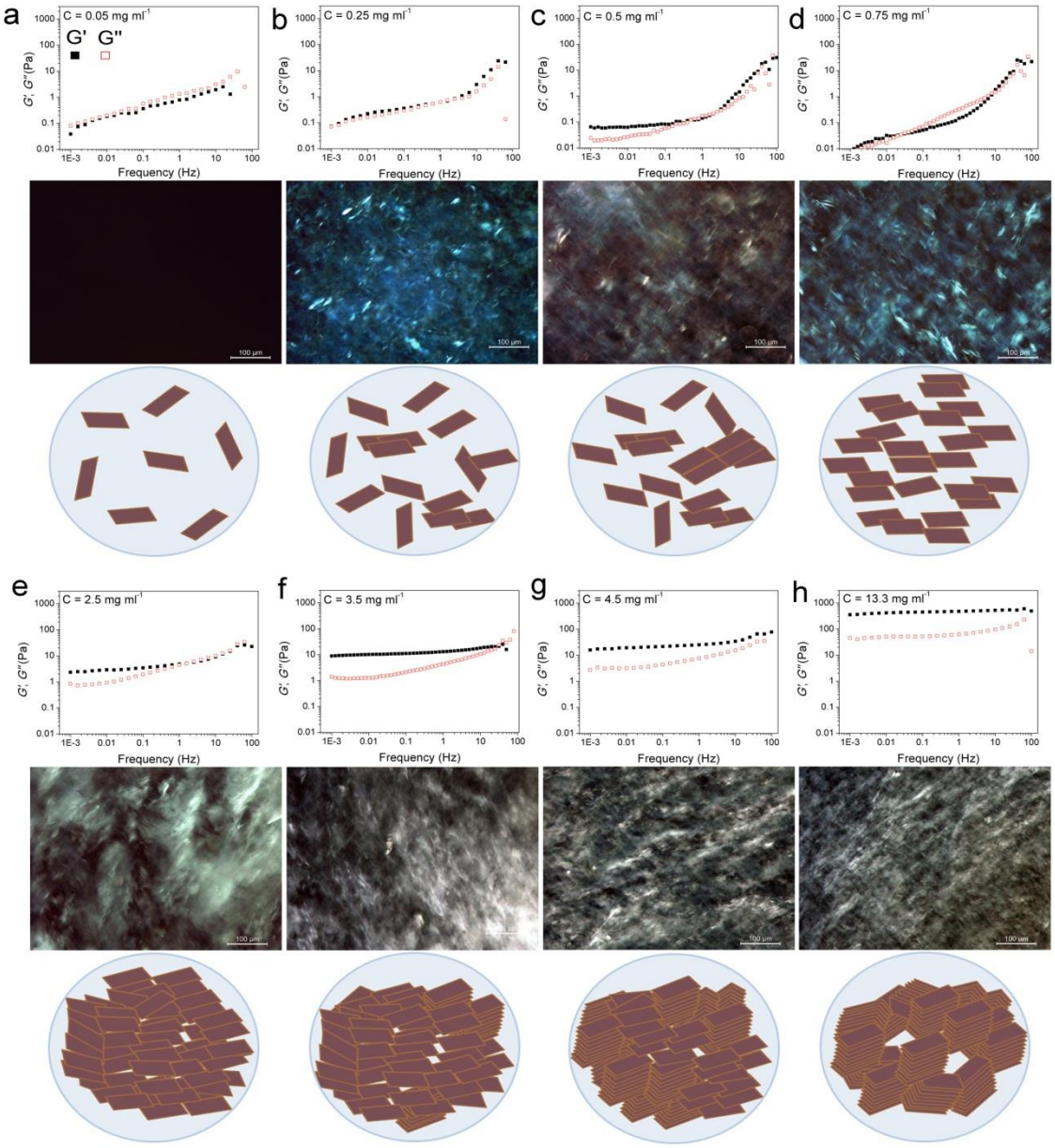

Figure 7. 2. Storage and loss moduli (filled squares and open squares, respectively) of GO suspensions as function of frequency accompanied with their polarized optical micrographs (POMs) and the schematic illustrations of the proposed model for the evolution of LC phases in GO dispersions upon increasing concentration. a) At this extremely low concentration, GO sheets are randomly dispersed in the solution. b, c) Upon increasing concentration to 0.25 mg ml^{-1} some nematic ordering starts to appear. At this region, the storage modulus increases and overtakes the loss modulus, while the loss modulus remains almost constant with frequency. This can be attributed to the increase in the volume fraction of colloidal particles imparting

elasticity to the system. However, this increase in concentration is very negligible to impart any serious effects on the loss modulus, as the dominating part is still water. d) The dispersion forms a single phase nematic liquid crystal. This phase transformation frees up some additional space in the dispersion resulting in subsequent gain in entropy as well as a drop in elastic modulus. e) Further increase in concentration results in higher packing of nematic phase. An increase in volume fraction of GO sheets results in a frequency dependent plateau-like behaviour which is the direct consequence of sheets being trapped by their neighbours preventing the stress relaxation on the longest time-scale of the measurement. (Jammed systems such as weak polymer gels, entangled polymer networks, concentrated emulsions or biological cells exhibit this generic behaviour).[10, 12, 13] f) In addition to long-range orientation in the nematic phase, some parts in GO exhibit long-range positional order. However, above this critical concentration, as the formation of nematic LC phase is completed, further increase in volume fraction results in the simultaneous increase in both moduli, with the storage modulus increasing much faster than the loss modulus. g and h) smaller monodomains are formed associated to exceptional increase in elastic modulus.

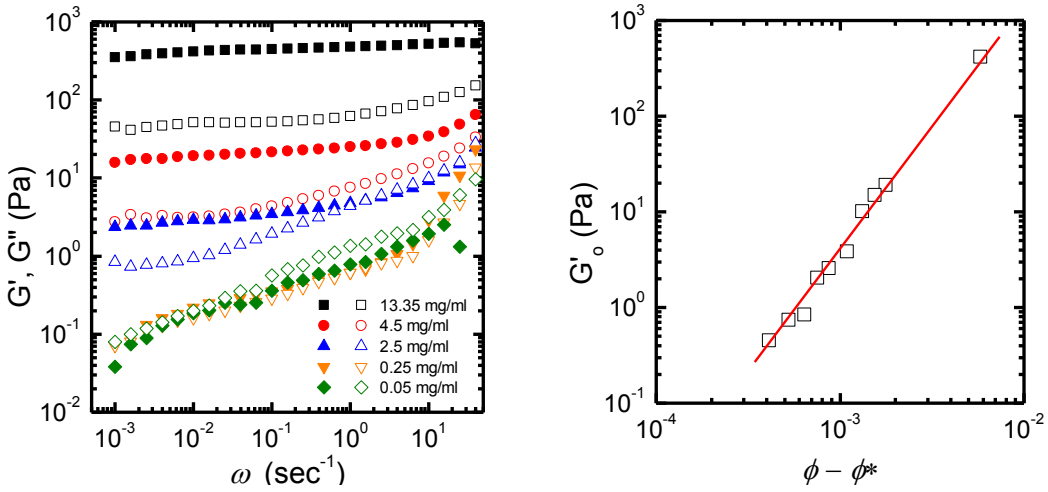

Figure 7. 3. (A) Storage and loss moduli of GO suspensions with varying concentration: 13.35 mg ml^{-1}, 4.5 mg ml^{-1}, 2.5 mg ml^{-1}, 0.25 mg ml^{-1} and 0.05 mg ml^{-1}. (B) Storage modulus of GO

suspension at 0.01 Hz vs $(\phi - \phi^*)$, where ϕ is GO volume fraction. $G_o' \sim (\phi - \phi^*)^v$: $\phi^* \cong 2.3\times10^{-4} \pm 0.7\times10^{-4}$; $v \cong 2.75 \pm 0.15$.

Quite interestingly, even at very low concentrations (as low as 0.05 and up to 0.25 mg ml^{-1}), previously thought to be a completely isotropic and viscous phase,[1, 5] a considerable elastic component still exists. Over all time-scales, in the low concentration region (<0.25 mg ml^{-1}), the dispersions exhibited a liquid-like response with *G''* being slightly higher than *G'* suggesting a viscoelastic liquid like behaviour similar to colloidal suspensions near their crystallization point at volume fractions $\phi_c \sim 0.5$.[10] The dominance of *G''* along with a large *G'* suggests the existence of so-called crowding or jamming.[10] This implies that the configurational rearrangement necessary for equilibration cannot be achieved within the time framework studied here. In our system, jamming resulted in the development of a finite yield stress [12] at concentrations approximately three orders of magnitude lower than the theoretical value for spherical colloidal suspensions ($\phi_{this\ study} \approx 2.2\times10^{-4}$ *vs.* $\phi_c \approx 0.5$).[10] Jamming at such low concentrations is due to the extremely large aspect ratio of ultra large wrinkled GO sheets used in this study (Figure 7.1). The dominance of the viscous part in all time scales (liquid-like behaviour) while having a considerable elastic and viscosity components, in such low concentrations, has a direct impact on processability and fabrication. Specifically this behaviour enables us to easily electrospray and spray-coat with a high level of control (Table 7.1 and Figure 7.4), while eliminating the drift perturbations typically associated with spraying of viscous fluids with no elastic component. These rheological features also allow us to spray at extremely low concentrations leading to low mass loading levels deposited at the substrate surface and subsequently enabling the fabrication of ultra-transparent GO thin films (Transparency of 98.04% and 95.4% at 633 nm for 1 and two-time coated glass slides after partial reduction by heat-treatment at 220ºC corresponding to approximately 1 layer of GO per

run (Figure 7.4d)). It should be noted that such a level of control is usually achieved through employing highly time consuming Langmuir-Blodgett method.[14, 15] Spray coating of GO dispersions has great potential in many industrial processes such as electronics, painting, microencapsulation, electroemulsification, fine powder production, or micro- and nano-thin film deposition.[16]

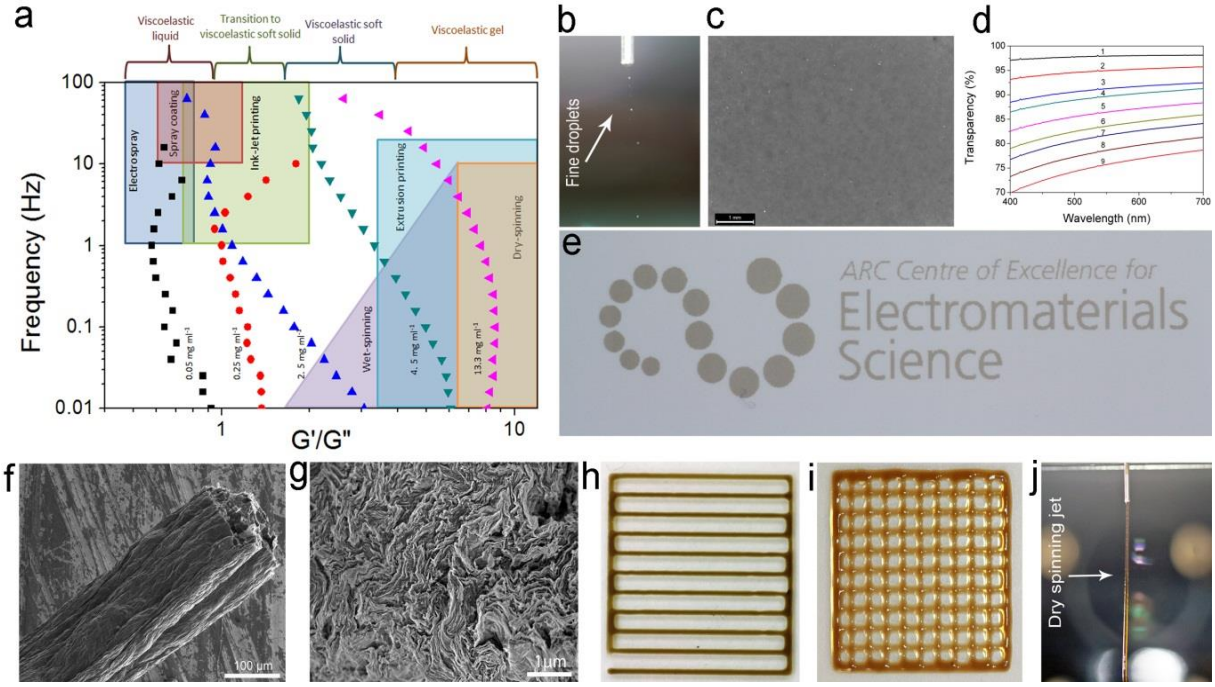

Figure 7. 4. A correlation between rheological properties and the key prerequisites for various manufacturing techniques enabled us to process and fabricate GO via a wide range of industrial techniques. a) Ratio of elastic and storage moduli for various GO concentrations measured over a range of testing frequencies. Overlaid are the approximate processing regimes for a number of industrial fabrication techniques. When the viscous modulus (G") dominates, the GO dispersion is suitable for high rate processing methods where the dispersion must spread on contact with the substrate. However, when the elastic modulus (G') is high the rheological properties suit fabrication methods requiring the dispersion to keep its given shape, such as extrusion printing and fibre spinning. b) Photograph of electrospraying of a viscoelastic liquid of GO dispersion at a concentration of 0.05 mg ml^{-1}. c) Photograph of a GO thin film that was spray coated and thermally reduced (overnight at 220 ^{o}C) utilizing a transitional state to

viscoelastic liquid GO dispersion of 0.25 mg ml^{-1}. d) Transparency of the spray coated reduced GO thin films as function of coating layers; the numbers show the number of coating layers. e) Ink-jet printed logo using LC GO viscoelastic soft solid at concentration of 0.75 mg ml^{-1}. f) As-prepared wet-spun fibers from LC GO viscoelastic soft solid at concentration of 2.5 mg ml^{-1}. g) Cross section of the wet-spun LC GO fiber, showing that GO sheets are stacked in layers with some degree of folding and are ordered due to the formation of nematic liquid crystals. h) Extrusion printed pattern using LC GO viscoelastic gel of 4.5 mg ml^{-1}. i) Extrusion printed 3D architecture using LC GO viscoelastic gel of 13.3 mg ml^{-1}. j) Dry-spinning of LC GO fibers utilizing LC GO viscoelastic gel of 13.3 mg ml^{-1}.

Table 7.1. Rheological characteristics of GO dispersions as function of GO concentration along with subsequent fabrication methods

Concentration range	LC Phase	Rheological characteristics					Electrostatic spraying	Ink-jet printing	Wet-spinning	Extrusion printing of 2D patterns	Extrusion printing of 3D architectures	Dry-Spinning
(mg ml-1)		Region	Viscosity by increasing the concentration	Viscoelastic behaviour								
				Long time scale (0.1Hz >)	Intermediate time scale (0.1Hz> >10 Hz)	small time scale (> 10 Hz)						
0.25 > C	Isotropic	Viscoelastic liquid	Negligible	G''> G'	G''> G'	G''> G'	suitable	not suitable	not suitable	not suitable	not suitable	not suitable
0.75> C ≥ 0.25	Biphasic	Transition state to viscoelastic soft solid	Increase to 16.5 Pa S^{-1} then decrease to 2.5 Pa S^{-1}	G''< G'	G''> G'	G''< G'	suitable	suitable	not suitable	not suitable	not suitable	not suitable
2.5 ≥ C ≥ 0.75	Nematic	Viscoelastic soft solid	Increase to 5 Pa S^{-1}	G''< G'	G''=G'	G''> G'	not suitable	suitable	suitable	not suitable	not suitable	not suitable
4.5 ≥ C > 2.5	Unknown	Viscoelastic gel	Increase to 67 Pa S^{-1}	G''< G'	G''< G'	G''> G'	not suitable	not suitable	suitable	suitable	not suitable	not suitable
C > 4.5	Unknown	Viscoelastic gel	Constant at around 70 Pa S^{-1} then increase up to 655 Pa S^{-1}	G''< G'	G''< G'	G''< G'	not suitable	not suitable	suitable	suitable	suitable	suitable

In the second region (GO concentration ~ 0.25 up to 0.75 mg ml^{-1}), GO dispersions show biphasic behaviour (coexistence of both isotropic and nematic phase). Here a viscoelastic behaviour which is in contrast with normal lyotropic liquid crystal phases can be observed.[17] In typical lyotropic liquid crystals, the viscous part (*G''*) is often dominant at large time-scales or towards the lower frequencies.[17] On the other hand, here *G'* appears to be higher than *G''* for GO dispersions falling in this region at large time-scales. This behaviour suggests the crowding of particles and consequently gelation of the system as a result of repulsive interactions experienced by neighbouring GO sheets which is also consistent with the yield point observed at this region (Figure. 7.5a).

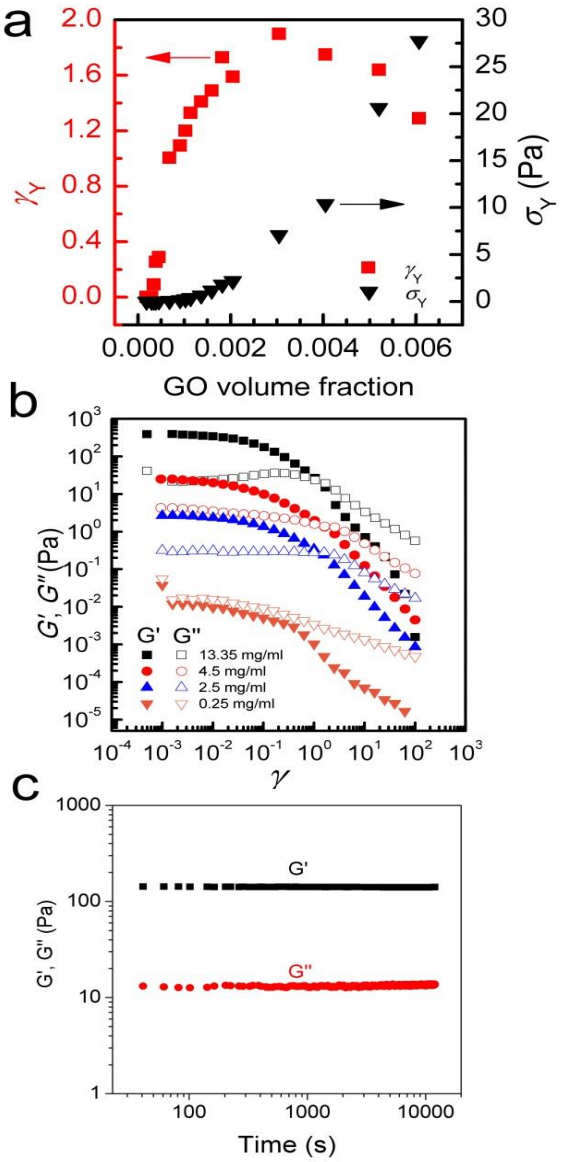

Figure 7. 5. Interpretation of rheological behaviour of LC GO dispersions. a) Yield strain (γ_Y) and yield stress (σ_Y) of various GO suspensions determined at different GO volume fractions. Yield point is considered as where the storage and loss moduli intercept when measured as a function of frequency. b) Storage (elastic) and loss (viscous) moduli of GO suspensions at the frequency of 0.01 Hz at different strains. No strain-stiffening can be observed even at very high concentrations which is consistent with SGM rheology generally exhibiting yielding and plasticity. However in contrast to soft glassy rheology (SGR), c) no aging after shear rejuvenation/fluidization can be observed.

Therefore, over long-time scales, GO dispersions respond more like a viscoelastic soft solid as

the "long-range" rearrangements (convolutions) are very slow. However, above the *G'-G''* crossover point, in an intermediate time scale, *G'* was found to be lower than *G''* suggesting a dominant viscous behaviour (liquid-like) implying that "short-range" rearrangements rapidly occur. Nevertheless, up to the concentration of 0.75 mg ml^{-1}, the difference is not considerable and the zones are not yet well-defined. These fluid properties are ideal for inkjet printing as the ink formulation should be designed to quickly regain viscosity and hence shapes (rearrange the mesogens) once they are printed on the surface to preserve the printed structure for accurate reproduction.[18] Importantly, this new finding enables us to formulate stable inks from pure GO dispersions without the need of any binders or additives to impart the dominant elastic components required for ink-jet printing (Figure 7.4e). It should also be noted that although the size of our GO sheets (average diameter 37 μm) are much larger than the safe zone [19] criterion for our inkjet printer nozzles (1 μm for a 50 μm nozzle), we were able to successfully print GO without any clogging side effects as a consequence of the highly flexible nature of GO sheets (Figure 7.1). The inkjet printing of binder free GO will enable the fabrication of high quality electrode materials that are critical for use in electronic applications such as organic field effective transistors (OFETs).

At higher concentrations (above 0.75 up to 2.5 mg ml^{-1}), the storage and loss moduli are completely and clearly well-separated from each other (Figure. 7.2d and 7.2e). This is the concentration range at which GO dispersions form single phase nematic liquid crystals. The two dimensional GO sheets form a tenuous network architecture with a very dominant elastic part in spite of the considerably low concentration. The *G'-G''* crossover point begins to shift towards higher frequencies. The rheological behaviour of GO dispersions at concentrations as high as 2.5 mg ml^{-1} resembles that of soft glassy materials (SGMs), liquid crystals, and/or weak gels.[10, 20] This rheological behaviour suggests that the processing of GO dispersions is possible with established fabrication techniques usually reserved for processing weak gel-like materials (such as the wet-spinning approach).[1, 21-24] However, in contrast to cross-linked

biopolymers [10] and biological gels [13] no strain stiffening is observed (Figure. 7.3b), and unlike gels of other disk-like colloids a fully frequency-dependent elastic modulus is not observed either (Figure 7.2e).[25] Another interesting aspect is the ability of these dispersions to retain their structure at very short time scales.

As concentration increases up to 4.5 mg ml^{-1} *G′* and *G″* become fully distinct with *G′* reaching 15-77 Pa at 4.5 mg ml^{-1} (depending on frequency, Figure 7.2f). This behaviour is slightly different to polymer networks and resembles the rheological characteristics of cells or SGMs.[10, 26] Purely elastic polymer networks exhibit a completely frequency-independent storage modulus plateau even at low frequencies.[10, 26] Similar to cells however,[10] GO dispersions at this region show power-law rheology with a weak non-universal exponent (i.e. the storage modulus increases slowly with frequency). In this region, it is only at very short time scales that the viscous part dominates. The magnitude of storage modulus increases with increasing concentration (volume fraction) and the crossover point (*G′=G″*) shifts to time scales as short as 0.01-0.1 sec as the network becomes more robust and exhibits a gel-like behaviour (Figure 7.1 g). This behaviour might suggest structural changes even though the rheological properties of liquid crystals of disk like particles are not simply correlated to the phase behaviour of the materials.[20, 25, 27] Upon increasing the concentration above 0.75, the nematic domains (with same orientation and brightness) decrease in size, this in turn, could contribute to substantial increase in the elastic modulus associated to a greater density of defects.[28]

At even higher concentrations (up to 13.35 mg ml^{-1}), no *G′-G″* crossover was observed in the frequency range studied here, resembling a gel-like (cells or SGMs) behaviour with an extraordinarily high elastic modulus of 350-490 Pa. The measured storage modulus at 13.35 mg ml^{-1} was considerably higher than the calculated elastic modulus of SWNT suspensions at the same concentration (~ 60 Pa).[29] GO dispersions at this concentration range, are therefore,

viscoelastic liquid crystals gel that can flow after a yield point. Furthermore, there are some unique characteristics that our as-prepared LC GO viscoelastic gels exhibit such as the anisotropy arising from having a liquid crystal network, and the exceptional uniformity of the network structure. Therefore, GO dispersions prepared in this region enabled us to process GO for the first time in a range of industrial processes such as gel-extrusion printing and dry spinning that are most beneficial for many industrial applications (Figure 7.4 h-j). During gel-extrusion through a nozzle (i.e. extrusion printer nozzle), the loss modulus will become dominant (Figure 7.5b, strain thinning effect), allowing for the dispersion to easily be extruded. However, when the LC GO viscoelastic gels leaves the nozzle (at low strain), the physical sheet entanglement forces them to regain their high elasticity. The high elasticity of LC GO viscoelastic gels retains the printed structure and makes it possible to print fine lines or 3D architectures (Figure7.4i).

To provide further understanding of the phase transition behaviour of the GO dispersion, we measured the viscosity and calculated the ratio of elastic and loss moduli of the system with increasing the GO concentration (Fig. 7.6). As expected, both viscosity and *G′/G″* increase with GO concentration in the low concentration range until a peak is reached at 0.5 mg ml^{-1}, then a sudden drop in both viscosity and *G′/G″* is observed. As we showed before,[5] entropy plays an important role in the ordering of GO sheets. Upon becoming concentrated, the isotropic fluid of two dimensional disk-like GO sheets must undergo a transition to a nematic phase in which GO sheets encompass a preferred orientation. This orientational ordering consequently results in loss of orientational entropy. However, this loss of entropy is compensated with an increase in free volume. Therefore, there will be a net gain of entropy, as a result of the increase in free volume (packing) entropy. This sudden free volume expansion accompanied by ordering in the direction of shear, because of the spontaneous formation of LC domains, results in a sudden drop of viscosity and the ratio of elastic to viscous moduli.[1, 5] By increasing GO

concentration furthermore, both viscosity and the moduli ratio gradually increase again until around 2.5 mg ml^{-1}. However, at the concentration range of 2.5 mg ml^{-1} to 4 mg ml^{-1}, a sudden drop of *G'/G''* can be observed suggesting a disturbance in the system. The latter might be due to an underlying phase transition with a tendency of the flakes to stack more regularly. Indeed, it has been observed that clays platelets can form columnar and hexagonal phases at high concentration.[25] The formation of such phases can be prevented in the present case by the polydispersity of the system or by dynamical arrest; but the tendency of the flakes to pack more regularly could explain changes in rheological properties. At the critical concentration (4 mg ml^{-1}), the increase in viscosity levels out and *G'/G''* ratio starts to increase again. Stacking of the GO mesogens results in further free volume expansion [30] and subsequently hinders any increase in the viscosity (Figure 7.2h).

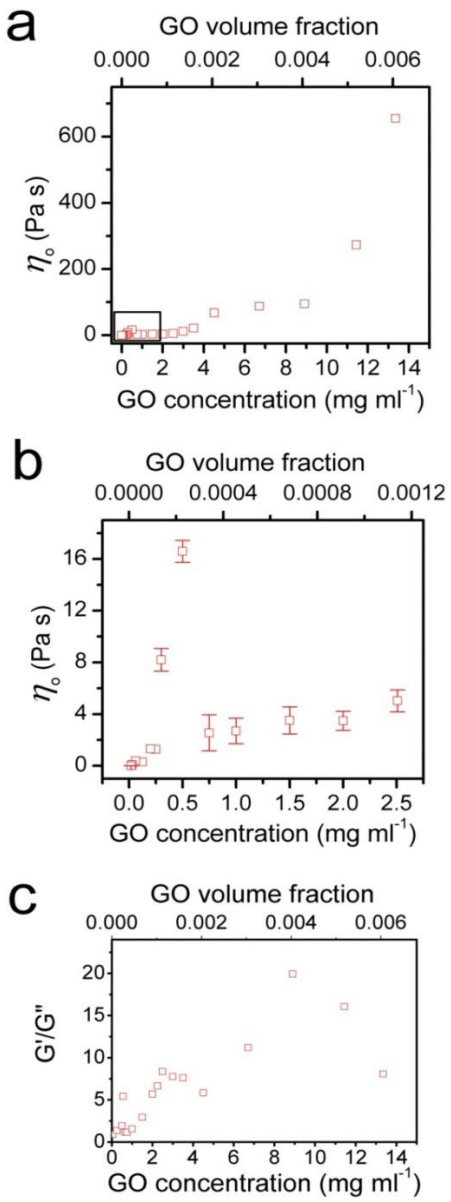

Figure 7. 6. Viscosity and the ratio of loss and storage moduli of GO dispersions at different GO concentrations. a) Viscosity ($\dot{\gamma} = 0.01$ s^{-1}) as a function of GO volume fraction. Increasing the concentration of GO results in an overall increase in viscosity until a peak at $\phi \sim 2.3\times10^{-4}$ (0.5 mg ml^{-1}). However as depicted in b) a sudden drop in viscosity as a result of ordering happens at higher concentrations. c) The same general trend also happens in the case of the ratio between loss and storage moduli. Moreover, at almost all concentrations, except in the very beginning, the ratio of G' to G" is higher than 1 indicating a very dominant elastic behaviour.

7.4 Conclusions

The viscoelastic behaviour of this fascinating material offers significant features that can prove to be useful for both fundamental researches in two-dimensional materials and practical applications as demonstrated by a wide range of processing techniques employed in the present paper. We emphasize that the characteristic flow behaviour of LC GO is fundamentally different from those associated with usual viscoelastic materials including polymers. The generic properties reported here can be considered as a universal guideline to process different GO dispersions based on their rheological properties. Therefore, a simple rheological test and the comparison with the guideline provided here can assist others in the field to decide on what processing techniques should be employed and why.

7.5 References

1. Jalili, R., et al., *Scalable One-Step Wet-spinning of Graphene Fibers and Yarns from Liquid Crystalline Dispersions of Graphene Oxide: Towards Multifunctional Textiles.* Adv. Funct. Mater., 2013. **23**(43): p. 5344-5344.

2. Aboutalebi, S.H., et al., *Spontaneous Formation of Liquid Crystals in Ultralarge Graphene Oxide Dispersions.* Adv. Funct. Mater., 2011. **21**(15): p. 2978-2988.

3. Xu, Z. and C. Gao, *Aqueous Liquid Crystals of Graphene Oxide.* ACS Nano, 2011. **5**(4): p. 2908-2915.

4. Kim, J.E., et al., *Graphene Oxide Liquid Crystals.* Angew. Chem. Int. Ed., 2011. **50**(13): p. 3043-3047.

5. Jalili, R., et al., *Formation and processability of liquid crystalline dispersions of graphene oxide.* Mater. Horiz., 2014. **1**(1): p. 87-91.

6. Jalili, R., et al., *Organic Solvent-Based Graphene Oxide Liquid Crystals: A Facile Route toward the Next Generation of Self-Assembled Layer-by-Layer Multifunctional 3D Architectures.* ACS Nano, 2013. **7**(5): p. 3981–3990.

7. Gudarzi, M.M., M.H.M. Moghadam, and F. Sharif, *Spontaneous exfoliation of graphite oxide in polar aprotic solvents as the route to produce graphene oxide – organic solvents liquid crystals.* Carbon, 2013. **64**(0): p. 403-415.

8. Xu, Z. and C. Gao, *Graphene chiral liquid crystals and macroscopic assembled fibres.* Nat Commun., 2011. **2**: p. 571.

9. Cheng, C. and D. Li, *Solvated Graphenes: An Emerging Class of Functional Soft Materials.* Adv. Mater., 2013. **25**(1): p. 13-30.

10. Chen, D.T.N., et al., *Rheology of Soft Materials.* Annu. Rev. Cond. Mat. Phys., 2010. **1**(1): p. 301-322.

11. Seth, J.R., et al., *A micromechanical model to predict the flow of soft particle glasses.* Nat Mater., 2011. **10**(11): p. 838-843.

12. Ovarlez, G., Q. Barral, and P. Coussot, *Three-dimensional jamming and flows of soft glassy materials.* Nat Mater., 2010. **9**(2): p. 115-119.

13. Storm, C., et al., *Nonlinear elasticity in biological gels.* Nature, 2005. **435**(7039): p. 191-194.

14. Li, X., et al., *Highly conducting graphene sheets and Langmuir-Blodgett films.* Nat. Nanotechnol., 2008. **3**(9): p. 538-542.

15. Zheng, Q., et al., *Transparent Conductive Films Consisting of Ultralarge Graphene Sheets Produced by Langmuir–Blodgett Assembly.* ACS Nano, 2011. **5**(7): p. 6039-6051.

16. Jaworek, A. and A.T. Sobczyk, *Electrospraying route to nanotechnology: An overview.* J. Electrostatics, 2008. **66**(3–4): p. 197-219.

17. Mezzenga, R., et al., *Shear rheology of lyotropic liquid crystals: a case study.* Langmuir, 2005. **21**(8): p. 3322-3333.

18. Derby, B., *Inkjet Printing of Functional and Structural Materials: Fluid Property Requirements, Feature Stability, and Resolution.* Annu. Rev. Mater. Res., 2010. **40**(1): p. 395-414.

19. Torrisi, F., et al., *Inkjet-Printed Graphene Electronics.* ACS Nano, 2012. **6**(4): p. 2992-3006.

20. Kroon, M., W.L. Vos, and G.H. Wegdam, *Structure and formation of a gel of colloidal disks.* Phys. Rev. E, 1998. **57**(2): p. 1962-1970.

21. Jalili, R., J.M. Razal, and G.G. Wallace, *Exploiting high quality PEDOT:PSS-SWNT composite formulations for wet-spinning multifunctional fibers.* J. Mater. Chem., 2012. **22**(48): p. 25174-25182.

22. Jalili, R., et al., *One-Step Wet-Spinning Process of Poly(3,4-ethylenedioxythiophene):Poly(styrenesulfonate) Fibers and the Origin of Higher Electrical Conductivity.* Adv. Funct. Mater., 2011. **21**(17): p. 3363-3370.

23. Esrafilzadeh, D., et al., *Multifunctional conducting fibres with electrically controlled release of ciprofloxacin.* J. Control. Release, 2013. **169**(3): p. 313-320.

24. Jalili, R., J.M. Razal, and G.G. Wallace, *Wet-spinning of PEDOT:PSS/Functionalized-SWNTs Composite: a Facile Route Toward Production of Strong and Highly Conducting Multifunctional Fibers.* Sci. Rep., 2013. **3**.

25. Mourad, M.C.D., et al., *Sol−Gel Transitions and Liquid Crystal Phase Transitions in Concentrated Aqueous Suspensions of Colloidal Gibbsite Platelets.* J. Phys. Chem. B, 2009. **113**(34): p. 11604-11613.

26. Sollich, P., et al., *Rheology of Soft Glassy Materials.* Phys. Rev. Lett., 1997. **78**(10): p. 2020-2023.

27. Michot, L.J., et al., *Sol−Gel and Isotropic/Nematic Transitions in Aqueous Suspensions of Natural Nontronite Clay. Influence of Particle Anisotropy. 2. Gel Structure and Mechanical Properties.* Langmuir, 2008. **25**(1): p. 127-139.

28. Zapotocky, M., et al., *Particle-Stabilized Defect Gel in Cholesteric Liquid Crystals.* Science, 1999. **283**(5399): p. 209-212.

29. Hough, L.A., et al., *Viscoelasticity of Single Wall Carbon Nanotube Suspensions.* Phys. Rev. Lett., 2004. **93**(16): p. 168102-168106.

30. Wensink, H.H. and H.N.W. Lekkerkerker, *Phase diagram of hard colloidal platelets: a theoretical account.* Mol. Phys., 2009. **107**(20): p. 2111-2118.

Chapter 8: High Performance Multifunctional Graphene Yarns: Towards Wearable All-Carbon Energy Storage Textiles

8.1 Introduction

The quest for achieving lightweight, flexible, mechanically strong carbon-based energy storage systems (including but not limited to graphene) as a possible energy source for smart wearable garments and miniaturized electronic gadgets has necessitated the demand for multifunctional high performance, cost-effective electrode materials [1-5]. However, most processing methods such as micro-electromechanical system technology are not practically scalable and do not yet have the ability to be integrated into commercially feasible processes [6-8]. Nevertheless, the electrochemical capacitance values of such graphene based devices still fall short of the theoretical value of 550 F g^{-1} [9, 10], with values of 265 F g^{-1} per electrode, the best to date [9].

8.1.1 3D fibrous architecture

In this regard, 3D architectures produced from fiber spinning can potentially provide conductive, highly porous 3D frameworks for designing multifunctional microsupercapacitor electrodes [5, 6, 11-14]. The fibrous architecture is fully scalable for large-scale applications such as integrated flexible and lightweight fabric supercapacitors which can be further used in smart garments and electronic gadgets [3, 4, 6, 15-18]. However, high-performance multifunctional synthetic fibers

produced to date, although of interest from mechanical and electrical point of view, suffer from low electrochemical performance which is crucial to realizing multi-functional textiles required for the advancement of smart electronic devices [14, 18-21].

8.1.2 Graphene oxide liquid crystal

Graphene oxide liquid crystal (LC) dispersions hold great promise in terms of flexibility in processing, high unidirectional properties of the final architectures and easy integration into complex architectures [12, 13, 22-29]. The recent breakthrough in wet-spinning of graphene fibers from graphene oxide LC dispersions is promising as a result of factors including outstanding mechanical and electrical properties, in a cost-effective manufacturing process [12, 13, 27, 29, 30]. However, in order to utilize these compelling architectural advances in electronic devices such as wearable electronic textiles and implantable medical devices, highly scalable graphene fibers and yarns with attractive supercapacitor performance need to be developed.

8.2 The aim of the present chapter

In the present chapter, it is demonstrated that the key to producing such fibers and yarns is to preserve the large sheet size even after the reduction of GO while simultaneously maintaining a high inter-layer spacing in between graphene sheets. This in conjunction with maximizing the number of covalently bonded carbon atoms per unit volume or mass and significantly reducing the number of other atoms present at the system and attached to graphene sheets resulted in exceptional electrochemical performance. To achieve this goal, an optimized commercially viable simple wet-spinning route, followed by an optimal facile heat-treatment regime is developed to achieve extraordinary capacitance values as high as 409 F g^{-1}/ electrode in a practical two-electrode configuration. Both fibers and yarns exhibited outstanding tensile strength and could be easily

weaved into conductive textiles opening up opportunities for the application of graphene in wearable electronic gadgets.

8.3 Spinning of GO fibers and yarns

The outstanding mechanical properties of large graphene oxide/graphene sheets suggest the possibility of processing them directly into fibers without the need for a subsequent cross-linking step. The LC spinning technique has this unique advantage in that, without the addition of any binders, can produce 3D self-assembled and aligned microstructures. To achieve 3D self-assembled, binder free, aligned microstructures with separated graphene oxide sheets, a continuous graphene oxide fiber spinning method from slightly acidic LC dopes (pH~3) in pure acetone bath is presented. LC GO dispersions were found to be easily spinnable in various wet-spinning methods through spinning of both fibers and yarns (Figure 8.1). The as produced fibers could maintain their structural integrity even in the presence of water (Figure 8.1b).The flexibility of the as-prepared fibers was also demonstrated by pulling a tied GO fiber to form an overhand knot. It should be noted that for as-prepared GO fibers spun using acetone, the lateral cohesion of the adjacent GO sheets was attributed to the strong van der Waals interactions (from the hydrophobic polyaromatic nanographene domains remaining on the basal planes) and the formation of hydrogen bonds (mediated by the oxygenated functional groups and water molecules) [12, 31-33].

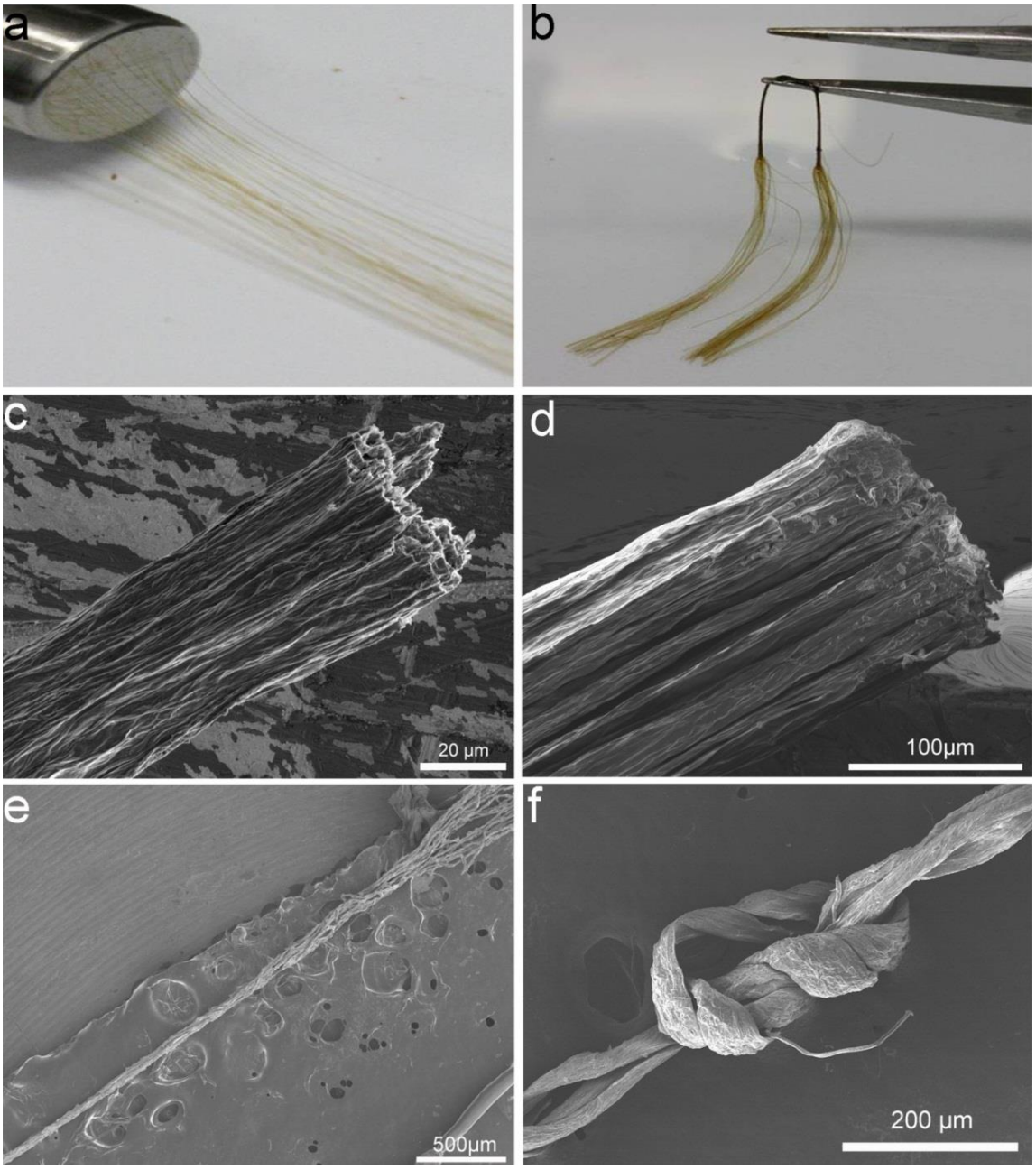

Figure 8. 1. Spinning of GO fibers and yarns. (a) Digital image of the formation of gel-state GO yarns produced using a multi-hole spinneret. As the LC GO is injected into the coagulation bath, GO filaments are being coagulated instantly by the coagulation solution. (b) Dried GO yarn can be easily separated into individual filaments when they are immersed in water. However, the fibers could still maintain their structural integrity in the presence of water. FESEM micrographs of (c) an irregular shape GO fiber, (d) a GO yarn composing of many GO fibers the rGO fiber,

(e) an Un-Weaved GO fiber yarns and (f) a loosely knotted GO yarn demonstrating the flexibility of the as-prepared GO fibers in acetone bath.

8.3 Physical characterization

The as-prepared GO fibers in acetone bath exhibited a layered structure as evidenced by the measured d-spacing in XRD analysis (Figure 8.2). The high inter-layer d-spacing in the fiber structure, if preserved, can then serve as a platform to translate the superior properties of graphene sheets into practical everyday use devices with complex geometrical architectures through the prevention of the agglomeration of these sheets at large scale.

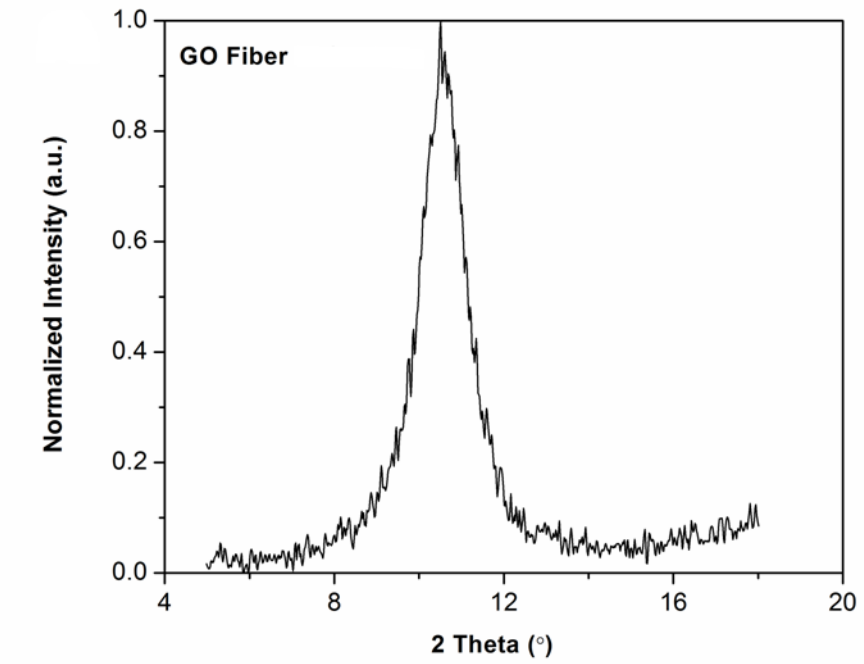

Figure 8. 2. XRD pattern of GO fiber demonstrating interlayer d-spacing ~ 0.84 nm.

8.3.1 Effect of coagulation bath: Alkaline baths

Although the underlying mechanism is still unclear, it is suggested that in the case of graphene oxide, the oxidative debris which mainly comprises of a mixture of complex aromatic structures containing COH rich functional groups and is strongly adhered to the surface of graphene sheets can be stripped from graphene oxide under alkaline conditions. [25, 34] However, there is also another study which denotes a fast irreversible deoxygenation of graphene oxide under basic conditions. [35] However, irrespective of the mechanisms involved, employing alkaline coagulation baths results in the removal of oxygen multifunctionalities and consequently water from the graphene oxide sheets which in turn results in the elimination of hydrogen bonds in between GO sheets and weakening of inter-layer crosslinking. [25, 34-36]

8.3.2 Effect of coagulation bath: NaCl and H_2SO_4 baths

In the above-mentioned baths, coagulation occurs as a result of charge destabilization and charge screening. Dispersion destabilization using acid, base or salt solutions typically results in the slippage of graphene oxide sheets on top of each other leading to lower mechanical properties.

8.3.3 Effect of coagulation bath: $CaCl_2$ bath

Ionic cross-linking using divalent cations is the main reason of the observed enhancement in mechanical strength. Divalent metal ions such as Mg^{2+}, Ca^{2+} and Cu^{2+} are known to readily react with carboxylate functional groups typically located at the edges of GO sheets.[37] This chemical interaction can then result in mechanical enhancement of the final architecture. Bearing in mind that these ions are very small, it is then expected that these ions can readily diffuse into the core of the fibers resulting in exceptional cross-linking within the fiber.

8.3.4 Effect of coagulation bath: Chitosan bath

In this case, both cross-linking and coagulation by oppositely charged polymers contribute to the enhancement in mechanical properties. However, it should be noted that chitosan cannot penetrate

into the internal of the fiber and the strengthening just happens at the surface. The SEM micrograph presented in Figure S. 5C clearly shows that the outer layer of the fiber is much more compact than the core of the fiber indicating that the interaction just happens at the surface.

8.3.5 Effect of coagulation bath: Acetone bath

For as-prepared GO fibers spun using acetone, the lateral cohesion of the adjacent GO sheets is attributed to the strong van der Waals interactions (from the hydrophobic polyaromatic nanographene domains remaining on the basal planes) and the formation of hydrogen bonds (mediated by the oxygenated functional groups and water molecules). [31, 38]

8.3.6 Coagulation Mechanism

In contrast to polymer/ion containing water-based coagulant baths, the acidic condition of the initial spinning dope promotes the rate of fiber formation/solidification resulting in a more porous fiber geometry as detailed in Figure 8.3. Acetone's advantage in this regard, compared to other coagulants, lies in the ability of acetone to expel water from the fiber at much higher rates enabling the formation of highly porous architectures (Figure 8.3b). This is a direct result of its very low viscosity (leading to viscosity difference displacement), high mobility, its high diffusion coefficient compared to water and finally the imbibition rate of acetone compared to other solvents. Employing slightly acidic GO dispersions (pH~3), therefore, leads to more enhanced porosity (Figure 8.3c). This structure resembles that of a freeze-dried structure due to the very fast dehydration rate of acetone exhibiting a very high surface area of 2605 m^2 g^{-1} (see Appendix section for surface area measurements).

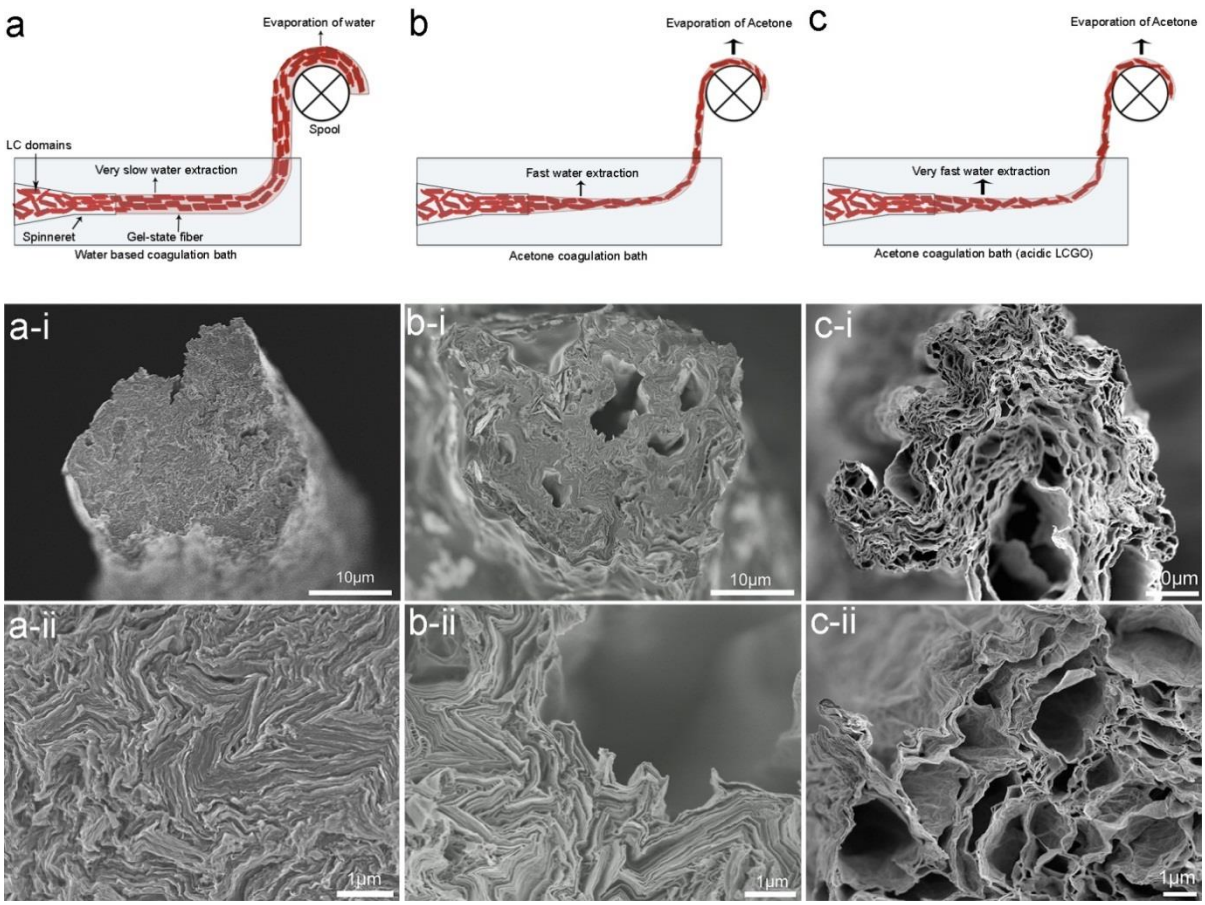

Figure 8. 3.Proposed strategies for the evolution of structure in different coagulation baths from (a) highly dense to (c) highly porous architectures. (a) Employing a water based coagulation baths results in slow expulsion of water from the as-injected gel state fiber like structure. Therefore, to be able to pick up such fibers, the length of the bath should be optimized to enable the formation of a solid-like sheath around the core of the fiber. The fiber can then be taken from the bath and transferred on a spool for the evaporation of the water from the fiber resulting in a highly dense structure (a-i and a-ii). (b) Using an acetone coagulation bath results in the high rate of water extraction from the surface as a result of the difference in imbibition rate (see appendix i) consequently leading to higher rate of solidification and porous fiber structure (b-i and b-ii). (c) The slight acidic condition of LC GO dopes (pH ~3) further changes the difference in imbibition

rate (see appendix section for explanation on imbibition rate) resulting in much higher water extraction rate and consequently more porous geometry (c-i and c-ii).

Furthermore, the enhanced hydrogen bonding between the sheets as a result of the acidic condition and the water molecules confined between the layers play a crucial role to separate the sheets in the ordered yet porous structures induced by the LC state as evident from the polarized optical micrograph presented in Figure 8.4.

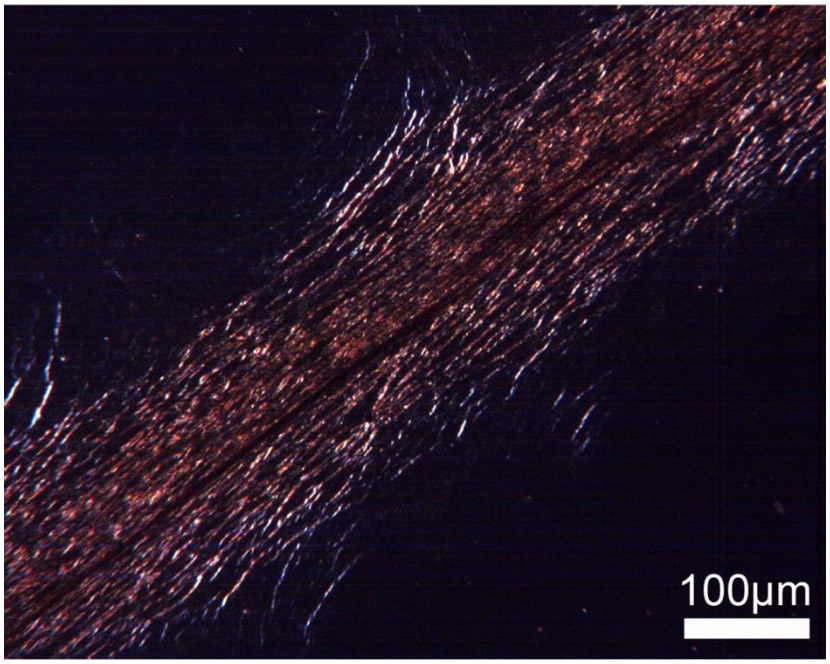

Figure 8. 4. Polarized optical micrograph of as-spun gel-state GO fiber showing birefringence. Birefringence properties confirmed that ordered LC domains were formed and preserved during the spinning process.

However, such a fiber architecture without the reduction of graphene oxide cannot be directly used in electrodes due to the lack of electrical conductivity which renders it impractical for energy

storage applications. However, the reduction of LC GO may result in the restacking of the sheets. Ideally, the restacking should be kept to minimum to maintain the required inter-layer spacing and porosity, as demonstrated by studies on quantum capacitance and ac-Line filtering performance where graphene has been shown to afford much higher storage capacities when individual, separated graphene sheets are predominant [10, 39]. Therefore, careful, rational nanoarchitectonic design and spacing of individual graphene layers is crucial for high-performance energy storage devices [40]. To this end, different research groups have implemented various strategies to prevent the restacking of graphene sheets; including introducing CNTs in between the sheets [23, 31], using hydrated chemically converted graphene sheets [41], and laser scribing of graphene oxide [9, 42]. The strategy here was to heat-treat the as-prepared graphene oxide fibers at an optimal temperature region of 200-220 ºC to minimize restacking and maintaining surface area while simultaneously reducing the GO sheets, as evidenced by XRD, SEM, Raman and XPS analysis (Figure 8.5). XRD pattern shows a broad distribution of d-spacing and pore sizes in the final architecture (from 0.3 to 0.65 nm). This spacing dimension is crucial for the functional design of our rGO fibers. This intersheet d-spacing was in accordance with self-stacked, solvated graphene (SSG) films which are known to afford high capacitance values [41]. Pore sizes at this region (less than 1 nm) cannot be directly investigated by BET-N_2 gas adsorption measurements as these pores are not sufficiently accessible to nitrogen because the filling of the pores takes place at relative pressures of 10^{-7} to 10^{-5} (see appendix i) [43, 44]. Therefore, XRD serves as the best technique to directly probe these pore sizes. The higher d-spacing value is attributed to the presence of some remaining functionalities on the surface of the reduced graphene oxide fiber after thermal reduction, as described previously and demonstrated in Figure 8.5C (XPS characterization of as prepared rGO) and Figure 8.6 and 8.7 (XPS and FT-IR characterization of as-prepared GO fibers

and rGO). Shown in the spectrum of the annealed rGO fiber after deconvolution of the peaks, are the major C in graphite (C1s A, 284.5 eV), and minor peaks C-OH (C1s B, 285.6 eV), C=O (C1s D, 28.2 eV), C(O)O (C1s E, 289.4 eV). Quantitatively, from the surveys, upon heat-treatment reduction, the oxygen content fell from 36.6 to 11 wt%. This translates to a carbon to oxygen ratio increase from 0.33 in GO to 0.89 in rGO, indicating the effectiveness of the reduction regime. These observations are in good agreement with literature values for rGOs, where the C content ranges from 60 to 86.4 wt% and the Oxygen content ranges from 11.3 to 34.6 wt% [24, 25, 45].

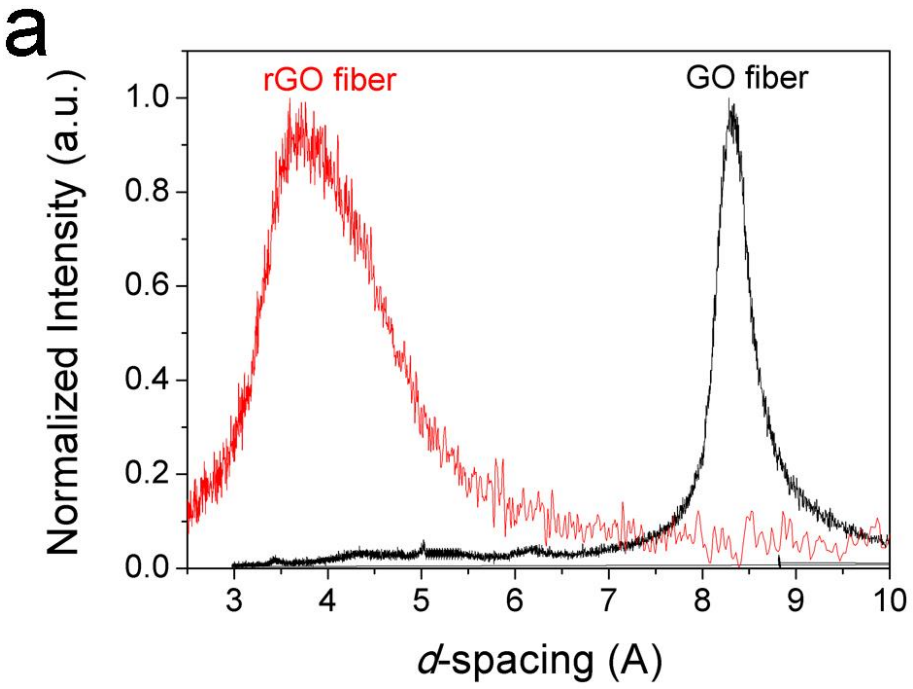

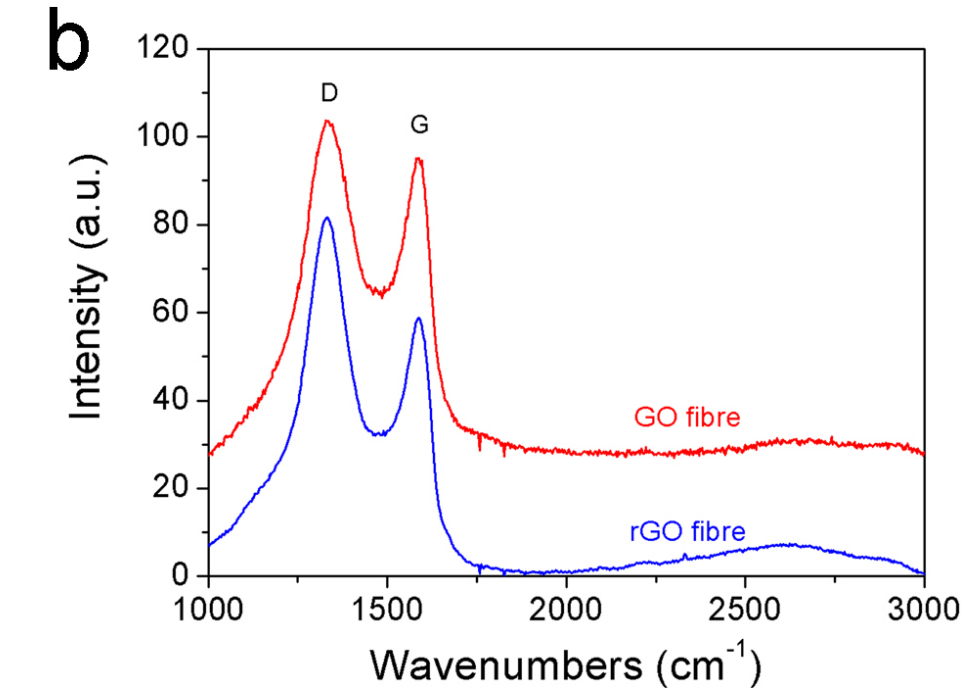
b
D
G
GO fibre
rGO fibre
Intensity (a.u.)
Wavenumbers (cm-1)
0
20
40
60
80
100
120
1000
1500
2000
2500
3000

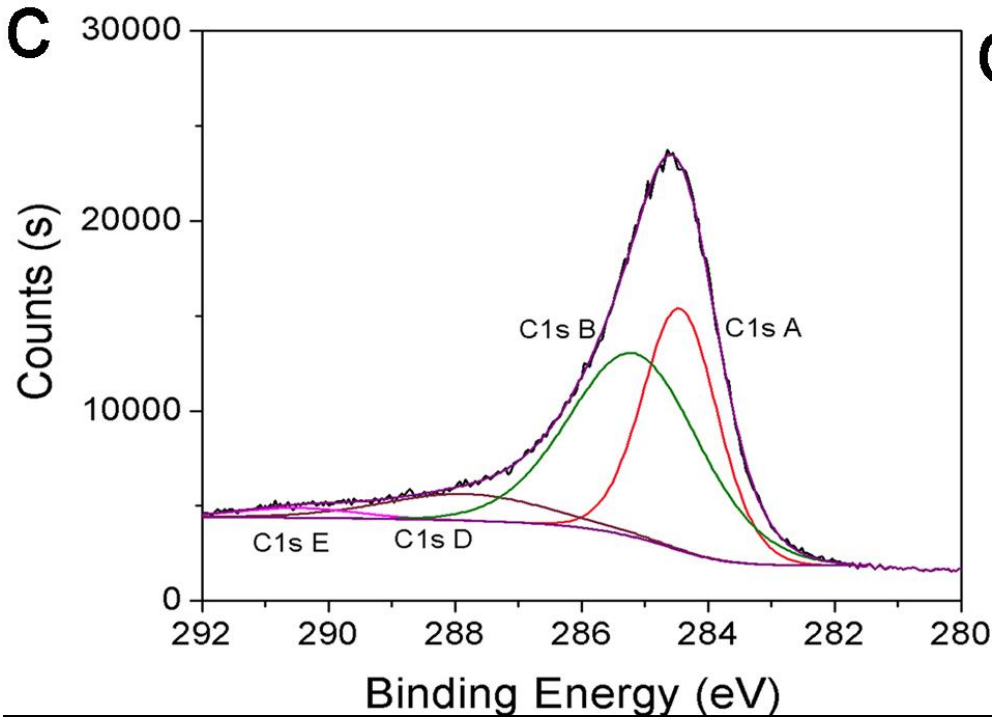
C
C1s B
C1s A
C1s E
C1s D
Counts (s)
Binding Energy (eV)
0
10000
20000
30000
292
290
288
286
284
282
280

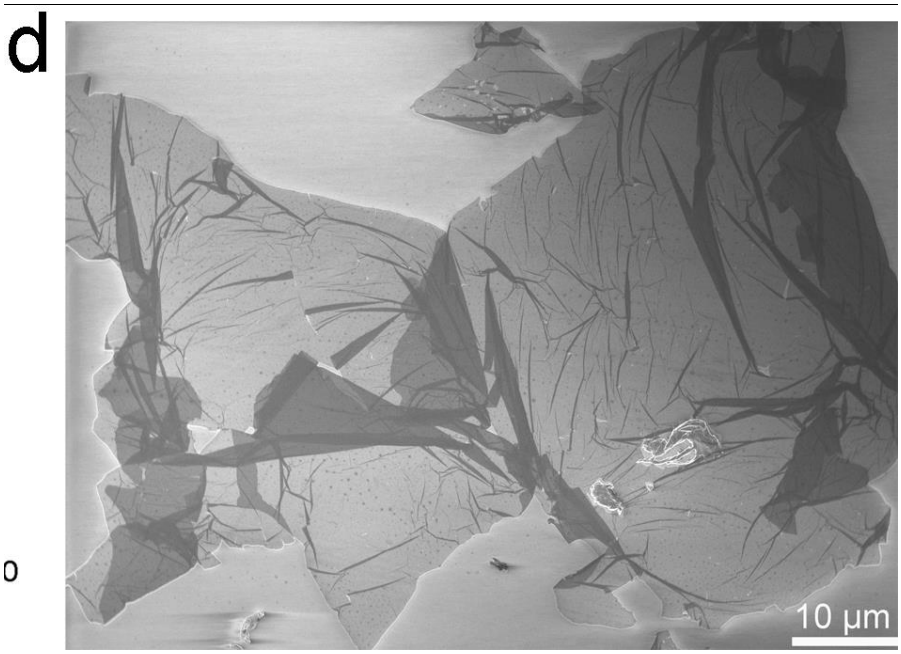

Figure 8. 5.Structural characterization of as-reduced graphene sheets. (a) Comparison of XRD patterns of GO fiber (d-spacing ~ 0.84 nm) and rGO fiber (d-spacing in the range of 0.3 to 0.65 nm). (b) Comparative Raman spectra of GO and rGO fiber showing the evolution 2D band at around 2600 cm^{-1} which serves as an evidence for the reduction of GO. (c) XPS spectra of C1s region of rGO structures after the deconvolution of the peaks. The oxygen content of the rGO was determined to be 11.0 % after quantitative measurement from the survey (Figure. 8.7). (d) Representative SEM micrograph of as-heat-treated rGO sheets verifying the ultra large nature of our as-prepared rGO.

Importantly, this reduction regime does not adversely affect the final sheet size of the layers as evidenced by Figure 8.5d (electron micrograph of ultra large rGO sheets in excess of 50 µm) and Figure 8.8 (high throughput optical micrograph of rGO sheets). As previously demonstrated by our group and others, fibers from large GO sheets can also give rise to higher electrical, and

mechanical properties as a result of the reduction of the number of graphene sheet ends in the fiber and reducing graphene junctions like the case with long CNTs [12, 13, 30, 46, 47].

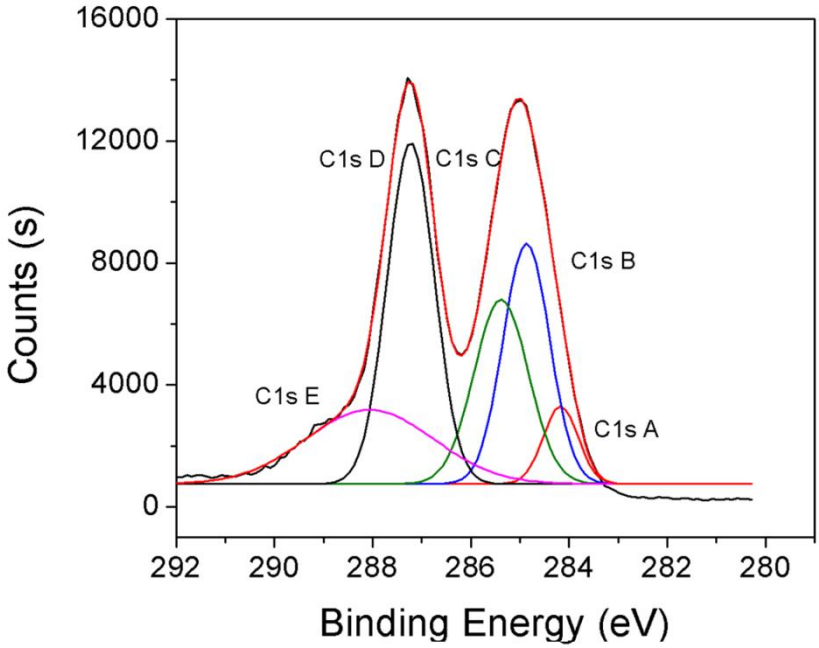

Figure 8. 6.Comparison of XPS spectrum of the as-prepared GO fiber. The XPS C1s spectra of the GO fiber shows two prominent peaks (C1s A and C1s B) and one minor peak (C1s C – 288.9eV). The C1s A peak at 284.5eV can be assigned to C=C as in graphite, with the C1s B peak at 287.2eV and C1s C shoulder at 288.9eV showing considerable functionalisation of the material with the oxygen containing species C-OH and C-O. Deconvoluted peaks are C in graphite (C1s A, 284.5 eV), C-OH (C1s B, 285.6 eV), C-O epoxy (C1s C, 286.7 eV), C=O (C1s D, 28.2 eV) and C(O)O (C1s E, 289.4 eV).

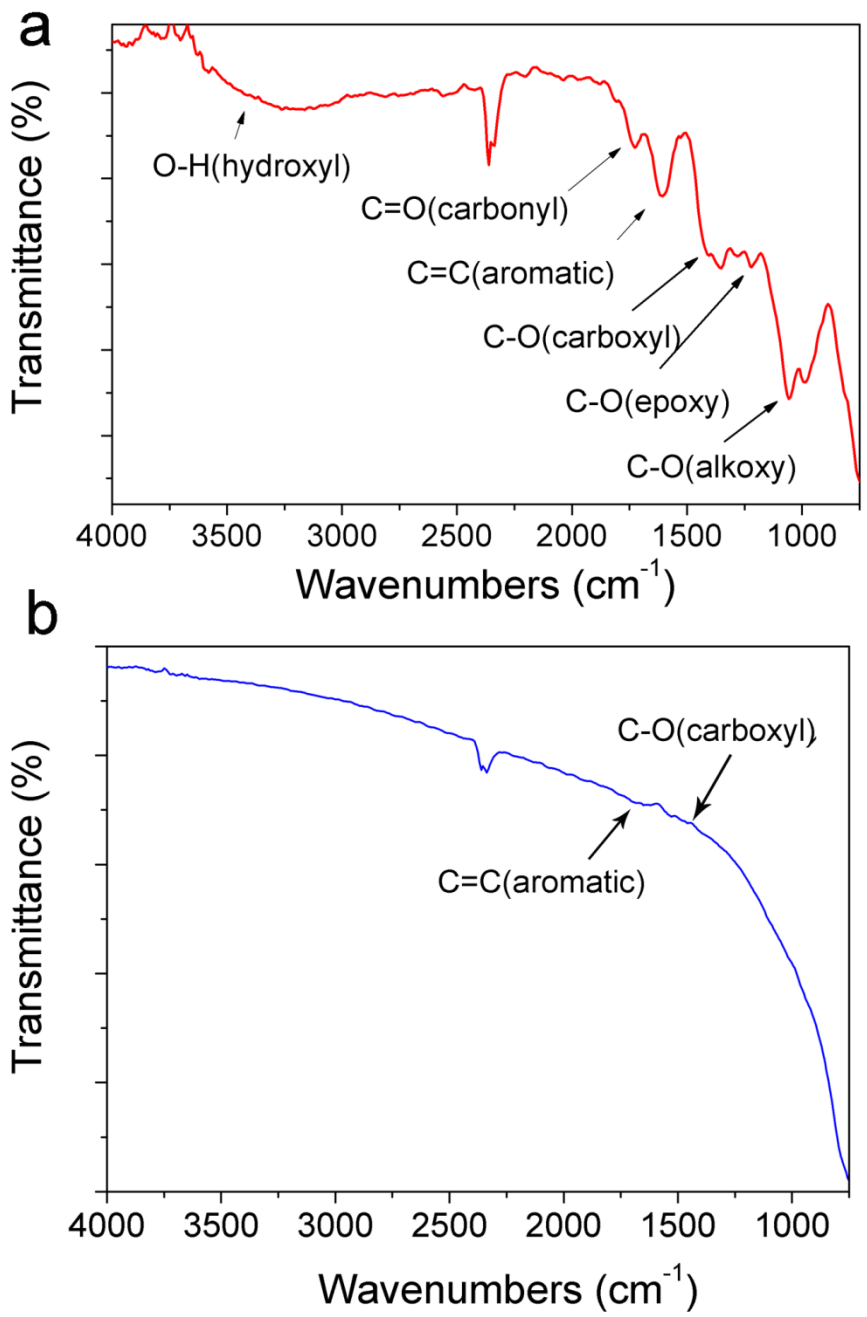

Figure 8. 7. Comparison of FT-IR spectra of various GO fibers. **a)** As-spun GO fiber prepared using acetone coagulation bath, **b)** reduced GO fiber. Identified peaks in the spectra are the following: alkoxy (1057 cm^{-1}), epoxy (1212 cm^{-1}), alkoxy (1400 cm^{-1}), aromatic (1600 cm^{-1}), carboxyl (1720 cm^{-1}) and hydroxyl (3000- 3800 cm^{-1}).

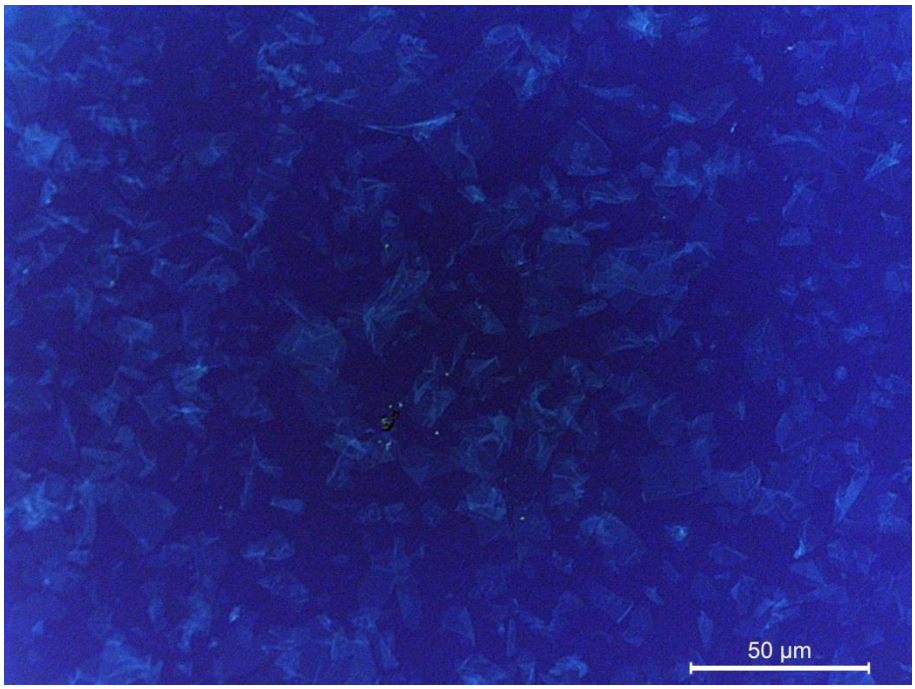

Figure 8. 8. High throughput optical micrograph of reduced GO sheets heat-treated at 220 ºC demonstrating ultra-large lateral sizes of rGO sheets.

8.4 Mechanical stability

Representative stress–strain curves of the rGO fibers and yarns spun are compared in Figure 8.9a. It should be noted that although promising breakthroughs have been made in the case of GO and rGO fibers [12, 13], no reports yet exist on mechanical properties of GO and rGO yarns which is the only practical form of these structures in real-life applications. The mechanical properties along with the comparison with previous reports on graphene fibers are summarized in Table 8.1.

Table 8.1. Mechanical properties of GO and rGO fibers and yarns prepared in this study and previous reports.

Production condition	**Young's Modulus**	**Ultimate Stress**	**Reference**

	(GPa)	(MPa)	
GO fibers coagulated in Acetone bath	20.5±2.75	61.7±4	Current study
GO yarns coagulated in Acetone bath	29.4±2.25	38.2±8.5	Current study
rGO fibers coagulated in Acetone bath and heat-treated at 220^{o}C	10.13±2.25	49.3±3	Current study
rGO yarns coagulated in Acetone bath and heat-treated at 220^{o}C	10.8±2	30.4±5.5	Current study
GO fibers coagulated by Chitosan	22.6±1.9	442±18	[1]
GO fibers coagulated by $CaCl_2$	20.1±2.1	412±30	[1]
rGO fibers coagulated by NaOH	11±2.4	183±25	[1]
rGO fibers coagulated by NaOH (further reduction at 220^{o}C)	9.0±2.1	115±19	[1]
Graphene nanoribbons fibers annealed at 1500^{o}C	36.2	378	[2]
rGO fiber (glass pipeline moulding, annealed at 230^{o}C)	-	180	[3]
rGO fiber (glass pipeline moulding, annealed at 800^{o}C)	-	420	[3]
rGO fiber (reduced by hydroiodic acid)	5.4	130	[4]
GO fibers coagulated by $CaCl_2$ (stretched)	6.3	364	[5]
rGO fibers coagulated by $CaCl_2$ (reduced by hydroiodic acid and stretched)	11.2	501	[5]

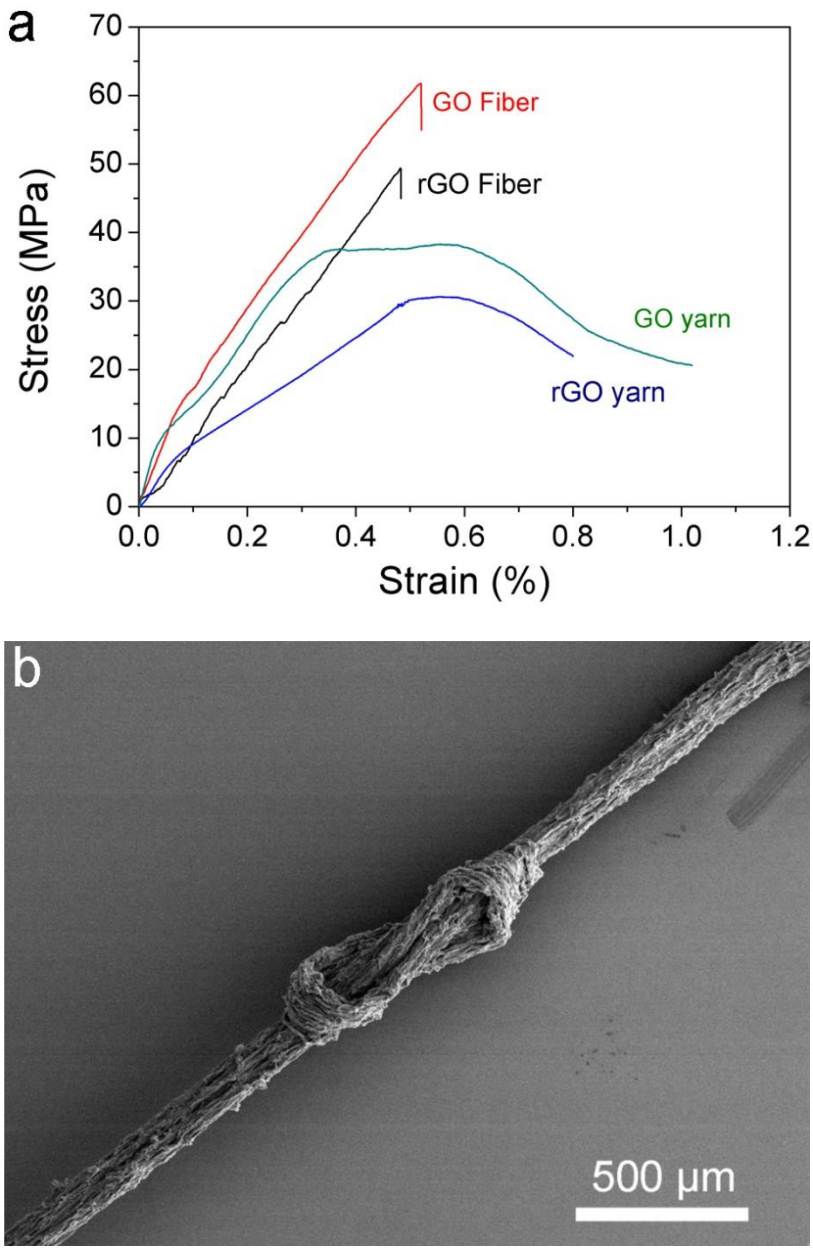

Figure 8. 9. Mechanical performance of fibers and yarns. (a) Representative stress-stain curves of GO and rGO fibers and yarns indicating high tensile strength of all architectures. (b) SEM micrograph of tight knotted rGO yarns demonstrating the mechanical stability of as–prepared rGO yarns.

It is evident from the results that the employed coagulation bath and reduction of the GO sheets influence the mechanical properties of GO and rGO fibers. Both fibers and yarns fabricated with

the method described here demonstrated exceptional tensile modulus which was indicative of high alignment of GO and reduced graphene sheets in the final architecture. The best GO fiber and yarns Modulus (ca. 20.5 and 29.4 GPa, respectively) was even higher than cross-linked GO and rGO-based fibers such as GO fibers coagulated in chitosan (ca. 22.6 GPa), and $CaCl_2$ (ca. 20.1 GPa) and higher than all of the other previously reported GO and rGO fibers [12, 13, 27, 48]. This can be explained by the higher degree of hydrogen bonding within the structure, due to the acidic condition in which GO fibers are formed, resulting in stronger interactions between GO sheets. The best rGO fibers and yarns also exhibited higher tensile modulus (ca. 10.13 and 10.8 GPa, respectively) compared to rGO fibers reduced by HI acid (ca. 5.4 GPa), [13] and partially reduced graphene oxide fibers using NaOH (9 GPa). [12] The results were also comparable with rGO fibers coagulated by NaOH and further reduced at 220º C (11 GPa) in our previous report [12]. In terms of ultimate stress and elongation at break, these GO and rGO fibers and yarns were inferior to our previous report which is due to the highly porous architecture of our as-produced fibers and yarns [12]. The annealed rGO fibers also exhibited a native conductivity of ca. 2508 ± 632 S m^{-1}, higher than both rGO fibers coagulated by NaOH and laser-scribed rGO, making them suitable for achieving high electrochemical double layer (EDL) capacitance [9, 12].

8.5 Electrochemical measurements

The mechanical stability and flexibility of these rGO fibers were verified by pulling a tied rGO yarn to form a tight overhand knot (Figure 8.9b). No breakage occurred when the fiber was curved to a tightened knot. The mechanical stability of these fibers was used to weave different patterns and geometries that are suitable for a range of different applications; including large area electronics (Figure 8.10a). This is important for electrochemical capacitor (EC) applications and

is mainly due to the fact that the need for any additional binders or conductive additives can be eliminated and the as-prepared hand-knitted textile fabricated from graphene fibers can act as both current collector and the active material simultaneously. This design concept can be further used to fabricate porous lightweight textile supercapacitors that can be integrated into smart garments. Devices can be fabricated by simply using a membrane separator in between two textile electrodes (Figure 8.10b). Other devices can also be made by spinning graphene fiber yarns directly on the top of a charge collector or putting these materials onto aluminium or titanium foils that are typically used in commercial devices. As a proof of concept, we prepared a range of different electrodes and devices to evaluate the capacitance performance of these materials; including both free-standing fibers and patterned geometries of graphene fiber yarns on titanium foils fabricated with different methods of wet-spinning: non-solvent precipitation, dispersion destabilization using acid, base or salt solutions and ionic cross-linking using divalent cations with the same reduction regime.

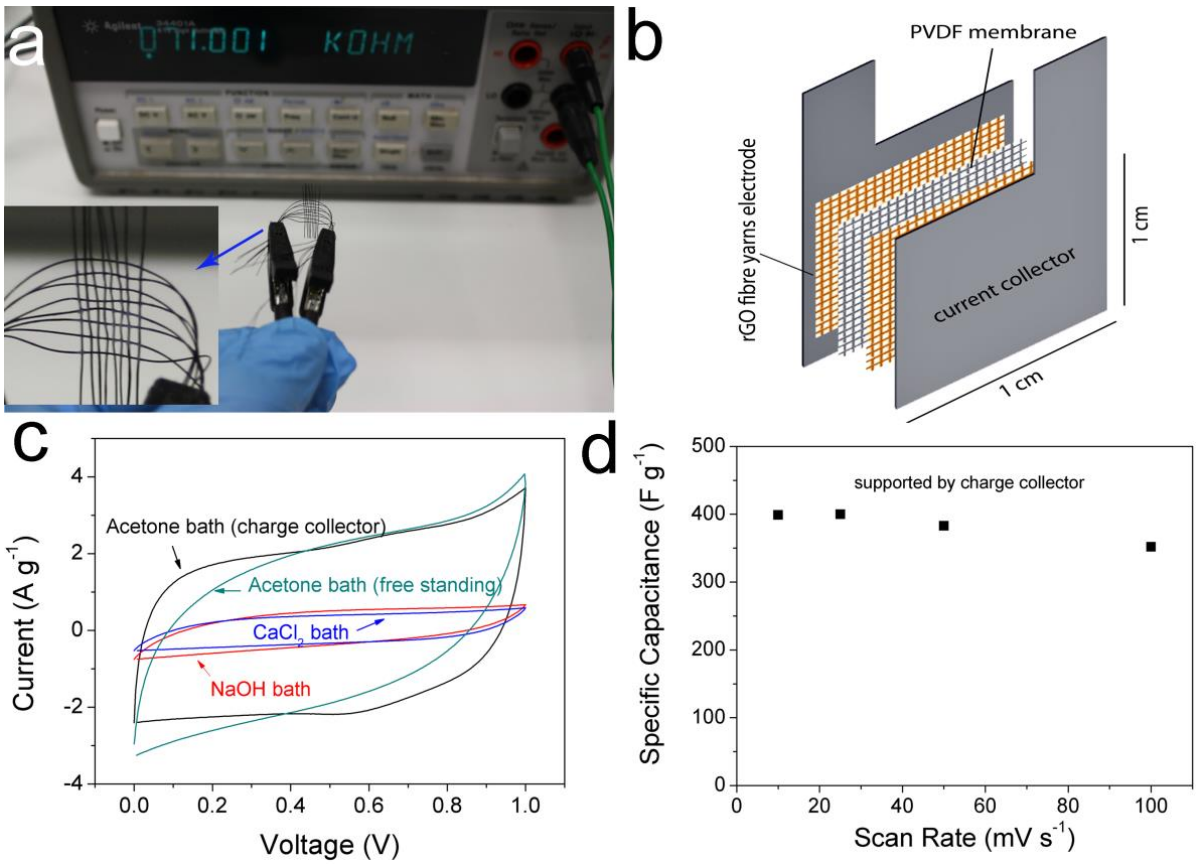

Figure 8. 10. Electrochemical capacitor: Design and performance. (a) Hand-weaving of rGO fiber yarns into a flexible and conductive textile. (b) Schematic of the electrochemical capacitor cell assembly fabricated in this study. (c) Cyclic voltammograms of heat-treated graphene fiber yarns produced in acetone bath(both free-standing and deposited on charge collectors), alkaline bath (NaOH), and ionic crosslinking using divalent cations bath ($CaCl_2$) in 1M H_2SO_4 at 10 mV s^{-1} clearly showing the superior performance of the fibers produced in acetone bath. (d) Calculated specific capacitance of rGO fiber yarns fabricated in acetone bath at various scan rates.

The heat-treated, graphene fiber yarns produced in acetone bath, alkaline bath (NaOH), and ionic crosslinking using divalent cations bath ($CaCl_2$), were all evaluated in terms of electrochemical

performance based on their cyclic voltammogram response at 10 mV sec^{-1} (Figure 8.10c). All systems showed a near-rectangular CV curve representative of good EDLC performance. However, yarns fabricated via wet-spinning of GO dispersions in an acetone bath exhibited much better electrochemical response (both as free-standing form or supported by charge collector, Figure 8.10c). Use of crosslinking agents results in the addition of impurities to the system and adulteration of carbon bonds consequently leading to much lower electric double layer capacitance (EDLC). Wet-spinning of GO dispersions in acetone bath prevents the adulteration effects of impurities into the system. The adulteration effect of impurity atoms in the case of other coagulant baths is therefore, the main reason behind the much lower observed electrochemical performance. The compact fiber architectures as shown in Figure 8.3a, which is a direct result of slow coagulation/dehydration process, can also adversely affect the electrochemical performance of the fibers as demonstrated in the cyclic voltammograms presented in Figure 8.10c.

Therefore, yarns prepared in acetone bath were chosen for the evaluation of their possible use as supercapacitor electrodes. Calculations for specific capacitance per electrode, energy density and power density were performed following the methods previously reported [15, 49, 50]. As-reduced acetone bath fabricated device showed remarkable electrochemical performance. The free-standing system showed a remarkable capacitance of 394 F g^{-1} (0.99 mF cm^{-1}) at a scan rate of 10 mV sec^{-1} (a total capacitance of 40 mF for device) and continued to provide outstanding capacitance of 160 at 100 mV sec^{-1} (Figure 8.12). The mass per length of yarns was measured to be 2.5 μg cm^{-1}. It should be noted that the concerns regarding shorter diffusion path do not apply here as the thickness of the active material is in the order of 30 μm which is higher than the cross-section of most graphene based devices and in the order of the thickness used in commercial cells.[[9, 49, 51, 52]] Moreover, the advantage of using fibers and yarns lies in the fact that

increasing the mass does not adversely affect the diffusion path as the diffusion path is always limited to the radius of the fiber. The capacitive behaviour of as-prepared electrodes exhibited low resistivity as evidenced by the rectangular shape observed in voltammograms (Figure 8.10c). However, even this low resistivity can limit the performance of the configurations at faster scan rates as demonstrated by the high drop in capacitance at higher scan rates. To overcome this problem, devices were fabricated using charge collectors. Employing charge collectors, resulted in higher capacitance (399 F g^{-1} at10 mV sec^{-1}). Even at a very high scan rate of 100 mV sec^{-1}, an outstanding capacitance of close to 300 F g^{-1} was obtained (Figure 8.10d and Figures 8.13 and 8.14).

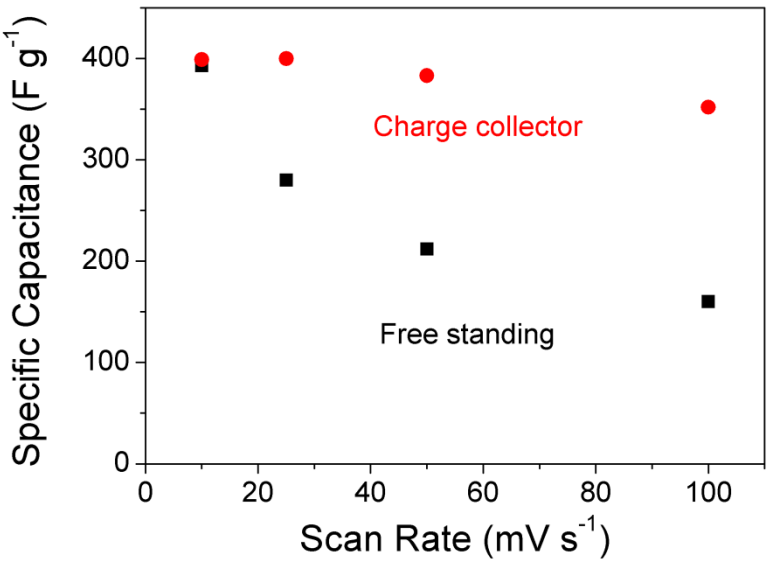

Figure 8. 11. Calculated specific capacitance of rGO fiber yarns fabricated in acetone bath at various scan rates.

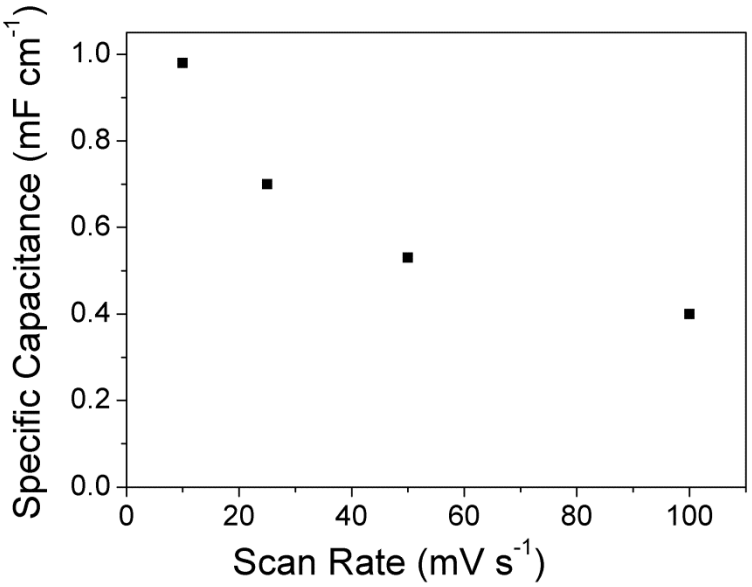

Figure 8. 12. Length-normalized capacitance for free-standing rGO fiber yarns fabricated in acetone bath at various scan rates.

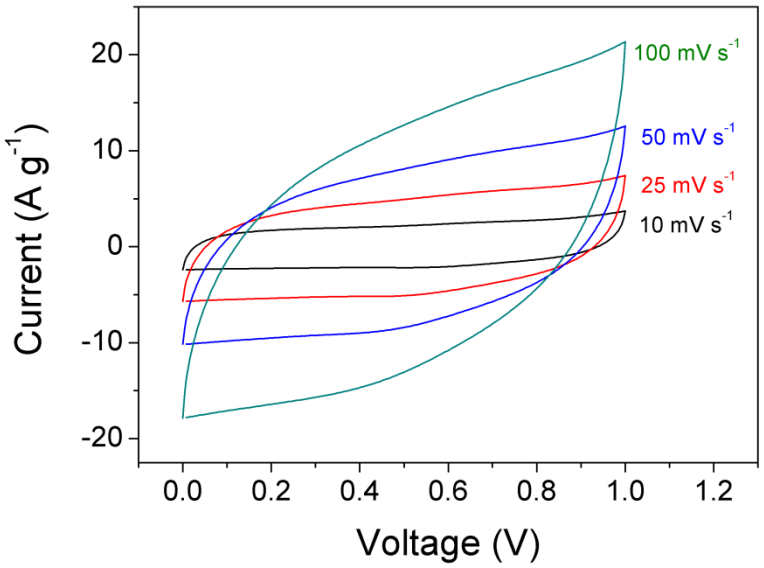

Figure 8. 13. Over-layed Cyclic voltammograms of heat-treated graphene fiber yarns produced in acetone bath (deposited on charge collectors).

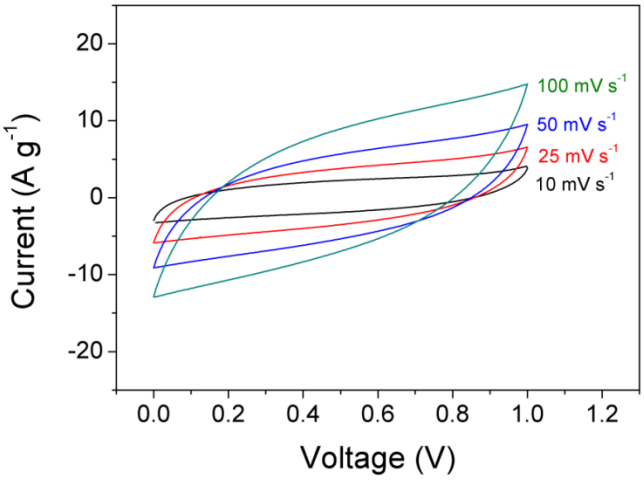

Figure 8. 14. Over-layed Cyclic voltammograms of heat-treated graphene fiber yarns produced in acetone bath (free-standing).

With galvanostatic cycling, even at a high current density of 10 A g^{-1}, the deviation from a triangular shape was minor, which shows the formation of an efficient EDL with fast ion transport implying the high rate capability of the as-prepared rGO yarns Figure 8.15.

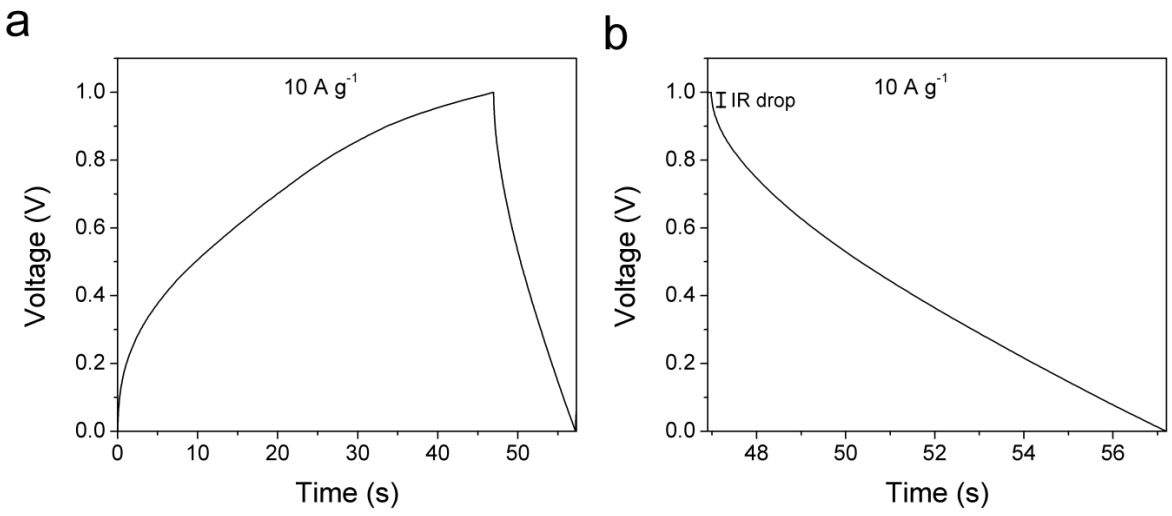

Figure 8. 15. (a)Galvanostatic charge-discharge curve at 10 A g^{-1} and (b) zoomed-in discharge curve at the same current density.

Moreover, the negligible iR drop at the start of the discharge curve was an indicator of a device with very low equivalent series resistance (ESR) as also evidenced by the high native conductivity of ca. 2508 ± 632 S m^{-1} of the yarn fibers and Figure 8.16.

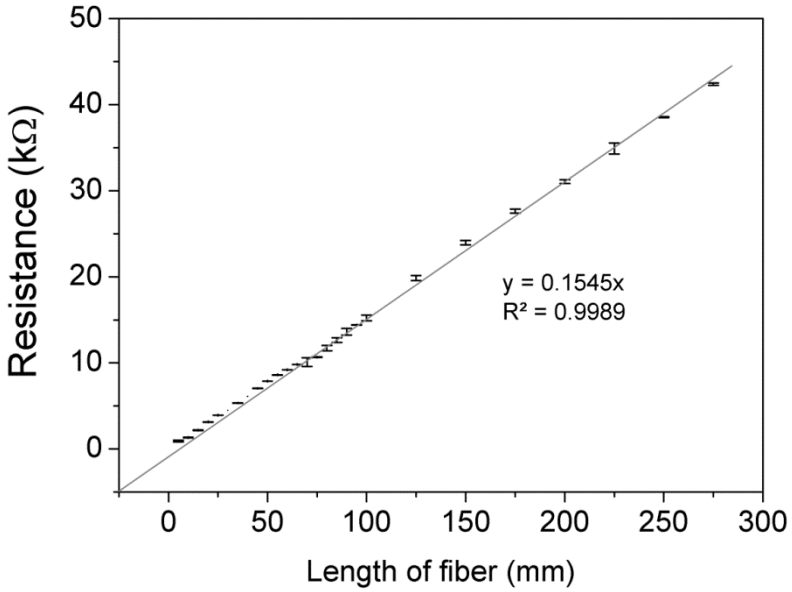

Figure 8. 16. Total resistance as a function of length showing no deviation from ohm law.

High specific capacitance value of 409 F g^{-1} at a current density of 1 A g^{-1} was obtained, comparable with the specific capacitance values extracted from voltammograms. This capacitance value was much higher than best microsupercapacitors (~265 F g^{-1}) and high performance multifunctional fibers. Table 6.2 sets the electrochemical capacitance values of our fibers in the context of a range of electrochemical data from high-performance multifunctional fibers in literature.

Table 8.2. Specific capacitance of rGO fibers and yarns prepared in this study against previous reports on multifunctional fibers.

Production condition	**Electrolyte**	**Voltage Window**	**Specific Capacitance ($F\ g^{-1}$)**	**Reference**
rGO yarns coagulated in Acetone bath and heat-treated at 220°C	1M H_2SO_4	(0-1V)	409 @ 1 A g^{-1} 400 @ 25 mV sec^{-1}	Current study
Twist-spun yarns of nitrogen-doped carbon nanotubes	0.5M H_2SO_4	(0-1V)	39 @ 5 mV sec^{-1}	[19]
PEDOT:PSS SWNT composite fiber	TBABF4/acetonitrile	(0-1V)	59 @ 50 mV sec^{-1}	[5]
Ethylene glycol treated PEDOT:PSS fiber	TBABF4/acetonitrile	(0-1V)	29 @ 20 mV sec^{-1} (three electrode configuration)	[11]
HA-CNT fiber	0.2M H_2SO_4	(0-1V)	44	[21]
graphene / porous carbon woven film	1M Na_2SO_4	(0-1V)	173	[20]
MnO_2 coated graphene / porous carbon woven film	1M Na_2SO_4	(0-1V)	225	[20]
Annealed Polymer free carbon nanotube fibers	Ionic liquid-solid	(0-1.5V)	100	[14]
Carbon microfiber bundles (MWCNTS/ Carbon fibers)	Water based gel electrolyte (PVA+H_3PO_4)	(0-1V)	80 @ 2 mV sec^{-1}	[53]
Knitted CF	Water based gel electrolyte (PVA+H_3PO_4)	(0-1V)	88 @ 10 mV sec^{-1} 76 @ 0.4 A g^{-1}	[4]

Woven CF	Water based gel electrolyte ($PVA+H_3PO_4$)	(0-1V)	63 @ 10 mV sec^{-1} 63 @ 0.4 A g^{-1}	[4]
Graphene microfibers	H_2SO_4 PVA gel	(0-1V)	40	[18]

The specific capacitance values were calculated over a range of current densities of up to 100 A g^{-1} (Figures 8.17 and 8.18 and 8.19 a). Graphene fibers continued to provide outstanding EDL capacitance (56 F g^{-1}) at the current density of 100 A g^{-1}, comparable with specific capacitance values of thin films supercapacitors and microdevices at much lower current densities. [1, 8] The electrodes were tested for 5000 cycles at a current density of 10 A g^{-1} and showed no visible capacitance loss (Figure 8.19c).

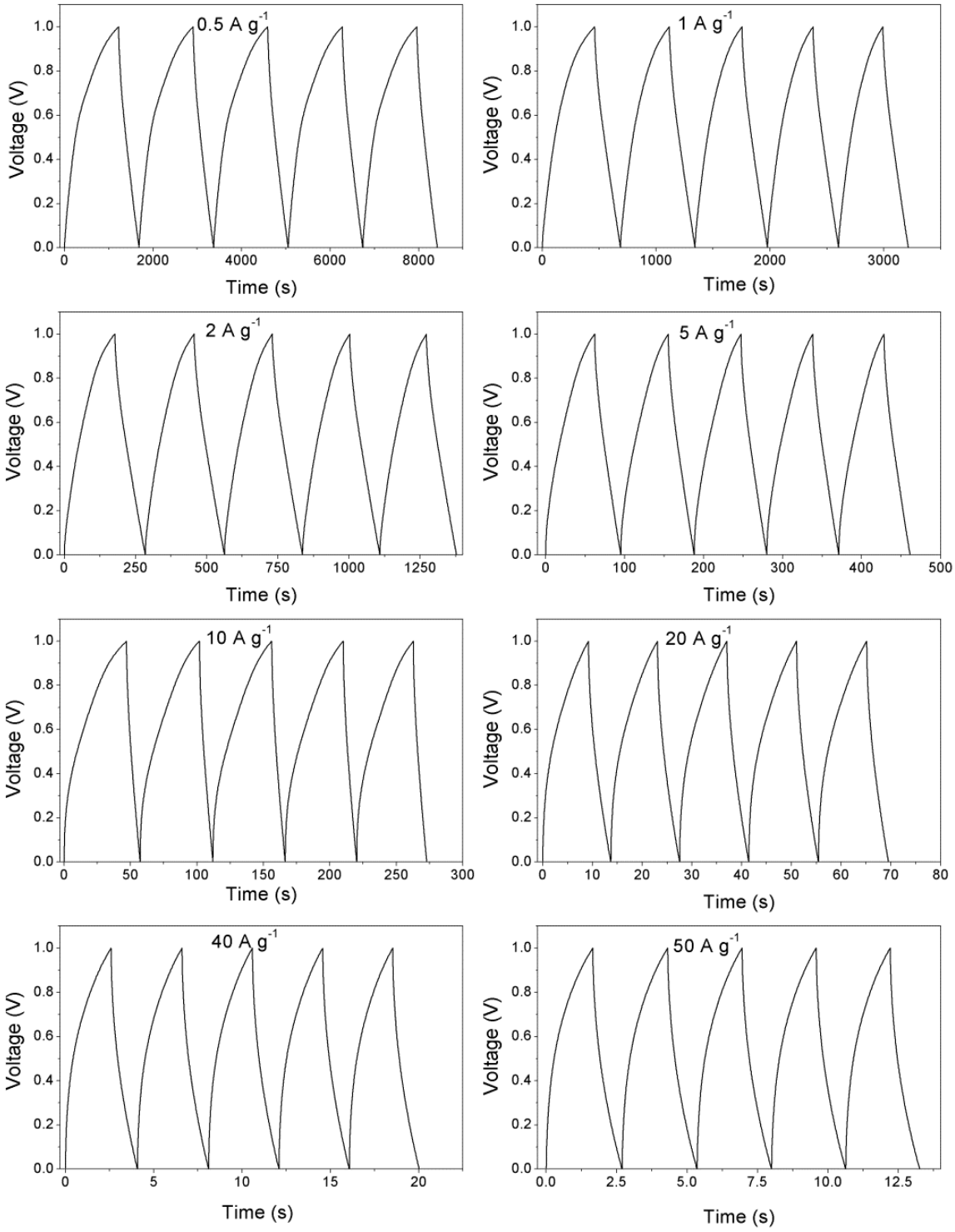

Figure 8. 17. Galvanostatic charge-discharge curves at different current densities.

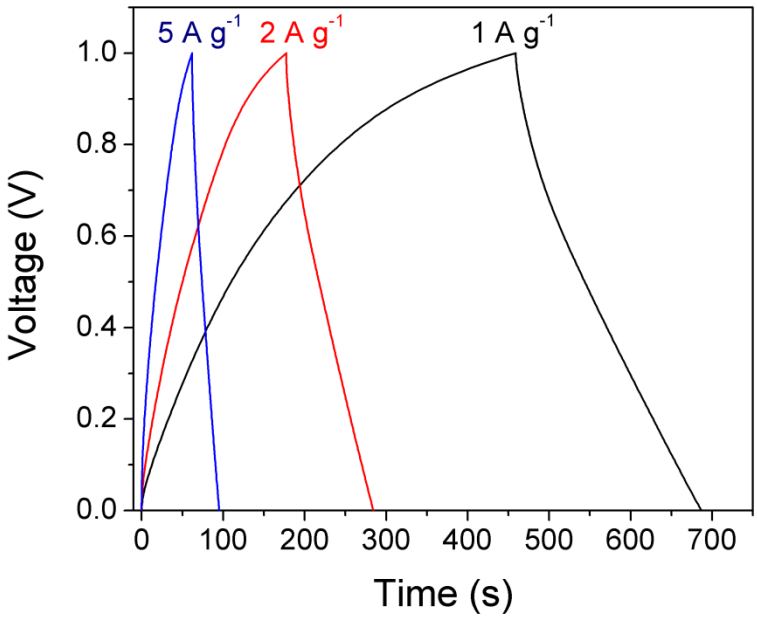

Figure 8. 18. Comparative galvanostatic charge-discharge curves at different current densities.

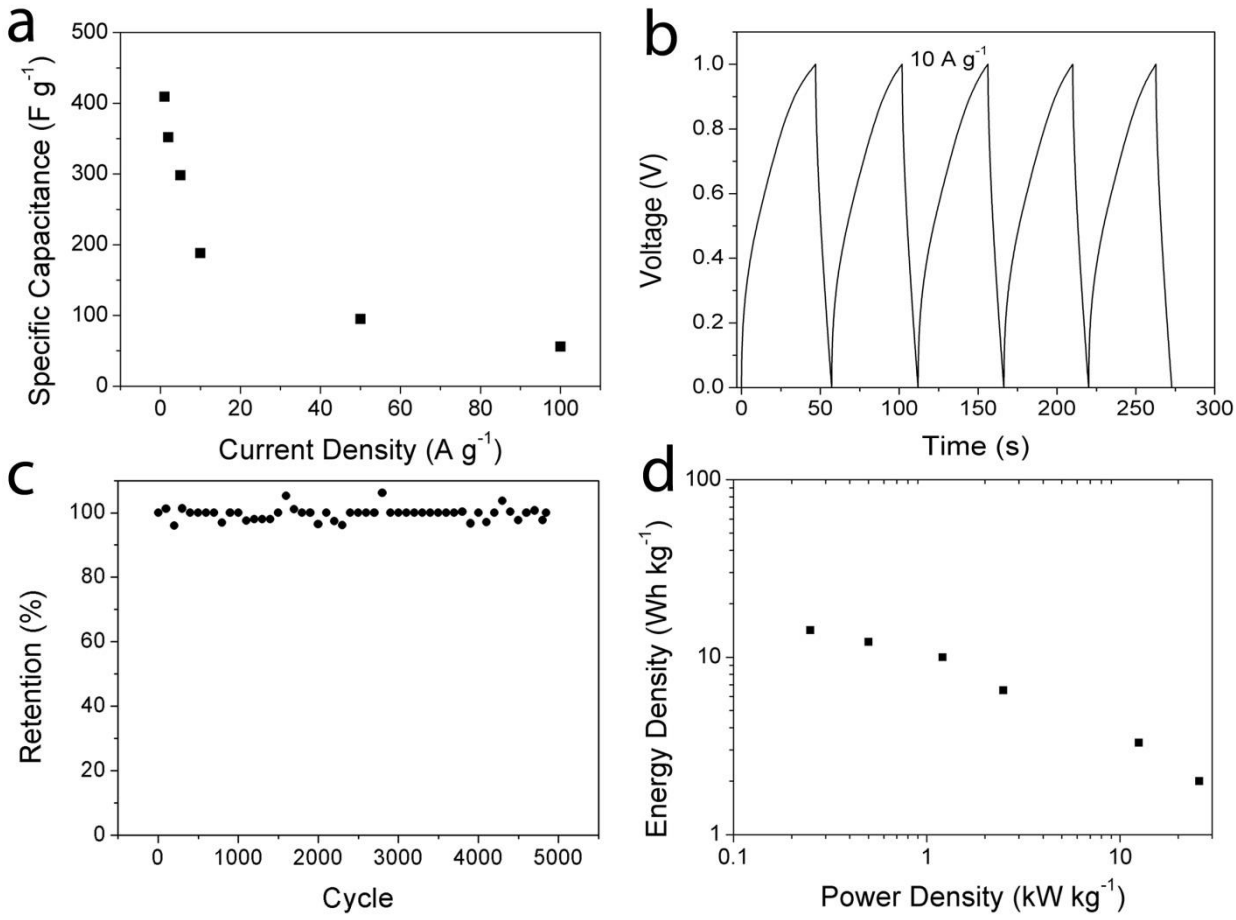

Figure 8. 19. Electrochemical performance of rGO fiber yarns. (a) Supercapacitor performance of rGO fiber yarns in 1 M H_2SO_4 using a two-electrode symmetrical cell showing specific capacitance for each evaluated current density. (b) Galvanostatic charge-discharge curves at constant current density of 10 A g^{-1}. (c) Capacitance retention for 5000 cycles at 10 A g^{-1} current density. (d) Ragone plot for each evaluated current density.

Substantial effort has been focused towards increasing the energy density of supercapacitors through the use of metal oxides or conducting polymers; which usually comes at the expense of cyclability or power, and they are the governing factors that distinguish supercapacitors from mediocre batteries [3]. Here, through the inducement of an appropriate nanostructure in graphene

based electrodes, we also demonstrate their impressive performance (device power and energy densities of 25 kW kg^{-1} and 14 Wh kg^{-1} respectively in a modest potential window of 1V), when used as flexible textile electrodes (Figure 8.19d).

Such a performance can be attributed to the increased interlayer spacing leading to enhanced access of ions to the inter-planar space between the sheets. Furthermore, the sheet size of individual graphene sheets play a crucial role in achieving high capacitance values, as large sheet size essentially means more uninterrupted surface and less grain boundaries which are essential for achieving both high conductivity and higher EDL capacitance. The prevention of restacking, as demonstrated in Figure 8.5a and fiber cross-sections (Figure 8.3c) can result in the easy access of electrolyte ions into the open pores of the structure. As only the surfaces which are in direct contact with the electrolyte contribute to overall capacitance, the open network structure results in the maximum theoretical surface and thus yielding enhanced capacitive performance. The open pores formed within fibers (Figure 8.3c), that essentially form during the coagulation process and structural freezing, and maintained even after reduction resulted in attaining extremely high surface area after the reduction of as-freezed structure (2210 m^2 g^{-1}), can facilitate the electrolyte accessibility and ionic diffusion in graphene fibers. Such a high surface area is an ideal medium for supercapacitors as the EDLC is directly proportional to the surface area [40]. This was also verified by the analysis of the cross-section of fibers with FESEM showing that the intersheet restacking has been effectively prevented (Figure 8.3c), thus allowing the separate sheets in our multilayered fibers to behave as individual sheets. Furthermore, due to the negative charge build up on the surface of rGO, it is safe to assume that positive ions; hydronium (H_3O^+) in acidic electrolyte will be adsorbed on the surface of the working electrode during the charge-discharge process. Acidic solution (H_2SO_4) produces SO_4^{2-} and H_3O^+. In terms of ionic size, hydrated ionic

radius of SO_4^{2-}, and H_3O^+ is reported to be 400 pm and 280 pm respectively, which is less than the inter-layer d-spacing of as-prepared rGO yarns (300 to 650 pm). Therefore, this proper spacing in our rGO architecture not only prevents restacking and keeps the surface area high, it also provides nanoengineered space for ions to intercalate. Therefore, the rGO fiber architecture provides an excellent platform to accommodate and intercalate both ions resulting in an enhanced capacitance values. According to Helmholtz formula, small ionic size results in lower charge separation distance; thus higher capacitance in a determined surface area can be realized. Therefore, the combination of both highly accessible surface area while maximizing the number of covalently bonded carbon atoms through spinning into acetone bath are the contributing factors towards the exceptional performance obtained here.

The key achievement is not only to construct renewable and sustainable energy sources but also, perhaps even more importantly, to store energy efficiently and deliver it on demand, often for mobile applications, such as transportation systems and portable electronic devices. The findings presented here will provide practical solutions for the fabrication of a wide range of large-scale 3D graphene-based architectures (including metallic or polymer-based composites) with extensive applications in multifunctional wearables, sensors, supercapacitor devices, and electronic gadgets.

8.6 Conclusion

In summary, flexible, durable and self-assembled graphene textile electrodes for supercapacitors were fabricated using a novel wet-spinning approach followed by heat-treatment to obtain graphene fibers. The fiber spinning route from ultra large graphene oxide liquid crystals provided a unique highly porous 3D platform with proper spacing dimensions which is highly desirable for a range of energy storage applications. The as-prepared material was then used as a building block

to fabricate cost-effective high-capacity supercapacitor devices. The electrodes showed unrivalled EDL capacitance performance close to the theoretical capacitance of graphene sheets. The approach is readily scalable and can be used to produce multifunctional flexible yarns. The electrochemical data and capacitances achieved along with high energy density of the devices demonstrate the considerable potential of graphene fiber assemblies in the quest for maximal electrochemical performance. The ease of synthesis along with the abundance of the starting material make the use of these architectures an attractive, alternative way of designing next generation of supercapacitors in both conventional fields and new emerging areas.

8.7 REFERENCES

1. Pech, D., et al., *Ultrahigh-power micrometre-sized supercapacitors based on onion-like carbon.* Nat Nano, 2010. **5**(9): p. 651-654.
2. Lee, S.W., et al., *Nanostructured carbon-based electrodes: bridging the gap between thin-film lithium-ion batteries and electrochemical capacitors.* Energ. Environ. Sci., 2011. **4**(6): p. 1972-1985.
3. Jost, K., et al., *Carbon coated textiles for flexible energy storage.* Energ. Environ. Sci., 2011. **4**(12): p. 5060-5067.
4. Jost, K.A., et al., *Knitted and screen printed carbon-fiber supercapacitors for applications in wearable electronics.* Energ. Environ. Sci., 2013.
5. Jalili, R., J.M. Razal, and G.G. Wallace, *Exploiting high quality PEDOT:PSS-SWNT composite formulations for wet-spinning multifunctional fibers.* J. Mater. Chem., 2012. **22**(48): p. 25174-25182.
6. Lee, J.A., et al., *Ultrafast charge and discharge biscrolled yarn supercapacitors for textiles and microdevices.* Nat Commun., 2013. **4**.
7. Wang, K., et al., *An All-Solid-State Flexible Micro-supercapacitor on a Chip.* Adv. Energy Mater., 2011. **1**(6): p. 1068-1072.
8. Gao, W., et al., *Direct laser writing of micro-supercapacitors on hydrated graphite oxide films.* Nat Nano, 2011. **6**(8): p. 496-500.
9. El-Kady, M.F., et al., *Laser Scribing of High-Performance and Flexible Graphene-Based Electrochemical Capacitors.* Science, 2012. **335**(6074): p. 1326-1330.
10. Xia, J., et al., *Measurement of the quantum capacitance of graphene.* Nat Nano, 2009. **4**(8): p. 505-509.

11. Jalili, R., et al., *One-Step Wet-Spinning Process of Poly(3,4-ethylenedioxythiophene):Poly(styrenesulfonate) Fibers and the Origin of Higher Electrical Conductivity.* Adv. Funct. Mater., 2011. **21**(17): p. 3363-3370.

12. Jalili, R., et al., *Scalable One-Step Wet-spinning of Graphene Fibers and Yarns from Liquid Crystalline Dispersions of Graphene Oxide: Towards Multifunctional Textiles.* Adv. Funct. Mater., 2013. **10**(6): p. 5345–5354.

13. Xu, Z., et al., *Ultrastrong Fibers Assembled from Giant Graphene Oxide Sheets.* Adv. Mater., 2013. **25**(2): p. 188-193.

14. Kozlov, M.E., et al., *Spinning solid and hollow polymer-free carbon nanotube fibers.* Adv. Mater., 2005. **17**(5): p. 614-617.

15. Hu, L., et al., *Stretchable, Porous, and Conductive Energy Textiles.* Nano Letters, 2010. **10**(2): p. 708-714.

16. Yu, G., et al., *Solution-Processed Graphene/MnO2 Nanostructured Textiles for High-Performance Electrochemical Capacitors.* Nano Letters, 2011. **11**(7): p. 2905-2911.

17. Bao, L. and X. Li, *Towards Textile Energy Storage from Cotton T-Shirts.* Adv. Mater., 2012. **24**(24): p. 3246-3252.

18. Meng, Y., et al., *All-Graphene Core-Sheath Microfibers for All-Solid-State, Stretchable Fibriform Supercapacitors and Wearable Electronic Textiles.* Adv. Mater., 2013. **25**(16): p. 2326-2331.

19. Lepró, X., et al., *Catalytic Twist-Spun Yarns of Nitrogen-Doped Carbon Nanotubes.* Adv. Funct. Mater., 2012. **22**(5): p. 1098-1098.

20. Li, X., et al., *Large-Area Flexible Core–Shell Graphene/Porous Carbon Woven Fabric Films for Fiber Supercapacitor Electrodes.* Adv. Funct. Mater., 2013. **23**(38): p. 4862–4869.

21. Razal, J.M., K.J. Gilmore, and G.G. Wallace, *Carbon nanotube biofiber formation in a polymer-free coagulation bath.* Adv. Funct. Mater., 2008. **18**(1): p. 61-66.

22. Mohsen, M.G., et al. *Self-aligned Graphene Sheets-Polyurethane Nanocomposites*. in *MRS Proceedings*. 2011: Cambridge University Press.

23. Yousefi, N., et al., *Self-alignment and high electrical conductivity of ultralarge graphene oxide-polyurethane nanocomposites.* J. Mater. Chem., 2012. **22**: p. 12709-12717.

24. Aboutalebi, S.H., et al., *Spontaneous formation of liquid crystals in ultralarge graphene oxide dispersions.* Adv. Funct. Mater., 2011. **21**(15): p. 2978-2988.

25. Aboutalebi, S.H., et al., *Enhanced Hydrogen Storage in Graphene Oxide-MWCNTs Composite at Room Temperature.* Adv. Energy Mater., 2012. **2**(12): p. 1439-1446.

26. Jalili, R., et al., *Organic Solvent-Based Graphene Oxide Liquid Crystals: A Facile Route toward the Next Generation of Self-Assembled Layer-by-Layer Multifunctional 3D Architectures.* ACS Nano, 2013. **7**(5): p. 3981–3990.

27. Xu, Z. and C. Gao, *Graphene chiral liquid crystals and macroscopic assembled fibres.* Nat Commun., 2011. **2**: p. 571.

28. Kim, J.E., et al., *Graphene oxide liquid crystals.* Angew. Chem. Int. Ed., 2011. **50**(13): p. 3043-3047.

29. Jalili, R., et al., *Formation and processability of liquid crystalline dispersions of graphene oxide.* Mater. Horiz., 2014. **1**(1): p. 87-91.

30. Xiang, C., et al., *Large Flake Graphene Oxide Fibers with Unconventional 100% Knot Efficiency and Highly Aligned Small Flake Graphene Oxide Fibers.* Adv. Mater., 2013. **25**(33): p. 4592-4597.

31. Aboutalebi, S.H., et al., *Comparison of GO, GO/MWCNTs composite and MWCNTs as potential electrode materials for supercapacitors.* Energ. Environ. Sci., 2011. **4**(5): p. 1855-1865.

32. Kim, J., et al., *Graphene Oxide Sheets at Interfaces.* J. Am. Chem. Soc., 2010. **132**(23): p. 8180-8186.

33. Guo, F., et al., *Hydration-Responsive Folding and Unfolding in Graphene Oxide Liquid Crystal Phases.* ACS Nano, 2011. **5**(10): p. 8019-8025.

34. Rourke, J.P., et al., *The real graphene oxide revealed: stripping the oxidative debris from the graphene-like sheets.* Angew. Chem. Int. Ed., 2011. **50**(14): p. 3173-3177.

35. Fan, X., et al., *Deoxygenation of Exfoliated Graphite Oxide under Alkaline Conditions: A Green Route to Graphene Preparation.* Adv. Mater., 2008. **20**(23): p. 4490-4493.

36. Lin, X., et al., *Fabrication of Highly-Aligned, Conductive, and Strong Graphene Papers Using Ultralarge Graphene Oxide Sheets.* ACS Nano, 2012. **6**(12): p. 10708-10719.

37. Park, S., et al., *Graphene Oxide Papers Modified by Divalent Ions—Enhancing Mechanical Properties via Chemical Cross-Linking.* ACS Nano, 2008. **2**(3): p. 572-578.

38. Cote, L.J., et al., *Tunable assembly of graphene oxide surfactant sheets: wrinkles, overlaps and impacts on thin film properties.* Soft Matter, 2010. **6**(24): p. 6096-6101.

39. Miller, J.R., R.A. Outlaw, and B.C. Holloway, *Graphene Double-Layer Capacitor with ac Line-Filtering Performance.* Science, 2010. **329**(5999): p. 1637-1639.

40. Pumera, M., *Graphene-based nanomaterials for energy storage.* Energ. Environ. Sci., 2011. **4**(3): p. 668-674.

41. Yang, X., et al., *Bioinspired Effective Prevention of Restacking in Multilayered Graphene Films: Towards the Next Generation of High-Performance Supercapacitors.* Adv. Mater., 2011. **23**(25): p. 2833-2838.

42. El-Kady, M.F. and R.B. Kaner, *Scalable fabrication of high-power graphene micro-supercapacitors for flexible and on-chip energy storage.* Nat Commun., 2013. **4**: p. 1475.

43. de Jonge, H. and M.C. Mittelmeijer-Hazeleger, *Response to Comment on "Adsorption of CO2 and N2 on Soil Organic Matter: Nature of Porosity, Surface Area, and Diffusion Mechanisms".* Environ. Sci. Technol., 1996. **30**(12): p. 3636-3637.

44. de Jonge, H. and M.C. Mittelmeijer-Hazeleger, *Adsorption of CO2 and N2 on Soil Organic Matter: Nature of Porosity, Surface Area, and Diffusion Mechanisms.* Environ. Sci. Technol., 1996. **30**: p. 408.

45. Gao, W., et al., *New insights into the structure and reduction of graphite oxide.* Nat Chem., 2009. **1**(5): p. 403-408.

46. Behabtu, N., et al., *Strong, Light, Multifunctional Fibers of Carbon Nanotubes with Ultrahigh Conductivity.* Science, 2013. **339**(6116): p. 182-186.

47. Koziol, K., et al., *High-Performance Carbon Nanotube Fiber.* Science, 2007. **318**(5858): p. 1892-1895.

48. Dong, Z., et al., *Facile Fabrication of Light, Flexible and Multifunctional Graphene Fibers.* Adv. Mater., 2012. **24**(14): p. 1856-1861.

49. Zhu, Y., et al., *Carbon-Based Supercapacitors Produced by Activation of Graphene.* Science, 2011. **332**(6037): p. 1537-1541.

50. Zhang, L.L. and X.S. Zhao, *Carbon-based materials as supercapacitor electrodes.* Chem. Soc. Rev., 2009. **38**(9): p. 2520-2531.

51. El-Kady, M.F. and R.B. Kaner, *Scalable fabrication of high-power graphene micro-supercapacitors for flexible and on-chip energy storage.* Nat. Commun., 2013. **4**: p. 1475.

52. Pech, D., et al., *Ultrahigh-power micrometre-sized supercapacitors based on onion-like carbon.* Nat. Nanotechnol., 2010. **5**(9): p. 651-654.

53. Le, V.T., et al., *Coaxial Fiber Supercapacitor Using All-Carbon Material Electrodes.* ACS Nano, 2013. **7**(7): p. 5940-5947.

Chapter 9: Organic Solvent-Based Graphene Oxide Liquid Crystals: A Facile Route Towards Next Generation of Self-Assembled Layer-by-Layer Multifunctional 3D Architectures

9.1 Graphene oxide (GO) liquid crystals

Lyotropic liquid crystalline (LC) phases in dispersions containing two dimensional graphene and graphene oxide (GO) sheets have added a new dimension to soft self-assembly science. [1-8] Soft self-assembly of materials, which is the route for engineering of amphiphilic molecules into different supermolecular assemblies in one, two, or three dimensions, has been of interest for decades. [9-11] Fields such as nano-medicine, biocatalysis, bio-active delivery systems, self-assembled composite and solar cells have taken advantage of the self-organization of amphiphilic molecules in recent years. [12-15] Recently, a series of graphene based macroscopic structures including paper and fibers have been fabricated employing the novel amphiphilic soft self-assembly route. [1, 16] The much expected enhancement in properties, self-assembly and alignment of GO might be achieved if the simultaneous dispersion of functional materials with GO in the liquid crystalline media is realized. [17] To date, the application of graphene-based liquid crystals as a promising building block in different fields has not yet been realized mainly because of the practical limitations induced by water, the only medium in which the formation of

LC GO has been reported. However, there are limitations for aqueous media to disperse many nanomaterials that would be expected to introduce enhanced properties to LC GO. For example, the introduction of highly debundled, isolated and self-oriented carbon nanotubes (CNTs) which has only been observed in CHP and never in water with LC GO would be expected to enhance electrochemical and mechanical properties. Understanding and manipulating the forces involved in amphiphilic self-assembly and expanding the range of solvents in which such phenomena can be exploited, will enable the development of new composites based on LC GO. [9]

9.2 The aim of the present chapter

In this chapter, the ability to support GO lyotropic LC phase formation in a wide range of organic solvents through the use of ultra-large GO sheets is reported. This approach enables the exploitation of LC order of GO sheets in organic solvents to organize and align single-walled carbon nanotubes (SWNTs). This work has enabled self-assembly of ultra-stiff, ultra-strong three dimensional (3D) GO-SWNT architectures with high elongation-at-break.

9.3 Formation of LC GO in various organic solvents

To date, water is recognized as the practical medium for the self-assembly of GO. [18] In the pursuit of rationally designed lyotropic LC GO dispersions in various organic solvents, ultra-large GO sheets in a number of common solvents were dispersed including: water, N-N-dimethylformamide (DMF), N-Cyclohexyl-2-pyrrolidone (CHP), Tetrahydrofuran (THF), acetone, ethanol and a number of other organic solvents, many of which were not known to afford solvophobic self-assembly prior to this report. The organic solvents, successfully used here, can support dissolution or dispersion of a wide range of materials. This means that self-assembly of a

variety of compositions in the solvent media that support LC GO formation would be possible. For example, DMF and THF are the most common solvents for processing polymers. Therefore, dispersing GO in these solvents and achieving LC GO would provide unique opportunities in the production of self-assembled, fully ordered and novel LC GO-based polymer composites. LC GO in THF might also be used as an ordered template for the synthesis and self-assembly of metallic nano-particles such as boron or magnesium, which are water and air sensitive. LC GO in CHP, being the best known solvent for debundling CNTs, [19] might promote fabrication of fully ordered self-assembled CNT-GO composites containing highly debundled CNTs. Ethanol and acetone are general purpose solvents which are commonly used as building blocks in organic chemistry. Acetone is also the solvent of choice for a wide range of epoxy families. Therefore, attaining LC GO in acetone would open an avenue for novel self-assembled epoxy based nano-composites. Other solvents in which lyotropic LC formation of GO was observed include ethylene glycol, methanol, acetonitrile, isopropanol, N-methyl pyrrolidone (NMP) and dimethyl acetamide (DMAc). All of the non-polar solvents were ineffective in dispersing GO and therefore could not afford any LC phase as expected. Representative polarized optical microscopy (POM) micrographs of the representative solvents are given in Figure 9.1 to 9.7

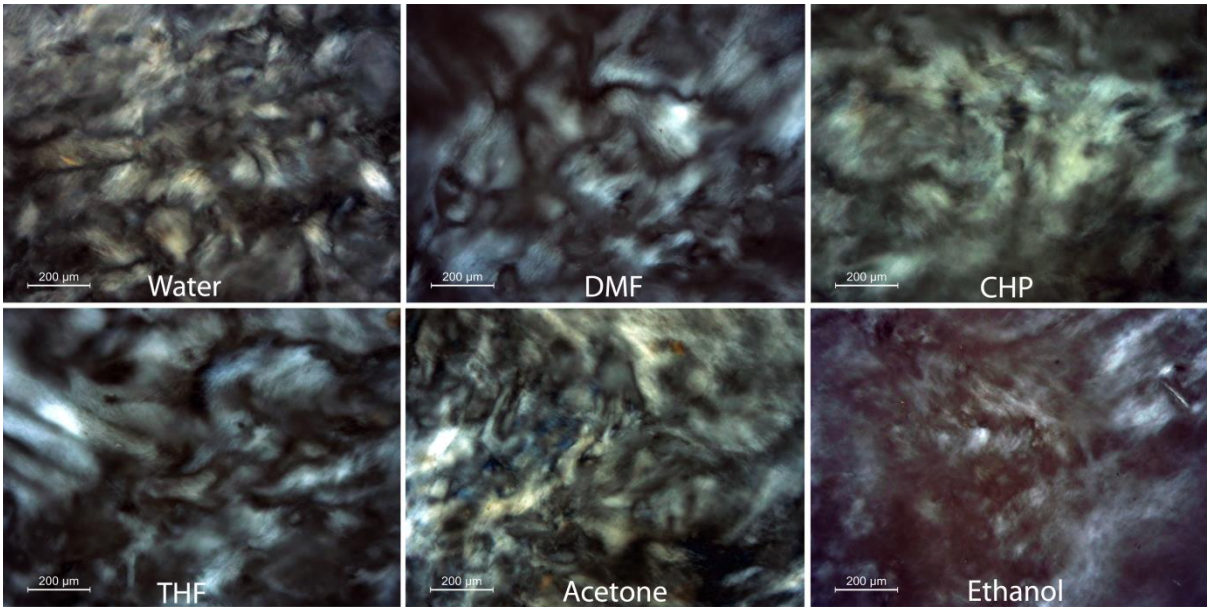

Figure 9. 1.Representative crossed polarized optical microscopy (POM) of LC GO in various organic solvents at a GO concentration of 2.5 mg ml^{-1}.

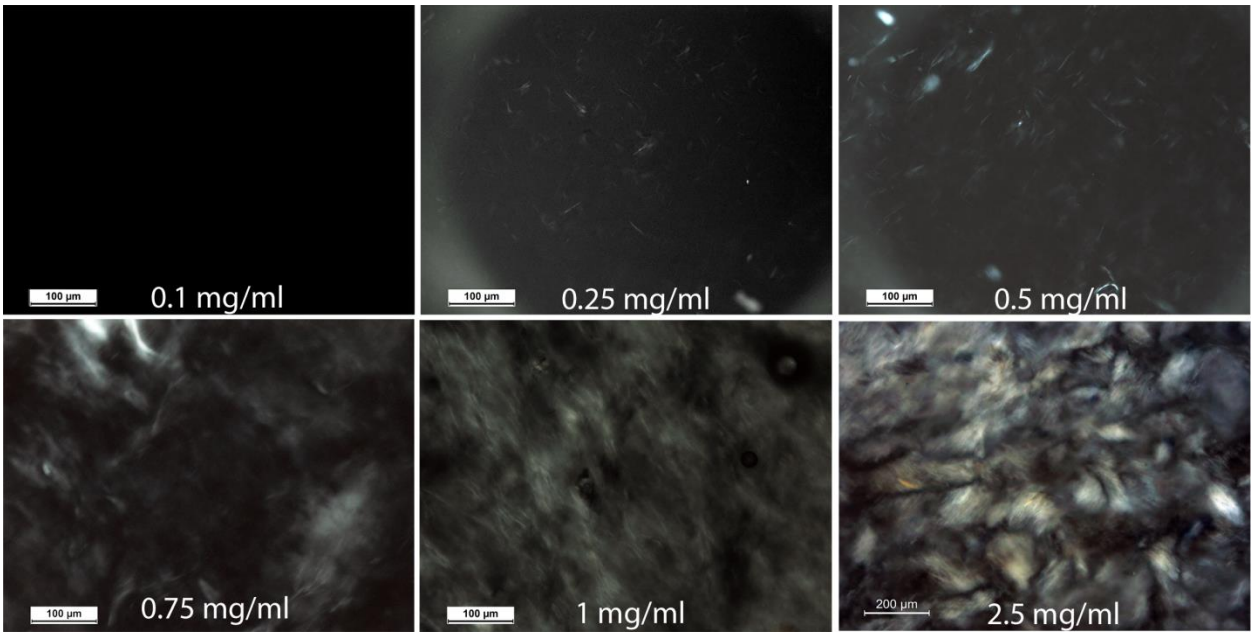

Figure 9. 2 Representative polarized optical micrographs of aqueous LC GO dispersions at various GO concentrations (0.1 to 2.5 mg ml^{-1}) evidenced LC formation at concentration as low as 0.25 mg ml^{-1}.

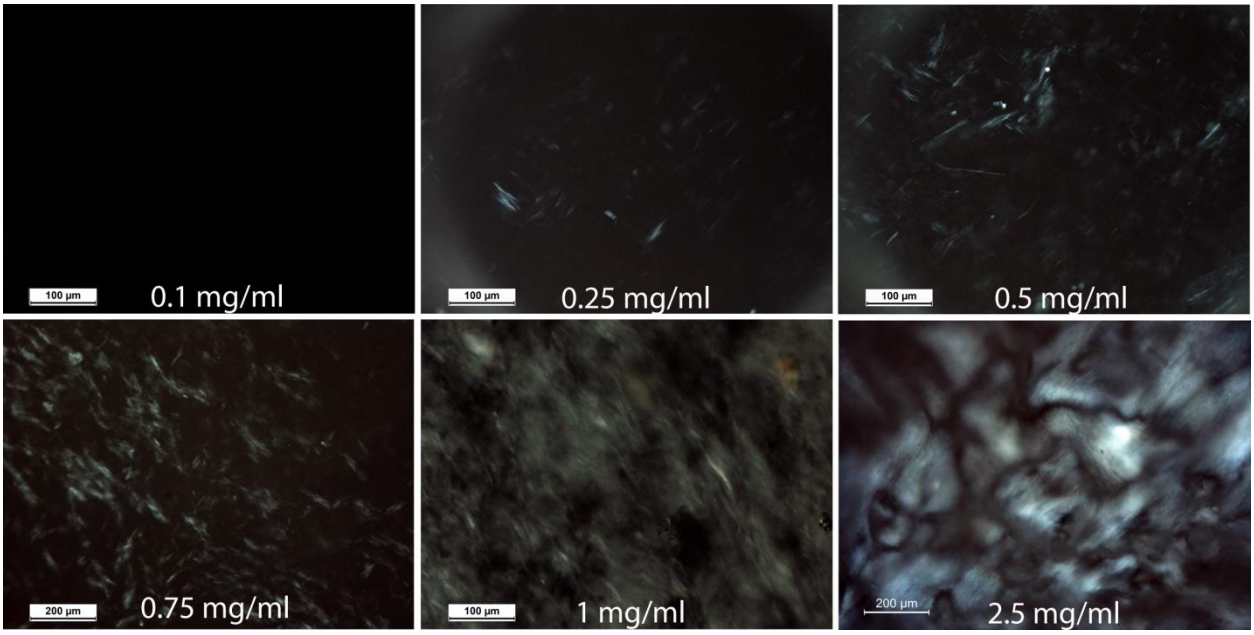

Figure 9. 3.Representative polarized optical micrographs of LC GO dispersions in DMF at various GO concentrations (0.1 to 2.5 mg ml^{-1}) evidenced LC formation at concentration as low as 0.25 mg ml^{-1}.

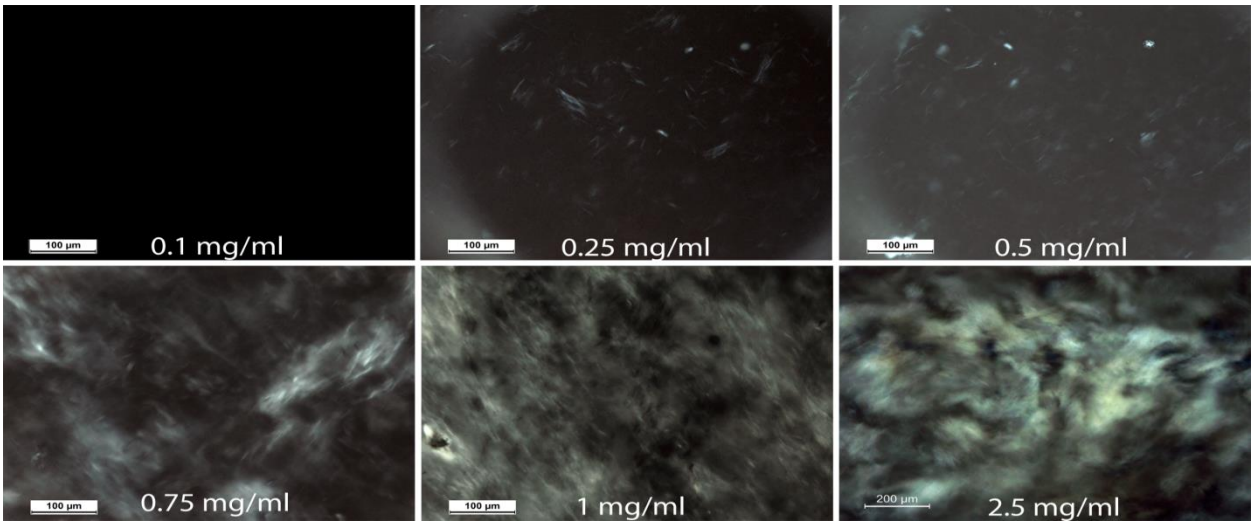

Figure 9. 4. Representative polarized optical micrographs of LC GO dispersions in CHP at various GO concentrations (0.1 to 2.5 mg ml^{-1}) evidenced LC formation at concentration as low as 0.25 mg ml^{-1}.

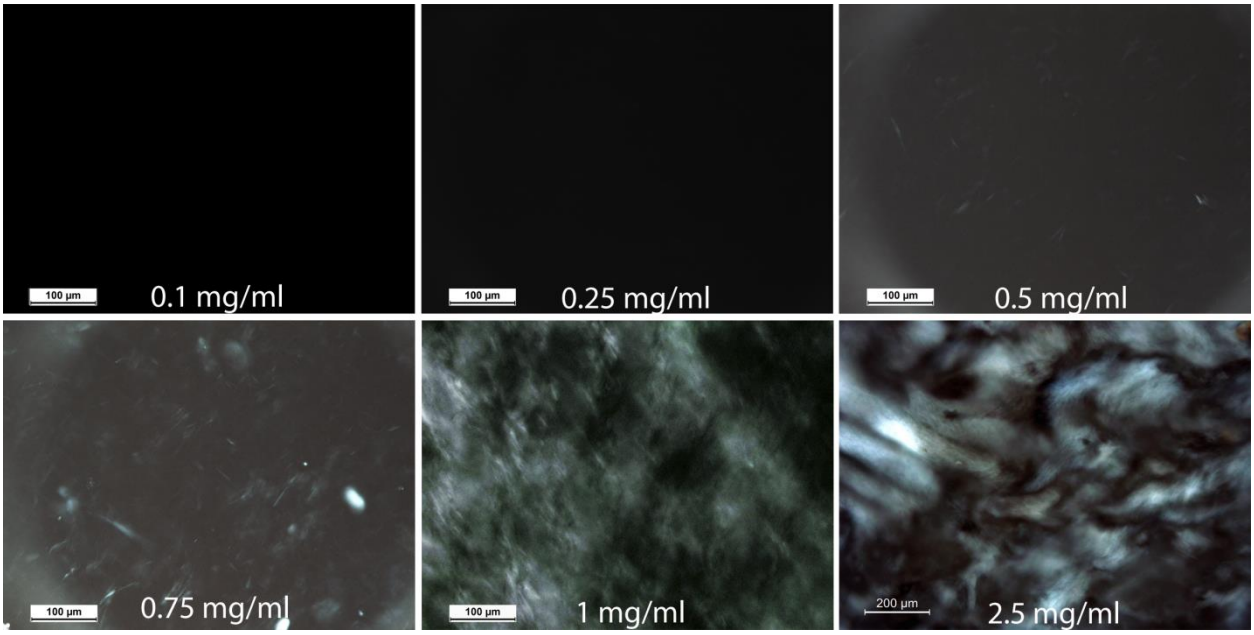

Figure 9. 5. Representative polarized optical micrographs of LC GO dispersions in THF at various GO concentrations (0.1 to 2.5 mg ml^{-1}) evidenced LC formation at concentration as low as 0.5 mg ml^{-1}.

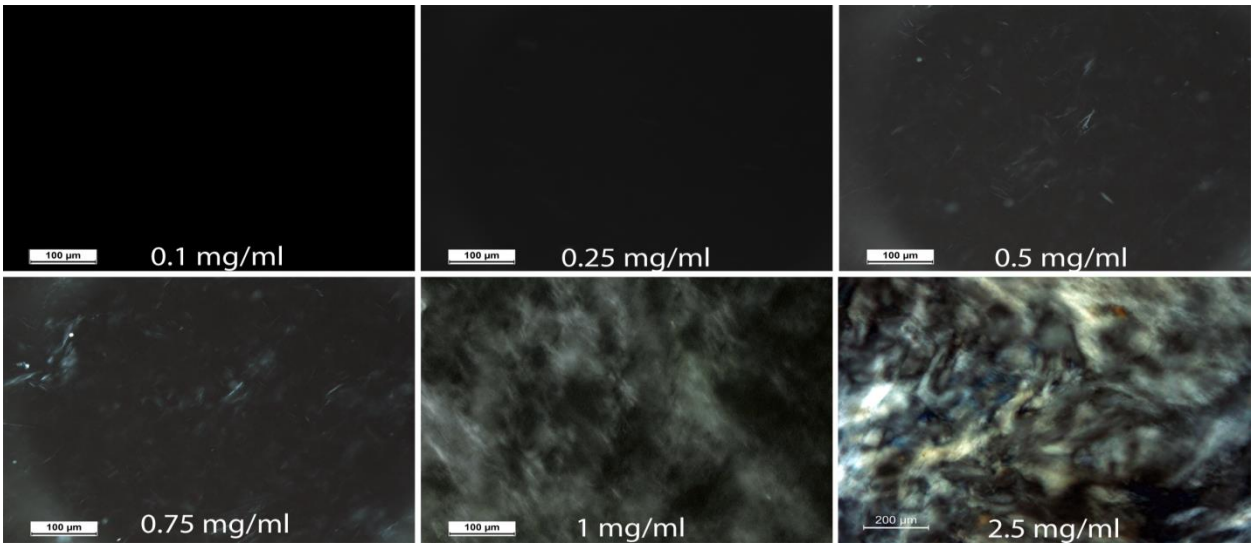

Figure 9. 6. Representative polarized optical micrographs of LC GO dispersions in Acetone at various GO concentrations (0.1 to 2.5 mg ml^{-1}) evidenced LC formation at concentration as low as 0.5 mg ml^{-1}.

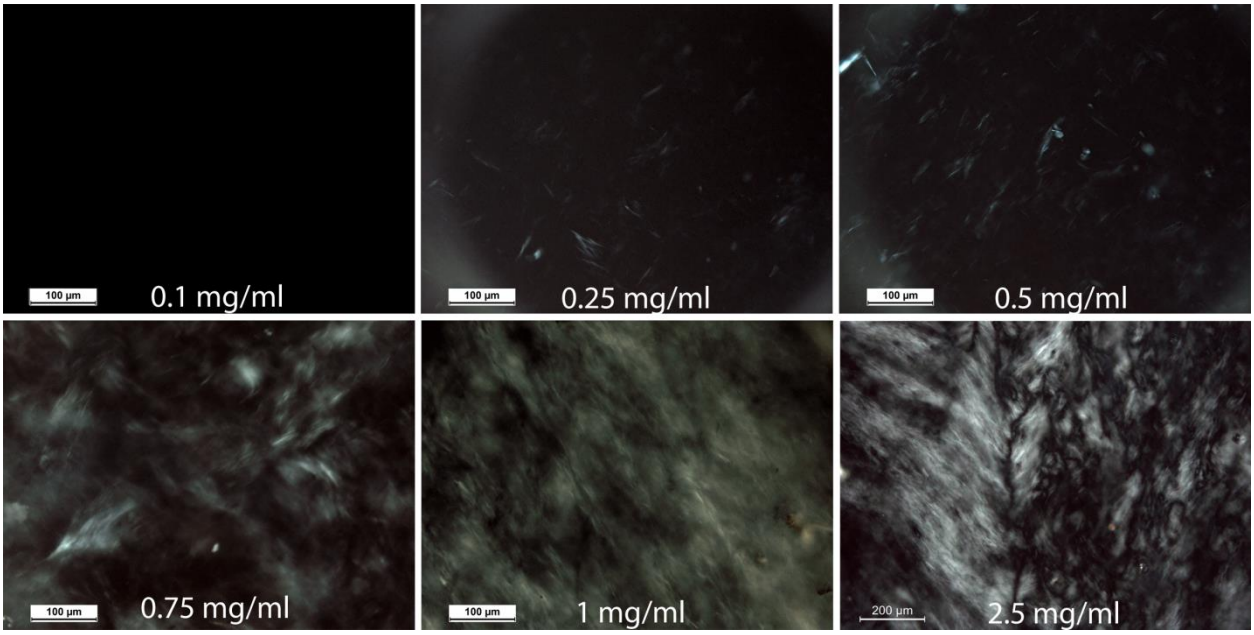

Figure 9. 7. Representative polarized optical micrographs of LC GO dispersions in Ethanol at various GO concentrations (0.1 to 2.5 mg ml^{-1}) evidenced LC formation at concentration as low as 0.25 mg ml^{-1}.

POM micrographs clearly show the birefringent lyotropic LC behaviour of GO in water and all of the above-mentioned organic solvents. The transition concentration from isotropic to the nematic phase was experimentally found to be ~0.25 mg ml^{-1} for water, DMF, CHP and ethanol, and ~0.50 mg ml^{-1} for acetone and THF (Table 9.1). At higher concentrations, the nematic phase formed in all of the solvents spontaneously. Depending on the concentration, as-prepared organic LC GO can be either stable for months or undergo what is stated as degradation. [20] It should be noted that these concentrations, although the lowest filler content ever reported for the formation of liquid crystals from any colloid, are still higher than the theoretical biphasic region between 0.05 to 0.09 mg ml^{-1} calculated for rigid platelets. This discrepancy can be attributed to the flexible nature of the monolayer GO sheets and their tendency of wrinkling especially in the presence of attached functional groups.

Table 9.1. LC formation concentration and GO sheet properties in different solvents.

Solvent	LC formation concentration	Sheet thickness*	d-spacing**
	(mg ml-1)	(nm)	(nm)
Water	0.25	0.83	0.825
DMF	0.25	1.1	1.05
CHP	0.25	1.0	0.101
THF	0.50	0.92	0.937
Acetone	0.50	0.86	0.846
Ethanol	0.25	0.83	0.820

*: Sheet thickness obtained from AFM images

**:*d-spacing* obtained from XRD patterns

9.4 Characterization of LC GO

Atomic force microscopy was employed to assess the number of layers and quality of GO sheets in the organic solvent-based LC dispersions, (Figure 9.8). No aggregation or restacking of GO sheets was observed in any solvent investigated here. As-prepared GO dispersions in all of the organic solvents contained GO sheets that are predominantly in the size of more than tens of micrometres. Step height measurements performed on the samples indicated that all of the samples contained single layer GO sheets; as the mean measured height was between 0.8 to 1.2 nm depending on the solvent used. The thickness of a monolayer of graphene is about 0.34 nm, [21] however, GO has functional groups that act as pillars giving rise to the larger measured height. Some solvent molecules are also expected to bond with the surface of GO and remain even after drying. Hydrogen bonding of each solvent molecule with GO resulted in different apparent sheet thickness, depending on the solvent molecular size and arrangement on the surface of GO sheets.

Moreover, the crumpling of GO sheets that occurs in the case of THF (Figure 9.8) might also result in lower effective aspect ratio which manifests itself in the observation of different phase boundaries presented in Table 9.1.

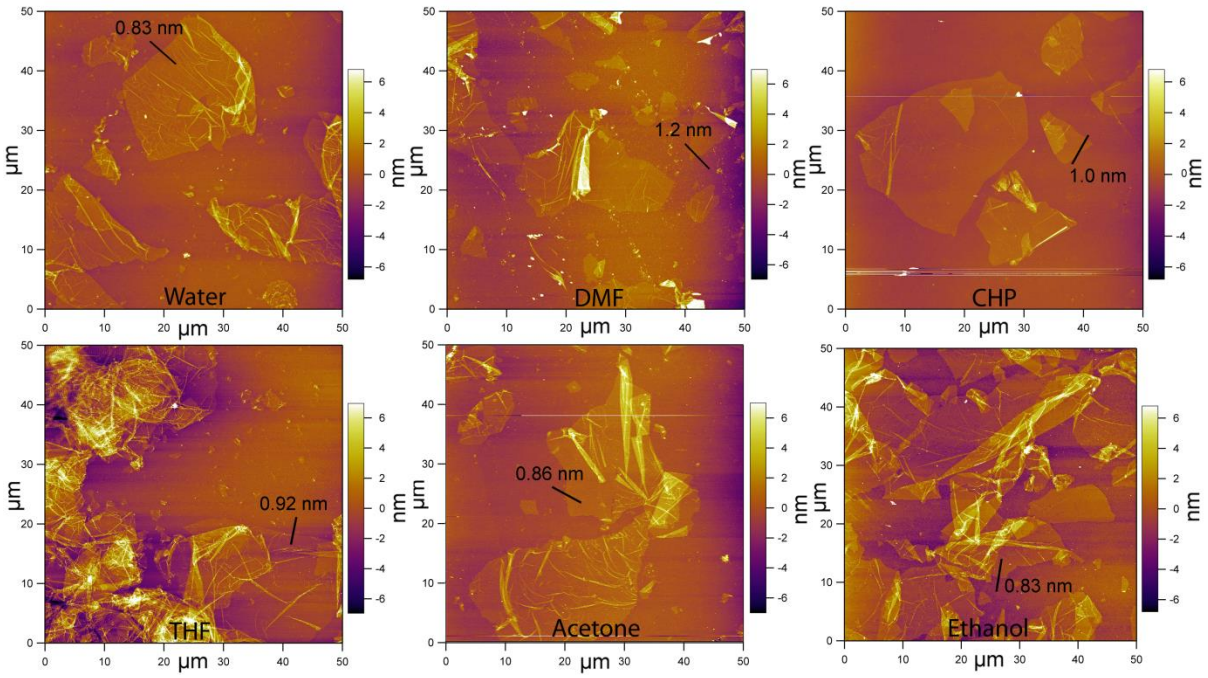

Figure 9. 8. AFM images of GO sheets prepared from various organic solvent based LC GO dispersions. Marked line in each image shows the measured thickness of the sheet.

The change in the apparent thickness of GO sheets as a result of bonding with different solvents can also be confirmed by measuring the interlayer *d*-spacing of GO sheets in cast dried films made from various solvent based GO (Table 9.1). The *d*-spacing represents the interlayer distance between individual GO sheets that are oriented perpendicularly to the diffraction plane. XRD measurements were performed to evaluate the effect of the solvents on the interlayer *d*-spacing of GO films (Figure 9.9a). The process of making GO in water or organic solvents is accompanied by an increase in the *d*-spacing between the graphene layers from about 0.34 nm to ≈ 0.8–1.1 nm, which is related to the degree of oxidation and the hydration level (in the case of GO prepared in

water) or the bonding of other solvent molecules to graphene sheets. [1, 22-25] Therefore, the peak in the XRD patterns of our as-prepared GO films corresponds to the layer-by-layer distance (*d*-spacing) of each sample prepared in each organic solvent according to the Bragg's law. The position of the peak and correspondingly the *d*-spacing values observed in the XRD patterns varied with the solvent used. The differences on *d*-spacing values could be attributed to the confinement of organic solvent molecules in the lamellar GO sheet layers, as in the case of water for aqueous LC GO dispersions. This result could be illustrated by the larger *d*-spacings for GO sheets when dispersed in acetone, THF, CHP and DMF, which had intersheet distances of 0.978 nm, 1.01 nm and 1.17 nm, respectively, than that of GO in water (0.846 nm). A very small shift (*d*-spacing 0.820 nm) was observed in ethanol-based LC GO consistent with the similarity of size with water. The measured *d*-spacing values were also in good agreement with the measured GO sheet thickness from AFM results (Table 9.1). Therefore, it is suggested that the individual GO platelets are interlinked via a non-uniform network of hydrogen bonds mediated by oxygenated functional groups and solvent molecules.

Thermal gravimetric analysis (TGA) was also performed on GO papers (Figure 9.9b). GO papers which were cast from organic solvents with high boiling point temperatures (154 ºC and 153 ºC for CHP and DMF, respectively) lost considerably more weight at higher temperatures compared to GO recovered from water. In contrast, GO dispersed in volatile solvents (acetone, THF and ethanol) started to lose weight at much lower temperatures. This behaviour can be attributed to the confinement of solvent molecules between GO sheets during film formation. The variation between the final weight losses was due to the different amount of solvents associated with each GO sample. The observed significant weight loss at around 180 ºC to 200 ºC is attributed to the partial reduction of GO.

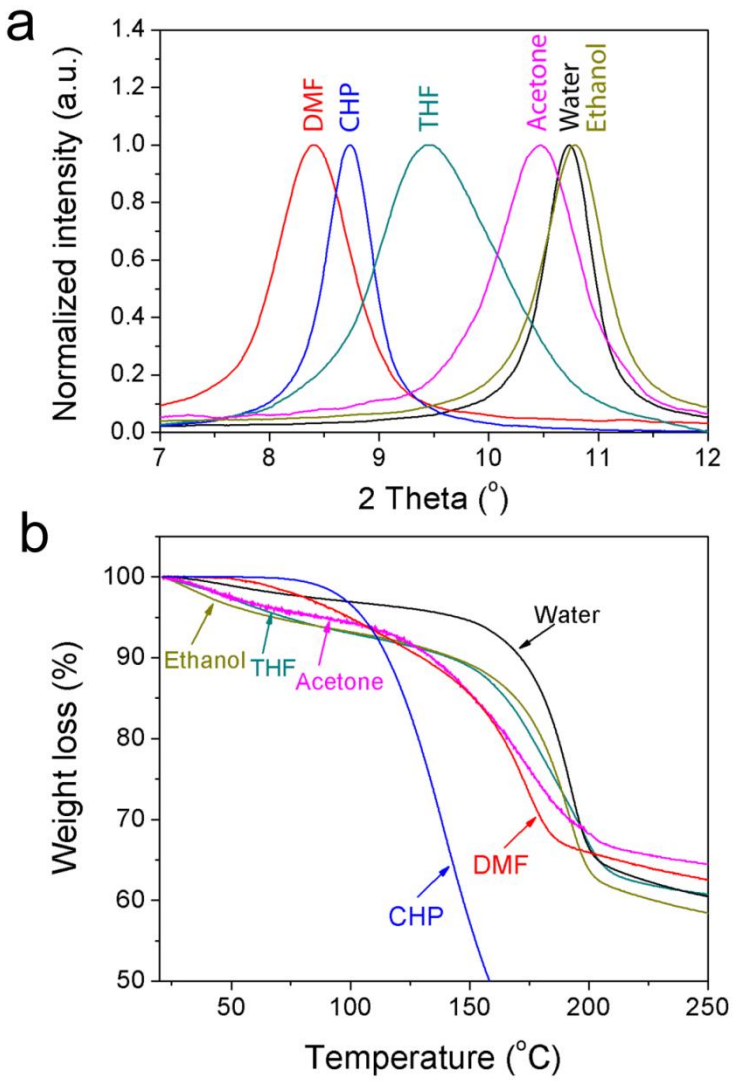

Figure 9. 9. a) X-ray diffraction patterns (XRD) and b) Thermal gravimetric analysis (TGA) of GO films as a function of solvents.

9.5 Insights into the formation of LC GO

The self-assembly of amphiphiles in water is generally driven by hydrophobic interactions, [22-24] which is an important component of a larger solvophobic effect. [22, 25-27] Studies into the thermodynamic driving force for the self-assembly of amphiphiles into LC phases have highlighted that the solvophobic force is almost always dominated by entropic contribution. [26,

28] This behaviour is very similar to hydrophobic forces in water where the nature of these interactions is entropic in origin as the enthalpy change is actually unfavorable in most cases. [29] Therefore, the process of self-assembly is an interplay of entropy and enthalpy terms in the free energy as given in Eq. (4.1).

$$\Delta G^{o}_{\text{self-assembly}} = \Delta H^{o}_{\text{self-assembly}} - T\Delta S^{o}_{\text{self-assembly}}. \quad (4.1)$$

Other contributing factors are hydrogen bonding, van der Waals interactions and electrostatic interactions. [29] Graphene oxide is typically considered as a negatively charged amphiphilic molecule and as a result, [1, 21, 30, 31] the $\Delta G^{o}_{self\text{-}assembly}$ in this case can be represented as the sum of the free energy change associated with hydrogen bonding, $\Delta G_{hydrogen\ bond}$, and electrostatic interactions, $\Delta G_{electrostatic}$ (see Eq. (2)).

$$\Delta G^{o}_{\text{self-assembly}} = \Delta G_{\text{hydrogen bond}} + \Delta G_{\text{electrostatic}} \quad (4.2)$$

With water as the self-assembly medium, both factors contribute to the free energy change term. Only a few other solvents other than water are capable of supporting amphiphilc self-organization. [25, 29, 32, 33]. These solvents include a very limited range of multifunctional alcohols (such as ethylene glycol) and amides and a wide range of protic ionic liquids widely known as PILs. [25, 29, 32, 33]. With PILs, where the solvent itself is an ion, the surface charge screening results in negligible electrostatic contribution, which is in contrast with water or organic solvents where the electrostatic charges play an important role in the free energy associated with ordering. [29] In the case of LC GO, the solvent confined between the charged GO sheets adopts a more structural arrangement to balance the steric and repulsive forces. In this sense, GO can be considered as a self-assembling material due to the fact that it involves supermolecular and supramolecular interactions such as electrostatic repulsion between the adjacent sheets and hydrogen bonding with the confined solvent molecules, which compensate for the loss of rotational entropy during the

self-assembly process. Therefore, in the case of organic solvents, it is the interplay between the ability to form multiple hydrogen bonds and electrostatic charges, manifested through Gordon parameter that governs the process of self-assembly.

The mechanism for the self-assembly process in organic solvents is considered to involve the solvophobic effect which is linked to the solvent cohesiveness. [25] The Gordon parameter ($G=\gamma/V_m^{1/3}$) is a direct measure of the solvent cohesiveness where γ is the surface tension and V_m is the molar volume. [34] High Gordon parameter represents firstly a higher chance to achieve self-assembled liquid crystalline phases and secondly a higher thermal stability. [35] However, the ultra large size of GO sheets used in this study may push the boundaries toward organic solvents with Gordon parameters which are normally considered to be too low to be able to support solvophobic self-assembly. So far, the lowest reported Gordon parameter that supports amphiphilic self-assembly was G = 0.576 J m^{-3} for a protic ionic liquid (EAB), [33] which is far beyond the limit predicted by Evans (G ≥1-1.2 J m^{-3}). [36] However, as the Gordon parameter is directly dominated by surface tension and surface tension is a direct result of electrostatic charges and hydrogen bonding, in the case of PILs, the use of Gordon parameter might be irrelevant as the only dominating force is the ability of the liquid to form extensive hydrogen bonding network. Recently, Drummond *et al*. also discovered that some low molecular weight amides can be utilized as self-assembly media with a Gordon value as low as 0.53 J m^{-3}, which is the direct result of the similarities between the chemical structure of PILs and the amides. [25] However, apart from these two groups of solvents, no other organic polar solvent with lower Gordon parameter less than 1.3 J m^{-3} is yet found to act as an amphiphilic self-assembly medium. However, employing ultra large GO sheets has enabled us to achieve LC GO dispersions in a wide range of organic solvents with

Gordon values previously deemed too low to support self-assembly. The list of solvents shown to support LC GO, along with Hansen parameter and Gordon parameter, are given in Table 9.2.

Table 9.2. Hansen parameters and Gordon parameter for the solvents could support LC GO.

Solvent	LC formation concentration	Hansen Parameter for solvents				Surface tension	Gordon parameter
	(mg ml^{-1})	dispersive	polar	hydrogen	total	(mN m^{-1})	(J m^{-3})
Water	0.25	15.5	16.0	42.3	47.8	72.8	2.77
ethylene glycol	0.25	17.0	11.0	26.0	33.0	47.7	1.25
N-methyl pyrrolidone	0.25	18.0	12.3	7.20	23.0	40.8	0.890
DMF	0.25	17.4	13.7	11.3	24.9	37.0	0.869
dimethyl acetamide	0.25	16.8	11.5	10.2	22.8	36.7	0.810
CHP	0.25	18.2	6.80	6.50	20.5	42.3	0.770
methanol	0.25	15.1	12.3	22.3	29.6	22.7	0.661
THF	0.50	16.8	5.70	8.00	19.5	26.4	0.610
Acetone	0.50	15.5	10.4	7.00	19.9	25.2	0.601
Ethanol	0.25	15.8	8.80	19.4	26.5	22.1	0.569
isopropanol	0.25	15.8	6.10	16.4	23.6	23.0	0.542

Apart from water which has a Gordon parameter higher than 1.2 Jm^{-3}, DMF (which is an amide) shares a degree of structural similarity with PILs and can form extensive hydrogen bonded networks similar to water. [33] Therefore, although the Gordon parameter is very low, DMF could afford formation of LC GO. For the case of other solvents, it is evident that the ability to support LC GO is largely governed by the capability of the solvents to form hydrogen bonds. As an example, although the Gordon value of isopropanol and ethanol is very low (G = 0.541 J m^{-3} and G = 0.569 J m^{-3}, respectively), their ability to form multiple hydrogen bonds which is even much higher than DMF, can overcome the low cohesive energy density of the solvent. On the other hand, the lower ability of acetone and THF to form hydrogen bonds resulted in an increased GO concentration required for LC formation (0.50 mg ml^{-1}) compared to ethanol (0.25 mg ml^{-1}), which has slightly lower Gordon parameter but much higher hydrogen bonding ability. As a result, it is safe to assume that the ability to form an extensive hydrogen bonding network is the most important parameter to govern the self-organization process in the case of LC GO. Consequently, the interplay between the hydrogen bonding and the Gordon parameter can effectively determine: (i) whether an organic solvent can induce the self-assembly process, and (ii) the lowest possible concentration in which spontaneous self-organization can occur.

9.6 Exploitation of the self-assembly nature of LC GO

The intrinsic self-assembly nature of LC materials can be used to exploit them as versatile templates for the synthesis and alignment of nanoparticles [10, 13]. LC GO was utilized to induce liquid crystallinity to SWNTs dispersion through the addition of LC GO to the SWNTs dispersion. POM micrographs of LC GO-SWNTs are presented at Figures 9.10a and 9.10b which show the nematic LC behaviour of as-prepared mixtures in CHP and DMF, respectively. Although SWNTs

and rod shaped particles under some specific conditions can form LC phases, this requires modification of the SWNTs surface by bio-polymers, [37, 38] functionalization (with a subsequent compromise in electronic properties), [39, 40] or the use of superacids. [41, 42] Here SWNTs were dispersed in CHP at concentrations as high as surfactant assisted dispersions (1 mg ml^{-1}). [19] Subsequent mixing of this SWNT dispersion with CHP- or DMF-based lyotropic LC GO resulted in birefringence yet preserves the fundamental properties of SWNTs (no dispersant was added). It has been shown that organic solvent stabilized SWNT dispersions are sensitive to the presence of water whereby the addition of very small amounts of water will cause the dispersion to agglomerate and crash out of solution. [43] The water free nature of our as-prepared LC GO in organic solvents is demonstrated by the fact that SWNTs do not agglomerate and crash out of the dispersion when they are added to the as-prepared LC GO in organic solvents. The quality of the dispersion even after addition of the GO is evidenced by the UV Vis spectra, (Figure 9.10c). The well-resolved inter-band transitions in the UV/Vis-near-IR spectra of the SWNT dispersion before and after the addition of LC GO indicate that SWNT sizes are preserved in the composite formulation. According to Smalley and Hague, [44] UV/Vis-near-IR spectroscopy is the most reliable method to determine SWNTs size distribution based on Van Hove singularities. As it is evident from UV/Vis-near-IR spectra, the size of our nanotubes is predominantly in the range of 1 nm and 0.95 nm corresponding to the wavelength of ~1300 nm and ~1150 nm in the as-prepared SWNTs dispersions, respectively. The quality of SWNTs dispersion (bundle size) was also preserved during the combination with LC GO.

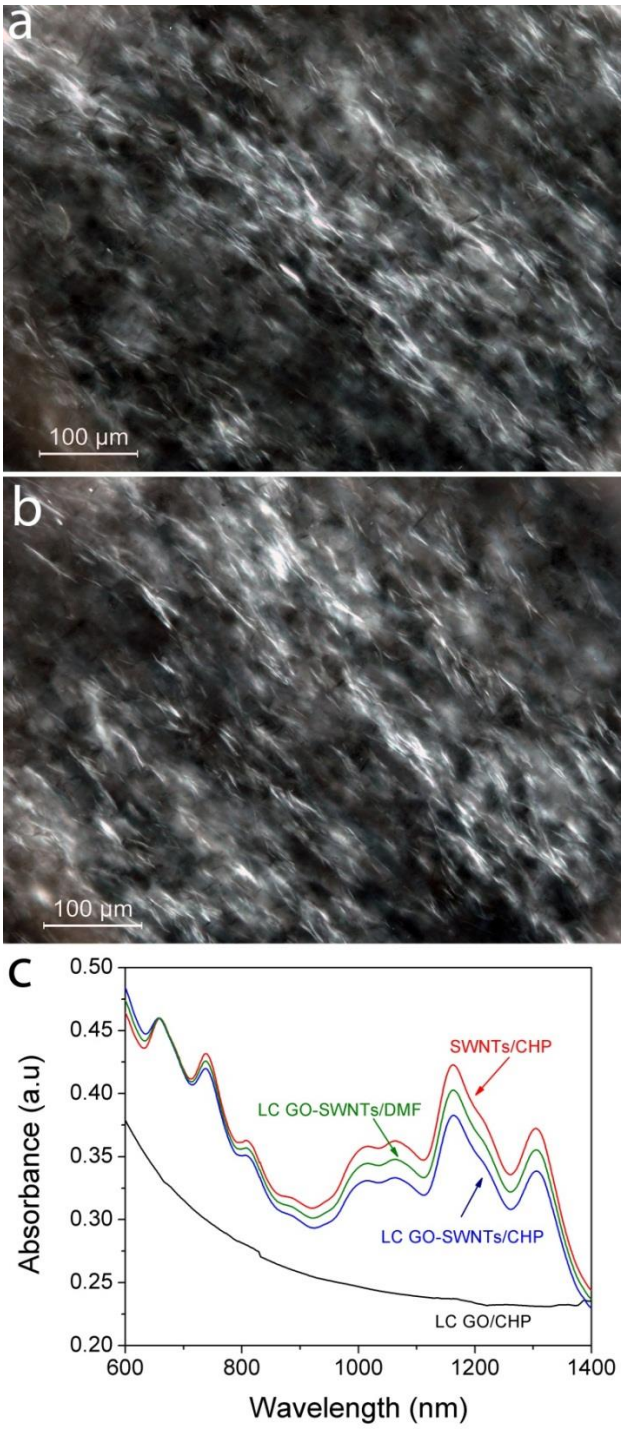

Figure 9. 10. Representative POM micrographs of a) LC GO-SWNTs/CHP (90:10 at ~1 mg ml^{-1}), b) LC GO-SWNTs/DMF (90:10 at ~1 mg ml^{-1}). c) UV/Vis-near-IR spectra of SWNTs and LC GO dispersions before and after mixing together.

It is pertinent to mention that although many particles can disturb the liquid crystal director field depending on the particle size, shape and surface interaction with liquid crystal media, [45] GO in this regard enjoys a unique benefit. This unique benefit is due to minimizing the exert forces or torques in the direction perpendicular to the director to promote a configuration in which the distortion is minimal, leading to the in-plane alignment of anisotropic particles (the ordering of particles on GO planes) such as SWNTs; as evident from the strength of our as-prepared composite films (see 9.7). Prior to this work [46-48], the only successful method of increasing the CNT concentration in lyotropic LCs has been through using extensive amounts of surfactants (which can adversely CNTs performance). [49] Only trace amounts of CNTs have been dispersed in thermotropic LCs in order to avoid CNT aggregation. [46, 48] However, in our case, dispersion and organization of substantial amounts of SWNTs (up to 10 wt%) in GO LC without losing birefringence properties and observing any aggregation was achieved. Therefore, this LC formulation was utilized for a facile fabrication of self-assembled layer-by-layer LC GO-SWNT 3D assemblies.

9.7 Self-assembled layer-by-layer multifunctional composite

The LC properties of our as-prepared LC GO-SWNTs dispersions in organic solvents induce a spontaneous self-assembly into engineered long range ordered layer-by-layer 3D structures upon simple casting and drying as shown in Figure 9.11. The ease of synthesis, much shorter processing time and high scalability of this route in contrast with other layer-by-layer production methods (such as Langmuir−Blodgett deposition) offers the opportunity for facile fabrication of 3D frameworks with exceptional properties. The excluded volume generated by large GO sheets for SWNTs results in an entropic rearrangement to form long range ordering. Therefore, LC GO in

CHP can be employed as a dispersing media to process SWNTs based on hydrophobic and π-π interactions as well as a medium in which SWNTs can be self-assembled. This can consequently result in the fabrication of highly aligned and macroscopically periodic self-assembled structures of GO-SWNTs hybrid material. The aggregate-free nature of our as-prepared LC GO-SWNTs enabled us to achieve ultra-stiff, ultra-strong layer-by-layer 3D architecture with high elongation-at-break which enjoy an average modulus of 51.3 GPa, tensile strength of 505 MPa and elongation at break of 9.8% (Figure 9.12), which is much higher than the parent GO architecture.

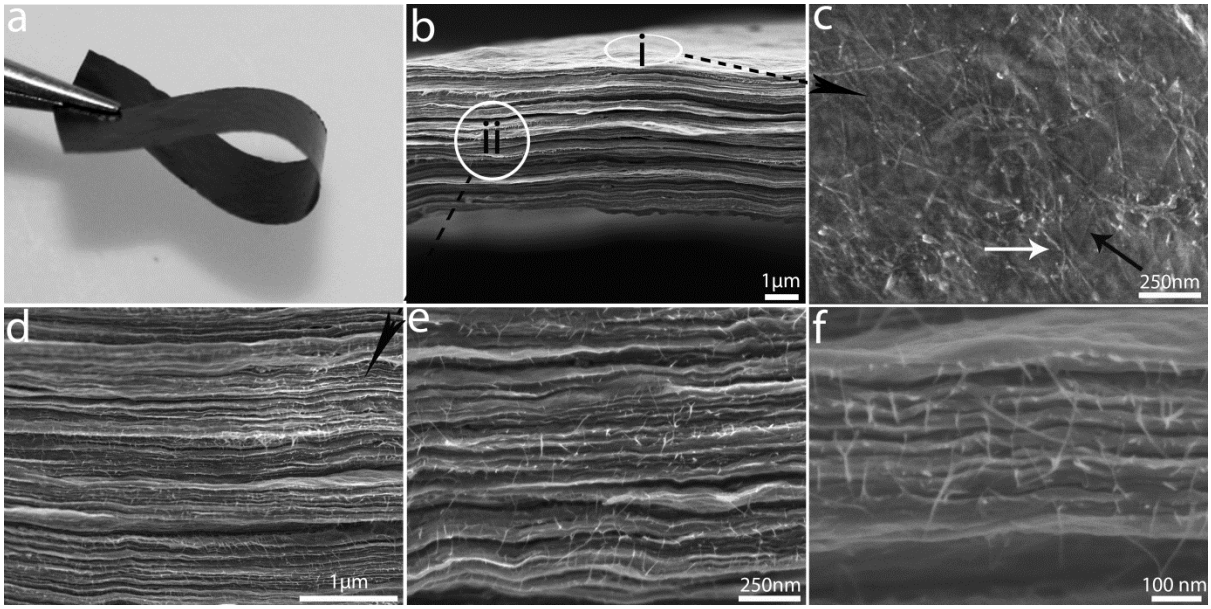

Figure 9. 11. a) Representative photograph of a flexible free-standing paper of LC GO-SWNT made by cast drying method. b) SEM image of the cross-section of as-cast dried LC GO-SWNT paper. c) SEM image of the surface of the layer-by-layer composite which is marked as region (i) in (b). Some of the SWNTs are laid on the surface of the paper (white arrow) while others are placed between layers of GO sheet (black arrow). Transparency of the monolayer/few layers of GO sheets allows observing tubes sites in different layers. d-f) Cross-section of composite paper at different magnifications (marked as (ii) in (b)), confirmed the self-oriented nature of the composite as well as maintaining SWNTs debundled after the fabrication of composite.

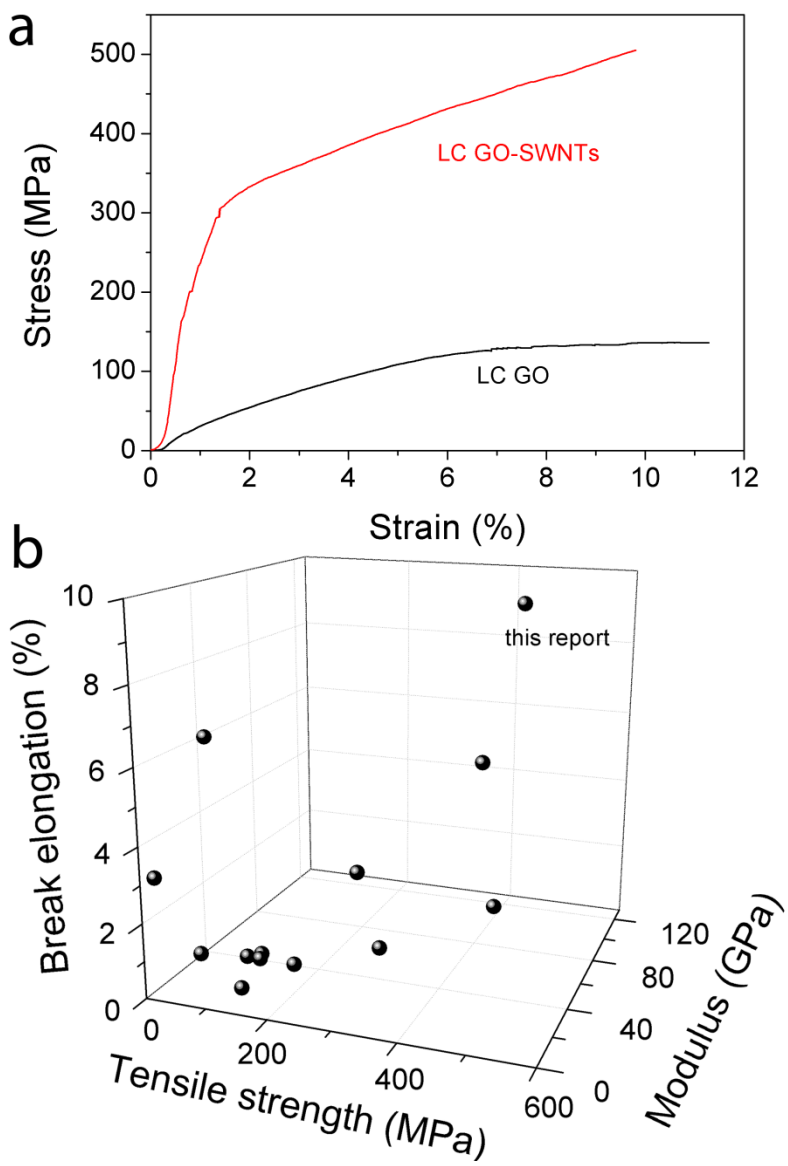

Figure 9. 12. a) Stress-strain curves of LC GO and LC GO-SWNTs self-assembled composite. b) Diagram of mechanical performance data for layer-by-layer nanocomposites and carbon-based neat papers and fibers in selected significant published reports and in this study (see also Table 9.3).

Table 9.3. Comparison of LC GO-SWNTs mechanical performance data with layer-by-layer nanocomposites and carbon-based neat papers and fibers in selected significant previous reports and in this study

Composite type	Modulus (GPa)	Strength (MPa)	Break elongation (%)	Ref
LC GO/ SWNTs	51	505	9.8	This report
bucky paper	1.7	20	3.2	[50]
GO paper	32	120	0.5	[51]
GO paper (cross linked)	33	92	0.32	[52]
GO paper (cross linked)	28	125	0.5	[53]
rGO paper (heated at 220 ^{o}C)	42	300	0.8	[54]
GO fiber	5.4	102	6.8	[16]
rGO fiber (cross linked)	11	501	6.7	[55]
Neat CNT fibers	12	65	1.0	[56]
Neat CNT fibers	120	116	0.4	[42]
LBL polymer nanocomposite	106	400	0.33	[57]
LBL SWNTs nanocomposite	12	218	1.1	[58]
LBL MWNTs nanocomposite	4.5	150	0.55	[59]

The average strength, reported here, is much higher than those reported for bucky papers, [50] GO and rGO papers (prepared by either filtration or casting strategies) and fibers (either as is or cross-linked), [16, 51, 52, 54, 60] paper-like materials based on vermiculite, [61] flexible graphite foil, [62, 63] neat SWNTs fibers, [41, 42, 56, 60, 64] and even layer-by-layer assembled polymer, [57] SWNTs, [58] or MWNTs nanocomposites. [59] As proposed by Ruoff *et al*. very high mechanical strength can be obtained if ordering and alignment of fibrils/macromolecules are achieved. [51] In comparison with irregularly laid-down individual fibrils obtained *via* filtration, the LC route provided us with a self-mediated platform to organize and order SWNTs resulting in an extraordinarily high mechanical strength. Our average Modulus is also considerably higher than all those (Figure 9.12 b and Table 9.3) and just inferior to either SWNT fibers composites with

polymers or extensively processed SWNTs. [42, 60, 65] The as-prepared composite paper exhibited an exceptional conductivity of 1500 S m^{-1}.

The ultra-large nature of our as-prepared GO sheets (with lateral size in excess of 32 μm compared to typically few hundreds of nm in the case of other reports) provides us with a highly wrinkled topography, [1, 66] which can first contribute to an overall increase in strain, and second maximize the fraction of the surface area available for mechanical reinforcement and toughening. [51, 60] Therefore, in the case of ultra large GO sheets, the initial straightening due to wrinkled topography plays a crucial role in the observed increase in elongation-at-break of our as prepared GO compared to other reports. Furthermore, this enhanced wrinkled topography provides us with a unique platform to accommodate individual, separated SWNTs in between the GO sheets resulting in an overall enhancement in exploitation of the extraordinary mechanical properties of SWNTs. Also, the introduction of SWNTs can prevent the restacking of individual two-dimensional GO sheets, further enhancing the properties of the hybrid material. Furthermore, our GO-SWNTs hybrid material exhibited a very high toughness in the order of 20 J g^{-1}, which is almost two orders of magnitude higher than GO paper, [51] three orders of magnitude higher than pristine bucky paper, [50, 67] and flexible graphite foils and even 7 times higher than GO/rGO fibers. [16] The flat fracture surface of our ruptured paper is evidence of the good material homogeneity and layer-by-layer nature of both our as-prepared neat and hybrid papers. The strong interfacial bonding in the case of our hybrid paper is also evident from the straight fracture surface in contrast to the rupture of bucky paper (Figure 9.12). In regards to mechanical properties, SWNTs act as bridging components between individual GO sheets (see high magnification SEM micrographs in Figure 9.11d-f). As the GO sheets are not strongly attached together, reinforcing them with SWNTs can result in an overall increase in mechanical properties. SWNTs can bridge individual GO sheets

and therefore increase the shear force between GO sheets. Furthermore, the most important limitation of using SWNTs as reinforcing agents is the intertube and interfacial slippage within bundles. The poor load transfer within bundles results in interfacial slippage as the effective moduli and strength for bundles are far below those expected for individual SWNTs. The individual nature of SWNTs reported in our study, as evident in high resolution SEM figures presented in Figure 9. 11 and the well-resolved inter-band transitions in the UV/Vis-near-IR spectra of the SWNT dispersion before and after the addition of LC GO presented in Figure 9.10, ensures that the shear slippage of nanotubes within the bundle does not occur and the mechanical properties of SWNTs used in this study are preserved resulting in an overall enhancement of the final composite properties. The findings presented here will pave the way to versatile and highly scalable routes for the fabrication of a wide range of large-scale 3D graphene based architectures (including metallic or polymer based composites) with extensive applications in multifunctional wearables, sensors, supercapacitor devices and electronic gadgets.

9.8 Conclusion

In summary, the discovery of lyotropic LC GO dispersions in a range of organic solvents contributes to the fundamental understanding of the solvophobic effect and the parameters affecting the self-assembly process. The ability of the solvents to promote self-assembly in GO is governed by their polarity and is linked to the ability to form extensive hydrogen bonding. The steric hindrance between the highly charged GO sheets is the factor that overcomes the unfavorable loss of rotational entropy associated with ordering. The expansion of the list of known solvents that can promote the self-assembly process and lyotropic liquid crystallinity has enabled us to tailor-make processable self-assembled, self-oriented SWNTs/GO hybrid composites with

superior mechanical performances (Table 4.3). This discovery could provide practical solutions to the processability of a wide range of materials that require organic solvents because of solubility issues and/or water sensitivity (*i.e.* metal oxides, polymers and nanomaterials).

9.9 REFERENCES

1. Aboutalebi, S.H., et al., *Spontaneous formation of liquid crystals in ultralarge graphene oxide dispersions.* Adv. Funct. Mater., 2011. **21**(15): p. 2978-2988.
2. Dan, B., et al., *Liquid crystals of aqueous, giant graphene oxide flakes.* Soft Matter, 2011. **7**(23): p. 11154-11159.
3. Guo, F., et al., *Hydration-Responsive Folding and Unfolding in Graphene Oxide Liquid Crystal Phases.* ACS Nano, 2011. **5**(10): p. 8019-8025.
4. Eda, G. and M. Chhowalla, *Graphene patchwork.* ACS Nano, 2011. **5**(6): p. 4265-4268.
5. Xu, Z. and C. Gao, *Aqueous liquid crystals of graphene oxide.* ACS Nano, 2011. **5**(4): p. 2908-2915.
6. Behabtu, N., et al., *Spontaneous high-concentration dispersions and liquid crystals of graphene.* Nat. Nanotechnol., 2010. **5**(6): p. 406-411.
7. Hu, X., Z. Xu, and C. Gao, *Multifunctional, supramolecular, continuous artificial nacre fibres.* Sci. Rep., 2012. **2**.
8. Zamora-Ledezma, C., et al., *Liquid Crystallinity and Dimensions of Surfactant-Stabilized Sheets of Reduced Graphene Oxide.* J. Phys. Chem. Lett., 2012. **3**(17): p. 2425-2430.
9. Fong, C., T. Le, and C.J. Drummond, *Lyotropic liquid crystal engineering-ordered nanostructured small molecule amphiphile self-assembly materials by design.* Chemical Society Reviews, 2012. **41**(3): p. 1297-1322.
10. Bisoyi, H.K. and S. Kumar, *Liquid-crystal nanoscience: an emerging avenue of soft self-assembly.* Chemical Society Reviews, 2011. **40**(1): p. 306-319.
11. Hamley, I.W., *Nanotechnology with Soft Materials.* Angewandte Chemie International Edition, 2003. **42**(15): p. 1692-1712.

12. Lagerwall, J.P.F. and G. Scalia, *A new era for liquid crystal research: Applications of liquid crystals in soft matter nano-, bio- and microtechnology.* Current Applied Physics, 2012. **12**(6): p. 1387-1412.

13. Dellinger, T.M. and P.V. Braun, *Lyotropic Liquid Crystals as Nanoreactors for Nanoparticle Synthesis.* Chemistry of Materials, 2004. **16**(11): p. 2201-2207.

14. Kijima, T., et al., *Noble-Metal Nanotubes (Pt, Pd, Ag) from Lyotropic Mixed-Surfactant Liquid-Crystal Templates.* Angewandte Chemie International Edition, 2004. **43**(2): p. 228-232.

15. Hulvat, J.F. and S.I. Stupp, *Anisotropic Properties of Conducting Polymers Prepared by Liquid Crystal Templating.* Advanced Materials, 2004. **16**(7): p. 589-592.

16. Xu, Z. and C. Gao, *Graphene chiral liquid crystals and macroscopic assembled fibres.* Nat Commun., 2011. **2**: p. 571.

17. Yousefi, N., et al., *Self-alignment and high electrical conductivity of ultralarge graphene oxide-polyurethane nanocomposites.* J. Mater. Chem., 2012. **22**: p. 12709-12717.

18. Krishnan, D., et al., *Energetic graphene oxide: Challenges and opportunities.* Nano Today, 2012. **7**(2): p. 137-152.

19. Bergin, S.D., et al., *New Solvents for Nanotubes: Approaching the Dispersibility of Surfactants.* J. Phys. Chem. C, 2009. **114**(1): p. 231-237.

20. Dimiev, A.M., L.B. Alemany, and J.M. Tour, *Graphene Oxide. Origin of Acidity, Its Instability in Water, and a New Dynamic Structural Model.* ACS Nano, 2013. **7**(1): p. 576-588.

21. Medhekar, N.V., et al., *Hydrogen bond networks in graphene oxide composite paper: structure and mechanical properties.* ACS Nano, 2010. **4**(4): p. 2300-2306.

22. Southall, N.T., K.A. Dill, and A.D.J. Haymet, *A View of the Hydrophobic Effect.* The Journal of Physical Chemistry B, 2001. **106**(3): p. 521-533.

23. Chandler, D., *Interfaces and the driving force of hydrophobic assembly.* Nature, 2005. **437**(7059): p. 640-647.

24. Meyer Emily E., Rosenberg Kenneth J., and Israelachvili Jacob, *Recent progress in understanding hydrophobic interactions.* PANS, 2006. **103**(43): p. 8.

25. Greaves, T.L., A. Weerawardena, and C.J. Drummond, *Nanostructure and amphiphile self-assembly in polar molecular solvents: amides and the "solvophobic effect".* Physical Chemistry Chemical Physics, 2011. **13**(20): p. 9180-9186.

26. Ray, A., *Solvophobic Interactions and Micelle Formation in Structure Forming Nonaqueous Solvents.* Nature, 1971. **231**(5301): p. 313-315.

27. Akhter, M.S., *Studies on solvophobic interactions and micelle formation in non aqueous solvents.* Colloids and Surfaces A: Physicochemical and Engineering Aspects, 1999. **150**(1–3): p. 25-30.

28. Evans, D.F., et al., *Micelle formation in ethylammonium nitrate, a low-melting fused salt.* Journal of Colloid and Interface Science, 1982. **88**(1): p. 89-96.

29. Greaves, T.L. and C.J. Drummond, *Ionic liquids as amphiphile self-assembly media.* Chemical Society Reviews, 2008. **37**(8): p. 1709-1726.

30. Withers, N., *Graphene oxide: Surfactant sheets.* Nat Chem, 2010.

31. Kim, J., et al., *Graphene Oxide Sheets at Interfaces.* J. Am. Chem. Soc., 2010. **132**(23): p. 8180-8186.

32. Ray, A., *Micelle formation in pure ethylene glycol.* Journal of the American Chemical Society, 1969. **91**(23): p. 6511-6512.

33. Greaves, T.L., et al., *Many Protic Ionic Liquids Mediate Hydrocarbon-Solvent Interactions and Promote Amphiphile Self-Assembly.* Langmuir, 2006. **23**(2): p. 402-404.

34. Evans, D.F., *Self-organization of amphiphiles.* Langmuir, 1988. **4**(1): p. 3-12.

35. Lee, W.B., R. Mezzenga, and G.H. Fredrickson, *Anomalous Phase Sequences in Lyotropic Liquid Crystals.* Physical Review Letters, 2007. **99**(18): p. 187801.

36. del Mar Graciani, M., et al., *Water−N,N-Dimethylformamide Alkyltrimethylammonium Bromide Micellar Solutions: Thermodynamic, Structural, and Kinetic Studies.* Langmuir, 2005. **21**(8): p. 3303-3310.

37. Moulton, S.E., et al., *Liquid Crystal Behaviour of Single-Walled Carbon Nanotubes Dispersed in Biological Hyaluronic Acid Solutions.* J. Am. Chem. Soc., 2007. **129**(30): p. 9452-9457.

38. Badaire, S., et al., *Liquid Crystals of DNA-Stabilized Carbon Nanotubes.* Advanced Materials, 2005. **17**(13): p. 1673-1676.

39. Song, W., I.A. Kinloch, and A.H. Windle, *Nematic Liquid Crystallinity of Multiwall Carbon Nanotubes.* Science, 2003. **302**(5649): p. 1363.

40. Zhang, S., I.A. Kinloch, and A.H. Windle, *Mesogenicity Drives Fractionation in Lyotropic Aqueous Suspensions of Multiwall Carbon Nanotubes.* Nano Letters, 2006. **6**(3): p. 568-572.

41. Davis, V.A., et al., *True solutions of single-walled carbon nanotubes for assembly into macroscopic materials.* Nat. Nanotechnol., 2009. **4**(12): p. 830-834.

42. Ericson, L.M., et al., *Macroscopic, neat, single-walled carbon nanotube fibers.* Science, 2004. **305**(5689): p. 1447-1450.

43. Sun, Z., et al., *Effects of Ambient Conditions on Solvent−Nanotube Dispersions: Exposure to Water and Temperature Variation.* J. Phys. Chem. C, 2009. **113**(4): p. 1260-1266.

44. Chiang, I.W., et al., *Purification and Characterization of Single-Wall Carbon Nanotubes.* The Journal of Physical Chemistry B, 2001. **105**(6): p. 1157-1161.

45. Hegmann, T., H. Qi, and V. Marx, *Nanoparticles in Liquid Crystals: Synthesis, Self-Assembly, Defect Formation and Potential Applications.* Journal of Inorganic and Organometallic Polymers and Materials, 2007. **17**(3): p. 483-508.

46. Lagerwall, J., et al., *Nanotube Alignment Using Lyotropic Liquid Crystals.* Advanced Materials, 2007. **19**(3): p. 359-364.

47. Lagerwall, J.P.F. and G. Scalia, *Carbon nanotubes in liquid crystals.* Journal of Materials Chemistry, 2008. **18**(25): p. 2890-2898.

48. Lynch, M.D. and D.L. Patrick, *Organizing Carbon Nanotubes with Liquid Crystals.* Nano Letters, 2002. **2**(11): p. 1197-1201.

49. Zeng, Q., et al., *Self-Assembled Graphene–Enzyme Hierarchical Nanostructures for Electrochemical Biosensing.* Adv. Funct. Mater., 2010. **20**(19): p. 3366-3372.

50. Sweetman, L.J., et al., *Synthesis, properties and water permeability of SWNT buckypapers.* Journal of Materials Chemistry, 2012. **22**(27): p. 13800-13810.

51. Dikin, D.A., et al., *Preparation and characterization of graphene oxide paper.* Nature, 2007. **448**(7152): p. 457-460.

52. Park, S., et al., *Graphene oxide sheets chemically cross-linked by polyallylamine.* J. Phys. Chem. C, 2009. **113**(36): p. 15801-15804.

53. Park, S., et al., *Graphene Oxide Papers Modified by Divalent Ions—Enhancing Mechanical Properties via Chemical Cross-Linking.* ACS Nano, 2008. **2**(3): p. 572-578.

54. Chen, H., et al., *Mechanically strong, electrically conductive, and biocompatible graphene paper.* Adv. Mater., 2008. **20**(18): p. 3557-3561.

55. Xu, Z., et al., *Ultrastrong Fibers Assembled from Giant Graphene Oxide Sheets.* Advanced Materials, 2013. **25**(2): p. 188-193.

56. Kozlov, M.E., et al., *Spinning solid and hollow polymer-free carbon nanotube fibers.* Adv. Mater., 2005. **17**(5): p. 614-617.

57. Podsiadlo, P., et al., *Ultrastrong and Stiff Layered Polymer Nanocomposites.* Science, 2007. **318**(5847): p. 80-83.

58. Shim, B.S., et al., *Transparent Conductors from Layer-by-Layer Assembled SWNT Films: Importance of Mechanical Properties and a New Figure of Merit.* ACS Nano, 2010. **4**(7): p. 3725-3734.

59. Olek, M., et al., *Layer-by-Layer Assembled Composites from Multiwall Carbon Nanotubes with Different Morphologies.* Nano Letters, 2004. **4**(10): p. 1889-1895.

60. Shin, M.K., et al., *Synergistic toughening of composite fibres by self-alignment of reduced graphene oxide and carbon nanotubes.* Nat Commun, 2012. **3**: p. 650.

61. Ballard, D.G.H. and G.R. Rideal, *Flexible inorganic films and coatings.* Journal of Materials Science, 1983. **18**(2): p. 545-561.

62. Reynolds Iii, R.A. and R.A. Greinke, *Influence of expansion volume of intercalated graphite on tensile properties of flexible graphite.* Carbon, 2001. **39**(3): p. 479-481.

63. Leng, Y., et al., *Influences of density and flake size on the mechanical properties of flexible graphite.* Carbon, 1998. **36**(7–8): p. 875-881.

64. Steinmetz, J., et al., *Production of pure nanotube fibers using a modified wet-spinning method.* Carbon, 2005. **43**(11): p. 2397-2400.

65. Dalton, A.B., et al., *Super-tough carbon-nanotube fibres.* Nature, 2003. **423**(6941): p. 703-703.

66. Aboutalebi, S.H., et al., *Enhanced Hydrogen Storage in Graphene Oxide-MWCNTs Composite at Room Temperature.* Adv. Energy Mater., 2012. **2**(12): p. 1439-1446.

67. Titelman, G.I., et al., *Characteristics and microstructure of aqueous colloidal dispersions of graphite oxide.* Carbon, 2005. **43**(3): p. 641-649.

Chapter 10: Multi-Step Multi-Level Self-Organization of 1D Nanoparticles: Towards Stigmergic Emergent-Intelligence

10.1 Building self-ordered complex systems

The inherent anisotropic properties of nano-scale building blocks, if harnessed, can enable the fabrication of conceptually complex self-organized macro-architectures. [1-9] Nature elegantly utilizes simple design principles to autonomously organize basic components into ordered, spatiotemporal complex patterns over a wide–range scale from the cosmic down to microscopic structures. [10-15] Arrangements with higher complexity can be generated from intricate orchestration of multi-step multi-level replications in response to subtle interplay of a multitude of interactions. However, natural processes are limited in a number of ways. To build such complex systems, it is vital to impose self-constraining elements to limit the system in its growth. To overcome such a challenge, nature combines its powerful design concepts with stigmergic intelligence as a self-limiting mechanism. [10-15] Stigmergy is the collective response of individual basic components of a system in response to the modification of the local environment that triggers a specific behaviour in the system. [15] Inspired by natural systems, great scientific interest has been focused on mimicking the biological systems to fabricate ordered materials and self-assembling devices. [1-4,16-18] To achieve such structural arrangements and patterns, many

biological systems implement anisotrpic building blocks and their related liquid crystalline (LC) properties to induce order into the system. LCs are often used in macromolecular domains to engineer architecturally designed materials. Regulating the interaction between the constituent building blocks, which is dictated by the overall macroscopic LC behaviour of the system, results in a system with intrinsic order which possess a unique mobility from the molecular to the macroscopic level imparted by the LCs itself. [5,7,19-22] As such, nematic liquid crystals (nematic LCs) have been used across a wide-range of disciplines to prepare self-ordered architectures. [6-8,19,23] However, nematic liquid crystals exhibit the lowest level of order which in turn limits their use to the fabrication of simple 3D architectures.

To achieve more complex multifunctional architectures, therefore, one needs to achieve higher ordered liquid crystalline phases such as biaxial phases. The biaxial phase, which has two main order directors, if achieved, can lead to multilevel self-organization of particles which are in principle hard to achieve. Moreover, if the biaxial phase can be achieved in a multicomponent system of dimensionally different materials, such as a mixture of 1D and 2D building blocks, can trigger the formation of self-constraint elements in the system as the dimensionally different materials tend to behave differently to local environmental stimuli. This challenge, if solved, could provide fundamental scientific and industrial opportunities giving rise to a generation of new exciting self-assembled materials. [5,19,24-27]

10.2 The aim of the present chapter

In the present chapter, a novel versatile strategy to fabricate highly ordered complex 3D architectures starting from biaxial liquid crystals is introduced and experimentally demonstrated.

As a proof of concept, high throughput individual dispersion, and alignment of one dimensional SWNTs in organic media containing ultra large two dimensional graphene oxide (GO) sheets is demonstrated while keeping high loadings of SWNTs (up to 80 wt%) intact. The stigmergic-emergent coordination of 2D and 1D nanoparticles, which can be triggered by mechanical stimuli, allows indirect communication between components through the modification of local environment leading to self-driven morphogenesis. It is shown that these dispersions can produce robust, self-organized LC gel networks comprising of a multi-level, multi-step self-organization. The as-prepared LC gels were then used to fabricate highly ordered self-assembled 3D architectures with an order parameter of S=0.87. These 3D architectures exhibited a remarkable three-fold increase in electrochemical capacitance in comparison with their non-aligned counterparts. We demonstrate that this phenomenon is scale-independent and can be utilized for self-constructing and manufacturing systems.

10.3 Spontaneous biaxial nematic liquid crystal phase formation

Morphology and geometry of individual building blocks play a crucial role in self-assembly science. By regulating inter and intra-particle interactions, final architectural design with precise structural control can be envisioned. However, to achieve such precise control over structural design and consequently final properties, anisotropic building blocks are needed to facilitate the design on-demand process. Ideally, the intricate orchestration of the geometric anisotropy of building blocks with tailored functionalities can serve as an enabling platform to direct interactions between multiple components and in practice assist their self-organization. [5,28] In this regard, the anisometric shape of rod-like and disk-like particles, as the most basic anisotropic building blocks, if combined with amphiphilic behaviour, can induce guided spontaneous self-assembly

driven morphogenesis into engineered long-range-ordered, layer-by-layer 3D architectures. It is long-predicted, but never experimentally realized, that in a mixture of rods and disks, the entropy-driven configuration as a result of the competition between excluded volumes of these distinct particles can lead to biaxial nematic phase resulting in mutual orientation and consequently self-organization of the whole system. [29] These biaxials exhibit two axes of symmetry compared with uniaxial nematic phase (major n and minor m directors).

Inspired by this idea, we introduced small amount of ultra-large graphene oxide (ULGO) dispersions as a model 2D disk-like particle to high quality dispersions of SWNTs as a model 1D rod-like particle in an organic solvent (see experimental section for more details). The final dispersion can, in theory, support the formation of biaxial phase (see schematic in Figure 10.1). Both pure dispersions at these concentrations showed no traces of LC behaviour and were fully isotropic. [20,33] However, the mixture exhibited birefringence beahviour typical of nematic liquid crystals. Typically, the requirement for a SWNTs LC dispersion is that high solute concentration is needed. However, the concentration of SWNTs was at least fifty folds less than the experimentally reported critical concentration (~40 mg ml^{-1} for SWNTs in superacids) required for the complete formation of nematic phase. [20,33,37-39]

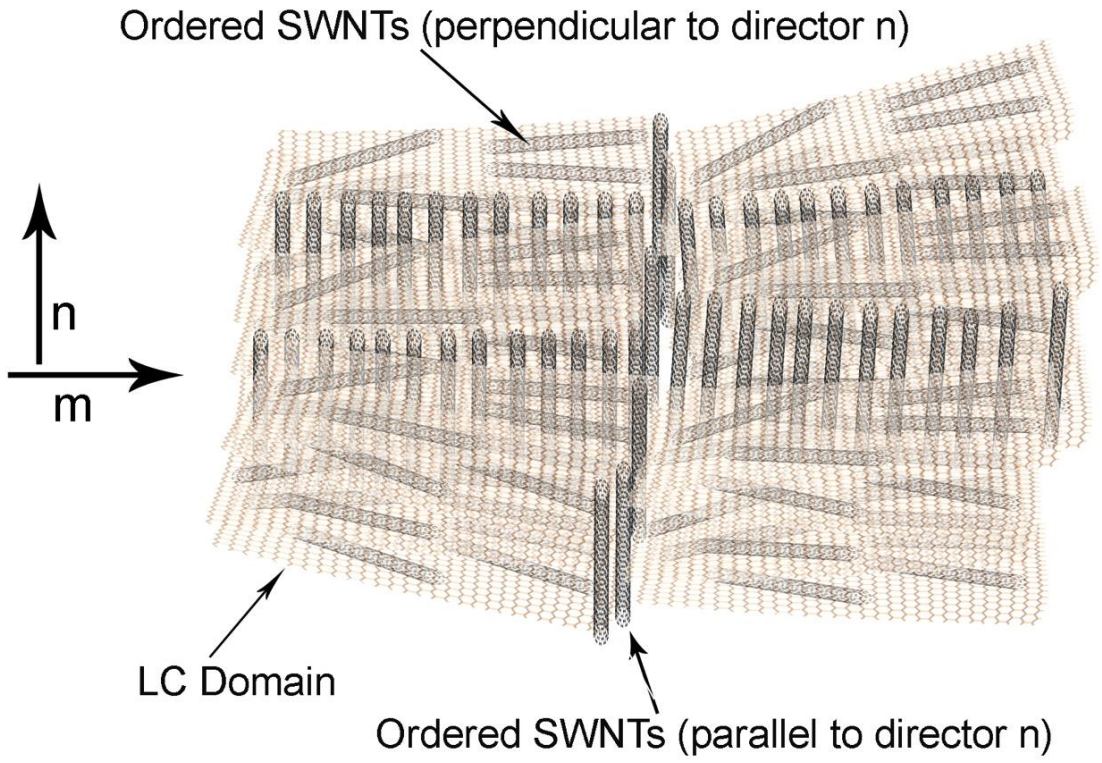

Figure 10. 1. Proposed schematic illustration for the evolution of biphasic nematic phase. SWNTs can be ordered either perpendicular to director n or parallel to director n. As we are employing ultra large graphene oxide, the configuration depends on how SWNTs arrange themselves on GO surface. It should be noted that GO is an amphiphile. [30,31] This amphiphilic behaviour, which is more pronounced in the case of ULGO, can facilitate its interaction with SWNTs and other particles and trap them on its surface. [20,21,32-36]. Therefore, the system ends up with tube alignments both parallel to the n director and perpendicular to n, resulting in the introduction of another director (m).

The high quality of the final dispersion was evidenced by the well-resolved inter-band transitions observed in UV/Vis–near-IR absorption spectrum (Figure 10.2a) which are only observable in the absecence of nanotube aggregation. [40,41] This observation verifies that ULGO stabilized

SWNTs do not form bundles in response to strong van der Waals interactions between tubes. In solution, SWNTs are commonly stabilized through short-range repulsive interactions coming from steric hindrance and electrostatic interactions from a surfactant-like dispersant. [21,33,34,42] In this case, the highly charged surface profile of ULGO, in combination to the higly planar sheets of the ULGO acts like a templating surfactant where by the SWNTs sp^2 functionality interacts with the ULGO sheet. This high quality dispersion was then characterised by polarized optical microscopy (POM). [20,38,39,43] Figure 2b, shows POM micrograph of the as-prepared material representing birefringence typical of lyotropic nematic liquid crystals under crossed polarizers. Therefore, the addition of such a small amount of ULGO promoted the formation of nematic phase in low concentration SWNT dispersions. This low concentration (0.8 mg ml^{-1} for SWNTs or 1 mg ml^{-1} for the overall carbonaceous materials) holds great promises that can enable a platform for a wide range of formulations of LC SWNTs with different materials such as graphene, metallic based particles and polymers that are not accessible in at low dispersion concentrations due to the viscosity limitation requirements typically required for nematic phase formation.

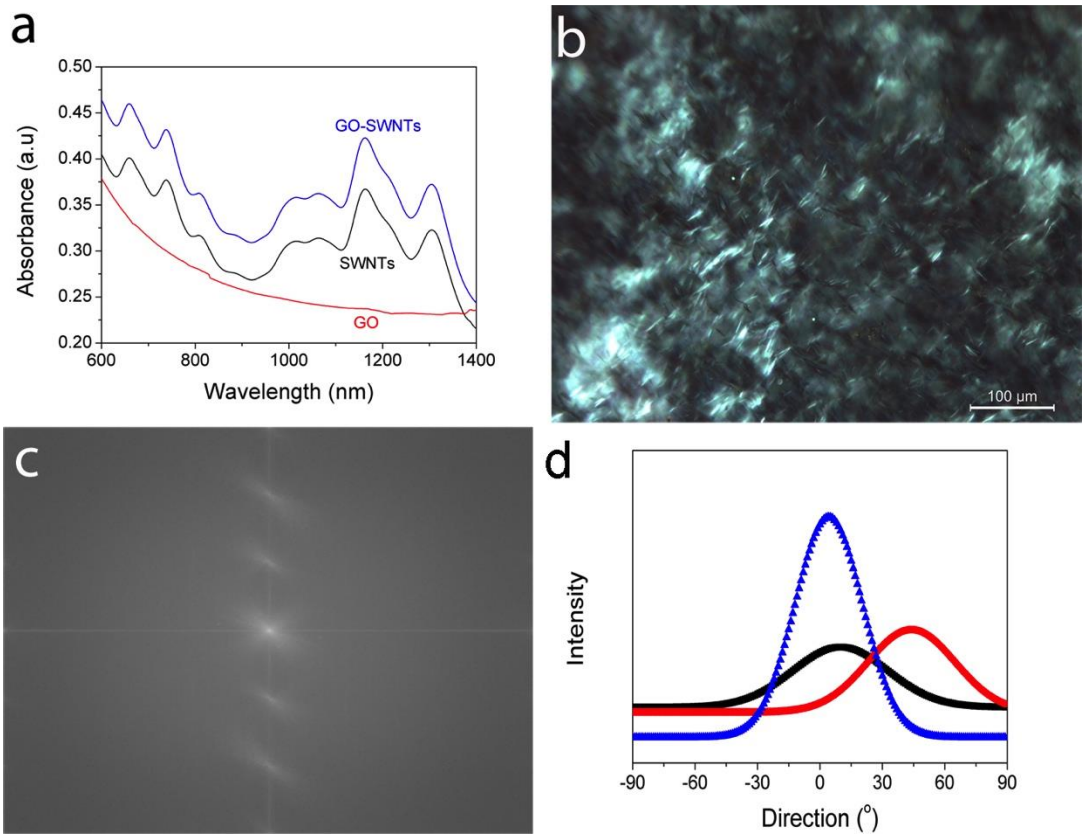

Figure 10. 2. Optical characterization of as-prepared hybrid LC. (a) UV/Vis–near-IR absorption spectrum of GO, SWNTs and GO-SWNTs, showing well-resolved inter-band transitions corresponding to SWNTs suggesting high quality individually dispersed nature of as prepared final material. (b) Polarized optical micrograph of the hybrid dispersion showing birefringence typical of liquid crystals. (c) Fast Fourier transform (FFT) transform of (b) resulting in a frequency domain micrograph. The transform image shows three distinct dominating directions in the Fourier transform: the DC-value and, as the Fourier image is symmetrical to its centre, two zones corresponding to the frequency of the patterns in the original micrograph originating from regular patterns in the micrograph. d) Directionality histogram of the POM micrograph computed based on local gradient orientation method using HOG descriptors showing three distinct alignment directions. HOG descriptors are known to outperform other algorithms for the determination of

orientations. Since HOG descriptors operate on localized cells, they can bypass variations in geometric and photometric transformations, except for object orientation, ensuring their superior performance.

In contrast to simple nematics, which exhibit a single preferred axis around which the system is rotationally symmetric, our as-prepared LC phase exhibits three distinct optical axes. To quantitatively measure the alignment direction, we developed two protocols based on fast Fourier transform and local gradient orientation methods. FFT frequency domain images demonstrate the existence of three distinct optical axes in the hybrid dispersion typical of biaxial liquid crystals (Figure 10. 2c) in contrast to a simple nematic LC GO (Figure 10.3). Histogram of oriented gradients (HOG) [44] for our as-prepared hybrid dispersions are presented in Figure 10. 2d. The histograms also verify the existence of three preferred orientations in the hybrid phase. This fundamentally suggests that there are three local minima in the potential energy landscape of the interactions among particles in the system (GO-GO, SWNTs - SWNTs, GO- SWNTs).

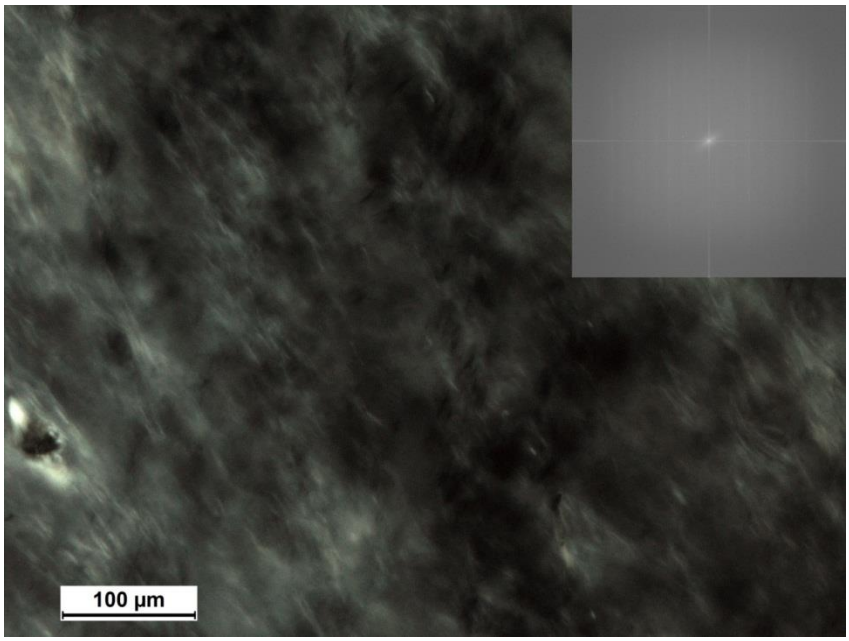

Figure 10. 3. Polarized optical micrograph of GO dispersion showing birefringence typical of liquid crystals. The inset shows Fast Fourier transform (FFT) transform resulting from a frequency domain micrograph. The transform image shows only one distinct dominating direction in the Fourier transform: the DC-value originating from regular patterns in the micrograph.

To get a better understanding on the nature of the interactions involved, we performed rheological studies on the samples. The existence of these local minima states can be verified by simply plotting shear stress and viscosity vs. shear rate and check the rheological response of nematogens as opposed to simple GO and SWNTs dispersions. If such states are present in the system, we can simply observe them by applying enough energy to break down these states (i.e. subjecting the system to macroscopic hydrodynamics or high rates of deformation). Figure 10.4a(iii) and Figure 10.4b(iii) show the consequential flow behaviour of the hybrid nematogens responding to macroscopic hydrodynamics (high rates of deformation). The system exhibited a yield value (the lowest shear stress necessary to produce viscous flow) that was typical of non-Newtonian fluids. Typically in the early shear stage, the system needs to overcome a certain yield value to be able to

flow readily. However, in this system two other shear stress barriers need to be broken (as indicated on the flow measurements curve) before the system can respond linearly to the shear strain. This multi-step response suggests the existence of a stigmergic-emergent behaviour, in which, the work executed by one component leaves traces behind that stimulates the performance of another action by the same/different component. Therefore, in a step-by-step process the system adapts itself to the local stimuli leading to a multi-step self-assembly process.

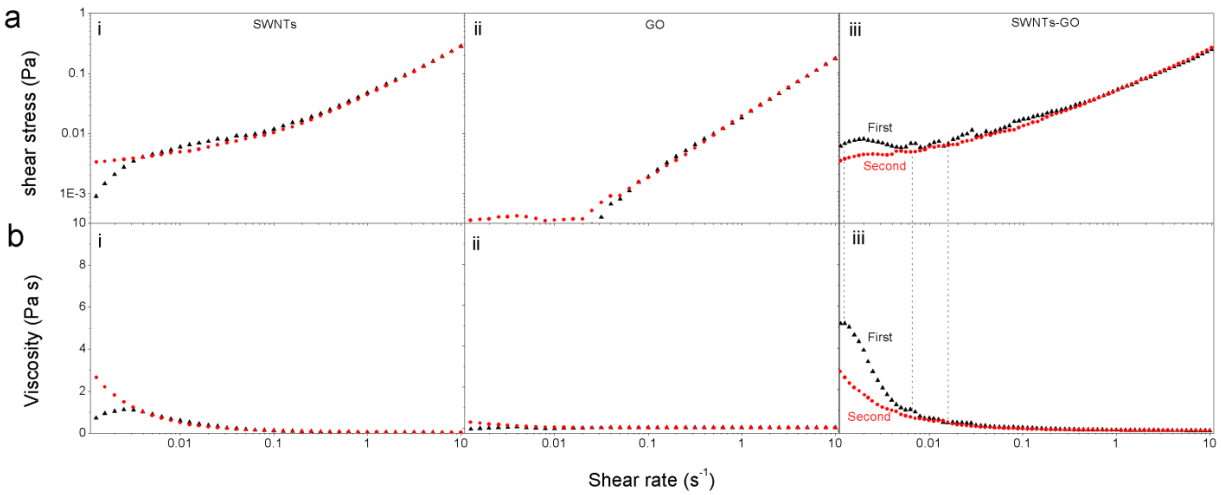

Figure 10. 4. Rheological response of SWNTs, GO and hybrid dispersions and subsequent orientation and processing. a and b)Shear stress and viscosity vs. shear rate. Apart from the very initial yield value, on applying shear to nematogens (a (iii)), two other distinct regions can be observed as marked. These distinct yield values correspond to different local minima energy states resulting from preferred orientations in the system. This further confirms the first experimental realization of the occurrence of biaxial LC phase by the use of mixtures of classical rodlike mesogens (SWNTs) and disk-like discotic mesogens (ULGO) which have been remained elusive, up to now. After overcoming these energy barriers, the inter-locked nematic domains are unlocked and can be aligned and ordered along the shear field direction.

The first measurement on the flow curve denotes such assembly as a shear-induced alignment in the system corresponding to that of an aligned sample. It shows that the shear stress serves as a trigger, which modifies the local environement leading to the alignment of the components in the direction of shear in an attempt to collectively respond to this stimuli. After repeating the flow measurements, the same behaviour with offsetted yield values was observed suggesting shear-induced history. This characteristic history dependency of the system, was also observed in the viscosity vs shear strain curve. However, if such a stigemtgic-emergent intelligence exists in the system, it should also manifest itself in the medium in which the components are present. Therefore, the overall collective behaviour of the meduim before and after being subejected to shear should also transform to contribute to the components behaviour. So can we observe such a phase change in the system before and after shear?

To answer this question and learn more about the nature of this behaviour, we measured the angular frequency response of elastic G' (storage) and viscous G" (loss) moduli of the dispersions at a constant strain amplitude of 0.1 both before shearing the sample and then afterwards (Figure 10.5).

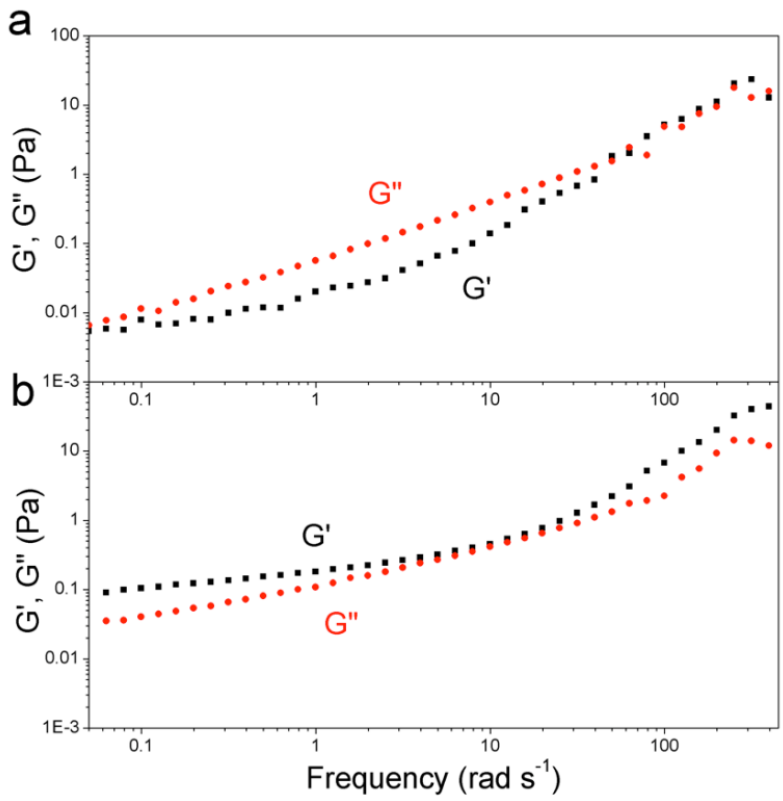

Figure 10. 5. Storage and loss moduli of the suspensions as function of frequency. In contrast with the sample that had not been subjected to any shear (a), the storage modulus is dominant in the pre-sheared sample (b). This suggests that upon shearing the sample, a semi-permanent gel-like phase forms. Quite interestingly, even at very short timescales, no cross over point can be observed suggesting the robustness of our as-prepared gel phase. This observance further verifies that local rules of interaction evolve spatiotemporally within the system and are indeed history dependant.

In the sample not subjected to pre-shearing (not experiencing any past actions), towards the low frequency region (long time-scales), a considerable elastic component exists which is in the order of viscous moduli, if not higher (Figure 10.5a). This behaviour suggests the possibility of a network structure which is the direct result of the dynamic association of mesogenic groups guiding the viscoelastic behaviour and is consistent with the observation of yield point at this

region. Therefore, over extremely long-time scales, GO dispersions respond more like a viscoelastic soft solid. However, in intermediate time scales, G' was found to be lower than G" suggesting a dominant viscoelastic liquid-like behaviour implying that dynamic short rearrengements can occur in the system. As the frequency increases (at very short-timescales and towards the high frequency region), G' overtakes G" at a specific point suggesting a dominant elastic behaviour (solid). Nevertheless, the difference is subtle and the zones are not well-defined. For the pre-sheared sample, however, quite interestingly, even at this very low concentration (0.8 mg ml^{-1} for SWNTs and 1 mg ml^{-1} for the whole system), over all time-scales, the dispersion exhibited a solid-like response with G' being higher than G" suggesting a viscoelastic solid like behaviour (Figure 10.5b). This behaviour suggests the formation of an out-of-equilibrium gel-like phase. It is interesting to note that upon applying even a very small shear to the sample, the system undergoes a phase transformation towards metastable gel phase at all time-scales studied here, in contrast to the gel formation of SWNTs in ionic systems which is restricted to very short time-scales. [28] Moreover, as this phase is a metastable phase, even a simple agitation can relax back the sytem towards the non-gel like phase which is not yet seen in other colloidal systems.

The measured elastic modulus was also considerably higher (~one order of magnitude) than the measured elastic modulus of the non-sheared suspension at the same concentration. [45] We assume that the hybrid system forms a semi-permanent tenuous solid network with a very dominant elastic part in spite of the concentration range we are working in. At this region, the elastic modulus, although dominant, is frequency dependant. This prevents the stress relaxation on the longest time-scale of the measurement as a result of particles being trapped by their neighbours (either SWNTs or GO sheets). As the relaxation towards equilibrium state is restricted, this suggests the formation of kinetic arrest of out-of equilibirum system leading to metastable gel.

[46] Soft glassy materials or Cells show this generic behaviour. [45] Also, in contrast to most polymer gels, [45] both storage and loss moduli increase with frequency (Figure 10.5 b). Another consequence of this stable gel-like behaviour is the inability of these dispersions to reorganise themselves even in very short time-scales. This offers, in principle, control over the structure of the final phase as the system is trapped in metastable kientic traps (dynamic arrest) and then cannot relax towards randomized state. The dynamics of the formation of such gel-like systems is completely different from ordinary LC GO or LC SWNTs dispersions, in none of which, stable LC gels can be formed unless going to much higher concentrations. [47]

At the initial stage, the addition of ultra large flexible GO sheets to the system gives rise to interesting possibilities. GO and SWNTs can interact via both π-π interactions and patchy interactions, a direct consequence of the existence of multifunctional oxygen based groups on the surface of GO sheets, as previously demonstrated by our group. [21,34] This introduces an interesting constraint to the system. The bonding of SWNTs and GO can adversely affect the flexibility of GO while introducing a large packing entropy as a result of a large number of energy positions available to the system based on GO-SWNTs planar configurations (attractive interactions, π-π interactions, steric hinderance, etc), as depicted in Figure 10.6. Therefore, the greater positional order in our case will be entropically favorable. In the nematic phase, the overall system of particles (GO with neighbouring SWNTs) must be more or less parallel to the director, which leads to a considerable loss in configurational entropy and consequently dynamic arrest of particles in the system leading to LC gel formation (Figure 10.6).Moreover, the introduction of shear force, enables us to further manipulate the architecture and fabricate structures with higher complexity and order, as evidenced by rheological response which demonstrates the formation of arrested gel phase in the system. At the final stage, the dynamic modification of viscocity which

results from the local generation of directed internal forces effectuates the evolution of control elements in spatiotemporal mechanics of the system leading to self-driven morphogenesis.

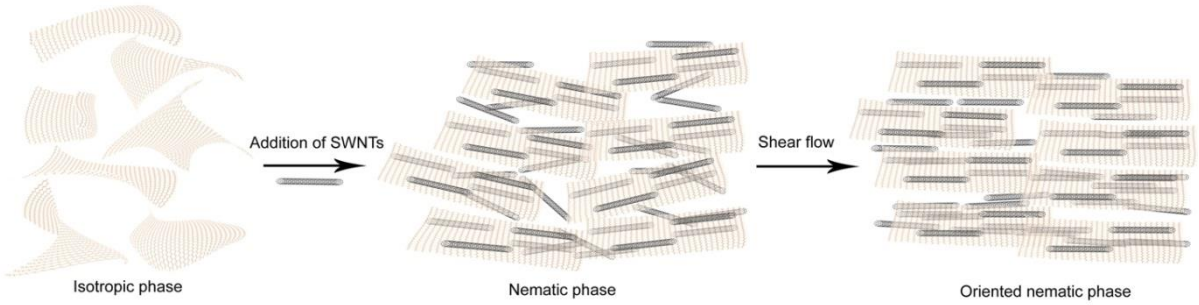

Figure 10. 6. Schematic illustrations of the proposed model for the evolution of LC phase and subsequent orientation upon being subjected to shear. In our multicomponent system, self-organization involves a multi-level multi-step self-assembly, and self-driven morphogenesis. In the very first step, self-assembly is associated with spontaneous formation of liquid crystals as a consequence of the position control of components relative to each other representing passive cooperative stigmergy, in which both GO and SWNTs alter their configuration such that the configurational changes made by the other is also modified. At higher level, self-driven morphogenesis, analogous to biological systems, happens, in which, as a response to mechanical stimulation, spatiotemporal evolution of positional order happens leading to morphogenesis in the system and acquiring anisotropic shape-specific properties. This, therefore, suggests that the as-prepared samples have undergone self-assembled arrested-like states in energetically favourable metastable states.

It should be noted that the amount of shear stress required to produce an aligned sample is very low, ca. less than 0.1 Pascal (see Figure 10.5), therefore, even subjecting the sample to the shear field produced as a result of dropping a droplet with a simple dropper is more than enough to induce alignment in the sample. To further verify this hypothesis, we employed polarized Raman

spectroscopy on LC droplets to quantify the degree of alignment. According to Onsager's prediction, for hard rigid and infinitely long rods, the orientational order parameter, S (Equation1), is expected to be 0.79. Perfect alignment is expected to afford an order parameter of 1. The order parameter for a three-dimensional system can be calculated following equation 10.1. [48]

$$\boldsymbol{S} = \frac{(\mathbf{3}\cos^{\mathbf{2}}\boldsymbol{\theta}-\mathbf{1})}{\mathbf{2}} \tag{10.1}$$

However, for most SWNTs LCs, this order parameter cannot be calculated due to topological defects. The order parameter, S, can also be related to absorption anisotropy through equation 10.2.

$$\boldsymbol{S} = \frac{(\boldsymbol{\Delta}-\mathbf{1})}{(\boldsymbol{\Delta}+\mathbf{2})} \tag{10.2}$$

Where Δ is the absorption anisotropy. Taking into account that the transition moment of SWNTs is along the tube axis, we can use equation 2 to approximate the order parameter. In the case of GO/ SWNTs hybrids, equation 2 can be rewritten as equation 10.3 accounting for the Raman dichroic ratio (see supporting information for more details); [26]

$$\boldsymbol{D} = \frac{\mathbf{2}\boldsymbol{I_{pk}}-\boldsymbol{I_p}}{\boldsymbol{I_p}} \tag{10.3}$$

Where, I_{pk} is the Raman intensity in light polarization perpendicular to k (k is the axis perpendicular to director n) and I_p is the Raman intensity in light polarization perpendicular to n (nematic director). The existence of UL GO sheets in our system can afford the orientation of SWNTs over large monodomains, as illustrated in Figure1. This enabled us to measure the degree of alignment in our as-prepared liquid crystal phase (depicted in Figure 10.3). We examined the RBM (radial breathing mode) part of the spectra, observable for SWNTs but not GO, to check for the alignment (Figure 10.7a and Figure 10.8). The alignment over 2D (G') and G band was also measured. However, as GO sheets can also contribute to these peaks, they have been reported for the sake of comparison. The values for the order parameter, measured by polarized micro-Raman

spectroscopy show a remarkable value of 0.63 which is much higher than all previously reported S values such as SWNTs stabilized by strands of DNA (0.19). [43,49,50]

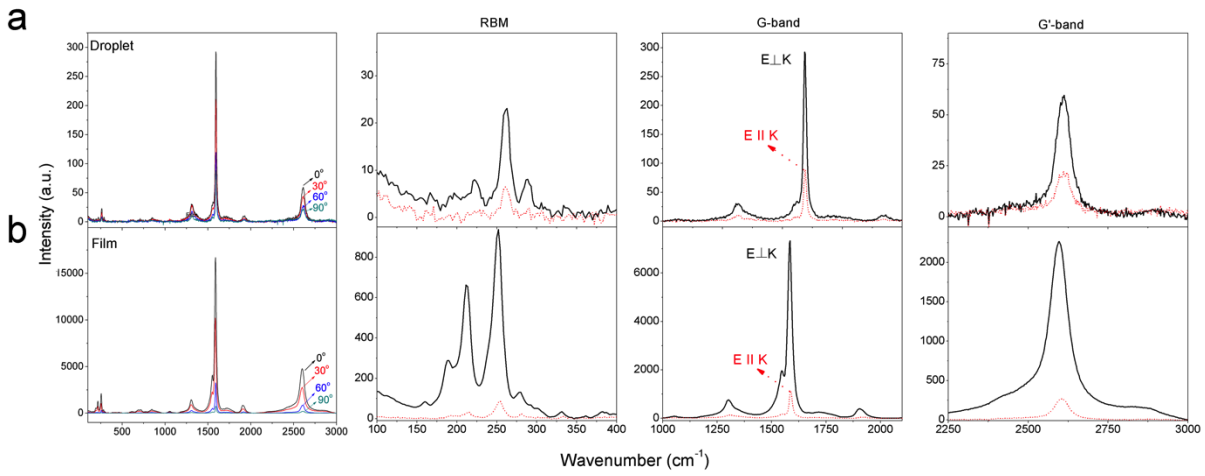

Figure 10. 7. Polarized resonant Raman characterization of the samples. Raman investigation of the overall and three specific characteristic SWNTs bands in both liquid form (a) and as-casted film (b). However, as graphene oxide shares almost the same G band with SWNTs, we mainly investigated the characteristic radial breathing mode (RBM) and G' band in both parallel and perpendicular configurations. The difference in response implies the aligned order of SWNTs.

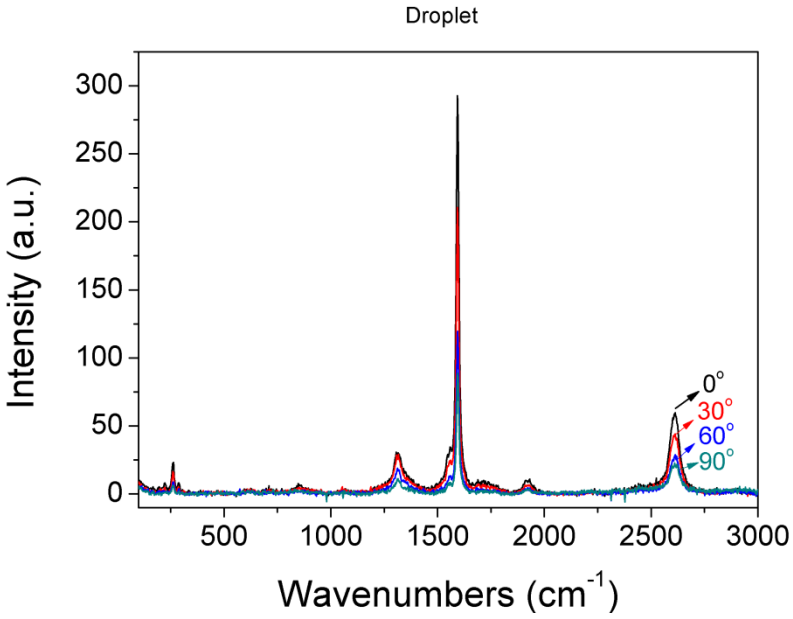

Figure 10. 8. Polarized resonant Raman characterization of the hybrid droplet.

Bearing in mind that the polarized micro Raman studies demonstrate high order parameter in the liquid state, this multi-step self-aseembly can enable further morphological manipulation by changing the timescale at which we are working towards long-time scales. As an example, these dispersions were also suitable for dry-casting or mold-casting due to the fact that at long time-scales, the material exhibits largely elastic behaviour which hinders any effective randomization as a consequence of the system being in an arrested gel state. Therefore, the high order parameter achieved in the liquid form can be preserved upon dry-casting. To examine this hypothesis we also performed polarized micro Raman studies on the as-casted dried films. These studies revealed the existence of alignment and order in our as-prepared system (Figure 10.7b and Figure 10.9 and 10.10), with orientational order higher than the liquid state, i.e. S=0.87. Such high order parameter can have significant outcomes in processing ordered nanotube systems making the manufacture of SWNT dispersions into aligned macroscopic architectures possible. This suggests that highly

ordered unlimited lengths of films can be achieved just by a routine evaporation process. Even spinning of SWNTs which require preorganization of SWNTs building blocks in LC state can be made possible.

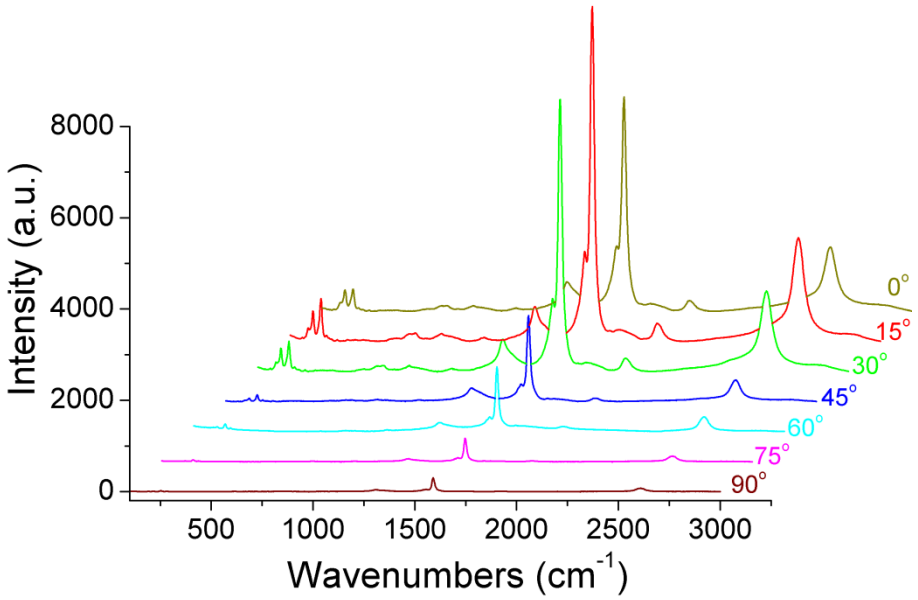

Figure 10. 9. Polarized resonant Raman characterization of the hybrid film.

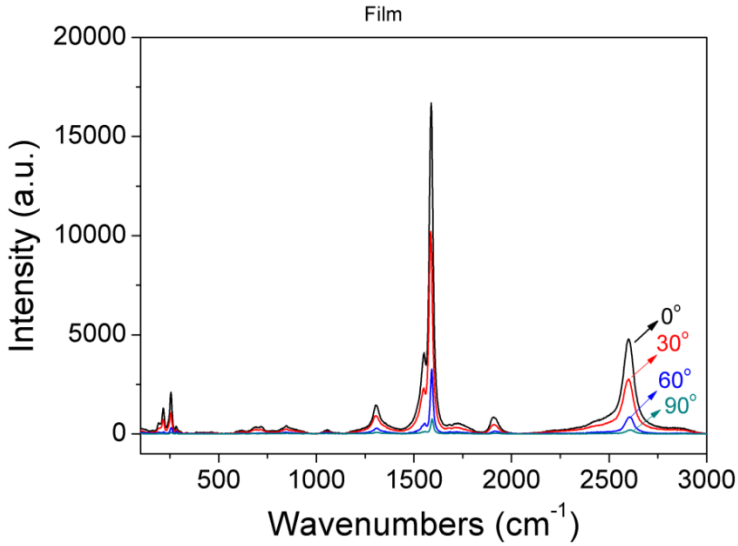

Figure 10. 10. Polarized resonant Raman characterization of the hybrid film.

As a proof of concept, both free-standing composite papers and composite films on substrates were fabricated by simple casting of dispersions and drying, as shown in Figure 10.11. SEM micrographs presented in Figure 10.11 show the aligned characteristic feature of our as-prepared architectures. Moreover, the combinatorial behaviour of SWNTs and GO sheets prevents the agglomeration and aggregation of both morphologies by preventing their restacking. In fact, GO sheets act as giant two-dimensional horizontal spacers between individual SWNTs providing long-range orientational order while simultaneously guiding the assembly of SWNTs through surface chemical functionalities. SWNTs also, in turn, inhibit uncontrolled re-stacking of GO sheets while bridging individual GO sheets, as demonstrated in cross-sectional SEM micrograph presented in Figure 10.11b. This results in the formation of a fully intercalated 3D architecture.

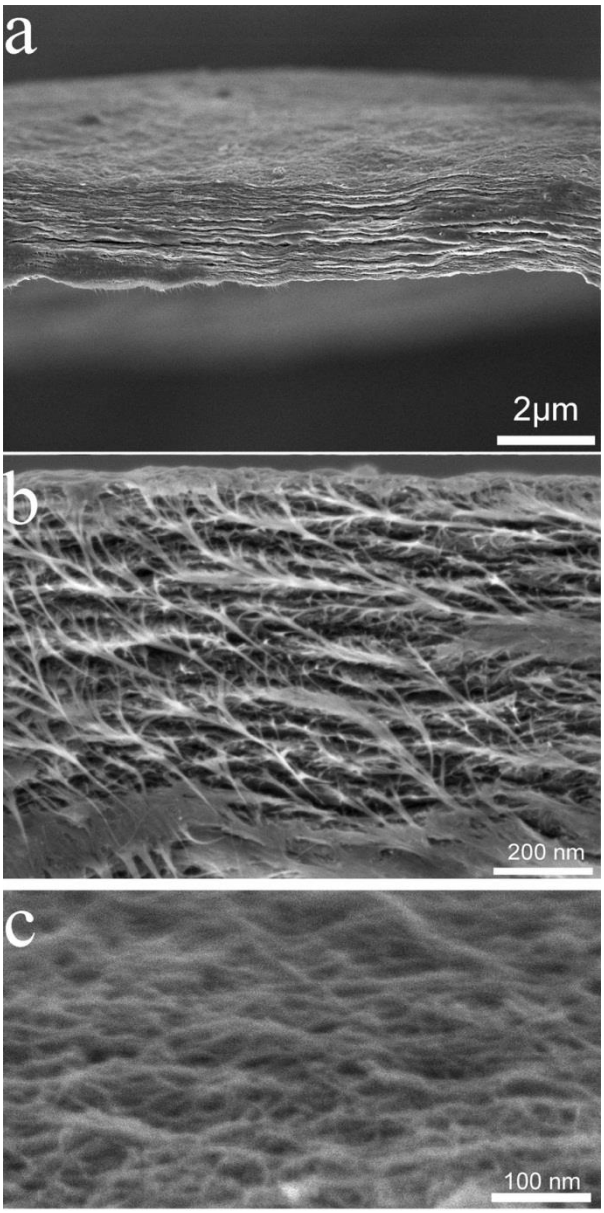

Figure 10. 11. Representative SEM micrographs of as prepared 3D architecture. (a) SEM image of the cross section of as-cast dried paper. (b) higher magnification images confirming the self-oriented nature of the system while maintaining the de-bundled nature of SWNTs intact after the fabrication. (c) SEM micrograph of the surface of the architecture.

10.4 Electrochemical performance of ordered architectures

We subsequently exploit this interesting architectural design and high alignment of nanotubes in a practical device. As a proof of concept, we prepared microsupercapacitor devices based on the engineered architecture to study the effect of nanotubes alignment on their intrinsic supercapacitive behaviour. Both entangled SWNTs film and ordered SWNTs films were evaluated in terms of electrochemical performance based on their galvanostatic charge/discharge cycling response at high current density of 10 A g^{-1} in a potential window of 1V(Figure 10. 12a). Even at this high current density, no significant deviation from triangular shape was observed. This implies the formation of an efficient electrochemical double layer (EDL) with fast ion transport indicating high rate capability of both architectures. Furthermore, the discharge curve exhibited no observable voltage drop at the initiation of the discharge curve suggesting a very low equivalent series resistance (Figure 10.12a and Figure 10.12b).

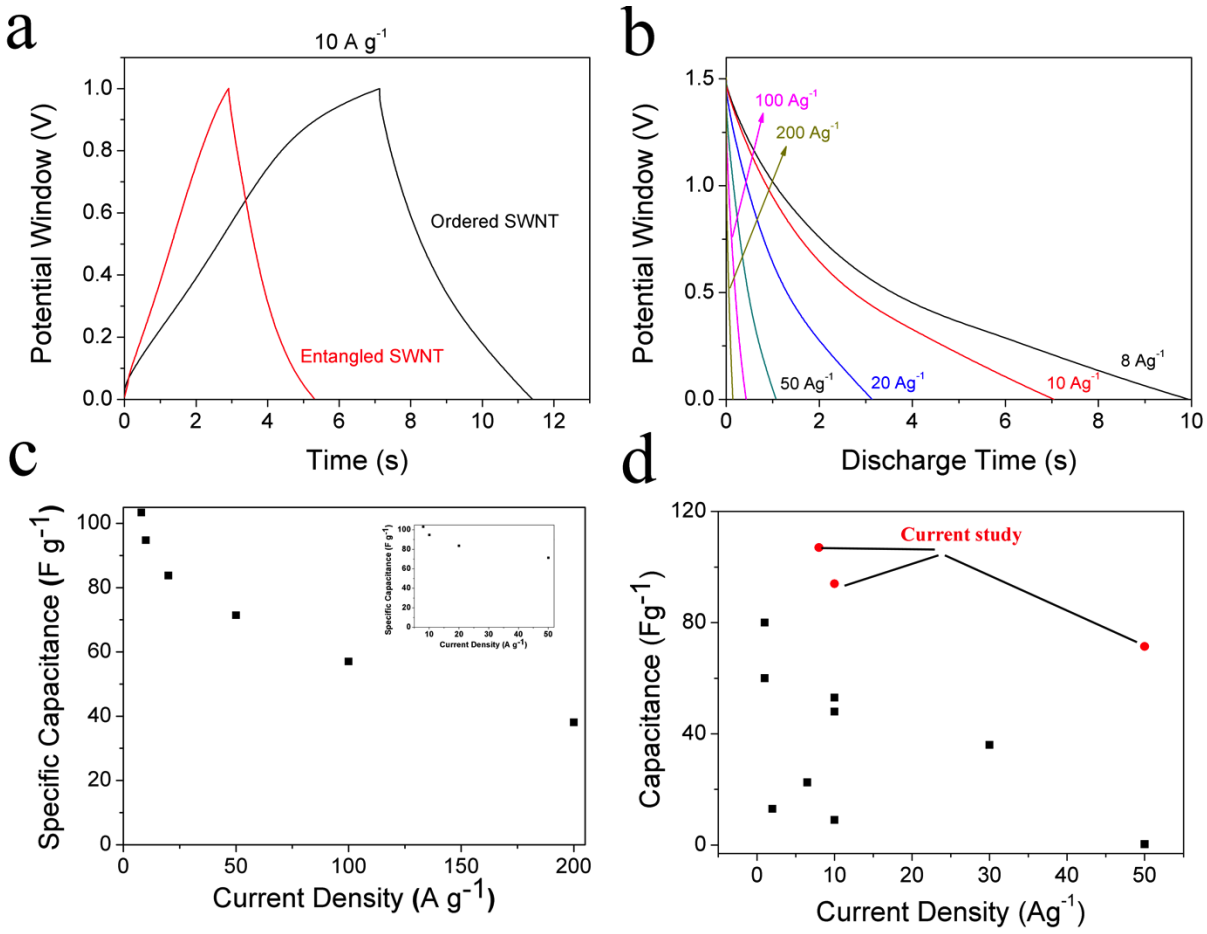

Figure 10. 12. Galvanostatic charge-discharge characterization based on two-electrode symmetrical cell configuration. (a) Galvanostatic charge-discharge curves for both entangled and ordered SWNTs at constant current density of 10 A g^{-1}. (b) Galvanostatic-Discharge curves at different current densities for the ordered sample showing the high-rate capability of the as-prepared sample. (c) Calculated specific capacitance of the ordered system at different current densities. (d) The capacitive performance of our as-prepared system compared to recent literature reports on SWNTs systems (either aligned or non-ordered) at different current densities showing the superior performance of the ordered material.

However, the system with the ordered architecture, showed superior electrochemical performance with capacitance values almost three times higher than the normal entangled SWNTs film (97 F g^{-1} vs 33.8 F g^{-1} at 10 A g^{-1} in 1V potential window, Figure 10.13).

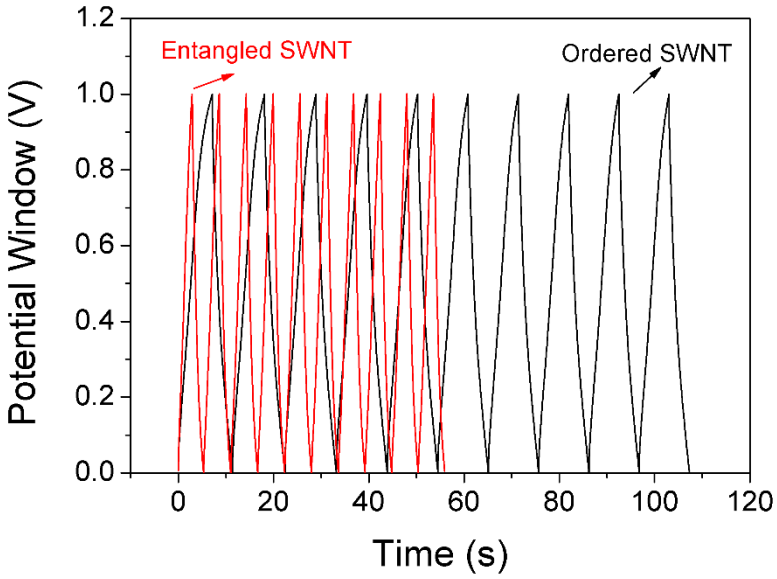

Figure 10. 13. Over-layed Galvanostatic charge-discharge curves of both entangled and ordered SWNT at 10 A g-1 in 1V potential window.

It should be noted that as SWNTs are highly anisotropic particles, the anisotrpocity of the system is also crucial for final material properties. Therefore, it is expected that the electrochemical performance characteristics of SWNTs are strongly linked to the degree of alignment as aligned /patterned structures for SWNTs can provide ease of access for solvated shells and can facilitate their incorporation into device applications. Also, the negligible iR drop at the start of the discharge curve demonstrates low ESR as also evidenced by the high native conductivity of ca. 1333 S m^{-1} of the ordered film in the perpendicular direction. The specific capacitance values for the films were calculated over a range of current densities from 8 to 200 A g^{-1} at a potential window of 1.5

V(Figure 10.12b and 10.12c and Figure 10.14). The ordered architecture continued to provide outstanding capacitance (72 F g^{-1}) even at very high current density of 100 A g^{-1} indicative of the excellent high rate capability of the system. This capacitance far exceeds the recent literature capacitance values reported for other comparable architectures including aligned/patterned SWNTs thin films supercapacitors and microdevices even at much lower current densities (Figure 10.12d and Table 10.1).

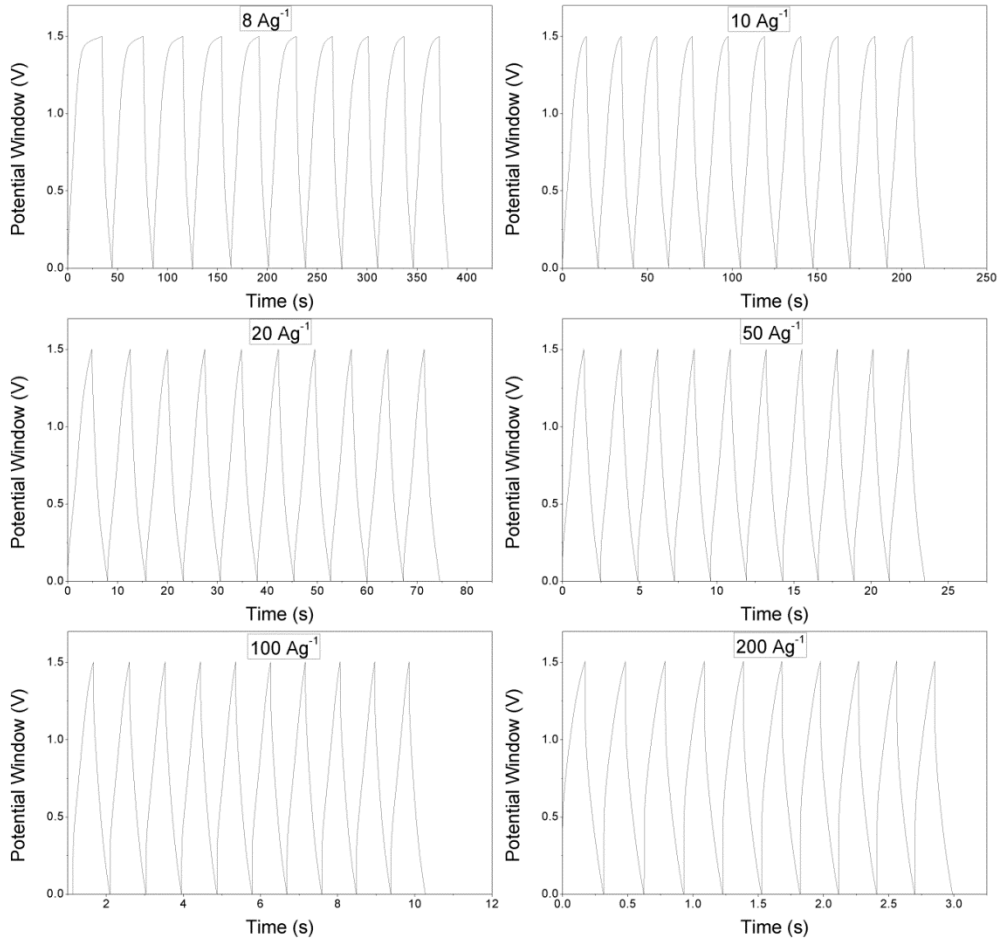

Figure 10. 14. Galvanostatic charge-discharge curves at different current densities.

Table 10. 1. Specific capacitance of ordered SWNTs films prepared in this study against previous reports on pristine or functionalized SWNTs thin films (either entangled or ordered).

Material	**Electrolyte**	**Specific Capacitance (F g^{-1})**	**Reference**
Ordered SWNTs films	1M H_2SO_4	107 @ 8 A g^{-1} 94 @ 10 A g^{-1} 309 @ 20 mV sec^{-1} 71.4 @50 A g^{-1}	Current study
Printed Thin Film Supercapacitors	1M H_2SO_4	36 @ 30 A g^{-1}	46
Bucky Paper	1M H_2SO_4	80 @ 1 A g^{-1}	46
SWNTs Films without Strain	Water based gel electrolyte ($PVA+H_3PO_4$)	48 @ 10 A g^{-1}	47
120% Strained SWNTs Films	Water based gel electrolyte ($PVA+H_3PO_4$)	53 @ 10 A g^{-1}	47
Ultra-thin SWNTs films	1M LiClO4 in EC, DEC and DMC	22.5 @ 6.5 A g^{-1}	48
Compact SWNTs Thin Films	1M LiClO4 in EC, DEC and DMC	35 @ 20 mV sec^{-1}	49
SWNTs Film	1M H_2SO_4	153.2 @ 2mV sec^{-1}	50
HiPco SWNTs Film	1M Et4NBF4/propylene carbonate	45 three electrode cell	51
Aligned Forests of SWNTs	1M Et4NBF4/propylene carbonate	13 @ 2 A g^{-1} 9 @ 10 A g^{-1}	51
Aligned Forests of SWNTs with MMC	1M Et4NBF4/propylene carbonate	80 @ 1 A g^{-1}	52
Aligned Forests of SWNTs without MMC	1M Et4NBF4/propylene carbonate	60 @ 1 A g^{-1}	52
Vertically Aligned SWNTs	6M KOH	52 @ 5 mV sec^{-1}	53

Functionalized CNTs	1 M lithium perchlorate ($LiClO_4$) in propylene carbonate (PC)	50 @ 0.3 A g^{-1} 120 @ 20 mV sec^{-1}	[54]
Nanotube Paper	1M NaCl	40 @ 5 mV sec^{-1}	[55]
Nanotube Paper	7M H_2SO_4	90 @ 5 mV sec^{-1}	

Furthermore, Cyclic Votammetry (CV), as a potentiodynamic electrochemical measurement, was employed to further characterize the electrochemical performance of the prepared architecture over a range of 20 mV sec^{-1} to 5000 mV sec^{-1} (Figure 10.15a and Figure 10.16). The system showed a remarkable capacitance value of 309 F g^{-1} at the lower end of scan rate range (20 mV sec^{-1}), while still capable of delivering a capacitance value as high as 46 F g^{-1} at very high scan rate of 5 V sec^{-1} (Figure 10.14 and 10.15b).

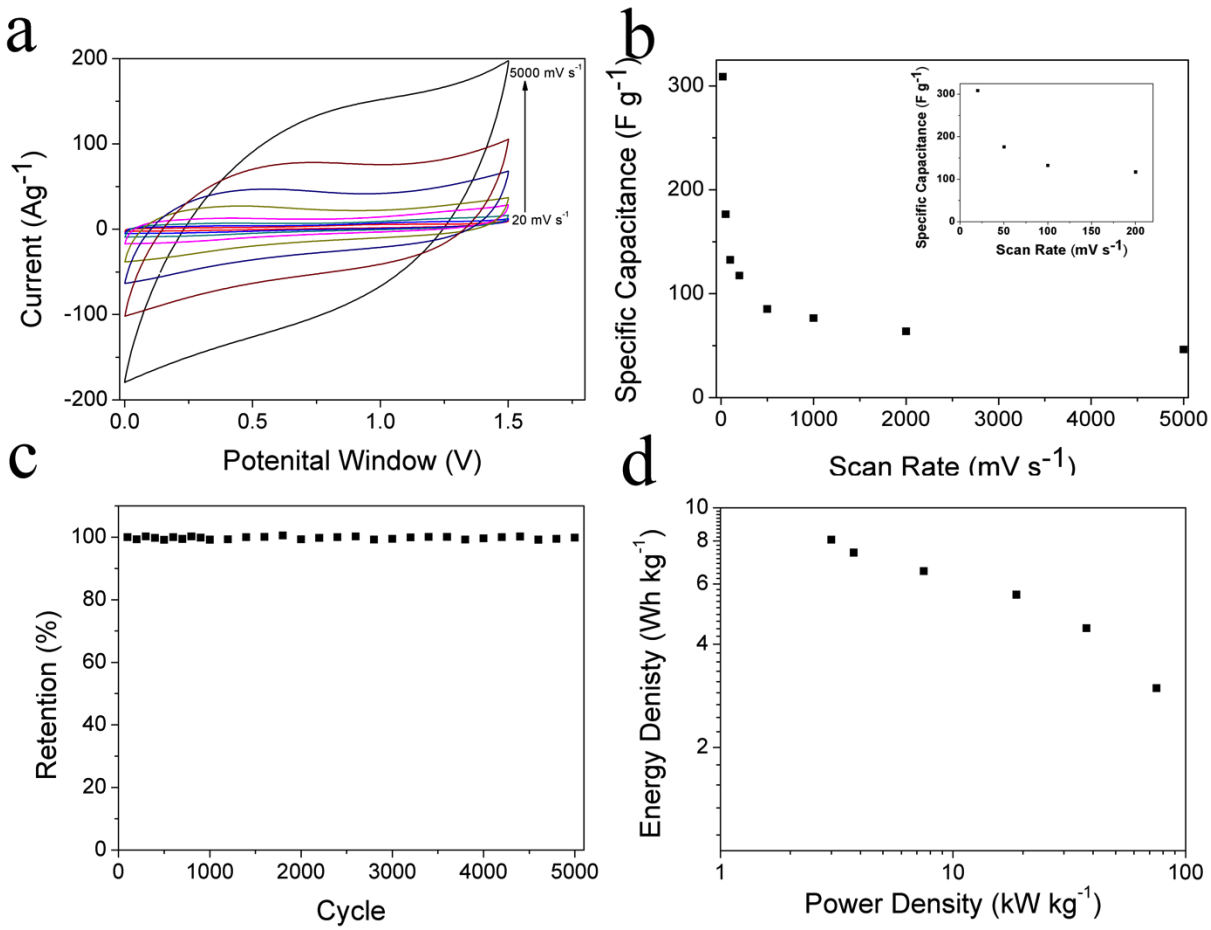

Figure 10. 15. Electrochemical capacitor: Design and performance in 1 M H_2SO_4 using a two-electrode symmetrical cell configuration. (a) Overlayed Cyclic voltammograms of the ordered sample up to a scan rate of 5000 mVs^{-1}. Even at such a high scan rate, the deviation from rectangular shape is not significant. (b) Calculated specific capacitance of the ordered system at scan rates. (c) Capacitance retention for 5000 cycles at 10 A g^{-1} current density demonstrating excellent cycle stability of the material. (d) Ragone plot for each evaluated current density.

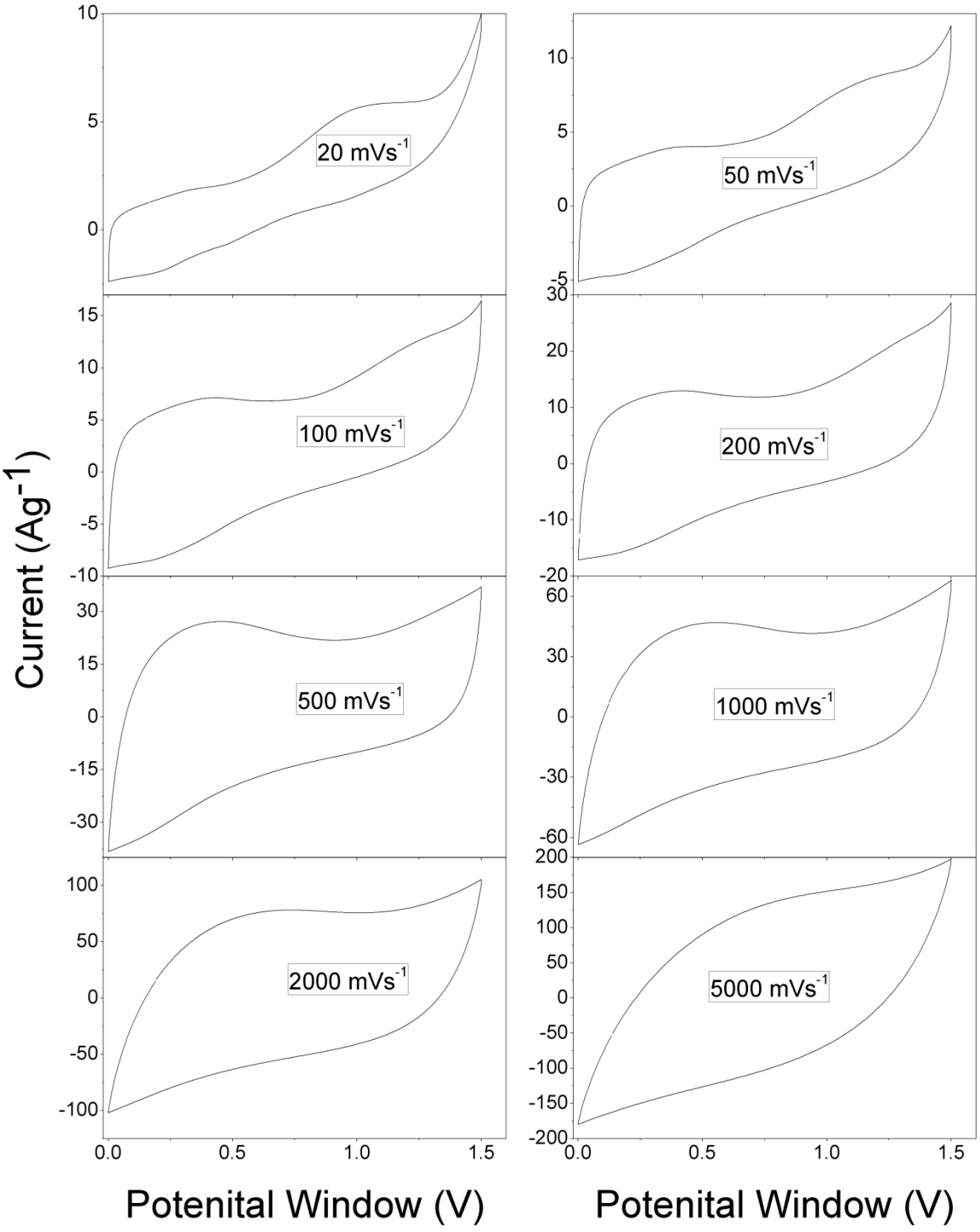

Figure 10. 16. Cyclic voltammograms at different scan rates.

This steady decrease with increasing scan rate is usually expected at very high scan rates due to intrinsic restricted aqueous diffusion in SWNTs pores at higher scan rates. The typical cyclic voltammograms in sulphuric acid presented a distorted rectangular shape with two broad peaks at around 0.4 V and 1 V more enhanced in CV curves obtained at lower scan rates. These peaks are associated with surface-bound redox reactions undergone by oxygen containing functionalities such as carboxylic acid and quinon, similar to those observed in the case of other nanotubes. The peak at around 0.4 V can be attributed to the transition between quinone/hydroquinone groups on the carbon material. The shape of the CV curve was maintained even upto a high scan rate of 5000 mV s^{-1} indicating good capacitive behaviour, rapid diffusion of electrolyte ions from the solution into the pores of the modified electrode and low ESR. It should be noted that the high conductivity of the ordered material coupled with its high porosity allows for the penetration by electrolyte ions to the electrode surface as supported by the shape of the CV curve at high scan rates. SWNTs can, therefore, act both as conducting wires providing a conductive path for movement of electrons and as nano-channels permitting the internal free flow of ions within them. Ordering SWNTs in this regard can substantially enhance the effective surface area accessible for ion exchange and ion movement by eliminating the entanglement and agglomeration of SWNTs. This leads to an increased charge storage capability as more channels for ion exchange are available in the system consequently resulting in facile diffusion of electrolyte. Furthermore, small SWNTs, with diameters less than 20 nm, are expected to yield higher double layer capacitance as they can afford higher energetic driving force for electron transfer. This effect can be more pronounced in the case of individual and fully separated SWNTs. Bundling of SWNTs can inhibit the diffuse double layer to extend further into the solution, however, based on the SEM pictures, no bundling of SWNTs can be observed in our case which might be partially responsible for the observed enhancement in

capacitance. It is proposed that a combination of these factors might be responsible for the observed enhancement in capacitance. The long-term cycle stability of supercapacitors is a critical requirement for practical applications. The electrodes were tested for 5000 cycles at a current density of 100 mV sec^{-1} and showed no attenuation (capacitance loss) suggesting the remarkable stability of the electrodes (Figure 10.15c). This outstanding cycling stability combined with excellent rate capability of the system (70% capacity retention at 100 A g^{-1} compared to the capacity recorded at 10 A g^{-1}) suggests good mechanical stability of the system. Device power and energy densities were also calculated at high current densities (8 A g^{-1}-200 A g^{-1}). The maximum device power and energy densities were calculated to be 75 kW kg^{-1} and 8 Wh kg^{-1} respectively in a modest potential window of 1V (Figure 10.15d).

10.5 Conclusion

In conclusion, we introduced a novel, yet, facile concept to process self-ordered one-dimensional (1D) nanoparticles through a scalable multi-level stigmergic –emergent self-organization process. As a proof of concept, we demonstrated, the long predicted but not yet realized, spontaneous formation of self-assembled biaxial nematic liquid crystals upon the addition of small amount of two dimensional ultra large graphene oxide to a model one dimensional material (SWNTs). We established that the complex collective behaviour of the mixture can enable the reversible autonomous fabrication of self-assembled geometrically functionalized materials with high order parameter in concentrations as low as (0.8 mg ml^{-1}). The self-assembled architecture showed an order parameter of 0.63 in the liquid form representing of its highly aligned structure. To understand the complex self-evolving nature of this behaviour, we tried to deduce the main regulatory principles governing the formation of such phases based on rheological and polarized

optical microscopy investigations. Rheological investigations revealed a history-dependant diachronic, self-driven morphogenesis in response to mechanical stimulation analogous to biological systems. Furthermore, the system showed a collective reversible gel formation in response to shear. It should be noted that the gel-formation was reversible and the system could be relaxed towards thermodynamically stable liquid like phase via simple agitation. The formation of such a self-organized, arrested, robust, yet semi-permanent gel network phase enabled us to construct highly ordered 3D architectures with a remarkable three-fold increase in electrochemical energy storage performance compared to their non-aligned counterparts.

10.6 REFERENCES

1 Whitesides, G. M. & Grzybowski, B. Self-Assembly at All Scales. *Science* **295**, 2418-2421, (2002).

2 Whitesides, G., Mathias, J. & Seto, C. Molecular self-assembly and nanochemistry: a chemical strategy for the synthesis of nanostructures. *Science* **254**, 1312-1319, (1991).

3 Zhang, Y., Lu, F., Yager, K. G., van der Lelie, D. & Gang, O. A general strategy for the DNA-mediated self-assembly of functional nanoparticles into heterogeneous systems. *Nat. Nanotechnol.* **8**, 865-872, (2013).

4 Zhang, S. *et al.* A self-assembly pathway to aligned monodomain gels. *Nat. Mater.* **9**, 594-601, (2010).

5 Sacanna, S. *et al.* Shaping colloids for self-assembly. *Nat. Commun.* **4**, 1688, (2013).

6 Raeburn, J., Zamith Cardoso, A. & Adams, D. J. The importance of the self-assembly process to control mechanical properties of low molecular weight hydrogels. *Chem. Soc. Rev.* **42**, 5143-5156, (2013).

7 Fong, C., Le, T. & Drummond, C. J. Lyotropic liquid crystal engineering-ordered nanostructured small molecule amphiphile self-assembly materials by design. *Chem. Soc. Rev.* **41**, 1297-1322, (2012).

8 Bisoyi, H. K. & Kumar, S. Liquid-crystal nanoscience: an emerging avenue of soft self-assembly. *Chem. Soc. Rev.* **40**, 306-319, (2011).

9 Jones, M. R. & Mirkin, C. A. Materials science: Self-assembly gets new direction. *Nature* **491**, 42-43, (2012).

10 Sasai, Y. Cytosystems dynamics in self-organization of tissue architecture. *Nature* **493**, 318-326, (2013).

11 FORREST, S. B. & HAFF, P. K. Mechanics of Wind Ripple Stratigraphy. *Science* **255**, 1240-1243, (1992).

12 Whitesides, G. M. & Boncheva, M. Beyond molecules: Self-assembly of mesoscopic and macroscopic components. *Proc. Natl. Acad. Sci. U. S. A.* **99**, 4769-4774, (2002).

13 Wang, Y. *et al.* Colloids with valence and specific directional bonding. *Nature* **491**, 51-55, (2012).

14 Harada, A., Kobayashi, R., Takashima, Y., Hashidzume, A. & Yamaguchi, H. Macroscopic self-assembly through molecular recognition. *Nat. Chem.* **3**, 34-37, (2011).

15 Camazine, S. *Self-organization in Biological Systems*. (Princeton University Press, 2003).

16 Gracias, D. H., Tien, J., Breen, T. L., Hsu, C. & Whitesides, G. M. Forming Electrical Networks in Three Dimensions by Self-Assembly. *Science* **289**, 1170-1172, (2000).

17 Reches, M. & Gazit, E. Casting Metal Nanowires Within Discrete Self-Assembled Peptide Nanotubes. *Science* **300**, 625-627, (2003).

18 Ouk Kim, S. *et al.* Epitaxial self-assembly of block copolymers on lithographically defined nanopatterned substrates. *Nature* **424**, 411-414, (2003).

19 Sorrenti, A., Illa, O. & Ortuno, R. M. Amphiphiles in aqueous solution: well beyond a soap bubble. *Chem. Soc. Rev.* **42**, 8200-8219, (2013).

20 Jalili, R. *et al.* Organic Solvent-Based Graphene Oxide Liquid Crystals: A Facile Route toward the Next Generation of Self-Assembled Layer-by-Layer Multifunctional 3D Architectures. *ACS Nano* **7**, 3981-3990, (2013).

21 Aboutalebi, S. H., Aminorroaya-Yamini, S., Nevirkovets, I., Konstantinov, K. & Liu, H. K. Enhanced Hydrogen Storage in Graphene Oxide-MWCNTs Composite at Room Temperature. *Adv. Energy Mater.* **2**, 1439-1446, (2012).

22 Chidembo, A. T. *et al.* Liquid Crystalline Dispersions of Graphene-Oxide-Based Hybrids: A Practical Approach towards the Next Generation of 3D Isotropic Architectures for Energy Storage Applications. *Part. Part. Syst. Charact.*, n/a-n/a, (2013).

23 Bisoyi, H. K. & Kumar, S. Discotic nematic liquid crystals: science and technology. *Chem. Soc. Rev.* **39**, 264-285, (2010).

24 Kim, F., Kwan, S., Akana, J. & Yang, P. Langmuir−Blodgett Nanorod Assembly. *J. Am. Chem. Soc.* **123**, 4360-4361, (2001).

25 Kumar, S. & Bisoyi, H. K. Aligned Carbon Nanotubes in the Supramolecular Order of Discotic Liquid Crystals. *Angew. Chem. Int. Ed.* **46**, 1501-1503, (2007).

26 Lagerwall, J. *et al.* Nanotube Alignment Using Lyotropic Liquid Crystals. *Adv. Mater.* **19**, 359-364, (2007).

27 Zan, X., Feng, S., Balizan, E., Lin, Y. & Wang, Q. Facile Method for Large Scale Alignment of One Dimensional Nanoparticles and Control over Myoblast Orientation and Differentiation. *ACS Nano* **7**, 8385-8396, (2013).

28 Zamora-Ledezma, C. *et al.* Carbon Nanotubes Induced Gelation of Unmodified Hyaluronic Acid. *Langmuir* **29**, 10247-10253, (2013).

29 Madsen, L. A., Dingemans, T. J., Nakata, M. & Samulski, E. T. Thermotropic Biaxial Nematic Liquid Crystals. *Phys. Rev. Lett.* **92**, 145505, (2004).

30 Kim, J. *et al.* Graphene Oxide Sheets at Interfaces. *J. Am. Chem. Soc.* **132**, 8180-8186, (2010).

31 Kim, J., Cote, L. J. & Huang, J. Two Dimensional Soft Material: New Faces of Graphene Oxide. *Acc. Chem. Res.* **45**, 1356-1364, (2012).

32 Kim, J. K. *et al.* (US Patent App. 13/803,282, 2013).

33 Aboutalebi, S. H., Gudarzi, M. M., Zheng, Q. B. & Kim, J.-K. Spontaneous Formation of Liquid Crystals in Ultralarge Graphene Oxide Dispersions. *Adv. Funct. Mater.* **21**, 2978-2988, (2011).

34 Aboutalebi, S. H. *et al.* Comparison of GO, GO/MWCNTs composite and MWCNTs as potential electrode materials for supercapacitors. *Energ. Environ. Sci.* **4**, 1855-1865, (2011).

35 Chidembo, A. *et al.* Globular reduced graphene oxide-metal oxide structures for energy storage applications. *Energ. Environ. Sci.* **5**, 5236-5240, (2012).

36 Moazzami Gudarzi, M. *et al.* Self-aligned Graphene Sheets-Polyurethane Nanocomposites. *MRS Proceedings* **1344**, (2011).

37 Davis, V. A. *et al.* Phase Behaviour and Rheology of SWNTs in Superacids. *Macromolecules* **37**, 154-160, (2003).

38 Jalili, R. *et al.* Formation and processability of liquid crystalline dispersions of graphene oxide. *Mater. Horiz.* **1**, 87-91, (2014).

39 Jalili, R. *et al.* Scalable One-Step Wet-Spinning of Graphene Fibers and Yarns from Liquid Crystalline Dispersions of Graphene Oxide: Towards Multifunctional Textiles. *Adv. Funct. Mater.* **10**, 5345–5354, (2013).

40 Jalili, R., Razal, J. M. & Wallace, G. G. Exploiting high quality PEDOT:PSS-SWNT composite formulations for wet-spinning multifunctional fibers. *J. Mater. Chem.* **22**, 25174-25182, (2012).

41 Jalili, R., Razal, J. M. & Wallace, G. G. Wet-spinning of PEDOT:PSS/Functionalized-SWNTs Composite: a Facile Route Toward Production of Strong and Highly Conducting Multifunctional Fibers. *Sci. Rep.* **3**, (2013).

42 Yousefi, N. *et al.* Self-alignment and high electrical conductivity of ultralarge graphene oxide-polyurethane nanocomposites. *J. Mater. Chem.* **22**, 12709-12717, (2012).

43 Zamora-Ledezma, C. *et al.* Anisotropic Thin Films of Single-Wall Carbon Nanotubes from Aligned Lyotropic Nematic Suspensions. *Nano Letters* **8**, 4103-4107, (2008).

44 Dalal, N. & Triggs, B. in *IEEE Computer Society Conference on Computer Vision and Pattern Recognition.* 886-893

45 Chen, D. T. N., Wen, Q., Janmey, P. A., Crocker, J. C. & Yodh, A. G. Rheology of Soft Materials. *Annu. Rev. Cond. Mat. Phys.* **1**, 301-322, (2010).

46 Di Michele, L. *et al.* Multistep kinetic self-assembly of DNA-coated colloids. *Nat. Commun.* **4**, (2013).

47 Naficy, S. *et al.* Graphene Oxide Dispersions: Tuning Rheology to Enable Fabrication. *Mater. Horiz.*, 10.1039/c1033mh00144j, (2014).

48 Zakri, C. *et al.* Liquid crystals of carbon nanotubes and graphene. *Phil. Trans. R. Soc. A* **371**, (2013).

49 Badaire, S. *et al.* Liquid Crystals of DNA-Stabilized Carbon Nanotubes. *Adv. Mater.* **17**, 1673-1676, (2005).

50 Puech, N. *et al.* Highly Ordered Carbon Nanotube Nematic Liquid Crystals. *J. Phys. Chem. C* **115**, 3272-3278, (2011).

51 Kaempgen, M., Chan, C. K., Ma, J., Cui, Y. & Gruner, G. Printable Thin Film Supercapacitors Using Single-Walled Carbon Nanotubes. *Nano Letters* **9**, 1872-1876, (2009).

52 Niu, Z. *et al.* Highly Stretchable, Integrated Supercapacitors Based on Single-Walled Carbon Nanotube Films with Continuous Reticulate Architecture. *Adv. Mater.* **25**, 1058-1064, (2013).

53 Niu, Z. *et al.* A Repeated Halving Approach to Fabricate Ultrathin Single-Walled Carbon Nanotube Films for Transparent Supercapacitors. *Small* **9**, 518-524, (2013).

54 Niu, Z. *et al.* Compact-designed supercapacitors using free-standing single-walled carbon nanotube films. *Energ. Environ. Sci.* **4**, 1440-1446, (2011).

55 Chen, J. H. *et al.* Electrochemical characterization of carbon nanotubes as electrode in electrochemical double-layer capacitors. *Carbon* **40**, 1193-1197, (2002).

56 Futaba, D. N. *et al.* Shape-engineerable and highly densely packed single-walled carbon nanotubes and their application as super-capacitor electrodes. *Nat. Mater.* **5**, 987-994, (2006).

57 Izadi-Najafabadi, A. *et al.* Extracting the Full Potential of Single-Walled Carbon Nanotubes as Durable Supercapacitor Electrodes Operable at 4 V with High Power and Energy Density. *Adv. Mater.* **22**, E235-E241, (2010).

58 Azam, M. A., Fujiwara, A. & Shimoda, T. Significant Capacitance Performance of Vertically Aligned Single-Walled Carbon Nanotube Supercapacitor by Varying Potassium Hydroxide Concentration. *Int. J. Electrochem. Sci* **8**, 3902-3911, (2013).

59 Park, S. K., Mahmood, Q. & Park, H. S. Surface functional groups of carbon nanotubes to manipulate capacitive behaviours. *Nanoscale* **5**, 12304-12309, (2013).

60 Barisci, J. N., Wallace, G. G. & Baughman, R. H. Electrochemical Characterization of Single-Walled Carbon Nanotube Electrodes. *J. Am. Chem. Soc.* **147**, 4580-4583, (2000).

61 Jalili, R. *et al.* Scalable One-Step Wet-spinning of Graphene Fibers and Yarns from Liquid Crystalline Dispersions of Graphene Oxide: Towards Multifunctional Textiles. *Adv. Funct. Mater.* **10**, 5345–5354, (2013).

Chapter 11: Conclusion and Future Work

11.1 Conclusion

11.1.1 Graphene oxide liquid crystals

The highly promised applications of graphene-based liquid crystals as a promising building block in different fields have not yet been realized mainly because of the practical limitations induced by water as the only medium in which graphene oxide liquid crystal is prepared. However, here, the discovery of solvophobic soft self-assembly of ultra-large liquid crystalline (LC) graphene oxide (GO) sheets in a wide range of organic solvents, many of which were not known to afford solvophobic self-assembly prior to this report, was demonstrated. This discovery could provide practical solutions to the processability of a wide range of materials that require organic solvents because of solubility issues and/or water sensitivity (i.e. metal oxides, polymers and nanomaterials) which is of both technological and fundamental interest for different applications. As an example, the LC behaviour of the as-prepared GO sheets in organic solvents enabled the dispersion and organization of substantial amounts of aggregate-free single walled carbon nanotubes (SWNTs, up to 10 wt. %) without any compromise in LC properties. The as-prepared LC GO-SWNTs dispersions were employed to achieve self-assembled layer-by-layer multifunctional 3D hybrid architectures comprising of individual SWNTs and GO with extraordinary mechanical properties (Young's modulus in excess of 50 GPa and tensile strength of more than 500 MPa). It is proposed that the expansion of the list of known solvents that can promote the self-assembly process and lyotropic liquid crystallinity acts as an enabling platform to tailor-make processable self-assembled, self-oriented graphene based hybrid composites with

large-area molecular ordering. This results in the expansion of micro/nanotechnology into areas other than micro/nanoelectronics.

11.1.2 Rheological properties

The rheological behaviour of graphene oxide (GO) dispersions and its microscopic origin still remain an unexplored area, despite of its importance for both fundamental and industrial applications. This challenge, if resolved, can serve as a platform to process these materials at industrially highly-scalable levels for a whole range of both novel and existing applications such as coatings, fillers, molecular electronics, wearables, smart garments, RDIF devices, printed electronics, organic field effective transistors and 3D bionic scaffolds. To that purpose, it was demonstrated that finite yield stress in ultra large GO dispersions occurs at a critical concentration approximately three orders of magnitude lower than the theoretical value for theoretical colloidal suspensions (ϕ_(this study)$\approx$ 2.2×10-4 vs. ϕ_c$\approx$ 0.5). This enabled the processing of this 2D material at the lowest concentration ever reported for any dispersions allowing the self-assembly of multi-functional architectures and inks which is critical for the advancement of multifunctional device fabrication methods. It was also shown that GO dispersions, as a model two dimensional soft material, exhibit a unique rich diverse rheological behaviour that constitutes them as a new class of soft-materials. Each of the unbinding rheological behaviours of GO dispersion can correspond to unique processing techniques, some of which have never been shown before possible, enabling the processing of this material based on its inherent complex flow properties. Compelling experimental evidence on why these unique characteristics represent a viable and substantive advance in tailor-making and processing GO dispersions in almost all industrially scalable processing methods including but not limited to a whole range of printing, spinning, and spraying techniques is also presented.

11.1.3 Electrochemical performance

The fibers and yarns produced based on fabrication protocols developed here were experimentally evaluated in terms of electrochemical performance. The high ion-accessible surface area and low ion transport resistance, as a result of maximizing the number of covalently bonded carbon atoms and significantly reducing the number of other atoms present at the system and attached to graphene sheets resulted in exceptional electrochemical performance (capacitances as high as 410 F g^{-1}/electrode in a practical two electrode configuration set-up). These graphene yarns, therefore, can lead the way to the realization of powerful next-generation multifunctional renewable wearable energy storage systems. The simplicity of the method used here and the abundance of graphene oxide precursors make these materials interesting and highly promising candidates for a range of applications such as wearable, light–weight multifunctional textiles and electronic gadgets and flexible energy storage devices to meet the demands of real-world energy storage systems.

11.1.4 Hydrogen storage performance and electrochemical performance of hybrid materials

The mechanisms involved in the intercalation procedure were fully discussed. The main concept behind intercalating one-dimensional spacers in between giant GO sheets represents a versatile and highly scalable route to fabricate devices with superior hydrogen uptake and electrochemical performance. It was also suggested that the reduction of graphene oxide can occur upon the addition of MWCNTs. Although the underlying mechanism is still unclear, the observed phenomena might be attributed to the always present oxidation debris on the surface of acid purified carbon nanotubes.

11.1.5 Stigmergic organization

It was highlighted that the indirect communication among components and medium in response to local stimuli leads to multi-step self-organization and consequently self-driven morphogenesis in the system. This controlled, yet facile, multi-step multi-level self-organization process enabled the fabrication of highly ordered unlimited length of self-assembled 3D architectures with an order parameter as high as S=0.87. Such high order parameter can have significant outcomes in processing and developing processing protocols for ordered 1D nanoparticles making the fabrication of complex, ordered macroscopic architectures possible. The simplicity of the method used here and the abundance of graphene oxide precursors make these materials interesting and highly promising candidates for a range of applications such as wearable, light–weight multifunctional textiles and electronic gadgets and flexible energy storage devices to meet the demands of real-world energy storage systems.

11.1.6 Future work

The generic properties reported here can be considered as a universal guideline to process different GO dispersions based on their rheological properties by advancing our fundamental knowledge of soft materials in general and by introducing this new class of soft materials. Furthermore, the fundamental insights accrued here can serve as the basis for the development of fabrication protocols for other two dimensional soft materials. The simplicity of the method used here and the abundance of graphene oxide precursors make these materials interesting and highly promising candidates for a range of applications such as wearable, light–weight multifunctional textiles and electronic gadgets and flexible energy storage devices to meet the demands of real-world energy storage systems.

Appendix I: High Performance Multifunctional Graphene Yarns: Towards Wearable All-Carbon Energy Storage Textiles

Fabrication of rGO Fiber Electrodes

The ability to simplify fabrication of textile based electrodes for use in a conventional supercapacitor device by spinning GO fiber yarns directly onto a current collector (titanium foil for this case) exemplifies the versatility of the fiber spinning of LC GO reported here. The gel-state GO fiber yarns conformed and adhered well to the substrate upon drying and annealing (this latter step also served as the protocol for reduction of GO) to prepare a high performance supercapacitor electrode. Furthermore, this direct-electrode preparation method eliminates several processing steps typically required in conventional assembly of such an electrode configuration. For instance, binders like Nafion or carbon black etc., typically combined with the active material to provide better conductivity and/or to improve adhesion to the current collector, are no longer required. Also, the associated steps required to achieve homogenous distribution of the active material within the binder is also eliminated, and processing parameters are minimized. It was also possible to weave textile and put on the top of charge collectors to fabricate a supercapacitor, as illustrated in Figure 5b.

Explanation on imbibition rate

It is the difference in imbibition rate, due to the capillary pressure gradient, that dominates the whole process. The imbibition rate is proportional to $(\frac{\sigma}{\mu})^{\frac{1}{2}}$.

Where k is a constant, σ is the surface tension of the spreading liquid and μ is the viscosity of the spreading liquid. In the case of solvent-non solvent method, the imbibition rate of the coagulant should be higher compared to the solvent and the ration should be higher than 1 to enable the wet-spinning process. In the case of acetone and water this ratio is 1.04 showing that the wet-spinning process is possible. However, increasing this ration by the addition of ions or surfactants to the solvent can result in a greater driving force behind the spinnability of a known dispersion consequently resulting in faster coagulation process.

Surface area measurements

Surface area of both GO and rGO (annealed at 220 °C) were measured using both titration method employing methylen blue. Surface area of GO and rGO was measured to be 2605 m^2g and 2210 m^2/g, respectively.

Surface area meausrements (BET-N_2)

In materials containing small pores lower than 2nm down to 1 nm BET-N2 surface area is overestimated as a result of capillary condensation at low relative pressures. In the contrast, when pores are smaller than 0.5 nm, which is the case here, the pore volume is hugely underestimated. As a guideline, whenever a type III isotherm is observed during BET experiment, it represents an extremely weak adsrobate-adsrbent interaction. Furthermore, Adsorption measurements using nitrogen at 77.4 K is difficult, because the filling of 0.5 - 1

nm pores occurs at P/Po of 10^{-7} to 10^{-5}, where the rate of diffusion and adsorption equilibration is very slow.

Surface area measurement (Methylene blue)

As described earlier N_2 adsorption method is unable to provide accurate surface area for GO and RGO samples. Therefore methylene blue (MB) dye adsorption in aqueous solution has been used to determine the surface area. Titration method by MB has been used for clay minerals and activated carbon generally by industries for several decades.

MB dye (formula $C_{16}H_{18}ClN_3S$), with a corresponding molecular weight of 319.87 g mol^{-1} is a cationic dye, $C_{16}H_{18}N_3S^+$, which strongly absorbs in large amounts onto the surface of negatively charged GO and RGO. The specific surface area of samples was calculated from the amount of absorbed MB on certain mass of adsorbent. The surface area covered by one methylene blue molecule is typically assumed to be 130 $Å^2$. [10] The value of specific surface is derived from the point of complete cation replacement determined on the titration curves showed in Figure . For this experiment 0.2 g of adsorbents were poured into a flask and 20 ml of 1 g L^{-1} of MB solution were added at regular intervals and the remnant concentration of MB in the solution was measured with UV-Vis spectrophotometer at 665 nm. Then the amount of MB added versus the amount of absorbed MB was plotted to identify the point of complete cation replacement (CPR shown as red points in Figure plots). The specific surface is calculated from the amount of absorbed MB at CRP point using equation S1.

$$S_s = \frac{m_{MB}}{319.87} A_V A_{MB} \frac{1}{m_s} \quad \text{(Eq. 1)}$$

Where m_{MB} is the mass of the absorbed MB at the point of complete cation replacement, m_s is the mass of GO and RGO samples, A_v is Avogadro's number (6.02×10^{23}/ mol), and A_{MB} is the area covered by one MB molecule (assumed to be 130 $Å^2$).

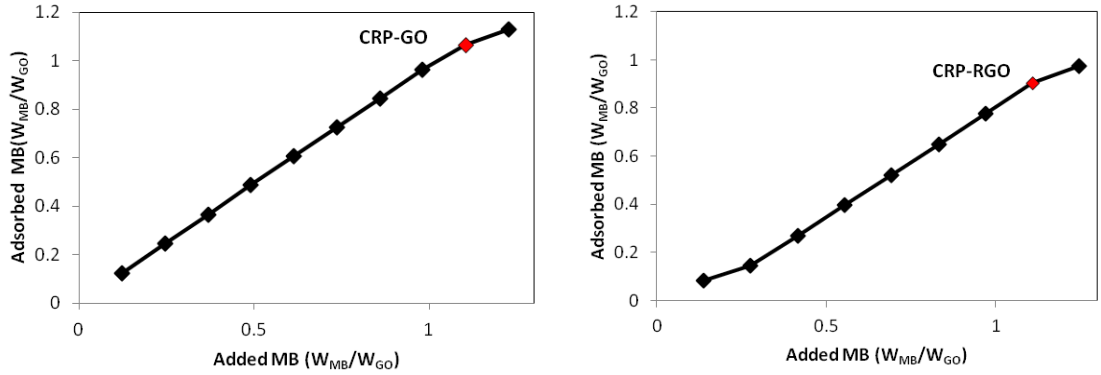

Figure S1. Determination of the point of complete cation replacement from the titration curve.

A summary of the surface areas obtained by the two techniques is presented in Table . There is a considerable difference between the surface area values reported by the two methods. The MB surface area for GO is 4 times higher and for RGO is 6 times higher than the ones reported from BET model. The specific surface area of both samples is in agreement with the theoretical surface area of graphene around 2630 $m^2 g^{-1}$.

Both techniques involve the sorption of an adsorbate (MB and nitrogen gas). The methylene blue technique involves high bonding energy (ionic Columbian attraction-chemisorption) and it is generally limited to a monolayer. In the nitrogen gas absorption, N_2 molecules are neutral and attracted to the surface by van-der Waals forces (physi-sorption), and multiple layers may form. This is schematically shown in Figure . The MB absorption method renders higher values of specific surface because of the strong bonding between MB and adsorbent surface and strong hydrogen bonding between water molecules and graphene plane in the aqueous solution.

Table S1. The comparison between surface areas obtained by N_2 adsorption (BET model) and MB absorption techniques

Sample	BET surface area (m^2 g^{-1})	MB surface area (m^2 g^{-1})
Graphene oxide	547.37	2605.5
Reduced graphene oxide	345.92	2210.2

Another disadvantage of the N_2 adsorption method is imposed by heating and degassing the specimen at high temperatures which can chemically alter the chemistry of the materials including the functional groups which causes dehydroxylation of the GO. Therefore for this study, it is concluded that the MB adsorption method is more accurate and reliable technique to measure the actual surface area of not only GO and RGO but also for all carbonaceous materials including carbon nanotubes and activated carbon.

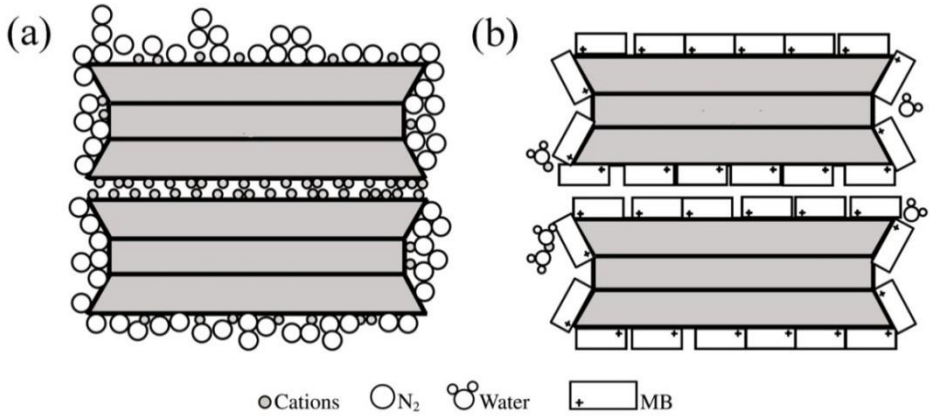

Figure S2. schematic illustration of MB wet adsorption and N_2 dry adsorption mechanism

REFERENCES

[1] R. Jalili, S. H. Aboutalebi, D. Esrafilzadeh, Shepherd Roderick L., Chen Jun, Aminorroaya-Yamini Sima, K. Konstantinov, Minett Andrew I. , J. M. Razal, G. G. Wallace, *Scalable One-Step Wet-spinning of Graphene Fibers and Yarns from Liquid Crystalline Dispersions of Graphene Oxide: Towards Multifunctional Textiles*, Adv. Funct. Mater. 2013, 10.

[2] C. Xiang, N. Behabtu, Y. Liu, H. G. Chae, C. C. Young, B. Genorio, D. E. Tsentalovich, C. Zhang, D. V. Kosynkin, J. R. Lomeda, C.-C. Hwang, S. Kumar, M. Pasquali, J. M. Tour, *Graphene Nanoribbons as an Advanced Precursor for Making Carbon Fiber*, ACS Nano 2013, 7, 1628.

[3] Z. Dong, C. Jiang, H. Cheng, Y. Zhao, G. Shi, L. Jiang, L. Qu, *Facile Fabrication of Light, Flexible and Multifunctional Graphene Fibers*, Adv. Mater. 2012, 24, 1856.

[4] Z. Xu, C. Gao, *Graphene chiral liquid crystals and macroscopic assembled fibres*, Nat Commun. 2011, 2, 571.

[5] J. Yan, T. Wei, B. Shao, Z. Fan, W. Qian, M. Zhang, F. Wei, *Preparation of a graphene nanosheet/polyaniline composite with high specific capacitance*, Carbon 2010, 48, 487.

[6] Y. Zhu, S. Murali, M. D. Stoller, K. J. Ganesh, W. Cai, P. J. Ferreira, A. Pirkle, R. M. Wallace, K. A. Cychosz, M. Thommes, D. Su, E. A. Stach, R. S. Ruoff, *Carbon-Based Supercapacitors Produced by Activation of Graphene*, Science 2011, 332, 1537.

[7] L. L. Zhang, X. S. Zhao, *Carbon-based materials as supercapacitor electrodes*, Chem. Soc. Rev. 2009, 38, 2520.

[8] J. Zhang, J. Jiang, H. Li, X. S. Zhao, *A high-performance asymmetric supercapacitor fabricated with graphene-based electrodes*, Energ. Environ. Sci. 2011, 4, 4009.

[9] M. F. El-Kady, R. B. Kaner, *Scalable fabrication of high-power graphene micro-supercapacitors for flexible and on-chip energy storage*, Nat Commun 2013, 4, 1475.

[10] J. C. Santamarina, K. A. Klein, Y. H. Wang, E. Prencke, *Specific surface: determination and relevance*, Canadian Geotechnical Journal 2002, 39, 233.

Appendix II: Some Notes of Importance

Introduction

In this part, I have added some points of importance mentioned by different reviewers during the review process. I have added this part, as it can provide some insights to parts of this work which cannot be directly incorporated into the main of body of this thesis.

Q1. As mentioned in Aboutalebi's paper (S. H. Aboutalebi, M. M. Gudarzi, Q. B. Zheng and J.-K. Kim, Adv. Funct. Mater., 2011, 21, 2978-2988) about the spontaneous formation of liquid crystals in ultralarge graphene oxide dispersions, the presence of smaller fragment GO sheets in large size graphene dispersion is inevitable due to breakages during the preparation process. The present method to produce difference size of GO is based on sonication bath. Thus, the SEM method to calculate size of GO is not sufficient, because it is difficult to visualise smaller size of GO under low magnification mode of SEM. I suggest the authors carry out DLS study to confirm the size distribution within the whole dispersion.

A1. The point the reviewer has raised about the existence of smaller fragment GO sheets is correct. However, with respect, we obtained SEM micrographs at different magnifications ranging from low magnification as low as 900x to high magnifications as high as 10000x covering the whole range of dimensions to cover even submicron sheet sizes. Therefore, we have been able to carry out the complete size characterization of the as-prepared materials.
It should also be noted that the only technique that can be used to directly observe particle size distribution is microscopy. All other techniques are sensitive to shape.

As for performing Dynamic light scattering (DLS) studies which is a known method to be used to determine the size distribution profile of small particles in suspensions there are some points that should be considered:

1- First and foremost DLS is limited to a maximum size of 8μm where two phases have similar density and usually less than 600-700 nm for carbon based materials where the theoretical density is calculated to be 2.2 g cm^{-3}. Therefore, DLS is not suitable for use here.

2- Since DLS essentially measures fluctuations in scattered light intensity due to diffusing particles, it can only calculate the hydrodynamic radius of a spherical particle or at least a 3D particle through the Stokes–Einstein equation and not the real dimension.

3- The hydrodynamic diameter of a nonspherical particle is the diameter of a sphere that has the same translational diffusion speed as the particle. If the shape of a particle changes in a way that affects the diffusion speed, then the hydrodynamic size will change. For example, small changes in the length of a rod-shaped particle will directly affect the size, whereas changes in the rod's diameter, which will hardly affect the diffusion speed, will be difficult to detect.

4- The DLS calculation is based on Rayleigh scattering and Mie Theory. It implies that If the particles are small compared to the wavelength of the laser used (typically less than $d = \lambda/10$ or around 60nm for a He-Ne laser), then the scattering from a particle illuminated by a vertically polarised laser will be essentially isotropic, i.e. equal in all directions. The Rayleigh approximation tells us that $I \alpha d6$ where I = intensity of light scattered, d = particle diameter. The d6 term tells us that a 1000nm particle will scatter 106 or one million times as much light as a 100 nm particle. Hence there is a danger that the light from the larger particles will swamp the scattered light from the smaller ones. This d6 factor also means it is difficult with DLS to measure, say, a mixture of 10000nm and 100nm particles because the contribution to the total light scattered by the small particles will be extremely small.

Therefore, the use of DLS here where we have significant fraction of large size sheets and a distribution of large size and small size sheets, would not be appropriate.

Q2. In the solvents replacement process (Five cycles), the ultimate solvents in GO liquid crystalline dispersions should have some water inside. Especially in acetone and THF, the existence of water has great influence on the solubility of GO. I recommend that the author can prepare dried GO fluffy foams first and dispersed in the aim solvents to investigate the liquid crystalline behaviours to get more solid conclusions.

A2. The water free nature of our as-prepared LC GO in organic solvents is ensured by the fact that SWNTs do not agglomerate when they are added to the as-prepared LC GO in organic solvents. It should be pointed out that the presence of even very small amount of water in LC GO dispersions results in aggregation of SWNTs which does not happen in our case indicating the water free nature of our as-prepared LC GO. It is also supported by our TGA graphs presented in which shows a completely different behaviour in case of water compared to other solvents. However, we do not rule out the possibility that very small amount of water might be present in our as-prepared dispersions.

We also wish to respectfully point out that preparing dried GO fluffy foams first and dispersing them again needs sonication which inevitably results in the breakage of GO sheets resulting in the alteration of the final liquid crystalline properties via changing the concentration range in which the liquid crystalline properties can be obtained. Furthermore, even doing so, does not ensure the water free nature of as-prepared LC –GO. Because GO is known to be prone to moisture and water adsrobance.

Q3. The criteria of the LC behaviour are ambiguous. How are the critical concentrations of the LC behaviour in different solvents same? Is there any possibility that it comes from experimental errors?

A3. With due respect, the criteria for the formation of LC domains are not ambiguous at all. The main important factors which influence the critical concentration are sheet size and polydispersity which are constant for all of the samples. The critical concentration is calculated irrespective of the solvent in which nematic LC forms.

The critical theoretical volume fraction (Φ) for the transition between isotropic to nematic phase can be calculated based on Equation 1 which served as a model system for liquid crystal phases of charged colloidal platelets, 4-5

$$\Phi = \frac{3}{8}\sqrt{3}\frac{L}{D}\frac{1+\sigma^2}{1+3\sigma^2}\rho D^3 \qquad (1)$$

The dimensionless number density (ρD3) was experimentally found to be ρisoD3=2.7 and ρnemD3=4.3 for isotropic and nematic transition concentrations, respectively. However, there are some assumptions in this model which should be taken into account for any further improvement of the theoretical foundation. These assumptions state that the particles are rigid and the diameter distribution is symmetric.

It should be noted that these concentrations, although the lowest filler content ever reported for the formation of liquid crystals from any colloid, are still higher than the theoretical biphasic region between 0.05 to 0.09 mg ml^{-1} calculated for rigid platelets (see supporting information for details). This discrepancy can be attributed to the flexible nature of the monolayer GO sheets and their tendency of wrinkling especially in the presence of attached functional groups. However, as we mentioned in the main text" the interplay between the hydrogen bonding and the Gordon parameter can effectively determine: (i) whether an organic solvent can induce the self-assembly process, and (ii) the lowest possible concentration in which spontaneous self-

organization can occur" which might be the reason for the very slight difference for the observation of nematic LCs in different organic solvents.

Q4. As the authors said, the alignment of fibril will improved the mechanical strength of fiber. However, the control GO paper also has aligned GO sheet, so the improvement of mechanical property by incorporation of SWCNT is not induced by the alignment. Incorporation of SWCNT in GO film seems to decrease the mechanical performance intuitively. It may decrease the contact between GO layers by insertion of SWCNT, so the shear force between the GO sheets can be reduced unless the interaction between CNTs and GO is high enough. It can also act as a crack initiation point. Therefore, the result is quite exceptional and required to be explained.

A4. The as-prepared LC GO-SWNTs dispersions were employed to achieve self-assembled layer-by-layer multifunctional 3D hybrid architectures comprising of SWNTs and GO by simply casting the hybrid composites.

However, in the case of mechanical properties, SWNTs act as bridging components between individual GO sheets. As the GO sheets are not strongly attached together, reinforcing them with SWNTs can result in an overall boost in mechanical properties. SWNTs can bridge individual GO sheets and therefore increase the shear force between GO sheets. Furthermore, the most important limitation of using SWNTs as reinforcing agents is the intertube and interfacial slippage within bundles. The poor load transfer within bundles results in interfacial slippage as the effective moduli and strength for bundles are far below those expected for individual SWNTs. The individual nature of SWNTs reported in our study, as evident in high resolution SEM figures and the well-resolved inter-band transitions in the UV/Vis-near-IR spectra of the SWNTs dispersion before and after the addition of LC GO, ensures that the shear

slippage of nanotubes within the bundle does not occur and the mechanical properties of SWNTs used in this study are close to theoretical values resulting in an overall enhancement of the final composite properties.

Q5. There is a very large difference exists between the mechanical properties of the plain GO paper and the GO/CNT hybrid. Please explain this result in more detail. Is it consistent with theory or literature?

A5. In the case of mechanical properties, SWNTs act as bridging components between individual GO sheets. As the GO sheets are not strongly attached together, reinforcing them with SWNTs can result in an overall boost in mechanical properties. SWNTs can bridge individual GO sheets and therefore increase the shear force between GO sheets. Furthermore, the most important limitation of using SWNTs as reinforcing agents is the intertube and interfacial slippage within bundles. The poor load transfer within bundles results in interfacial slippage as the effective moduli and strength for bundles are far below those expected for individual SWNTs. The individual nature of SWNTs reported in our study, as evident in high resolution SEM figures presented in Figure 5 and the well-resolved inter-band transitions in the UV/Vis-near-IR spectra of the SWNT dispersion before and after the addition of LC GO, ensures that the shear slippage of nanotubes within the bundle does not occur and the mechanical properties of SWNTs used in this study are preserved resulting in an overall enhancement of the final composite properties.

Q6. Could the author give the definition of what they call the “d-spacing”. In general the d-spacing corresponds to the periodic distance in a layered structure. It should be substantially

greater than the thickness of the graphene flakes since there is some solvent in between the sheets. Can the authors clarify this point?

A6. The change in the apparent thickness of GO sheets as a result of bonding with different solvents can also be confirmed by measuring the interlayer d-spacing of GO sheets in cast dried films made from various solvent based GO. XRD measurements were performed to evaluate the effect of the solvents on the interlayer d-spacing of GO films. The process of making GO in water or organic solvents is accompanied by an increase in the d-spacing between the graphene layers from about 0.34 nm to ≈ 0.8–1.1 nm which is related to the degree of oxidation and the hydration level (in the case of GO prepared in water) or the bonding of other solvent molecules to graphene sheets. The d-spacing shows the interlayer distance between individual GO sheets in the paper material that are oriented perpendicularly to the diffraction plane. Therefore, the peak in the XRD of our as-prepared GO films corresponds to the layer-by-layer distance (d-spacing) of each sample prepared in each organic solvent according to the Bragg's law.

This value corresponds with AFM results. The reason is while you are probing the surface with AFM tip, you are actually measuring the thickness of the graphene sheet with bound solvent molecules on both surfaces. Resulting in a correct estimate of the sheet sizes which go hand in hand with XRD results. The same results are reported in a number of papers for the case of GO prepared in water. As mentioned in the manuscript: the measured d-spacing values were also in good agreement with the measured GO sheet thickness from AFM results. Therefore, we suggest that the individual GO platelets are interlinked via a non-uniform network of hydrogen bonds mediated by oxygenated functional groups and solvent molecules.

Q7. It is indicated in page 10 and in the conclusion that the formation of liquid crystal is associated to a loss of entropy. This is not correct. Actually according to Onsager's theory, there is a gain of entropy when the particles adopt a long range orientational at high concentration. The loss of rotational entropy is in fact compensated by a greater gain of packing (or translational) entropy. Can the authors check this point?

A7. Onsager only considered completely rigid rods. In contrast, in our system, GO is flexible, a property associated with configurational entropy. In the nematic phase, all GO sheets are more or less parallel to the director, which leads to a considerable loss in configurational entropy. This entropy replaces the orientational entropy for rods and was first derived by Khokhlov and Semenov as an extension of the Lifshitz theory for flexible polymers to stiff polymers. Furthermore, here we are dealing with very long carbon chains, so the translational entropy per persistence length unit is small.

In contrast to a hard rigid rod, a semi-flexible chain like GO loses much more entropy, mainly because each segment of the chain loses configurational entropy while a rigid particle only loses orientational entropy as a whole. Furthermore, the effects of electrostatic interactions and steric hindrance among sheets are not adequately considered in the theoretical framework. It should also be noted that both these effects can result in a greater gain of packing (or translational) entropy. Another contributing factor which is often neglected is the effect of solvent molecules. Solvent molecules are integral to the structural formation of LC GO dispersions as they disturb the particle interaction as a result of the strong electrostatic repulsion forces following Coulomb's inverse-square law.

It should also be noted that the steric hinderance itself can result in a greater gain of packing (or translational) entropy. Therefore, the statement given in the text is fundamentally correct.

However, for the sake of consistency, we replaced loss of entropy with the loss of rotational entropy in the main text.

Publications

Direct Results Stemmed from this thesis

*Denotes equal contribution

2014

1. **S. H. Aboutalebi**, R. Jalili, K. Konstantinov, P. C. Innis, *Multistep multilevel self-organization of 1D nanoparticles: Towards stigmergic emergent-intelligence,* submitted to Nature Communications.

2. **S. H. Aboutalebi***, R. Jalili*, D. Esrafilzadeh, M. Salari, Z. Gholamvand, S. Aminorroaya-Yamini, K. Konstantinov, R. L. Shepherd, J. Chen, S. E. Moulton, P. C. Innis, A. I. Minett, J. M. Razal and G. G. Wallace, *Multifunctional graphene yarns: Towards wearable all-carbon energy storage textiles,* ACS Nano **DOI:** 10.1021/nn406026z.

3. **S. Naficy*, R. Jalili***, **S.H. Aboutalebi***, R. A. Gorkin III, K. Konstantinov, P. I. Innis, G. M. Spinks, P. Poulin, G. G. wallace, *Graphene oxide dispersions: tuning rheology to enable fabrication,* Materials Horizons, 2014.

4. **Jalili, R.***, **S.H. Aboutalebi***, D. Esrafilzadeh, K. Konstantinov, J.M. Razal, S.E. Moulton, and G.G. Wallace, *Formation and processability of liquid crystalline dispersions of graphene oxide.* Materials Horizons, 2014. **1**(1): p. 87-91.

5. Chidembo, A. T., **S. H. Aboutalebi**, Ch. Jafta, K. Konstantinov, H. K. Liu, and K.Ozoemena, *In-situ engineering of urchin-like reduced graphene oxide-Mn2O3/Mn3O4 nanostructures for supercapacitors,* RSC Advances, 2014. **4**(2): p. 886-892.

6. Chidembo, A. T., **S. H. Aboutalebi**, K. Konstantinov, D. Wexler, H. K. Liu, and S. X. Dou,*Spray Pyrolysis of liquid crystalline dispersions of graphene oxide based hybrids: a practical approach towards next generation of 3D isotropic architectures for energy storage applications,* Particle and Particle Systems Characterization, 2014.

2013

7. Jalili, R., **S.H. Aboutalebi**, D. Esrafilzadeh, R.L. Shepherd, J. Chen, S. Aminorroaya-Yamini, K. Konstantinov, A.I. Minett, J.M. Razal, and G.G. Wallace, *Scalable One-Step Wet-Spinning of Graphene Fibers and Yarns from Liquid Crystalline Dispersions of Graphene Oxide: Towards Multifunctional Textiles.* Advanced Functional Materials, 2013. **23**(43): p. 5345-5354.

8. **Jalili, R.***, **S.H. Aboutalebi***, D. Esrafilzadeh, K. Konstantinov, S.E. Moulton, J.M. Razal, and G.G. Wallace, *Organic Solvent-Based Graphene Oxide Liquid Crystals: A Facile Route toward the Next Generation of Self-Assembled Layer-by-Layer Multifunctional 3D Architectures.* ACS nano, 2013. **7**(5): p. 3981-3990.

9. De Silva, K., **S. Aboutalebi**, X. Xu, X. Wang, W. Li, K. Konstantinov, and S. Dou, *A significant improvement in both low and high field performance of MgB_2 superconductors through graphene oxide doping.* Scripta Materialia, 2013. **69**(6): p. 437-440.

2012

10. **Aboutalebi, S.H.,** S. Aminorroaya-Yamini, I. Nevirkovets, K. Konstantinov, and H.K. Liu, Enhanced Hydrogen Storage in Graphene Oxide-MWCNTs Composite at Room Temperature. Advanced Energy Materials, 2012.

11. Yousefi, N., M.M. Gudarzi, Q. Zheng, **S.H. Aboutalebi**, F. Sharif, and J.-K. Kim, *Self-alignment and high electrical conductivity of ultralarge graphene oxide–polyurethane nanocomposites.* Journal of Materials Chemistry, 2012. **22**(25): p. 12709-12717.

12. Chidembo, A., **S.H. Aboutalebi**, K. Konstantinov, M. Salari, B. Winton, S.A. Yamini, I.P. Nevirkovets, and H.K. Liu, *Globular reduced graphene oxide-metal oxide structures for energy storage applications.* Energy & Environmental Science, 2012. **5**(1): p. 5236-5240.

2011

13. **Aboutalebi, S.H.,** M.M. Gudarzi, Q.B. Zheng, and J.K. Kim, Spontaneous formation of liquid crystals in ultralarge graphene oxide dispersions. Advanced Functional Materials, 2011. 21(15): p. 2978-2988.

14. **Aboutalebi, S.H.**, A.T. Chidembo, M. Salari, K. Konstantinov, D. Wexler, H.K. Liu, and S.X. Dou, *Comparison of GO, GO/MWCNTs composite and MWCNTs as potential electrode materials for supercapacitors.* Energy & Environmental Science, 2011. **4**(5): p. 1855-1865.

Indirect Results Stemmed from this thesis

1. M. Salari, **S.H. Aboutalebi,** A. T. Chidembo, P. C. Innis, K. Konstantinov, H.K. Liu, P, schmuki, *Design of Self-assembled TiO2 Architectures: Towards Hybrid Nanotubular Interfaces,* Physica Status Solidi A: Applications and Materials Science, Advanced Materials Physics Section, 2014.

2. Salari, M., **S. H. Aboutalebi**, A. T. Chidembo, K. Konstantinov, H. K. Liu, *Surface Engineering of Self-Assembled TiO2 Nanotube Arrays a Practical Route Towards Energy Storage Applications,* Journal of Alloys and Compounds 2014. **4**(2): p. 886-892.

3. Salari, M., **S.H. Aboutalebi**, A.T. Chidembo, I.P. Nevirkovets, K. Konstantinov, and H.K. Liu, *Enhancement of the electrochemical capacitance of TiO2 nanotube arrays through controlled phase transformation of anatase to rutile.* Physical Chemistry Chemical Physics, 2012. **14**(14): p. 4770-4779.

4. Salari, M., **S. Aboutalebi**, K. Konstantinov, H. Liu, K. Lee, S. Deng, H. Fan, S. Mhaisalkar, H. Tan, and E. Tok, *ZrO2-WO3 Mixed Anodic Oxide Nanotubular Arrays as Electrochemical Capacitors Stuart R. Whitman and Krishnan S. Raja Department of Chemical and Materials Engineering University of Idaho, Moscow, Idaho 83844-3024.* Nanoscale, 2012. **4**: p. 2958-2961.

5. Salari, M., **S.H. Aboutalebi**, K. Konstantinov, and H.K. Liu, *A highly ordered titania nanotube array as a supercapacitor electrode.* Physical Chemistry Chemical Physics, 2011. **13**(11): p. 5038-5041.